

# Improvements in Multi-physics and Multi-scale Methodologies for Safety-related Investigations of Pressurized Water Reactors within the NURESIM Platform

Zur Erlangung des akademischen Grades

Doktor der Ingenieurwissenschaften (Dr.-Ing.)

Der Fakultät für Maschinenbau  
Karlsruher Institut für Technologie (KIT)

genehmigte

Dissertation

von

M.Sc.-Ing. Manuel Calleja Reyna  
aus Tequesquitengo, Mexiko

Tag der mündlichen Prüfung: 22 März, 2013.

Hauptreferent: Prof. Dr.-Ing. Robert Stieglitz  
Karlsruher Institut für Technologie (KIT)

Korreferent: Univ.-Prof. Rafael Macián-Juan, Ph.D.  
Technische Universität München (TUM)



1. Hauptreferent: Prof. Dr.-Ing. Habil Robert Stieglitz  
Karlsruher Institut für Technologie (KIT)
2. Korreferent: Univ.-Prof. Rafael Macián-Juan, Ph.D.  
Technische Universität München (TUM)
- Betreuung: Dr.-Ing. Victor Sánchez Espinoza  
Karlsruher Institut für Technologie (KIT)



*A mi padre, Oscar, mi mejor amigo y compaero.*



# ACKNOWLEDGEMENT

First and foremost, I would like to express my deep gratitude to Professor Dr. Robert Stieglitz and Dr. Victor Sanchez, my research supervisors, for their patient guidance, encouragement and useful critiques of the research work. Dr. Sanchez trusted in me and had always time to discuss technical and personal issues giving always wise solutions, fact that I will always appreciate and acknowledge. I am very grateful to Professor Dr. Rafael Macián, from the Technical University Munich (TUM), which accepted to be one my thesis supervisors. I want also to thank the support provided by my technical advisor, Dr. Philipp Oberle from EnBW, who provided me with useful advices and discussions. I also have to thank the Institute of Neutron Physics and Reactor Techniques (INR) from the Karlsruhe Institute of Technology (KIT), for providing me with a good environment and facilities to complete this project.

I wish to thank two of my colleagues, Dr. Javier Jimenez and Dr. Uwe Imke, for their valuable technical support on this work. Without the invaluable help of Dr. Jimenez this Ph.D. work would have been never accomplished. I appreciate the time he spent to advise me about technical matters and his will to improve the work done. I wish to acknowledge the help provided by Dr. José Herrero, from the Polytechnic University Madrid (UPM), which contributed substantially for the development of the work during my second stay at the UPM.

My special thanks are extended to EnBW, sponsoring organization of my Ph.D. work and its staff, including Dr. Tim Vogel and Mrs. Regina Lübben. I would like to show my gratitude to the members of the Institute of Nuclear Fission of the UPM, especially Dr. Carolina Ahnert, who gave me the opportunity to work at her institute and Dr. Nuria Garcia, who provided me with fruitful discussions concerning my technical work.

Deepest gratitude is also due to the members of the INR. Moreover, I am indebted to many of my colleagues at KIT, particularly Ana Berkhan, Dr. Armando Gomez, Christoph Hartmann, Cristian Garrido, Jorge Pérez, Markus Schlenker, Roberto López, Rodrigo Gómez, Richard Molitor, Sara Pérez and Dr. Wadim Jäger.

Last but not least, I want to thank and dedicate this Ph.D. work to my parents, Oscar and Maricela, who have supported me unconditionally during all my life.



# ABSTRACT

In the frame of this doctoral thesis, two main contributions were achieved. The first one is based on the integration of a thermal-hydraulic sub-channel code named SUBCHANFLOW inside the NURESIM platform and its coupling with the reactor dynamic code COBAYA3. This coupling is done for studying the core behavior of light water reactors as well as their performance and assessment inside a user friendly and innovative platform. The need of coupled neutronic/thermal-hydraulic schemes is reflected on the necessity for predicting accurately local safety parameters, e.g. local temperatures, which are influenced by heterogeneous fuel compositions and geometrical configurations of different fuel assembly designs, among others. This coupling scheme is extended to regular square nodal and cell based calculations, as well as nodal hexagonal whole core solutions.

The second contribution is focused on the development of hybrid schemes (non-conform geometry) for both neutronic and thermal-hydraulic domains. The hybrid approach is of special interest because it allows the combination of coarse (nodal/channel) and fine (cell/sub-channel) nodalizations of both the neutronic or thermal-hydraulic domains applied only to specific regions of the core. According to this, detailed simulations at cell level are only applied in selected regions of the core where localized perturbations of e.g. the power, are expected to happen. This innovative methodology allows local mesh refinements while retaining flexibility as well as a physical consistent solution within an acceptable time scale. Only steady state hybrid solutions are envisaged in the frame of this dissertation, in addition to the coupling of both codes dealing with hybrid discretizations.

To achieve these contributions, the NURESIM platform (based on the open source software SALOME) was used as the coupling interface. The objective of this platform is to provide a new generation of nuclear reactor simulation tools with the best physical thermo-mechanical, thermal-hydraulic and neutron physical models and coupling approaches based on the novel mesh superposition approach, involving automatic interpolation tools for the information exchange. The project also develops capabilities for multi-scale and multi-physics calculations, facilitating the use in a generic environment dealing with a wide variety of problems. The coupling within SALOME enables a dynamic data exchange, suitable for specific neutronic/thermal-hydraulic feedback exchange.

Several experiments and benchmarks were used in order to verify and validate the coupling of COBAYA3 and SUBCHANFLOW inside the simulation platform. The modeling of these benchmarks is presented for steady state and transient solutions at fuel assembly level, including mini-cores (square geometries) and full cores (square and hexagonal geometries). The testing of stand alone hybrid meshes in the thermal-hydraulic and neutronic solution domains also includes these types of models.

The obtained results demonstrate the prediction capability of the developed coupled scheme for different reactor conditions such as steady states at hot full power and hot zero power, as well as and transient scenarios. These transient scenarios involve fast reactivity insertion accidents and long term simulations, suitable for studying the thermal-hydraulic impact on the neutronic side after strong and localized perturbations. The results are compared with both reference solutions and nuclear plant data e.g. for hexagonal core geometries. Simulations involving boron dilution scenarios were performed for testing the boron transport model implemented in SUBCHANFLOW. Finally, the new hybrid simulation capability of COBAYA/SUBCHANFLOW developed in this doctoral thesis is shown by the analysis of a full 3D PWR MOX/UO<sub>2</sub> core and by comparing the obtained results with the ones calculated by the whole core pin-by-pin solution provided by the COBAYA/COBRA-TF code using the domain decomposition approach.

# KURZFASSUNG

Die vorliegende Arbeit stellt zwei Beiträge zu den Multi-Physik und Multi-Skalen Methoden zur Untersuchung von Leichtwasserreaktoren in der NURESIM Plattform dar.

Der erste Teil der Arbeit stellt die Implementierung des thermohydraulischen Unterkanalprogramms SUBCHANFLOW in die NURESIM Plattform und die anschließende Kopplung mit dem Reaktordynamikprogramm COBAYA3 dar. Diese Kopplung wurde realisiert um das Verhalten von Reaktorkernen innerhalb einer innovativen benutzerfreundlichen Simulationsplattform zu untersuchen. Diese Kopplung umfasst dabei sowohl reguläre quadratische Gitter für nodale und für Einzelstabuntersuchungen als auch hexagonale Gitter für Ganzkernuntersuchungen.

Die NURESIM Plattform basiert auf dem open-source Programmsystem SALOME. Ziel ist es, mit Hilfe dieser Plattform verschiedene physikalische Phänomene innerhalb der analytischen Reaktoranalyse präziser beschreiben zu können. Dieses wird durch speziell für die Thermohydraulik und Neutronik entwickelte Best-Estimate Programme bzw. deren Kopplung untereinander erreicht. Die Modellierungsmöglichkeiten dieser Programme wurden dabei durch Multi-Skalen und Multi-Physik Methoden erweitert. Gegenstand dieser Arbeit ist dabei die Integration dieser Programme in die Plattform und deren Kopplung, sowie der Verifizierung und Validierung.

Um die Kopplung von COBAYA3 und SUBCHANFLOW innerhalb von NURESIM zu testen wurde eine Vielzahl von Experimenten und Benchmarks mit stationären und transienten Randbedingungen herangezogen. Dabei wurde der Reaktorkern bis zum Brennelement aufgelöst. Im Speziellen wurden die Bortransportmodelle mittels Vermischungs- bzw. Verdünnungstransienten für Mini- und Ganzkerne validiert.

Der zweite Teil dieser Arbeit befasst sich mit der Entwicklung von sogenannten hybriden Schemata (Nicht-konforme Geometrie) für Neutronik und Thermohydraulik. Die Verifizierung hybrider Gitternetze wurde für die Neutronik und die Thermohydraulik anhand von Mini- und Ganzkernen jeweils getrennt voneinander durchgeführt. Die Verifikation und Validierung des gekoppelten COBAYA3/SUBCHANFLOW Programms wurden durch die Berechnung eines ganzen nodalen Kerns und eines bis zum Brennstab aufgelöstes Brennelement durchgeführt. Systeme mit nicht-konformen Geometrien kommen zum Einsatz bei lokalen Störungen innerhalb des Kerns, die Auswirkungen auf Neutronik und Thermohydraulik haben. Die Arbeiten beschränkten sich hierbei auf stationäre Untersuchungen.



## List of Publications

1. M. Calleja, R. Stieglitz, V. Sanchez, J. Jimenez and U. Imke, A coupled neutronic/thermal-hydraulic scheme between COBAYA3 and SUBCHANFLOW within the NURESIM platform, *PHYSOR, Advances in Reactor Physics*, USA, April 2012.
2. M. Calleja, J. Jimenez, U. Imke and V. Sanchez, Validation of the coupling between COBAYA3 and SUBCHANFLOW for the simulation of boron dilution transients, *Annual meeting of the Spanish nuclear society*, Cáceres, Spain, 2012.
3. M. Calleja, V. Sanchez U. Imke, Implementation of SUBCHANFLOW in the SALOME platform and coupling with the reactor dynamic code COBAYA3, *Jahrestagung Kerntechnik (KTG)*, Berlin, May 17-19, 2011.
4. M. Calleja, R. Stieglitz, V. Sanchez and U. Imke, Investigations of boron transport in PWRs with the coupled codes COBAYA/SUBCHANFLOW and DYN3D/SUBCHANFLOW inside the NURESIM platform, *Annals of Nuclear Energy*. Vol. 66, 2014. Pages 74-84.
5. M. Calleja, V. Sanchez and J. Jimenez, Coupling of COBAYA3-SUBCHANFLOW inside the NURESIM platform and Validation Using Selected Benchmarks, *Annals of Nuclear Energy*. Vol. 71, 2014. Pages 145-158.
6. M. Calleja, J. Jimenez, U. Imke, V. Sanchez, J. Herrero and J. Macián, Implementation of Hybrid Simulation Schemes in COBAYA3-SUBCHANFLOW Coupled Codes for Efficient Direct Prediction of Local Safety Parameters, *Annals of Nuclear Energy*, Vol. 70, 2014. Pages 216-229.

# TABLE OF CONTENTS

List of acronyms .....	xx
1 Introduction .....	1
1.1 Motivation .....	1
1.2 Objectives .....	4
1.3 Solution methodology .....	5
1.4 Structure of the thesis .....	6
2 State of the art .....	9
2.1 Multi-physics and multi-scale methodologies .....	9
2.2 3D Core neutronic solvers for light water reactors .....	11
2.3 Core thermal-hydraulic calculations .....	17
2.4 Multi-physical coupling approaches between codes .....	22
2.4.1 Coupling methodologies .....	24
2.4.2 Convergence of coupled steady state solutions .....	25
2.4.3 Temporal coupling .....	26
2.5 Non-conform geometry .....	29
3 The NURESIM platform and the mathematical-physical fundamentals of the involved codes .....	33
3.1 The NURESIM platform .....	33
3.1.1 General description .....	33
3.1.2 Peculiarities of the platform for multi-physic developments .....	34
3.2 The sub-channel code SUBCHANFLOW 2.1 .....	36
3.2.1 General description .....	36
3.2.2 Solution approach .....	37
3.2.3 Boron dilution model .....	42
3.3 The reactor dynamic code COBAYA3 .....	44
3.3.1 General description of the code .....	44
3.3.2 The nodal solver ANDES .....	46
3.3.3 The cell solver COBAYA3k .....	48
4 Integration and testing of SUBCHANFLOW in the NURESIM platform .....	51
4.1 Main steps for the integration of SUBCHANFLOW .....	51
4.2 Testing of the SUBCHANFLOW integration in the NURESIM platform .....	53
5 Extensions of SUBCHANFLOW and COBAYA3 for hybrid solutions .....	59
5.1 SUBCHANFLOW: Extensions for hybrid analysis .....	59
5.1.1 Description of the methodology .....	59
5.1.2 Verification of the thermal-hydraulic hybrid scheme .....	61

5.2	COBAYA3: Extensions for hybrid analysis.....	63
5.2.1	Description of the methodology .....	63
5.2.2	Verification of the neutronic hybrid scheme .....	68
6	Development of a coupling scheme between COBAYA3 and SUBCHANFLOW .....	73
6.1	Coupled solutions at nodal level.....	73
6.1.1	COBAYA3/SUBCHANFLOW: Coupling for steady state simulations.....	74
6.1.2	COBAYA3/SUBCHANFLOW: Coupling for transient simulations .....	78
6.2	Coupling scheme for steady state hybrid core analysis.....	81
6.3	Verification of the developed nodal coupling scheme in SALOME.....	84
6.3.1	NEABEN - LWR transient, case A1 (description and modeling) .....	84
7	Validation of the COBAYA3/SUBCHANFLOW coupling.....	91
7.1	3D nodal simulations of PWR cores.....	92
7.1.1	Validation of CBY/SCF using the OECD/NEA and US NRC PWR MOX/UO2 core transient benchmark.....	92
7.1.2	Validation of CBY/SCF using the PWR Main Steam Line Break benchmark.....	99
7.1.3	Validation of CBY/SCF by using PWR MOX/UO2 boron dilution problems.....	107
7.2	3D Simulation of a core with hexagonal fuel assemblies at nodal level .....	122
7.2.1	Validation of CBY/SCF using the Kalinin-3 coolant transient benchmark.....	122
7.3	Code –to-Code validation of the coupled COBAYA3/SUBCHANFLOW hybrid solution....	129
7.3.1	Introductory remarks.....	129
7.3.2	Description of the scenario and boundary conditions.....	129
7.3.3	Description of the models used and simulations.....	130
7.3.4	Verification of the mesh and field for the hybrid structures .....	131
7.3.5	Selected results of the CBY/SCF hybrid steady state solution .....	133
8	Summary and conclusions .....	141
9	Outlook.....	143
10	References .....	146
	Nomenclature .....	158
	APPENDIXES .....	165
	Appendix A: Details on the models used for the validation process .....	166
	Appendix B: Additional exercises .....	171
	Appendix C: Support for Chapters four to seven.....	176

## LIST OF TABLES

Table 1. Methods used to perform 3D core neutronic calculations.	12
Table 2. List of coupled codes used around the world.	23
Table 3. Heat transfer correlations commonly used by SCF.	37
Table 4. Normalized axial power distribution for the (3x3) pin cluster model.	53
Table 5. SUBCHANFLOW stand alone hybrid tests of a 3x3 PWR mini-core.	61
Table 6. Model parameters for the hybrid mini-core study.	68
Table 7. Comparison of the results predicted by ANDES, COBAYA3k and the hybrid scheme.	68
Table 8. Hybrid results for the 3D PWR MOX/UO2 full core simulation.	70
Table 9. Flow of information between N and TH (exchange of parameters).	73
Table 10. Temporal coupling scheme between CBY and SCF.	80
Table 11. Parameters (arrays) needed by ANDES and COBAYA3k for the XS update.	82
Table 12. Steady state results for the NEABEN LWR transient benchmark at HZP.	85
Table 13. Benchmarks used for the validation process of the coupling CBY/SCF.	91
Table 14. Comparison of the results for the HFP scenario of the PWR MOX/UO2 benchmark.	95
Table 15. Comparison of the results for the HZP scenario of the PWR MOX/UO2 benchmark.	95
Table 16. Comparison of the results for the transient scenario of the PWR MOX/UO2 benchmark.	96
Table 17. Sensitivity related to different time steps for the PWR MOX/UO2 benchmark.	98
Table 18. Initial operating conditions corresponding to the HFP state of the MSLB benchmark.	100
Table 19. Steady state HFP results for the heterogeneous case of the MSLB benchmark.	104
Table 20. Steady state HFP results for the homogeneous case of the MSLB benchmark.	104
Table 21. Initial conditions (HZP) applied to the 3x3 mini-core boron dilution problem.	108
Table 22. Boron concentration defined for each FA at selected times during the transient for the boron dilution mini-core scenario.	108
Table 23. Selected parameters of the HZP steady state boron dilution mini-core exercise.	110
Table 24. Boron dilution sensitivity analysis, results with different axial discretization.	112
Table 25. Operating conditions at HZP of the PWR MOX/UO2 full core boron dilution benchmark.	113
Table 26. HFP and HZP results for the full core boron dilution benchmark.	114
Table 27. Results obtained for the full core boron dilution transients (slugs 1, 2 and 3).	116
Table 28. Operating conditions at HFP and HZP, Kalinin-3 benchmark.	122
Table 29. HFP and HZP steady state results, Kalinin-3 benchmark.	125
Table 30. Operating conditions at HP for the 3D full core hybrid model.	130
Table 31. Main results for the 3D full core HP hybrid model.	133
Table 32. Modeling parameters for the hybrid models (independent CBY and SCF).	166
Table 33. Modeling parameters for the hybrid models (independent CBY and SCF).	166
Table 34. Modeling parameters for the NEABEN LWR transient benchmark.	167

Table 35. Modeling parameters for the PWR MOX/UO <sub>2</sub> benchmark.	167
Table 36. Modeling parameters for the PWR MSLB benchmark.	168
Table 37. Modeling parameters for the MOX/UO <sub>2</sub> boron dilution (3x3) mini-core.	168
Table 38. Modeling parameters for the MOX/UO <sub>2</sub> boron dilution 3D full core.	169
Table 39. Modeling parameters for the Kalinin-3 cooling transient benchmark.	170
Table 40. Modeling parameters for the Kalinin-3 cooling transient benchmark.	170
Table 41. Differences between the simulated models for one FA at HFP.	171
Table 42. Operating condition for all models A, B, C, D and D (one fuel assembly).	171
Table 43. Main results for models A, B, C, D and E (one fuel assembly).	172
Table 44. Operating conditions at HFP and HZP for the 3x3 mini-core REA transient.	173
Table 45. Steady state results for the mini-core exercise models at HFP and HZP.	174
Table 46. HFP (normalized radial power).	174
Table 47. HZP (normalized radial power).	174
Table 48. Normalized axial power per node at HFP.	174
Table 49. Normalized axial power per node at HZP.	175
Table 50. Transient parameters obtained for the REA mini-core exercise.	175

# LIST OF FIGURES

Fig. 1. Selected solution methodology for the thesis.	5
Fig. 2. Coolant centered (a), rod centered (b) and triangular (c) sub-channels.	20
Fig. 3. External (a), internal (b) and combined (c) coupling approaches.	24
Fig. 4. Steady state convergence definition (calculation-feedback-calculation).	25
Fig. 5. Implicit (a), semi-implicit (b), explicit (c) and staggered OS (d) coupling schemes.	27
Fig. 6. Illustration of different types of FA radial discretizations (nodal, local and hybrid).	30
Fig. 7. SALOME peculiarities: functionality levels (a) and coupling philosophy (b).	34
Fig. 8. SUBCHANFLOW solution algorithm for transient and steady state analysis.	38
Fig. 9. Lateral and axial discretization of the thermal-hydraulic control volume.	38
Fig. 10. Iterative steady state solution scheme of ANDES (nodal solver of COBAYA3).	46
Fig. 11. Directory tree of SUBCHANFLOW which allows its integration inside SALOME.	52
Fig. 12. Normalized radial power distribution for the (3x3) pin cluster model (top view).	53
Fig. 13. Study of different sub-channel discretizations implemented in four models.	54
Fig. 14. Convergence evolution for the 1 <sup>st</sup> , 2 <sup>nd</sup> , 3 <sup>rd</sup> and 4 <sup>th</sup> models (Fig. 13).	54
Fig. 15. Normalized radial power map for 1/4 of a PBP FA: MOX FA (left), UO2 FA (right).	56
Fig. 16. Coolant centered mesh isometric view (a) and top view (b), and rod centered mesh isometric view (c) and top view (d).	56
Fig. 17. Neighboring sub-channels related to hybrid TH solutions.	60
Fig. 18. Doppler temperature calculated for the hybrid mini-core tests at half core height.	62
Fig. 19. Hottest pin location (a) and Doppler temperature deviation (b) between the central hybrid FA for test case two and the central FA for the full PBP solution test case eight.	63
Fig. 20. Calculation scheme for the hybrid treatment of the neutronic code COBAYA3.	64
Fig. 21. Mapping (N discretization) scheme for data exchange between ANDES and COBAYA3k.	65
Fig. 22. Hybrid solution scheme implemented in the neutronic code COBAYA3.	67
Fig. 23. Radial peaking factors ( $F_{xy}$ ) calculated by ANDES, COBAYA3k and the hybrid solution.	69
Fig. 24. Deviation (in %) for the hybrid solution from the PBP reference solution for the central FA.	69
Fig. 25. Deviation (in %) of the radial power predicted by CBY for the second case (hybrid solution) and the one predicted by the first case (full nodal solution).	70
Fig. 26. Deviation (in %) of the radial power predicted by CBY for the third case (hybrid solution) and the one predicted by the first case (full nodal solution).	71
Fig. 27. Iterative scheme between CBY and SCF for steady state calculations.	74
Fig. 28. Coupling inside SALOME (CBY/SCF) based on the MED structure for feedback exchange.	75
Fig. 29. Radial mapping between the N (left-blue) and TH (right-cadmium orange) domains for nodal base solutions.	76
Fig. 30. Steady state convergence loop for the CBY/SCF coupling scheme.	78

Fig. 31. Feedback interaction at every time step $\rightarrow n$ .	78
Fig. 32. Operator splitting approach for the coupled scheme CBY/SCF.	79
Fig. 33. CBY/SCF solution methodology for an OS coupling approach in SALOME.	81
Fig. 34. Steady state convergence loop for the coupled hybrid scheme (CBY/SCF).	83
Fig. 35. Location of control assemblies in 1/8 of the core, NEABEN benchmark.	84
Fig. 36. Normalized power (a) and avg. Doppler temperature (b) vs. time, NEABEN benchmark.	86
Fig. 37. MED philosophy: Mesh superposition and correspondence between the N and TH domains.	87
Fig. 38. Axial (a) and radial (b) power distribution making use of the SALOME post-processing capabilities.	87
Fig. 39. Coolant temperature (a), coolant density (b), Doppler temperature (c) and total power (d) of the NEABEN benchmark at the core center and power peak time.	88
Fig. 40. Top view of the PWR MOX/UO <sub>2</sub> benchmark (1/4 core).	93
Fig. 41. Reactivity and CR position (a), total power (b), Doppler temperature (c) and moderator density (d) vs. time.	96
Fig. 42. Time step sensitivity analysis for the PWR MOX/UO <sub>2</sub> REA benchmark.	97
Fig. 43. Control rod position (localization) in the core corresponding to the MSLB benchmark.	100
Fig. 44. TH BCs associated to the TMI-1 MSLB benchmark: inlet temperature (a), calculated core avg. coolant temperature (b), inlet mass flow rate (c) and core outlet pressure (d).	101
Fig. 45. Steady state convergence for the heterogeneous case of the MSLB benchmark.	103
Fig. 46. Total power evolution (a), total power detail at SCRAM (b), core avg. Doppler temperature (c), core avg. Doppler temperature detail (d), core avg. moderator density (e) and online visualization of the total power evolution (f) for the MSLB benchmark.	106
Fig. 47. Total power (a), and Doppler temperature and reactivity (b) evolution for the mini-core.	110
Fig. 48. Boron concentration (a), and moderator density and temperature (b) evolution for the mini-core.	111
Fig. 49. Core average boron concentration evolution for slugs 1, 2 and 3.	115
Fig. 50. Detail at around $t = 5.0$ s for the total power (a) and the total reactivity (b) evolution for slugs 1, 2 and 3.	115
Fig. 51. Boron slug 1: Total power (a, b), total reactivity (c) and boron concentration (d) evolution.	117
Fig. 52. 3D time evolution of the boron concentration during the transient for the first slug.	118
Fig. 53. Boron slug 2: Total power (a, b), total reactivity (c) and boron concentration (d) evolution.	119
Fig. 54. Boron slug 3: Total power (a, b), total reactivity (c) and boron concentration (d) evolution.	120
Fig. 55. Top view of the core and control rod position for the Kalinin-3 benchmark.	123
Fig. 56. Time dependent BCs for the Kalinin-3 transient phase: mass flow rate (a), CR position (b), mass flow rate detail (c), coolant temperature (d), coolant temperature detail (e) and power (plant data)/reactivity (f).	124
Fig. 57. Kalinin-3 benchmark: Total power evolution (presented for two different time frames).	126

Fig. 58. Kalinin-3 benchmark: Total power evolution from $t = 80.0$ s to $t = 300.0$ s.	126
Fig. 59. $P_{\text{tot}}$ , reactivity and $T_{\text{Dopp}}$ evolution for the transient analysis of the Kalinin-3 benchmark.	127
Fig. 60. Total reactivity (a), core avg. $T_{\text{mod}}$ and $D_{\text{mod}}$ (b), core avg. $T_{\text{Dopp}}$ (c) and maximal $T_{\text{Dopp}}$ (d) for the transient analysis of the Kalinin-3 benchmark.	128
Fig. 61. Generated hybrid mesh for CBY based on the TH (SCF) mesh.	132
Fig. 62. Hybrid coupled solution scheme inside SALOME using hybrid fields.	133
Fig. 63. Axial shape of the Doppler temperature (a) and fuel pellet radial temperature profile (b).	134
Fig. 64. Axial shape of the Doppler temperature (a) and fuel pellet radial temperature profile (b).	135
Fig. 65. Comparison of the FA base normalized 2D power distribution of one fourth of the core according to the benchmark specifications for the PBP computation and the hybrid CBY/SCF simulation.	135
Fig. 66. Hybrid FA: Percent error between the PBP (reference) and the hybrid solution (isometric top view of the FA).	136
Fig. 67. Hybrid FA: Percent error between the PBP (reference) and the hybrid solution (isometric bottom view of the FA).	137
Fig. 68. Hybrid FA: Percent error between the PBP (reference) and the hybrid solution (2D top view of the FA).	137
Fig. 69. Configuration of the fuel assemblies surrounding the hybrid (central) assembly.	138
Fig. 70. Coolant temperature at the core exit predicted by the hybrid scheme CBY/SCF.	139
Fig. 72. Total power (a), Doppler temperature (b), total reactivity (c) and moderator temperature (d) evolution for the REA mini-core exercise.	175
Fig. 73. Output 1: First model in Chapter 4.2, Fig. 13.	177
Fig. 74. Output 2: Fourth model in Chapter 4.2, Fig. 13.	177
Fig. 75. Output 3: PBP solution for the coolant centered discretization in Chapter 4.2.	178
Fig. 76. Output 4: PBP solution for the rod centered discretization in Chapter 4.2.	178
Fig. 77. Output 5: test case two in Chapter 5, Fig. 18.	179
Fig. 78. Output 6: test case eight in Chapter 5, Fig. 18.	179
Fig. 79. Coolant temperature evolution for the PWM MOX/UO2 REA benchmark.	180
Fig. 80. Total power detail (a), Doppler temperature (b) and total reactivity evolution for the TMI-1 MSBL benchmark.	180
Fig. 81. YACS diagram for a SCF stand alone simulation.	181
Fig. 82. Coupled CBY/SCF YACS diagram for a steady state simulation.	182
Fig. 83. Online visualization of the $k_{\text{eff}}$ convergence evolution within a YACS diagram of the NURESIM platform.	182
Fig. 84. Online visualization of the total power evolution for a typical REA transient simulation inside the NURESIM platform.	183
Fig. 85. Verification of the 3D mesh for a full core (one hybrid central assembly) inside SALOME.	183

- Fig. 86. Representation of the meshing elements (full core – left, hybrid central assembly - right) inside SALOME. 184
- Fig. 87. Display of the moderator temperature field (left) and density field (right) inside SALOME. 184
- Fig. 88. Doppler temperature field with a horizontal cut at half of the active core. 185
- Fig. 89. Vertical cut applied to a 3D power distribution field for a hexagonal reactor core model. 185

# List of acronyms

1D	One dimension	JFNK	Jacobian-Free-Newton-Krylov
2D	Two dimensions		
3D	Three dimensions	LB	Large Break
ACMDF	Analytic Coarse Mesh Finite Difference	LOCA	Loss Of Coolant Accident
A.O.	Axial Offset	LWR	Light Water Reactors
API	Application Programming Interface	max.	maximum
ARI	All Rods In	MCNP	Monte Carlo N-Particle
ARO	All Rods Out	MCP	Main Circulation Pumps
ATWS	Anticipated Transient Without SCRAM	MCPR	Minimum Critical Power Ratio
avg.	average	MED	Memory Exchange Data
BEM	Boundary Element Method	MOC	Method of Characteristics
<b>BC</b>	<b>Boundary Condition</b>	MOX	Mixed Oxide fuel
BWR	Boiling Water Reactor	MPI	Message Passing Interface
<b>CBY</b>	<b>COBAYA3 (reactor dynamic code)</b>	MSIV	Main Steam Isolation Valve
CFD	Computational Fluid Dynamics	MSLB	Main Steam-Line Break
CFL	Courant Friedrichs Law	mod	moderator
chan	channel	<b>N Neutronics</b>	
CHF	Critical Heat Flux	NCG	Non-Conform Geometry
CMFD	Coarse Mesh Finite Difference	NDE	Neutron Diffusion Equation
CPM	Collision Probability Method	NFC	Neutron Flux Control
CR	Control Rod	NPP	Nuclear Power Plant
CV	Control Volume	NSOL	Neutronic SOLution
D	Density	<i>nax</i>	number of axial levels
DBA	Design Base Accidents	OS	Operator Splitting
DEM	Data Exchange Model	PBP	Pin by Pin
DFM	Drift Flux Model	pcm	parts per cent mille
DNB	Departure from Nuclear Boiling	PM	Power Map
DO	Discrete Ordinates	Pow	Power
Dopp	Doppler	ppm	parts per million
eff	effective	PWR	Pressurized Water Reactor
EG	Energy Group	REA	Rod Ejection Accident
EHT	Equivalence Homogenization Theory	ref	reference
EOC	End Of Cycle	refl.	reflector
<b>FA</b>	<b>Fuel Assembly</b>	RIA	Reactivity Initiated Accident
FDM	Finite Difference Method	SB	Small Break
FEM	Finite Element Method	<b>SCF</b>	<b>SUBCHANFLOW (thermal-hydraulic code)</b>
GEN	GENERation	SCRAM	Safety Control Rod Axe Man
GMRES	Generalized Minimal RESidual	SEC	System of Experimental Control
HDD	Hierarchical Domain Decomposition	SOR	Successive Over Relaxation
HEM	Homogeneous Equilibrium Model	<b>TH</b>	<b>Thermal-Hydraulic</b>
HFP	Hot Full Power	THSOL	Thermal-Hydraulic SOLution
HPC	High Performance Computing	TMI	Three Mile Island
HZP	Hot Zero Power	UOX	Uranium OXide fuel
ICMS	In-Core Monitoring System	UVET	Un-equal Velocity Equat Temperature
ISP	International Standard Problems	UVUT	Un-equal Velocity Un-equal Temperture
it	iteration	UBLS	Upper Level unit control System

w/r	With respect	VVER	Vodo-Vodzanoi Energetischeky Reactor
wd	withdraw	XS	Cross-Section

## Codes, projects, organizations and software platforms

ANDES	Analytic Nodal Diffusion Equation Solver	OECD	Organization for Economic Cooperation and Development
ATHLETE	Analysis of Thermal Hydraulics of LLeaks and TransiEnts	PARCS	Puerdue Advanced Reactor Core Simulator
CASL	Consortium for Advance Simulation of Light water reactors	PSI	Paul Scherrer Institute
CATHARE	Code for Analysis of THERmal hydraulics during Accident of Reactor and safety Evaluation	PVM	Parallel Virtual Machine
CEA	Commissariat à l'Énergie Atomique	RELAP	Reactor Excursion and Leak Analysis Program
COBRA	COolant in Boiling Rod Arrays	TRACE	TRAC/RELAP Advanced Computational Engine
CRISTAL	Criticality Safety Package		
CTF	COBRA-TF		
DeCART	Deterministic Core Analysis base on Ray Tracing	UPM	Universidad Politécnica de Madrid (Technique University of Madrid)
DOE	Department Of Energy		
DYNSUB	DYN3D/SUBCHANFLOW	VERA	Virtual Environment for Reactor Analysis
EnBW	Energie Baden Württemberg		
EURATOM	EUROpean ATOMIC energy comunity		
FENAT	Finite Element Neutral Atom Transport		
GRS	Gesellschaft für anlagen und ReaktorSicherheit		
HEMERA	Highly Evolutionary Methods for Extensive Reactor Analysis		
IAEA	International Atomic Energy Agency		
INRS	Institute National de Recherche et de Securite		
INR	Institut für Neutronenphysik und Reaktortechnik		
KAERI	Korean Atomic Energy Research Institute		
KIT	Karlsruhe Institute of Technology		
LAPACK	Linear Algebra PACKage		
MELCOR	Methods for Estimation of Leakages and CONsequences of Releases		
MOOSE	Multi-physics Object Oriented Simulation Environment		
NEA	Nuclear Energy Agency		
NEM	Nodal Expansion Method		
NNR	Numerical Nuclear Reactor		
NRC	US Nuclear Regulatory Commission		
<b>NURESIM</b>	<b>NUcleaer Reactor SIMulation</b>		
NURISP	NUclear Reactor Integratede Simulation Project		

---

# 1 Introduction

## 1.1 Motivation

High accuracy simulations for nuclear power plants (NPPs) have become more practical with the rapid growth of computer power and improved algorithms. Especially, coupling of codes is a beneficial approach for safety analysis of nuclear reactor cores.

The major advantage of these high accuracy simulations is the improvement on the prediction capability of safety parameters and the identification of major impact parameters. The precise simulation and forecast of power distribution, heat transport and flow behavior in the reactor core is very important to demonstrate that NPPs meet safety requirements. For instance, accurate knowledge of the specific heat of the fuel material is needed for the assessment of reactor behavior under steady state and transient conditions. The understanding of the interaction between neutronics (N) and thermal-hydraulics (TH) is important to achieve several objectives, e.g. safety analysis and precise prediction of local parameters. In addition, numerical tools describing different physical phenomena have to be improved by coupling with each other for analyzing e.g. normal plant conditions as well as loss of coolant accidents (LOCAs), reactivity transients and anticipated transients without SCRAM (ATWS). Many of the current codes used for light water reactor (LWR) analysis are based on 3D nodal diffusion N methods coupled with first order 1D TH without considering cross flows [Grandi01].

Nowadays, several computer codes that solve the time-dependent neutron diffusion and/or transport equation are coupled with TH codes. Such N codes are for instance, DYN3D [Rohde01], COBAYA3 (CBY) [Herrero01] and PARCS [Downar04], [Demazier01]. These reactor kinetic codes are coupled with TH codes that are either one dimensional system codes or multidimensional sub-channel codes or computational fluid dynamics (CFD) codes. Some of these codes are TRACE [Spore01], FLICA4 [Toumi01], SUBCHANFLOW (SCF) [Imke01], [Sanchez01] and Neptune-CFD [Guelfi01].

The most mature multi-physical coupling scheme is the coupling of nodal diffusion codes with 1D simplified TH codes using a rigid mapping (non-flexible spatial correspondence) scheme between them and using coarse spatial meshing. This coarse spatial discretization of both N and TH does not allow the prediction of local phenomena at pin or cell level.

The necessity to better describe the most important safety-related physical phenomena prevailing in modern LWR core loadings characterized by increasing heterogeneity at local scale is driving the extension of current core designs and N/TH coupled transient analysis methodologies. These improvements consider a more detailed spatial description of both N and TH computational domains. The de-

velopment of flexible coupling approaches as well as the use of improved diffusion or higher order approximations of the neutron transport equation is expected.

In addition, these new capabilities allow the prediction of local safety parameters as e.g. departure from nuclear boiling (DNB), minimum critical power ratio (MCPR), maximum cladding and fuel temperature, instead of the conservative prediction of these parameters based on hot channel factors. Different groups in Europe and worldwide are working on the development of novel coupling approaches for multi-physics nuclear reactor simulations e.g. in the European Union the Nuclear Reactor Integrated Simulation Project (NURISP) [Bestion01] [Royer01], included in the 6<sup>th</sup> EURATOM framework program and in the USA, the MOOSE software [Gaston02], NNR [Weber01] [Downar03] and the CASL project [Kothe01].

Other important projects involve the Criticality Safety Package (CRISTAL), which has been developed mainly to take into account burn-up in criticality safety studies [Leclaire01] and the Highly Evolutionary Methods for Extensive Reactor Analysis (HEMERA) [Bruna01], developed by the Commissariat à l'Énergie Atomique (CEA) in collaboration with the Institut National de Recherche et de Sécurité (INRS). HEMERA is based on a coupling scheme between the French codes CATHARE (system TH) [Bazin01], [Polidor01] and FLICA4 (TH), with CRONOS (N) [Megnaudo01].

The novel coupling approach followed within NURISP is based on a mesh superposition of two domains (N and TH within the context of this dissertation), where the specific challenge encountered is to formulate a consistent procedure to overlap the two geometrical discretizations. To do this, the full integration of the different codes in the Nuclear Reactor Simulation (NURESIM) platform (the SALOME software) is required so that all codes inside can take advantage of the common memory exchange data (MED) format. This is a very flexible tool that allows the use of different meshes by performing data interpolation between them and provides also a powerful user friendly simulation platform for specific multi-physics simulations. The Multi-physics Object Oriented Simulation Environment (MOOSE) approach is based on solving all systems in a fully coupled manner using the Jacobian-Free-Newton-Krylov (JFNK) methodology. The main objectives of MOOSE focus on parallel performances, usage of software engineering principles and engineering analysis tools for pre- and post-processing. The Numerical Nuclear Reactor (NNR) is a high fidelity (in terms of accuracy) software that performs integrated core analyses that include sophisticated first principles based models and multi-physics. Other project developed mainly by the Department of Energy (DOE) of the USA, is the Consortium for Advance Simulation of Light water reactors (CASL), which is based on the Virtual Environment for Reactor Analysis (VERA) platform. VERA is a code system for scalable simulations of nuclear reactor core behavior. Its goal is to deliver to the industry solutions via modeling and simulations addressing key scientific challenges through the use of integrated codes inside a platform. The previously mentioned

projects take into consideration the use and implementation of best estimate codes (based on the best available coupled methods and models) to provide realistic solutions that can be used to optimize safety and operability.

Currently, core pin by pin (PBP) simulations are performed using different strategies and codes. They are based on:

1. Development of cell solvers based on improved neutron diffusion theory, e.g. in the parallel code CBY.
2. Development of spherical harmonics ( $P_n$ ) transport codes, e.g. the simplified transport approximation ( $SP_3$ ) as implemented in the codes DYN3D and PARCS.
3. Developments of discrete ordinate (DO) transport codes, e.g. TORT-TD, [Seubert02].
4. Further development of the transport solution through the method of characteristics (MOC) by combining 2D (radial) with 1D (axial) solutions e.g. DeCART, [Zhong01].

The main drawback of the previously listed approaches is the considerable computational time needed for:

1. The N cell based simulation of a whole core despite parallelization and improved diffusion approximations coupled with sub-channel codes (e.g. DYN3D/FLICA4 [Gomez02], COBAYA3/COBRA-TF, [Lozano01], [Jimenez03]).
2. The N cell base simulation of a mini-core or pin cluster despite parallelization coupled to a system (TORT-TD/ATHLET, [Seubert01], DYN3D/ATHLET [Kliem03]) or a sub-channel code (TORT-TD/COBRA-TF, [Velkov01], [Christinne01]).
3. The N cell based simulation of a sector of the core despite the simplified transport approximation coupled with a sub-channel code (DYNSUB, [Gomez01], [Gomez03]).
4. The N cell based transport simulation (even Monte-Carlo with MCNP/STAR-CCM+, [Cardoni01]) of a core coupled with a CFD code, e.g. DeCART/STAR-CD [Thomas01].

Furthermore, there is not always a need to simulate the whole LWR core behavior during non-symmetrical transients at pin level since the perturbations mainly affect few assemblies or assembly clusters only. In addition, the majority of the mentioned codes are not fully parallelized and hence one cannot take advantage of high performance computing. Therefore, the main deficiencies of current nuclear reactor simulations can be summarized hereafter:

1. Usage of rigid meshes (non-flexible) for coupled schemes.

2. Nodal base coupling using diffusion codes and sub-channel codes (not accurate to predict local safety parameters).
3. Pin level improved diffusion is still time consuming for 3D core simulations.
4. Pin level coupling relying on simplified transport solutions require a lot of computational power.
5. Current lack of parallelization schemes for most of the coupled codes.

Consequently, new fast running and accurate approaches are needed for simulating reactor cores using multi-physics and multi-scale methodologies. These approaches facilitate both the improvement of core designs regarding safety parameters and fuel utilization, as well as the more precise quantification of the safety margins for normal operation and accidental conditions.

Alternatively, novel solution approaches that are fast running and preserve the high accuracy predictions of pin level calculations are urgently needed to meet the industrial requirements. This type of analysis involve for instance, the usage of mixed nodal base solutions with pin level solutions, for both N and TH, in addition to flexible mapping schemes between them. These hybrid schemes have been developed within the context of this thesis.

## 1.2 Objectives

The main objectives of the doctoral thesis are focused on both the further development of multi-physics and multi-scale core simulation methodologies for a more realistic prediction of key safety relevant phenomena with less conservatism, and on the validation of the developed coupling schemes using code-to-code or code-to-data comparisons. The following major codes were selected for the doctoral work: the reactor dynamic code CBY and the sub-channel TH code SCF. In addition, these codes should be implemented and coupled within the European simulation platform NURESIM.

The contributions are focused on the following thematic challenges:

1. Implementation of a new coupling scheme between a reactor dynamics code and a TH sub-channel code within the NURESIM platform (SALOME software) for nodal based core simulations including both cores with square and hexagonal fuel assemblies. This includes the following goals:
  - a. Full integration of the INR-KIT sub-channel code SCF.
  - b. Implementation of a coupling approach exploiting the platform's features for both the nodal steady state coupled solution and the time-dependent coupled solution for square and hexagonal geometries.

- c. Development of computational routes using all NURESIM platform services to take advantage of the user-friendly pre- and post-processing capabilities of SALOME, including the online supervision of computational routes and the animation for simulation results of the involved codes.
2. Validation of the developed coupled scheme CBY/SCF inside SALOME.
  3. Development of non-conform geometry (NCG: combination of nodal and cell solutions - hybrid) methodology for fast running reactor core simulations using CBY/SCF (also known as local zooming capability). This includes the direct prediction of the pin power and local safety parameters without using pin power reconstruction methods. For this functionality, it is necessary to take into account the feedback effects on the cross sections (XSs) during a coupled N/TH simulation at both cell and nodal level. This goal includes:
    - a. Development of hybrid stand alone solutions for both N (CBY) and TH (SCF) domains separately.
    - b. Development of a steady state coupling scheme between CBY/SCF hybrid solvers inside the NURESIM platform.

### 1.3 Solution methodology

The chosen solution methodology is sketched in Fig. 1. It shows the iterative approach followed to find the optimal coupling approach and the best validation approach for the development of the coupling scheme between CBY and SCF.

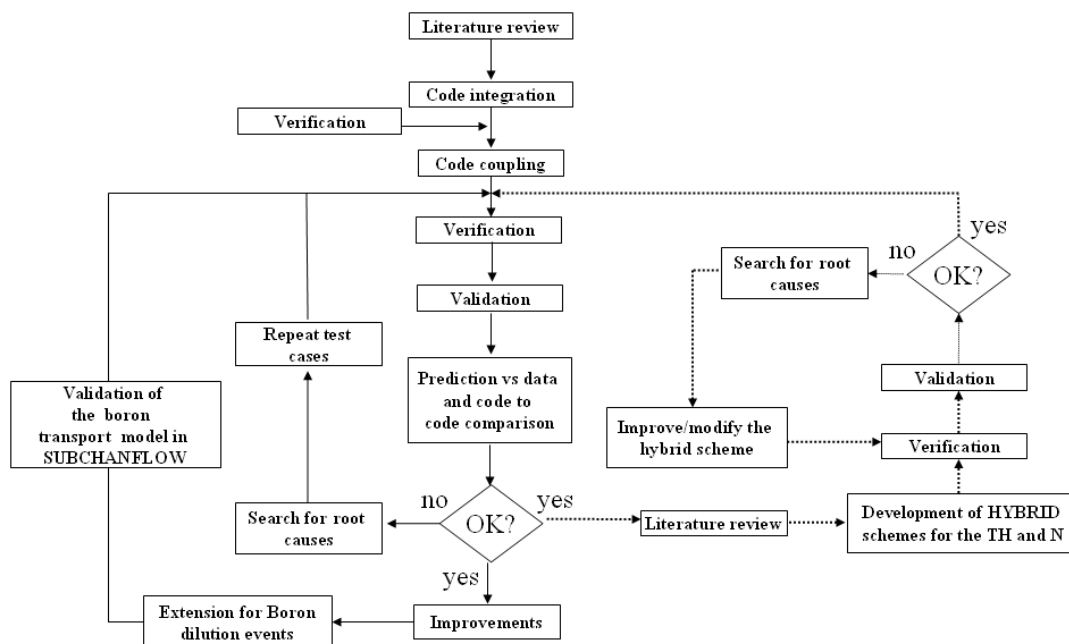


Fig. 1. Selected solution methodology for the thesis.

After the integration of the SCF code inside the platform, the next step is to verify the consistency of the coupled solution (verification and validation). It has to be noted that CBY was already implemented and validated inside the SALOME platform by [Jimenez01]. Finally, the innovative concept of non-conform geometry will be explored, leading to the development of novel coupled N/TH hybrid solutions.

#### 1.4 Structure of the thesis

The structure of the doctoral thesis is based on nine chapters, the references, nomenclature and the appendixes sections. In the **first section**, an introduction in addition to the background of the doctoral thesis, motivations and objectives are discussed. The **second section** describes the state of the art of the current work involving multi-physics and multi-scale methodologies, core N, core TH, coupling approaches and hybrid solutions. The **third section** describes the general and theoretical bases of the three main working tools used in the dissertation, the NURESIM platform (SALOME), SCF and CBY. The **fourth section** specifies the implementation of SCF inside the NURESIM platform and the steps required for this implementation. This section is also devoted to the analysis of the performance of SCF inside the NURESIM platform in terms of compatibility in the solution (outside and inside the platform) and sensitivity analysis applied to pin clusters and mini-cores. **Section five** describes the methodology and developments done on both TH and N to perform coupled hybrid solutions. In addition, stand alone solutions are presented to demonstrate the potential use of these schemes. **Section six** is devoted to the coupling scheme implemented between CBY and SCF for steady state and transient solutions in addition to the hybrid coupling scheme. A representative benchmark problem is used for testing the integration of SCF and its coupling with CBY inside SALOME. The **seventh section** shows the verification and validation process of the previously mentioned methodologies. Specific benchmarks were selected for this purpose. The last **sections (eight and nine)** refer to the conclusions and outlook of the dissertation. Finally, the references used are found in addition to the nomenclature, which is a valuable support for all the equations mentioned in this work. In the **appendix section**, additional information about the details of the models used in the dissertation, additional coupled exercises concerning a steady state model for a single fuel assembly and a transient scenario for a 3x3 mini-core, outputs that support the derived conclusions for chapters four to seven and the pre- and post-processing capabilities of SALOME, are summarized.

---

---

## 2 State of the art

The following chapter discusses the theoretical background needed for the development of coupled schemes between N and TH. Multi-physical and multi-scale approaches are discussed in addition to the coupling strategy followed for steady state and transient solutions. Attention is given to core N (focus on diffusion theory) and core TH (focus on sub-channel analysis). A state of the art of non-conform geometries solution approaches (hybrid analysis) is presented. For the equations used to describe the N and TH theoretical basis, a brief description of their symbols are given under each equation. Symbols are not repeated in further equations and therefore, for a more detailed description of these symbols the reader should refer to the nomenclature.

### 2.1 Multi-physics and multi-scale methodologies

The use of numerical tools supported by powerful computers makes possible the detailed analysis of whole 3D LWR NPP cores at nodal level. On one side, the nuclear industry has the need to meet important safety requirements which requires the development of multi-scale (study at core level and pin level of relevant nuclear reactor core configurations) and multi-physics coupled codes in order to predict accurate local safety parameters. These safety requirements are strongly affected by the increasing complexity of material composition (heterogeneous core loadings), geometrical characteristics (pin rod configuration and fuel assembly (FA) structures) and changing operating conditions, enrichment and burn-up. A very important aspect in nuclear engineering is the validation of these coupled systems (numerical simulation tools) [Taitano01] used for the design and safety evaluation of reactor cores, which turn out to be the ultimate goal.

The level of validation required for numerical codes is determined by the nature of the intended use and is based on: experimental data at different scales (e.g. bundle tests and integral tests), code-to-data, code-to-code or code-to-analytical solution comparison. In addition, international standard problems (ISP) of the OECD and IAEA and benchmarks involving transients and relevant N/TH perturbations are studied for this type of coupled schemes, where the main goal of this international trend is to avoid very costly experiments. The use of best estimate numerical tools in the frame of a licensing process requires the quantification of codes uncertainty and sensitivity [Macian01]. While the uncertainty and sensitivity methods for TH codes are well developed, the corresponding methodologies for neutronic and reactor kinetic parameters are still under development. Especial attention must be given to the propagation of uncertainties from different domains, e.g. TH and N to a coupled simulation [Uam01].

For the analysis of ATWS and design basis accidents (DBA), these codes can be categorized in two groups: reactor dynamic codes and TH codes including system codes, sub-channel codes and CFDs (other type of codes can be mentioned and include fuel behavior codes, containment analysis, atmospheric dispersion and structural codes [Cooper01]). Coupling of these codes reduce errors associated with the transfer of data, reduce conservatism and improve the accuracy of the calculation which is correlated by physical laws, e.g. Doppler feedback for N and TH. Nowadays, the improvement and development of coupled numerical simulations are fostered by:

1. The need to reduce conservatism and number of expensive experiments.
2. The need to increase the spatial resolution of the computational domain, e.g. sub-channel level instead of channel (FA) level for TH, or cell level instead of node level for N.
3. The advances in the fundamental understanding of N, TH, heat transfer, fluid dynamics, etc. based on experimental or theoretical research at different scales.
4. The trend to integrate mathematical and physical models devoted to single areas in a multi-physical approach by developing different coupling schemes between different fields.
5. The need in nuclear engineering to move from coarse solutions (FA base) to more detail solutions (pin base) of reactor core analysis.
6. The need to use high performance computers (huge computational power available at relatively low cost).

The use of more heterogeneous cores affects directly both the N and TH (coupled or separated). Therefore, numerical simulation tools need to consider both the multi-physics and multi-scale nature of the problems, as mentioned hereafter. Within the frame of this thesis, multi-physics involve the application of different codes that treats individually different fields in nuclear reactor physics. The main interest of these codes lies in different areas such as N and TH, among others. The combination of these codes, however, is done externally or internally to perform their desired objectives [Jimenez01], where the multi-physic approach treats correlated simulations or solves coupled systems of partial differential equations to obtain more precise solutions. The objective of multi-scale schemes is to integrate all effects involved at different levels of the physical systems [Cooper01]. These levels of physical fidelity can be coupled within the same simulation, either weakly or strongly. For example, in a nuclear reactor core, fuel assemblies of about 20.0 cm width are composed of fuel rods with diameter of around 1.0 cm, producing bubbles after heating with a size in the order of millimeters. In a general way, three different scales are encounter in nuclear reactors. The macro-scale allows the simulation of the primary and secondary loops using system codes such as CATHARE, TRACE, RELAP5 [Relap01] and ATHLET [Burwell01]. The next scale is the meso-scales, in which the spatial discretization is reduced to component level as in the case of sub-channel codes such as FLICA4, COBRA-TF, SCF, etc. The last scale is the micro-scale, where the TH domain between fuel rods is discretized

down to very fine resolutions depending on the purpose of the investigations (CFD and direct numerical simulation codes). In other words, two branches can be differentiated:

1. Thermal-hydraulics multi-scale: The physical phenomena that affect the TH involve all the previously mentioned scales. Micro-scales are encountered at the level of bubble formation (e.g. boiling), boundary layer calculation and turbulence, which are also observed at meso-scales, just as pressure and temperature gradients. Macro-scales contemplate the influence of steam generators, pressurizers and other plant components within a model.
2. Neutronics multi-scale: Highly heterogeneous cores impose sharp neutron flux gradients which are encountered at meso-scales at the interfaces, for instance, of uranium oxide (UOX) and mixed oxide (MOX) FAs and fuel reflector boundary. Due to this fact, diffusion approximation with two energy groups is not accurate enough and additional energy discretization is required. At cell level (PBP) the neutron mean free path is in the order of centimeters and neutron collisions between cells or within the same cell emphasizes the need to consider the micro-scale for the N, especially when homogenizing and condensing from the detail cell level meshes to coarse nodal meshes.

Current developments of multi-scale and multi-physics involve the coupling of system codes with sub-channel codes such as RELAP5/PANBOX/COBRA [Jackson01], MARS [Jeong01] and RELAP5/COBRA-TF [Aumiller01]. The coupling of system codes with CFD codes, e.g. RELAP5/FLUENT [Cadinu01], TRACE/CFX [Bertolotto01] and ATHLET/CFX [Papukchiev01], multi-physics coupling approaches for time dependent neutron diffusion codes with CFD, e.g. PARCS/CFX [Monferrer01] and DYN3D/CFX [Kliem02] and diffusion codes with sub-channel codes, COBAYA3/COBRA(III-TF) [Jimenez01] and within the topic of this thesis, COBAYA3/SUBCHANFLOW (CBY/SCF) [Calleja01]. In addition, time dependent transport codes coupled with sub-channel codes include, TORT-TD/COBRA-TF [Velkov01] and DYN3D-SP3/SUBCHANFLOW (DYNSUB) [Gomez01].

## 2.2 3D Core neutronic solvers for light water reactors

For solving 3D N problems two methodologies are widely used nowadays, deterministic (transport and diffusion) and Monte Carlo (stochastic). These methodologies require specific information for the description of the neutron interactions with matter in a multiplying media such as a reactor core: geometrical definition, material composition, operating and boundary conditions (BC)s and XSs in dependence of the instantaneous state variables and history parameters (XSs which are generated by lattice codes in so called branch calculations, e.g. APOLLO [SanchezR01], DRAGON [Marleau01] and SCALE [Bowman01]).

In the last years, multi-group solutions of the diffusion equation as well as a transport solution based on  $SP_3$  (simplified transport) have been added to LWR core simulators for both square and hexagonal geometries. The general transport equation can be formulated in different ways: differential formulation ( $S_n$ : discrete ordinates and  $P_n$ : spherical harmonics) and integral formulation (collision probability method (CPM) and method of characteristics (MOC)). These methods however, require large computational time compared to diffusion theory [Lewis01]. Some of the most common codes using transport theory are DeCART, DOORS [Azmy01], DANTSYS [Busch01], PARTISN [Alcouffe01], PARAFISH [Criekingen01], DYN3D-SP3, PARCS and CRONOS. Diffusion theory has the advantage of providing fast solutions with a penalty on the accuracy; codes which use these methodologies involve FENAT [Zahid01], PARCS, COBAYA3, NEM [Christensen01] and CORETRAN [Ferroukhi01], among others. Deterministic methods are suitable for TH coupling, where the interaction scale is based at channel and sub-channel level.

The CBY core simulator (detailed in Chapter 3.3) is one of the few codes that include both nodal and local level solvers, which allows the description of the core in either FA level or pin (cell) level. Despite the parallel capability of CBY, a whole core 3D simulation at cell level is still very demanding in terms of computational power; nevertheless, new methods such as NCG could have promising future in this area. This is also valid for  $SP_3$  transport simulations of LWR [Gomez03].

Finally, stochastic methods as Monte Carlo (found in codes such as MCNP [Mcnp01], SERPENT [Fridman01] and TRIPOLI [Diop01]) which work with multi-group and continuous energy XSs libraries as well as space and angle fine treatment, give an idea of the degree of complexity involved in the solution of this kind of methods. Hence, for a given set of XSs data, the errors in Monte Carlo take the form of stochastic uncertainties. These stochastic methods are subject of specific interest due to the accuracy of the results (usually establishing the basis for reference solutions), with the drawback of very high computational time, see Table 1 [Kulikowska01].

Table 1. Methods used to perform 3D core neutronic calculations.

Method		Advantages	Disadvantages
Deterministic – Diffusion		Fast	Poor accuracy
Deterministic Transport	Differential form – $S_n$ and $P_n$ methods	Faster for transport	Ray effect negative scalar flux
	Integral form – CPM	Good usage of 3D	Slow
	Integral form – MOC	Precise	Slow
Stochastic Methods		Very accurate	Very slow

While using deterministic approaches to solve neutron transport, substantial computing errors in the solution are unavoidable (integral transport, collision probability, diffusion approximations, self-shielding, energy group condensation and spatial homogenization are based on simplified assumptions). Two main factors influence these errors:

1. Uncertainties in the XSs.
2. Time and space (nodalization) discretization.
3. Energy and angle discretization.

For every kind of method used to solve the neutron transport equation, the main idea of the solution is to obtain a detailed description of the system and minimize the errors associated to heterogeneities in the reactor core. Nevertheless, the accuracy of this system of coupled equations depends on the limit or truncation error of the series leading to the paradigm of precision vs. computational cost. The method used during the dissertation involves the diffusion approach. Therefore only this method will be described in the following subchapter.

### 2.2.1 Methods used to solve the neutron diffusion equation

The diffusion equation (approximation) is a simplification of the transport operator; it can avoid the usage of the neutron angular dependency (flux anisotropy) and express the transport of neutrons through the mathematical Laplacian operator. This approximation is necessary due to the great mathematical complexity of the Boltzmann transport equation. In addition to the angular discretization, the diffusion approximation consists in integrating the solution over  $N$  intervals of different energy groups. This leads to the existence of  $N$  coupled multi-group equations. In practice, the detail in the energy approximation could vary from two groups to thousands of groups. This theory consists in decouple a global interval of energy,  $[0, E_0]$  (where  $E_0$  is the maximum energy that a neutron could achieve), into sub-intervals  $E_0, E_1, E_2, \dots, E_{N-1}, E_N = 0$ , where a group of neutrons “g” is conformed by the ensemble of neutrons which energy lies in the interval “g”, in other words,  $[E_{g-1}, E_g]$  (a second energy interval is defined as “y”). For each of this energy groups, neutron transport is assumed to be mono-kinetic. This assumption leads to acceptable results in terms of precision for most problems that does not involve abrupt changes in flux or highly heterogeneous cores [Reuss01]. The multi-group neutron diffusion equation (NDE) is approximated as in eq. (2.1).

$$D_g \Delta \phi_g - \sum_{a,g} \phi_g - \sum_g (\sum_{s,g \rightarrow y} \phi_g) + \sum_y (\sum_{s,y \rightarrow g} \phi_y) + \chi_g \sum_y (v \sum_{f,y} \phi_y) = 0, \quad (2.1)$$

where;

- $D_g$  : Diffusion coefficient.  
 $\phi_g$  : Neutron flux.  
 $\Sigma_{a,g}$  : Macroscopic absorption XS ( $\Sigma_{a,g} = \sigma_{a,g}N$ ).  
 $\Sigma_{s,g \rightarrow y \rightarrow s, y \rightarrow g}$  : Macroscopic scattering XSs.  
 $\chi_g$  : Fraction of neutrons produced by fission.  
 $\nu$  : Total fission yield (avg. number of *neutrons = prompt + delay*).  
 $\Sigma_{f,y}$  : Macroscopic fission XS.

In eq. (2.1) the first term exemplifies the leakages, the second the absorptions, the third out-scattering from one group ( $g$ ) to another ( $y$ ), the fourth term in-scattering from one group ( $y$ ) to another ( $g$ ) and the last one, neutron generation by fission.

A source for errors obtained by the diffusion approximation comes from the hypothesis of isotropic diffusions (required for simplification). These errors could be minimized by applying a transport correction factor, which consists on replacing the total XS by a “transport” XS. Through the integration of the transport equation over all angles (P<sub>1</sub> approximation, [Lewis01]) and taking into account time dependent factors such as delay neutron source, external neutron sources and current, the diffusion equation in operator notation is given by eq. (2.2);

$$\frac{1}{\nu} \frac{\partial \phi(\vec{r}, E, t)}{\partial t} = (F_p - M^*) \phi(\vec{r}, E, t) + S_d + S. \quad (2.2)$$

In this eq. the operators are defined as illustrated in equations (2.3), (2.4) and (2.5).

Prompt fission source; 
$$F_p \phi(\vec{r}, E, t) = \chi_p(E) \int_0^\infty dE' \nu_p(E') \Sigma_f(\vec{r}, E', t) \phi(\vec{r}, E', t). \quad (2.3)$$

Leakage, absorption and scattering as;

$$M^* \phi(\vec{r}, E, t) = -\vec{\nabla} D(\vec{r}, E) \vec{\nabla} \phi(\vec{r}, E, t) + \Sigma_a \phi(\vec{r}, E, t) - \int_0^\infty dE' \Sigma_s(\vec{r}, E' \rightarrow E, t) \phi(\vec{r}, E', t). \quad (2.4)$$

The sources (delay neutron source resulting from the radioactive decay of precursors with  $\chi_{dk}$  as the delay neutron emission spectra);

$$S_d(\vec{r}, E, t) = \sum_{k=1}^K \chi_{dk}(E) \cdot \lambda_k \cdot C_k(\vec{r}, t). \quad (2.5)$$

To solve the diffusion equation, two continuity (interface) conditions (neutron flux and current, Ficks law) were established in order to find a solution among the coupled system of equations [Reuss01]. These conditions, equations (2.6) and (2.7) and the fact that diffusion approximation is based on isotropy, remark that this method will have weaknesses while encountering highly heterogeneous media, strong absorbing and reflector regions and in general, locations where there are strong changes in the XSs.

$$\phi_{(1)}(\vec{r}, E, \bar{\Omega}, t) = \phi_{(2)}(\vec{r}, E, \bar{\Omega}, t). \quad (2.6)$$

$$J_{(1)}(\vec{r}, E, t) = J_{(2)}(\vec{r}, E, t) = -D_g \nabla \phi_g = J_{(g)}(\vec{r}, E, t). \quad (2.7)$$

Nevertheless, to solve (2.1) several methods have been studied and implemented for its discretization. These methods are discussed hereafter, which include finite difference methods, finite element methods, nodal methods and synthetic methods [Cho01]. Finite difference methods (FDM) consists in discretize each of the variables of the problem (to approximate the derivatives) by small quotients of finite differences. In two dimensions and after applying FDM, the diffusion equation looks as follows;

$$\sum_i \sum_j D_g (\Delta \phi)_g - \sum_{a,g} \phi_g + S = 0. \quad (2.8)$$

By varying the indexes  $i$  and  $j$  over the reactor (space), a linear system of equations is obtained over a meshing element. Even though similar in nature as the FDM, the finite element method (FEM) [Coulomb01] involves the usage of test functions. Each of these test functions corresponds to one and only one decoupled system of equations, where linear, quadratic or cubic functions are adopted in order to (similar to FDM):

1. Assure the continuity of the functions (elements).
2. Approximate the solution with a desired degree of accuracy.

Especially for parabolic or cubic approximations of the test functions, this method shows improvements compared to FDM in terms of precision if the solution has similar spatial discretization. For the specific case of the neutron flux and applying the finite element method, the following equation is obtained;

$$\phi(\vec{r}) = \sum_{\varpi} A_{\varpi} \varphi_{\varpi}(\vec{r}). \quad (2.9)$$

In this case, equation (2.9), the flux is composed of  $\varphi_{\varpi}(\vec{r})$  (the expansion test functions) and the unknown coefficients  $A_{\varpi}$ , where “ $\varpi$ ” range over the full space of the problem. This method is also valid for homogenization at FA level. For nodal methods their advantage relies on the application of coarse meshes to represent the core, useful when dealing with 3D FA base problems. Similarly to the FEM, polynomial functions are used to approximate the solution, where the main differences are:

1. Neutron flux is considered not only inside the meshing nodes, but also at the faces.
2. The degree of approximation for the flux at internal and external faces is different.
3. The internal flux is calculated based on: *Absorptions + Leakage = Source*.
4. Incoming and outgoing currents are considered.
5. Neutron currents are used as BCs for the nodes.

Modern nodal methods involve equivalence homogenization theory (EHT), transverse integration procedures and analytic function expansion nodal methods. The last method involves synthetic methods, which have a completely different philosophy compared to nodal or finite difference methods. The method could be summarized in three steps [Reuss01]:

1. Division of the core in the axial direction (according to its heterogeneity) and obtaining the 2D radial flux  $(x,y)$  for each of these segments.
2. Application of the synthetic operator by trying to find the flux in the 3<sup>rd</sup> dimension  $(z)$ , with a linear combination of the 2D radial fluxes and a coefficient depending on  $z$  (separation of variables).

$$\phi(x, y, z) = \sum_{\varpi} \psi_{\varpi}(z) \varphi_{\varpi}(x, y). \quad (2.10)$$

3. Determination of the unknown coefficient  $\psi_{\varpi}(z)$ .

This method could also be applied to multi-dimensional problems involving synthesis of space and time for point kinetic problems.

## 2.3 Core thermal-hydraulic calculations

In addition to the N behavior of the core, the TH analysis of NPPs is critical for the correct study of phenomena that affect the reactor performance and safety. The energy deposited in the fuel caused by fission is transferred to the coolant by conduction, convection and radiation. Therefore, the TH (heat transfer and fluid mechanics) analysis is of extreme importance for the correct study of flow in motion and heat exchange inside a nuclear reactor. The main objectives of TH core design and safety include the precise calculation of local parameters, complemented to the achievement of high power density (minimize core size) and high specific power (minimize fuel inventory) so that safety parameters do not exceed a critical value independent of any anticipated transient [Coppolani01].

Important developments in TH systems have been derived in the last fifty years, starting from simple homogeneous models up to two phase flow modeling using CFD tools. As mentioned in Chapter 2.1, three different scales used to solve the core TH phenomena are observed: 1D and 3D system code such as RELAP5, RELAP5-3D, TRACE [Trace01] and CATHARE, quasi 3D sub-channel codes like the COBRA family, FLICA4 and SCF (sub-channel codes which perform a more detailed solution of the fuel elements leading to more accurate results at meso-scales) and finally the CFD codes such as STAR-CD, NEPTUNE and ANSYS-CFX [Ansys01] that are able to provide detailed solutions at meso and micro-scales. The following subchapter is limited to sub-channel TH codes only because they are used in the frame of this dissertation.

### 2.3.1 Mathematical basis of core thermal-hydraulic codes

The main equations that rule the TH in a reactor core are classified in terms of mass, momentum and energy conservation (typical two phase flow six-equations model). The ones described hereafter involve one dimensional space averaged transport of mass (eq. 2.11), momentum (eq. 2.12) and energy (eq. 2.13) for phase “ $k^*$ ” [Kazimi01]. Definitions are found after each equation (for the sake of simplification, repeated terms are not duplicated).

$$\frac{\partial[(\rho_{k^*}\alpha)A_z]}{\partial t} + \frac{\partial[(\rho_{k^*}\bar{v}_{k^*z}\alpha)A_z]}{\partial z} = \Gamma_{k^*}A_z, \quad (2.11)$$

where;

$\rho_{k^*}$  : Phase density.

$\alpha$  : Void fraction.

$A_z$  : Cross sectional surface area at axial level  $z$ .

$\bar{v}_{k^*z}$  : Phase mass velocity.

$\Gamma_{k^*}$  : Mass exchange rate  $\left(\frac{\dot{m}_{k^*}}{V}\right)$ .

$$\begin{aligned} \frac{\partial[\rho_{k^*}\bar{v}_{k^*z}\alpha]A_z}{\partial t} + \frac{\partial[\rho_{k^*}\bar{v}^2_{k^*z}\alpha]A_z}{\partial z} &= \{\Gamma_{k^*}\bar{v}_{k^*s} \cdot \bar{n}_z\}A_z + \{\bar{F}_{wk^*}^m \cdot \bar{n}_z\}A_z - \\ \frac{\partial[\rho_{k^*}\alpha]A_z}{\partial z} + \{\bar{F}_{wk^*}^m \cdot \bar{n}_z\}A_z + \{\rho_{k^*}\alpha\}\bar{g} \cdot \bar{n}_z A_z, \end{aligned} \quad (2.12)$$

where;

$\bar{n}_z$  : Normal vector in flow direction.

$\bar{F}_{wk^*}^m$  : Net shear force at fixed wall boundary.

$p_{k^*}$  : Pressure for the phase in question.

$\bar{g}$  : Gravitational constant.

$$\begin{aligned} \frac{\partial[\rho_{k^*}\overset{\circ}{u}_{k^*}\alpha]A_z}{\partial t} + \frac{\partial[\rho_{k^*}h_{k^*}\bar{v}_{k^*z}\alpha]A_z}{\partial z} &= \left\{\Gamma_{k^*}\overset{\circ}{h}_{k^*s}\right\}A_z - p_{k^*}\frac{\partial[\alpha]A_z}{\partial z} + \\ \{q_{k^*}^m\alpha\}A_z - q_{wk^*}^n\alpha P_w - \{\rho_{k^*}h_{k^*}\bar{g} \cdot \bar{v}_{k^*z}\alpha\}A_z + \{Q_{sk^*}\}A_z + \xi, \end{aligned} \quad (2.13)$$

where;

$\overset{\circ}{u}_{k^*}$  : Stagnation energy.

$h_{k^*}$  : Phase enthalpy.

$\overset{\circ}{h}_{k^*s}$  : Stagnation enthalpy.

$q_{k^*}^m$  : Volumetric heat flux.

$q_{wk^*}^n$  : Surface heat flux at the wall.

$P_w$  : Wall wetted perimeter.

$Q_{sk^*}$  : Rate of volumetric heat generation.

$\xi$  : Viscous dissipation term.

The BCs necessary to obtain the steady state solutions include parameters at the wall, inlet and outlet of the control volume (CV). The resolution of these general balance equations will be described in more detail in Chapter 3.2, focusing on the specific equations of the SCF code. In addition to this basic formulation, the majority of the TH models used to solve the system of equations by system and core TH codes are mentioned hereafter [Bonalmi01], [Kazimi02], [Ishii01]. These models differ in terms of complexity, details to describe two-phase flow phenomena, number of resolved equations and assumptions.

1. Homogeneous Equilibrium Model (HEM): Assumes that the velocity, temperature and pressure are the same between fluid phases (liquid and vapor). This assumption is based on the fact that these parameters do not create rapid changes in the conservation equations, so that thermal and dynamic equilibrium is reached between phases. The model is good for high pressure and high flow rate conditions. As a drawback, rapid accelerations or pressure changes and unequal velocities and temperatures, cannot be accurately modeled with HEM.
2. Un-equal Velocity Equal Temperature (UVET): The model assumes TH equilibrium between phases, leading to the solution of two global equations, energy and momentum and two equations for the conservation of mass, one for each phase. The UVET model is widely used for analyzing pressurized water reactors (PWRs) however; it is not precise when dealing with transients involving transitional flow regimes.
3. Un-equal Velocity Un-equal Temperature (UVUT) model: One of the most accurate TH models used to study two phase flow phenomena. This model does not assume dynamical and thermal equilibrium, leading to the solution of six equations, three for the liquid phase and three for the gaseous phase.
4. Drift Flux Model (DFM): General approach to obtain the slip ratio by considering the average velocity of the vapor in a channel. The DFM is particularly useful when dealing with flows in which relative motion is controlled by buoyancy forces and fluid drag. As a drawback, DFM cannot approximate multi-phase flows since the relative motion is driven by the pressure and velocity gradients between the two phases.

To close the system of equations several closure laws must be established. Some of these will be mentioned in Chapter 3.2. In addition to the general balance equations encountered in TH codes, cross flows between channels or sub-channels have to be considered specially when dealing with heterogeneous TH BCs inside the reactor core or pin clusters.

At sub-channel level, phasic TH properties such as axial velocity and density are represented by single averaged values over a specific sub-channel volume. In this sub-channel approach, the rod bundle or FA is subdivided into several interconnected parallel channels. The idea of these types of methods is that they assume that the flow is predominant in the axial direction and therefore a simplification of the 3D modeling of the energy and momentum equations can be applied. By introducing the cross-flow terms in the equations, exchanges in the radial direction are considered. Conservation equations like energy and lateral momentum must take into account exchange rates between adjacent sub-channels. The coolant enthalpy and velocity is found by solving these conservation equations. At the moment, three types of sub-channels are considered in the modeling; coolant centered CV, rod centered CV and triangular shape sub-channels [Anglar01], as shown in Fig. 2.

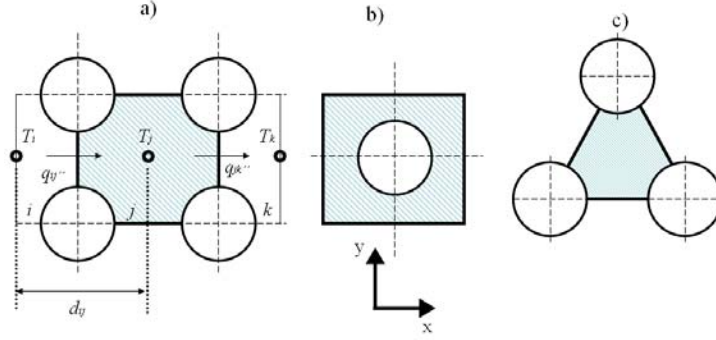


Fig. 2. Coolant centered (a), rod centered (b) and triangular (c) sub-channels.

In the following equations related to the mass (2.14), axial momentum (2.15), lateral momentum (2.16) and energy (2.17), the study is limited to the coolant centered sub-channel discretization. In addition to the manipulation of the previously discussed general conservation equations (2.11), (2.12) and (2.13), a fourth equation to the transverse momentum is implemented, eq. (2.17). Hereafter, a condensation of these equations for single phase flows [Todreas01], which are based on Fig. 2 (a) and correspond to mass, energy and axial and lateral momentum respectively.

$$A_z \frac{\partial \langle \rho_i \rangle}{\partial t} + \frac{\Delta \dot{m}_i}{\Delta z} = \sum_{j=1}^J W_{ij} \quad (2.14)$$

where;

$i$  : Current sub-channel.

$j$  : Neighbouring sub-channel.

$\rho_i$  : Sub-channel density.

$\dot{m}_i$  : Axial mass flow rate ( $\rho_i v_z A_z$ ).

$W_{ij}$  : Diverse cross flow from sub-channel  $i$  to  $j$ .

$$A_z \frac{\partial \langle \rho h \rangle_i}{\partial t} + \frac{\Delta \dot{m}_i h_i}{\Delta z} = \langle \dot{q}_i \rangle - \sum_{j=1}^J W_{ij}^{*H} [h_i - h_j] - \sum_{j=1}^J W_{ij} \{h^*\} + A_z \left\langle \frac{\partial p_i}{\partial t} \right\rangle, \quad (2.15)$$

where;

$h_{i,j}$  : Enthalpy from sub-channel  $i$  or sub-channel  $j$ .

$\dot{q}_i$  : Sub-channel linear heat rate generation.

$W_{ij}^{*H}$  : Energy transfer from sub-channel  $i$  to  $j$ .

$h^*$  : Characteristic enthalpy related to  $W_{ij}^{*H}$  .

$p_i$  : Pressure related to sub-channel  $i$ .

$$\frac{\partial \langle \dot{m}_i \rangle}{\partial t} + \sum_{j=1}^J W_{ij} \{v_z^*\} + \frac{\Delta \dot{m}_i v_{iz}}{\Delta z} = -A_z \langle \rho_i \rangle \bar{g} - A_z \frac{\Delta \{p_i\}}{\Delta z} - \sum_{j=1}^J W_{ij}^{*M} (v_{iz} - v_{jz}) - \left\{ \frac{F_{iz}}{\Delta z} \right\}, \quad (2.16)$$

where;

$v_z^*$  : Characteristic velocity related to  $W_{ij}^{*M}$  .

$v_{iz}$  : Flow velocity.

$W_{ij}^{*M}$  : Momentum transfer from sub-channel  $i$  to  $j$ .

$$\frac{\partial \langle W_{ij} \rangle}{\partial t} + \frac{\Delta}{\Delta x'} (W_{ij} \{v_x\}) + \frac{\Delta}{\Delta x'} (W_{ij} \{v_z\}) = - \left( S_{ij}^y \frac{\Delta}{\Delta x'} \{p_i\} \right) - \left\{ \frac{F_{ix}}{\Delta x' \Delta z} \right\}, \quad (2.17)$$

where;

$\Delta x'$  : Transverse length (distance between rods).

$S_{ij}^y$  : Gap between rods along “y” direction.

$F_{ix}$  : Averaged force per unit length of the fluid on the solid.

For the case of coolant centered sub-channels, lateral gradients of flow and enthalpy are relevant within the sub-channel (across the sub-channel boundaries). In this case, flow parameters (density, void fraction and temperature) are averaged over the sub-channel area and located at the sub-channel geometrical centre, leading in transverse one dimensional heat conduction from sub-channel “ $i$ ” to “ $j$ ” (see Fig. 2 (a)) as;

$$q''_{ij} = C_{\tau,ij} \frac{T_i - T_j}{d_{ij}}, \quad (2.18)$$

where  $C_{\tau,ij}$  is the thermal conductivity,  $T_i$  and  $T_j$  are the temperatures of sub-channels  $i$  and  $j$ , and  $d_{ij}$  is the distance between rods. The assumption of average localized parameters is valid for low thermal conductivity coolants and loose rod bundles as the ones used in typical LWRs.

## 2.4 Multi-physical coupling approaches between codes

The main objective of the multi-physics coupling approach is to obtain accurate results of problems that are correlated in nature. Nowadays, this coupling is realized at different scales through the interaction of best estimate codes developed around the world. For this purpose, several requirements to achieve efficient coupled schemes must be respected [DAuria01], e.g.:

1. Spatial nodalization and mapping of the involved computational domains of the different codes.
2. Development of algorithms for feedback handling.
3. Definition of numerical schemes: steady state and transient solutions.
4. Convergence control algorithm.

In addition, the following aspects are important for the acceptability of coupled codes in industry-like applications in the frame of safety analysis: adequate computer capacity and efficient coupling procedures, validation of coupled codes and evaluation of uncertainties. Table 2 shows a recapitulation of some coupled codes used around the world. Not only core N and TH coupled codes have been investigated, also codes in the areas of severe accidents RELAP5/MELCOR [Cole01], [Rodriguez01], containment RELAP5/GOTIC [Keco01], RELAP5/COCO [Stosic01] and fuel behavior PARCS/FRAPCON [Ivekovic01], play important roles in the area of nuclear safety.

Developments in the N and TH solvers for improved schemes are envisaged in the future. The next generation of coupled code methods will conserve the multi-physics, multi-scale characteristics of current coupled schemes, provide fully integrated and precise codes that can be use for the analysis of LWRs, and exploit high performance computing (HPC). In the N side, MOC looks as an important methodology with promising future for the improvement of N solvers, in addition to the use of 3D Monte Carlo in massively HPC. On the TH side research in interfacial area transport (e.g. explicit modeling of bubble interactions) is under development, finite volume based codes are envisaged for the solution of pressure, 3D momentum, enthalpy and turbulent equations over arbitrary meshes. Consequently new requirements for this purpose are considered, for instance, development of multi-phase models, conjugate heat transfer, moving BCs and parallel computing [Downar01].

Table 2. List of coupled codes used around the world.

Neutronics/ Thermal-Hydraulics	Comments	Neutronics/ Thermal-Hydraulics	Comments
<b>DYN3D/SUBCHANFLOW</b> [Gomez01] GERMANY	DYN3D: Multi-group SP <sub>3</sub> neutron transport solver for 3D hexagonal and square geometries. SUBCHANFLOW: Sub-channel TH code based on the COBRA family. Extended to hexagonal geometries and GEN-IV coolants for assembly and pin wise solutions.	<b>ATHLETE/QUABOX</b> [NEA01] GERMANY	ATHLETE: Modular TH code for the analysis of anticipated and abnormal plant transients, small and intermediate leaks as well as large breaks in LWRs. QUABOX: 3-D core model used for stationary and transient calculations of reactor cores in LWR. The neutron solution is based on the diffusion approximation of the transport equation in two energy groups, which is solved by a coarse grid method.
<b>COBAYA3/FLICA4</b> [Crouzet01] SPAIN/France	COBAYA3: Multi-group 3D diffusion code for hexagonal and square geometries, applied for FA base and pin base calculations. FLICA4: 3D and two phase flow TH computer code with advanced numerical methods for nuclear applications.	<b>TRACE/PARCS</b> [Downar04] USA	TRACE: 3D TH code using working fluids such as He, CO <sub>2</sub> and Pb-Bi. PARCS: As before.
<b>RELAP5/PARCS</b> [Downar02] [Vedovi01] USA	RELAP5: 1D systems TH. SBLOCA and system transient tool for LWRs analysis. PARCS: Solves the time-dependent two-group neutron diffusion equation in 3D cartesian geometry using nodal methods with extension to hexagonal geometries.	<b>CAT-HARE/CRONOS/FLICA4</b> [Giquel01] FRANCE	CATHARE: TH system code for PWR safety analysis, accident management and definition of plant operating procedures. CHRONOS: Environment dedicated for integrated simulations. FLICA4: As before.
<b>TRAC/BF1/NEM</b> [Finnemann01] USA	TRA-BF1C: Capable to model TH phenomena in 1D or 3D and analyze LB-SB/LOCAs and system transients. NEM: Nodal expansion method for the multi-group neutron diffusion equation, based on a 1D polynomial flux expansion.	<b>RETRAN3D/SIMULATE3K</b> [NEA01] USA/FINLAND	RETRAN3D: Based on HEM, is a transient TH core design tool used for evaluating LWRs. SIMULATE3K: Is a two-group 3D advanced nodal reactor analysis transient code which solves the frequency-transformed time-dependent diffusion equation.
<b>DYN3D/RELAP5</b> [Kliem03] GERMANY/RUSSIA	DYN3D: As before. RELAP5: As before.	<b>COBAYA3/COBRATF</b> [Jimenez03] SPAIN/USA	COBAYA3: Multi-group 3D diffusion code for hexagonal and square geometries, applied for FA base and pin base calculations. COBRA-TF: TH code applied to transient analysis of LWR cores starting from steady state conditions and modeling at FA or sub-channel level.
<b>UMK/BARS/KORSAR</b> [Parisi01] RUSSIA	UNK: Neutronic library generation tool. BARS-KORSAR: Coupled 3D N/TH plant transient analysis tool.	<b>RELAP5/PANTHER</b> /COBRA-TF [Bosso01] BELGIUM	RELAP5: As before. PANTHER: Multi-group 3D nodal diffusion code for steady state and transient analysis. COBRA-TF: As before.

### 2.4.1 Coupling methodologies

A coupling scheme between codes is referred as a special technique that involves the execution of two or more codes in such a way that these codes are able to exchange relevant variables (information). To properly resolve the multi-scale multi-physics problems discussed in Chapter 2.1, three different approximations for this coupling between codes are present [Baerd01], [DAuria01], and [NEA01].

1. External coupling, Fig. 3 (a): The objective is to give the BCs obtained by one code to the second code so it can perform its solution, leading to a feedback exchange at the CV boundaries. This is an iterative process at which the second code also gives the feedback BCs to the first code (explicit coupling), leading to a need for modeling transient scenarios with very small time steps to ensure stability in the calculation (Courant condition).
2. Integrated coupling, Fig. 3 (b): In this case both codes are embedded and both solve their set of equations, however, the level of integration requires wide knowledge in informatics and modeling is usually complex. For the feedback exchange the meshing elements are mapped directly between the two codes.
3. Combined coupling, Fig. 3 (c): Also called parallel coupling, is based on the idea of making the codes interact between each other keeping in mind the philosophy of code independency. Each code must be able to perform stand alone calculations; however, it may be required to interact with the other code at specific time steps.

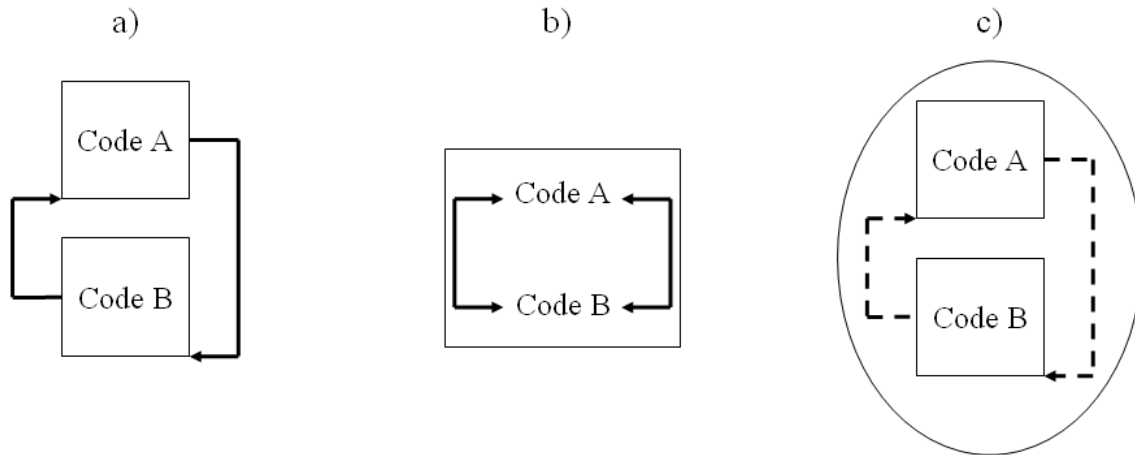


Fig. 3. External (a), internal (b) and combined (c) coupling approaches.

For obtaining a good solution (balance between precision in the solution and computing time optimization), usually a more refined mesh (for spatial coupling and not including CFDs) is required (smaller mesh refinements lead to more accurate solutions, domain discretization is finer and geometrical details are represented in a better way) [Downar05]. This however, results in long computational time

due to the increase of meshing elements. These types of problems give rise to important coupling methodologies such as explicit, semi-implicit, SETS [Junge01] and implicit schemes among others. A modern way to approximate numerical problems is to write the governing differential equations in a finite difference form. Generally, there are three types of finite difference formulations, forward differencing eq. (2.19), backward differencing eq. (2.20) and central differencing eq. (2.21) [Watson01];

$$f'(x) = \frac{f(x+h) - f(x)}{h}, \quad (2.19) \quad f'(x) = \frac{f(x) - f(x-h)}{h}, \quad (2.20) \quad f'(x) = \frac{f\left(x + \frac{h}{2}\right) - f\left(x - \frac{h}{2}\right)}{h}. \quad (2.21)$$

Even though they are not mentioned, the reader should know that there are other types of spatial discretization techniques, involving finite volume method, finite elements and fine mesh methods. Similarly to the spatial discretization of the differential equations, time discretization must be applied to the previously mentioned techniques [Mousseau01]. Another critical topic to mention is the interaction between codes, which rule the way information (feedback) flows from one code to another for steady state and transient scenarios. The fundamental aim behind the simulation of steady state coupled schemes is to obtain N parameters (power distributions, neutron velocities, etc...) and TH parameters (coolant and fuel thermo-physical properties) to obtain localized information about safety relevant parameters. Details about this kind of coupling will be discussed in Chapter 6. Two important issues for coupling codes are studied hereafter; they involve time step synchronization for the case of temporal coupling and feedback treatment of parameters.

#### 2.4.2 Convergence of coupled steady state solutions

A convergence criterion for the steady state coupled solution is applied iteratively following an explicit approach. However, it is important to mention that each code has its own convergence criteria, which will be discussed in Chapters 3.2 and 3.3. The convergence is based on a calculation-feedback-calculation strategy, which is depicted in Fig. 4.

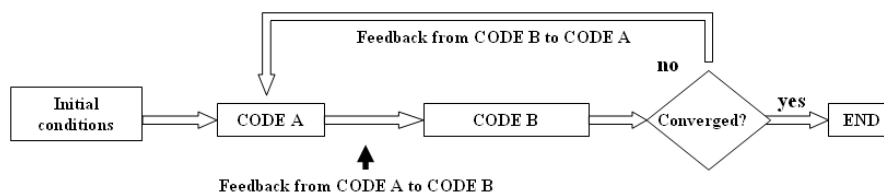


Fig. 4. Steady state convergence definition (calculation-feedback-calculation).

In this case, CODE A (N) begins its calculation with pre-defined fixed TH conditions representing an average value for the steady state and planar distribution of the fuel Doppler temperature based on the

input deck for the first XS update. Once CODE A converge its own solution, the 3D power distribution is updated in the global parameters of CODE B (TH), which performs its own solution with this “new” power distribution. New TH parameters are calculated and passed to CODE A in order to perform the next iteration’s calculation. The analysis of this steady state convergence scheme will be detailed in Chapter 6.1.1.

From [Gomez03], it was shown that the coupled solution must consider both N and TH parameters for convergence check. The convergence of the global parameter, multiplication factor ( $k_{\text{eff}}$ ), does not guarantee the convergence of the local TH parameters. Just for the sake of exemplification, a study was performed (related to the benchmark TMI-1 MSLB and discussed in detail in Chapter 7.1.2) where the convergence criterion for the  $k_{\text{eff}}$  ( $\epsilon_N$ ) was set to  $\epsilon_N = 0.1$  parts per cent mille (pcm) and fuel Doppler temperature ( $T_{\text{Dopp}}$ ), moderator temperature ( $T_{\text{mod}}$ ) and density ( $D_{\text{mod}}$ ) criteria ( $\epsilon_T$ ) to  $\epsilon_T = 1.0^{-4}$ . These variations are derived from the difference of the selected parameters between two consecutive iterations, e.g. if the variation of  $k_{\text{eff}}$  is less than a defined criterion, convergence is achieved for this parameter.

### 2.4.3 Temporal coupling

For both FA and pin-wise based coupling, the managing and well adaptation of the time steps between the TH and N codes is important since both codes have their own time step selection algorithm. The coupling of two different codes has to be implemented for both stationary and transient conditions. The most widely used option is the loose (“low”) coupled methods, which differently from tight (“high”) [Gaston01], provide certain independence between the coupled codes. Here, four kinds of solutions are encountered (illustrated in Fig. 5), semi-implicit [Jeong01], explicit (also referred as “marching solution method” or “asynchronous models” [Grandi01]), staggered Operator Splitting (OS) coupling and implicit schemes (also known as “synchronous models”). The nonlinear behavior of this coupled scheme between the N and TH models raise a challenge to find an accurate and efficient solution for LWR transients. For instance, the temporal and spatial discretizations affect stability parameters such as decay ratios and key parameters of reactivity insertion accidents (powers peak, Doppler temperatures and coolant enthalpies), which are very sensitive to the degree of implicitness in the coupling between the N and the TH models. Therefore, several approaches for the temporal coupling between codes must be precisely understood. The following figures show these approaches [Ragusa01], [Watson01], where special emphasis is done for N and TH.

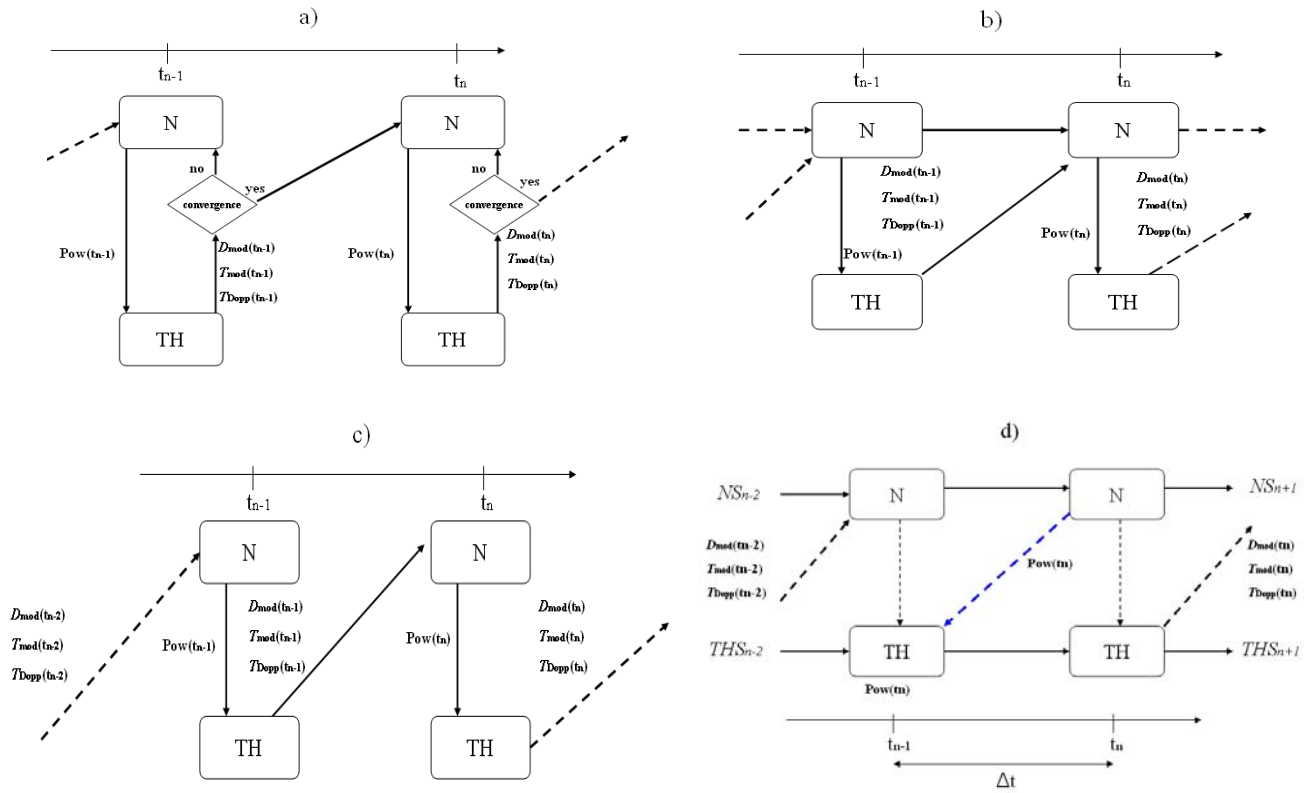


Fig. 5. Implicit (a), semi-implicit (b), explicit (c) and staggered OS (d) coupling schemes.

As can be seen in Fig. 5 (d), the  $N$  solution ( $NS$ ) and the  $TH$  solution ( $THS$ ) between two consecutive time steps are given by equations\* (2.22) and (2.23) respectively;

$$NS_{\Delta t} = N(\Delta t, NS_{n-1}, THS_{n-1}), \quad (2.22)$$

$$THS_{\Delta t} = TH(\Delta t, NS_n, THS_{n-1}). \quad (2.23)$$

Multiple time steps marching schemes allow the solution of a selected code to proceed with several steps, while the other coupled code marches only with one large step. This temporal adaptive algorithm was developed to perform the synchronization and optimization of the performance of 3D N/TH FA and sub-channel analysis coupled code systems. However, it was noted [Grandi01] that applying automatic time steps selection to some models, did not increase the qualitative precision of the solution compared to fix time steps implicit schemes, but it reduces significantly the computational cost. Coming back to the staggered OS [Zerkak01], the convergence of the solution is ruled by the time step where in general a master code controls the time advancement. Small time steps are required specifically for the  $N$  (e.g. very small neutron generation time in the order of  $t = 10.0^{-4}$  s). Examples of this

\* The subscript “ $n$ ” represents the current time step.

type of coupling which involve OS schemes are TRACE/PARCS, RELAP5/PARCS and CRONOS2/FLICA4 [Royer02].

In the implicit approach (Fig. 5 (a)), convergence of the individual codes and of the feedback is required. This method has the advantage of being the most accurate and stable out of the others. Several different approaches to solve the implicit coupling involve: Implicit-Runge-Kutta methods [Lozano02], nested loops approximations and JFNK methods [Mousseau01], where improvements in the areas of convergence, dynamic time steps and non-linearities are envisaged. Lastly, semi-implicit methods, Fig. 5 (b), have the advantage of employing feedback parameters from old and new time steps (as done in TRAC-PF1/NEM). This might be of specific interest when dealing with power maps (PMs) as done with SCF. The main disadvantage of this method is its instability caused by the non-converged feedback parameters.

Implicit methods are required for many coupled problems due to the presence of non-smooth or rapidly varying transients, in the case of the neutronic solution. Especially in reactor analysis, these fast transients take into account the presence of inverse neutron velocity terms, which usually have convergence instabilities. In principle, it is desired to implement the temporal coupling with an implicit approach to ensure that the scheme will be stable, leading to the usage of longer time steps during the transient. Nevertheless, this type of approach is extensive in the way that each code requires complex modifications; therefore, other methods are encountered, such as the explicit method which presents limitations in the time step control to ensure stability.

#### **2.4.3.1 Time step synchronization**

For transient analysis the easiest way to couple these kinds of systems is by fixing the time step based on one of the two involved codes. This approach may lead to inaccurate predictions of the time dependent power behavior in continuous fast transients where the neutron flux (refer to Chapter 2.2.1) distribution and power shape change rapidly. In the counterpart, when the N code is the master, the computation time may increase due to the rapid repartition of time steps that could be easily managed with longer time step periods. Coupled time dependent algorithms can be found in the literature [Zerkak01]. For some time step control and calculation models, each code performs independently from each other. In this particular case, the vector containing the state variables is used to check the “global” time step and predict a new time step. A restart of the coupled code system from the previous time point is required if the criterion is not met.

In discussion of time step control schemes, it is instructive to consider the semi-implicit method. In order for the semi-implicit solution to be numerically stable, it must respect the material Courant limit, which dictates the maximum time step size based on the stability of computational parameters passing through a calculation node. This issue will be discussed in more detail in Chapter 7.1.3.

For some other coupled schemes (e.g. TRAC-BF1/NEM), variable time step algorithms have been developed in such a way that the kinetics algorithm has an automatic time step control routine that monitors temporal changes (global total power and local neutron flux) during a given time step and adjusts the time step size automatically. Other coupling approach involves the use of message passing interface (MPI) [Perez01] and the executive parallel virtual machine (PVM) [Geisto01] program, which is able to handle two of the major challenges for coupled calculations, exchange of boundary condition information between codes with different data structures and coordination of the time dependent advancement. The PVM philosophy is based on the definition of variables to be exchanged and the coordination of the advancement through time (calling for exchange variables between similar tasks, controlling of output generation and shutting down virtual memory after termination). The executive program also allows for “synchronous” and “asynchronous” exchange of data between tasks. For “synchronous” exchange, the process is forced to have similar time steps, with interaction every time step [Jimenez01]. Some examples are found in RELAP5/PARCS, ATHLET/QUABOX, TRACE/PARCS and CRONOS/FLICA4. For “asynchronous” exchange, time steps are matched and data are exchanged at predefined time intervals only. Moreover, the executive program allows for other types of schemes, including “semi-implicit” coupling.

## 2.5 Non-conform geometry

In the last years, strong efforts have been made to develop detailed solutions in the areas of coupled neutron kinetics and TH codes with emphasis on local refinement of the N and TH solution known as NCG or hybrid analysis approach (concept developed in the frame of this thesis concerning localized mesh refinement). This type of hybrid models that allow doing “zooming” in some parts of the core, are necessary for predicting safety parameters based on local information, e.g. information at pin level concerning temperature profiles along the hottest pins. Nowadays, two types of calculations are widely used within coupled N/TH codes, nodal (FA) base, or local (PBP) base solutions. Both analyses have advantages and disadvantages, as discussed hereafter.

Nodal base solutions aim for fast running calculations with the drawback of losing precision or accuracy compared to PBP solutions. PBP solutions work with more refined or detailed models, leading to the accurate prediction of local safety parameters with the drawback of high computational power.

Hybrid solutions on the other hand, try to combine the advantages of both types of calculations (FA level and PBP level) while minimizing their disadvantages.

Specific attention has been given to the N side. In [Chiba01] a hierarchical domain decomposition - boundary element method (HDD-BEM) for solving the 3D NDE has been proposed. The domain is decomposed into homogeneous regions, where two types of calculations are applied. “Lower level” calculations involve enforcing assumed BCs and  $k_{\text{eff}}$  to the NDE which is applied to the decomposed homogeneous region. At “higher level” calculations (assumed values) internal BCs and  $k_{\text{eff}}$  are modified so as to satisfy the continuity condition for the neutron flux and currents, eq. (2.7), in the inner boundaries. Furthermore, [Zhang01] proposed a p-refinement technique (adaptive selection of the polynomial approximation) for the inter-element approximation in a hybrid finite element technique. Other techniques involve the use of different N kernels for one solution. The “post-refinement” multi-scale method uses the global solution to determine the BCs for the local solution. The local solution is solved using either fixed or albedo BCs and has no impact on the global solution. The “embedded” multi-scale method allows the local solver to change the global solution by imposing BCs and improve the global-local solution scheme [Collins01]. In terms of complexity, due to the nature of the transport equation, NCG in the N side has not yet been widely used in nuclear engineering. Consequently, numerical approximations have been developed for the multi-group diffusion equation, often employed in 3D reactor core analysis [Ragusa02].

The main objective is to obtain numerical solutions with high accuracy and resolution while requiring less memory and shorter CPU time. For doing that the full computational mesh only needs to be fine where the solution is rough and can be coarse in areas where the solution is smooth and well resolved even on large cells. The main feature of this hybrid method is the usage of separate meshes for individual regions in both N and TH, e.g. regions where a control rod (CR) ejection is expected or a MOX assembly is encountered surrounded of typical uranium oxide type of assemblies for LWR. The Fig. 6 exemplifies this type of discretization, where nine fuel assemblies (3x3 mini-core with outer reflectors) are modeled at FA level (nodal), PBP level (local) and a mix of both – hybrid.

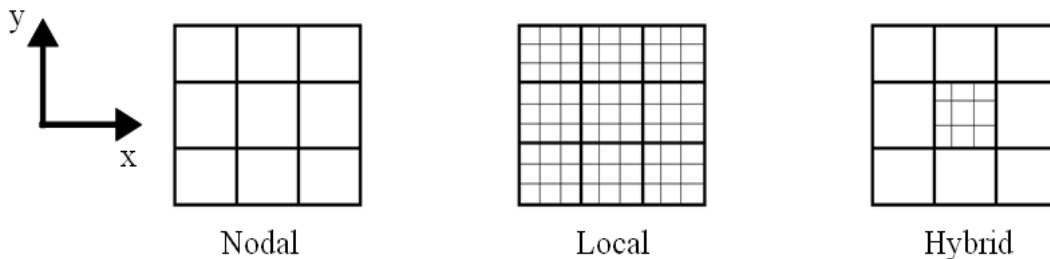


Fig. 6. Illustration of different types of FA radial discretizations (nodal, local and hybrid).

The problem is mostly encountered on the N domain, where it is noted that fast and thermal neutrons behave differently within a computational domain. Fast neutrons tend to travel further and are less affected by local variations in the material properties, whereas thermal neutrons perceive more localized effects. Therefore, smoother solutions are expected for higher energy neutrons and more rapidly varying solutions for lower energy ones. From [Ragusa02] is concluded that these types of refinement techniques provide 1.0% accuracy five times faster than uniform refinement and 0.01% accuracy twenty times faster. In addition, the mesh refinement technique becomes competitive compared to uniform meshes since its solution has deviations in the 1.0 pcm range.

Other type of approaches involve the pin power reconstruction method, where a fast calculation of pin power distributions in a FA is obtained through a combination of an analytical solution of the NDE and form functions taking into account heterogeneities. The idea is to reconstruct the pin powers based on the power peak as a power value of a hot channel (hot channel analysis is considered as the basis for the pin power reconstructions method implemented, e.g. in DYN3D [Gomez03]). Even though the solutions obtained are relatively efficient in terms of computational power, the solution itself does not consider the real solution for the NDE in the localized place of interest.

---

## 3 The NURESIM platform and the mathematical-physical fundamentals of the involved codes

This chapter is devoted for describing the NURESIM platform, its peculiarities and the fundamentals of two of the codes that interact through its interface. One code is the TH sub-channel code SCF developed at the KIT, including the boron transport model description. The other code is the reactor dynamic code CBY, developed by the UPM.

### 3.1 The NURESIM platform

#### 3.1.1 General description

The NURESIM platform is under development in the frame of the European collaborative projects named NURESIM and NURISP (a partnership between fourteen European countries and twenty-two organizations) [Bestion01]. This platform facilitates a more accurate simulation of the physical phenomena by coupling the most advanced core physics, single and two phase flow TH and fuel mechanics European codes following a multi-scale and multi-physics approach. Codes will be connected to the platform and new steps will be made for integration, model development, coupling, uncertainty and sensitivity analysis, and verification and validation with broader applications. During the course of NURISP the focus will be on present (GEN-II) and future (GEN-III) PWRs, VVERs and boiling water reactors (BWRs), but care will be taken to use generic methods so that future extension to GEN-IV reactors will be possible. Different reactor dynamic solvers (CRONOS2, DYN3D and CBY) have been implemented into the NURESIM platform and coupled with the sub-channel code FLICA4 at a nodal and pin level [Ferraresi01], [Gomez02]. One of the novel aspects of the NURESIM platform is the way how the different solvers are spatially mapped to each other based on a mesh superposition (automatic mapping) and using an in-built interpolation module INTERP\_2\_5D. This offers the user a mapping flexibility.

The platform is based on the open source software SALOME [Royer01] which is suitable for advanced multi-physics and multi-scale numerical simulations including a powerful pre- and post-processor. It allows the chaining and coupling of codes devoted to different fields like TH (macro-, meso- and micro scale), N (nodal and cell level) and pin mechanics. The NURESIM platform permits the realization of flexible coupling schemes between different fields taking advantage of a unique memory exchange data (MED) file as a key element. SALOME is based on a flexible structure suitable for the integration of different kinds of codes. These SALOME functionalities can be used for de-

veloping computer aided design (CAD) models, meshes, computational flow diagrams and online visualization [EDFCEA02].

### 3.1.2 Peculiarities of the platform for multi-physic developments

The goal of the NURESIM platform is to provide a more accurate representation of the physical phenomena by developing and incorporating codes which reflex the latest advances in core physics, two-phase TH and fuel modelling. SALOME is composed of several modules (e.g. GEOM, MESH, POST-PRO and YACS) which perform the pre- and post-processing of input data and simulations respectively, in addition to online visualization of simulations.

At present, merely the external coupling of codes were implemented in the NURESIM platform based on the exchange of information via meshes and fields (it is mandatory that the codes have to be integrated inside SALOME meeting standard rules following [Baudron01]). The different solvers can be integrated in the platform using an automatic tool to generate interfaces merging Python scripts, C/C++ and FORTRAN components inside SALOME. The MED binary format is the reference for meshes, supports and fields.

SALOME is divided in three different levels as seen in Fig. 7 (a); the first one is the “End User” at which the user interacts with the tools already implemented in the platform. The second one is the “Advanced User”, level for a more complex way of integrating codes using scripts and C++ interfaces. The integration of SCF however, has been done at this level, which is in charge of modularizing the code, coupling interfaces development (exchange of information between C/C++ and FORTRAN to allow communication between codes) and implementation of routines [Bestion01]. The last one is the “Developer User” level, which is needed for the integration of specific internal structures of SALOME. The work falls under the second functionality level. In Fig. 7 (b), the main elements of SALOME (NURESIM platform) are shown.

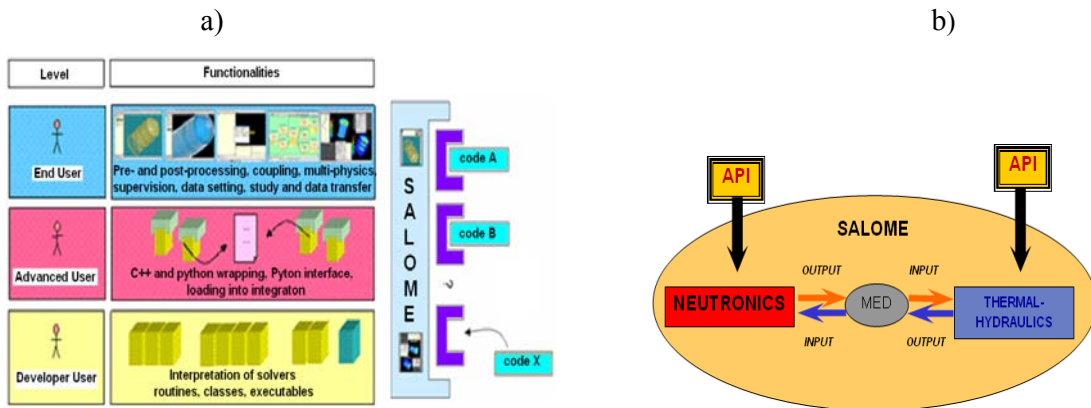


Fig. 7. SALOME peculiarities: functionality levels (a) and coupling philosophy (b).

The novel aspect of spatial coupling between the TH and the N computational domains compared to regular coupled codes is the automatic mapping of both domains using an in-built interpolation module of SALOME. For a proper integration inside the platform (Chapter 4), it is necessary to modify the code in a way that it behaves as a component (the SALOME software is based on the concept of independent components). These components can provide services, such as reading input data, perform calculations, extract parameters, create fields, construct meshes, etc. The components follow a hierarchical structure composed of a lower, middle and top level. At the lowest level the original source code that could be written in FORTRAN or C/C++ is found. However, it must be packaged in the form of static libraries or even external binary files, “black box”. The middle level is related to the C/C++ class, which defines the application programming interface (API) and is in charge of calling and manipulating functions, executables and libraries previously defined in the first level. The final level is the “Top Level”, which refers to the integration of the class as a SALOME component, ready to be use inside the platform. This is done automatically by using the tool “hxx2salome”, which performs the wrapping to SALOME, making an automatic code generation, compilation and update of the environmental variables.

The exchange of information is done in a 3D way, where elements of two meshes interact (one element of a first mesh corresponds to one element of a second mesh on a perfect mapping). The spatial mapping between N and TH (valid for steady state and transient solutions) was performed using an individual interpolation component (INTERP\_2\_5D) already integrated in SALOME [Jimenez02]. The objective of this component is to derive the data transferred weighting factors from the N mesh to the TH mesh and vice-versa. The principle lies on the exchange of data fields associated with two different 3D meshes (where one mesh is called the source and the other one the target). In order to perform the interpolation of the fields, the intersection volumes for all meshing elements of two coupled domains should be determined.

The procedure follows the following steps [Royer01]: triangulation (reduce the complexity of the problem), localization (superimpose the two triangulated meshing schemes and calculate the intersection area for all pairs intersecting the source and target triangles), propagation (account for all source triangles intersecting the target in question) and reconstruction (of the total area intersection between one target radial mesh and one source radial mesh). Employing this tool to the coupled solution allow to have different radial and axial discretizations (provided that the 3D meshing schemes are composed of 2D radial non-regular meshes extruded in the third 1D axial direction) for the N and TH and providing accurate feedback management from one domain to the other.

The “mesh” however, is a class containing 2D or 3D meshing objects based on a specific geometry (usually generated from the information read in the input deck of each integrated code). The “support”

is a class containing a list of the different meshing elements and finally, the “field” is the class template containing mainly a list of values lying on a particular support, which is filled with the user’s desired data. These fields can be later on used for post-processing purposes. The way of accessing these fields is done by pointers, where a specific value (data) is assigned to a volume element found in the “mesh”. This field could have any value e.g. power density, fuel and moderator temperature, moderator density, void fraction or boron concentration ( $B_{ppm}$ ). The characteristics of these fields in terms of data management, storage and exchange, make the coupling of codes inside SALOME possible. As previously mentioned this exchange of information is done in a 3D space where one volume element of one field corresponds to another volume element of a second field. In this way, the solver is able to use the information stored in each of these elements and use it to calculate its solution. The required approach for a full implementation of a code in the NURESIM platform is discussed in Chapter 4, “Integration and testing of SUBCHANFLOW in the NURESIM platform”.

## **3.2 The sub-channel code SUBCHANFLOW 2.1**

### **3.2.1 General description**

SUBCHANFLOW (SCF), developed at the Institute for Neutron Physics and Reactor Technology (INR) of KIT, is programmed in FORTRAN 95 with global variables and dynamic allocation. It solves the coolant mixture balance equations coupled with the fuel rod heat transfer at sub-channel level. The solution of the heat conduction equation is realized by a fully implicit method. SCF (based on the COBRA family of TH codes) can be used to solve channel and sub-channel based problems (where it shows great variability for solving square and hexagonal bundle geometries for stationary and transient solutions). Additional model extensions for the analysis of innovative reactors include the state properties for different coolants such as liquid metals (lead, sodium, Pb-Bi), gas (air, Helium) and water (properties obtained from IAPWS97) but also models to simulate the thermo-physical properties of UO<sub>2</sub> and MOX fuel rods in dependence of the temperature and burn-up and of various cladding materials like Zircalloy, Inconel-600 and Stainless Steel-SS316.

SCF describes the TH phenomena in FAs or cores of LWR and innovative reactors allowing the prediction of important parameters such as core pressure drop, static losses and frictional losses. The solution method involves a weakly compressible approach (no pressure wave propagation). Moreover, the solution of the TH equations is done layer by layer in the axial direction. SCF calculates a stationary converged solution to start the transient analysis (suitable for code coupling with N). Like every sub-channel TH code in the nuclear field, SCF make use of several empirical TH correlations to close the system of equations. SCF requires a set of constitutive equations which are divided in three groups, pressure drop, void fraction and heat transfer correlations. The following table mentions only some of

the most familiar TH correlations used by SCF and some of their general characteristics, [Armand01], [Dittus01], [Blasius01], [Vojtek01] and [Ferrouk01]. The heat transfer from the rod to the bulk fluid ( $q_r'' = h_r(T_{wall} - T_{mod})$ ) is dependent on the heat transfer coefficient ( $h_r$ ) prevailing in each transfer model. This coefficient can be determined by using correlations which are function of several parameters according to the boiling curve covering different flow regimes.

Table 3. Heat transfer correlations commonly used by SCF.

Correlation name	Characteristic flow regime
<i>Levy</i>	Sub-cooled boiling
<i>Armand</i>	Two phase flow friction model
<i>Dittus-Boelter</i>	Single phase heat transfer correlation
<i>Blasius</i>	Single phase friction model
<i>Churchill</i>	Single phase friction model

### 3.2.2 Solution approach

For steady state and transient solutions SCF solves the heat transport in three steps:

- 1) Radially within the fuel rods.
- 2) Radially between fuel rods and coolant.
- 3) Axially (from bottom to top) following a first order upwind-method to solve the three mixture balance equations.

The general solution approach is shown in Fig. 8. Generally speaking, SCF performs steady state and implicit transient solutions for a given set of inlet boundary and initial conditions. The model implies a fully implicit method (Chapter 2.4.2) for the solution approach. The system of equations related to the mass and momentum conservation are condensed in a linear system of axial pressure gradient equations solved according to the Successive-Over-Relaxation (SOR) method. The energy equation is solved by the same method. The transient solution also follows an implicit scheme. Convergence of the solution is derived through the change of the axial mass flow rate, leading to a flow error criterion between consecutive iterations.

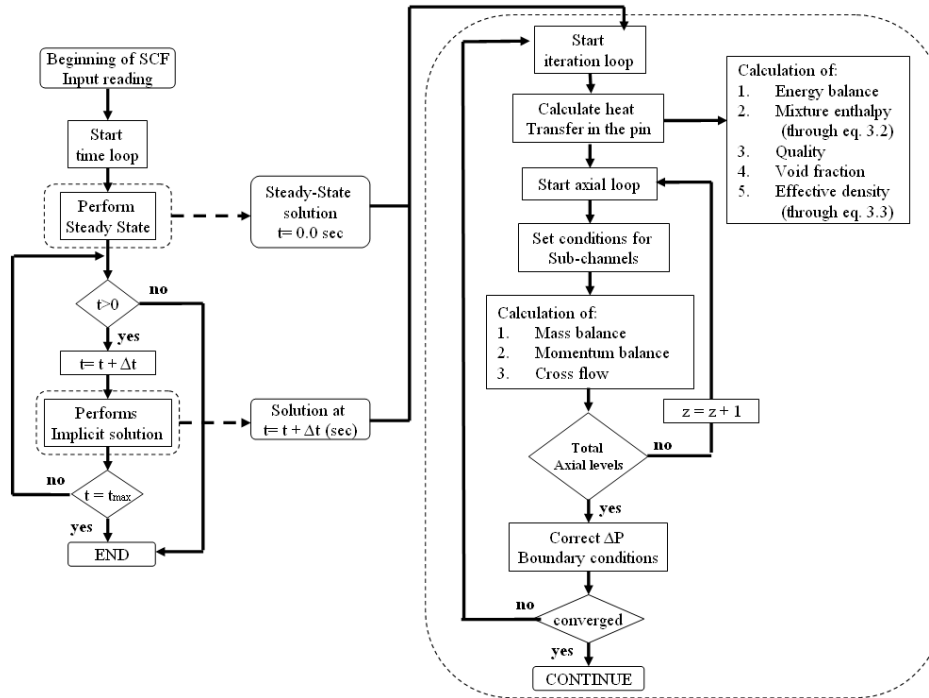


Fig. 8. SUBCHANFLOW solution algorithm for transient and steady state analysis.

The TH equations that the code solves are discretized by applying a finite difference method (heat conduction in the radial and axial direction), leading to a system of four mixture equations (conservation of mass, energy and momentum [axial and radial]) with their corresponding closure relations (constitutive models: pressure drop for single and two phase flow, void fraction and heat convection). The balance equations are based on the diagram shown in Fig. 9 [Kazimi01].

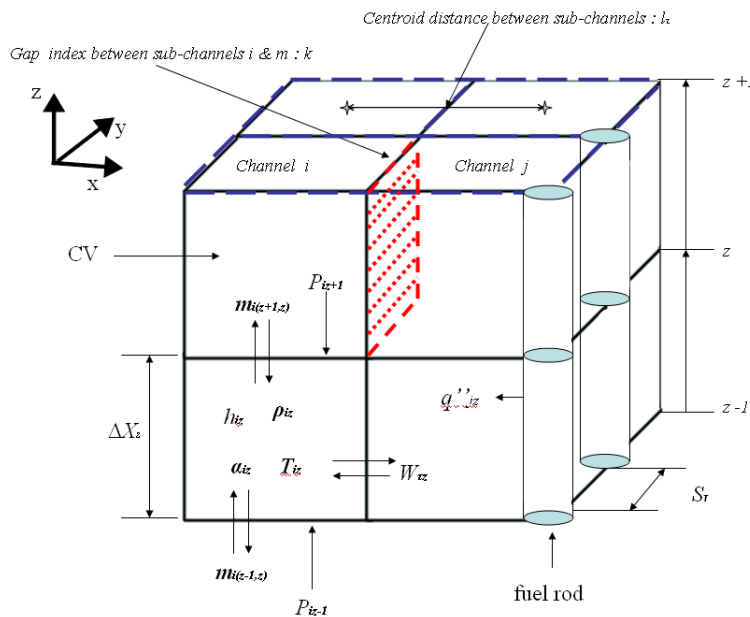


Fig. 9. Lateral and axial discretization of the thermal-hydraulic control volume.

Hereafter, the equations solved by SCF for the fluid dynamic model.

### 1. Mass balance equation for two phases.

The mass balance equation for two phases is described by eq. (3.1) as follows:

$$A_{i\zeta} \frac{\Delta X_\zeta}{\Delta t} (\rho_{i\zeta} - \rho_{i\zeta}^n) + (\dot{m}_{i\zeta} - \dot{m}_{i\zeta-1}) + \Delta X_\zeta \sum_{\tau \in i} \bar{e}_{i\tau} w_{\tau\zeta} = 0, \quad (3.1)$$

where;

- $i$  : Index of individual sub-channel.
- $\zeta$  : Index of axial level.
- $A_{i\zeta}$  : Flow cross section (axial direction).
- $\Delta X_\zeta$  : Differential length between axial nodes.
- $\rho_{i\zeta}$  : Density of the mixture ( $\rho_{i\zeta} = \alpha \rho_{i\zeta v} + (1 - \alpha) \rho_{i\zeta l}$ ).
- $\rho_{i\zeta}^n$  : Density of the mixture at previous time step.
- $\dot{m}_{i\zeta}$  : Axial mass flow rate  $\rightarrow \dot{m}_{i\zeta}^n$  (axial mass flow rate at previous step).
- $\bar{e}_{i\tau}$  : Transverse flow direction.
- $\tau$  : Index of gaps between sub-channels.
- $w_{\tau\zeta}$  : Transverse mass flow due to pressure gradients.
- $\Delta t$  : Differential time.

### 2. Energy balance equation.

The energy balance equation is described by eq. (3.2) as follows:

$$\begin{aligned} \frac{A_{i\zeta}}{\Delta t} [\rho_{i\zeta}^n (h_{i\zeta} - h_{i\zeta}^n) + h_{i\zeta} (\rho_{i\zeta}^n - \rho_{i\zeta}^n)] + \frac{1}{\Delta X_\zeta} (\dot{m}_{i\zeta} h_{i\zeta} - \dot{m}_{i\zeta-1} h_{i\zeta-1}) + \sum_{\tau \in i} \bar{e}_{i\tau} w_{\tau\zeta} h_{\tau\zeta} = \\ \sum_{r \in i} P_r \phi_{ir} q'_{r\zeta} - \left[ \sum_{\tau \in i} w'_{\tau\zeta} (h_{i\zeta} - h_{i\zeta}^n) + \sum_{\tau \in i} C_\tau S_\tau (T_{i\zeta} - T_{i\zeta}^n) \right] + \sum_{r \in i} r_Q \phi_{ir} q''_{r\zeta}, \end{aligned} \quad (3.2)$$

where;

- $h_{i\zeta}$  : Enthalpy of the mixture in axial direction ( $h_{i\zeta} = x h_v + (1 - x) h_l$ ).

- $v$  : Vapor phase.  
 $l$  : Liquid phase.  
 $h_{i\zeta}^n$  : Enthalpy of the mixture at previous time step.  
 $q_{r\zeta}''$  : Surface heat flux from pin to coolant.  
 $q_{r\zeta}'$  : Linear heat rate.  
 $w'_{\tau\zeta}$  : Cross flow due to mixing ( $w'_{\tau\zeta} = \beta_{i\zeta} S_\tau (G_i + G_\zeta)$ ).  
 $\beta_{i\zeta}$  : Mixing coefficient.  
 $G$  : Mass flux.  
 $T_{i\zeta}$  : Coolant temperature.  
 $P_r$  : Heated perimeter.  
 $\phi_{ir}$  : Fraction of the heated perimeter for a specific sub-channel.  
 $C_\tau$  : Thermal conductivity.  
 $S_\tau$  : Gap width.  
 $r_Q$  : Total power directly released in the coolant.  
 $r$  : Index of pin rod.  
 $\alpha$  : Void fraction.

With effective density (mixture) given in eq. (3.3);

$$\rho_{i\zeta}'' = \left( \rho_{i\zeta}^n - h_{mix} \frac{\partial \psi}{\partial h} \right) \rightarrow \psi = \rho_l x (1 - \alpha) - \rho_v \alpha (1 - x), \quad (3.3)$$

where  $x$  is the flow quality.

### 3. Momentum balance equations.

The axial momentum balance equation is described by eq. (3.4) as follows:

$$\frac{\Delta X_\zeta}{\Delta t} (\dot{m}_{i\zeta} - \dot{m}_{i\zeta}^n) + \dot{m}_{i\zeta} U_{i\zeta}' + \Delta X_\zeta \sum_{\tau \in i} \bar{e}_{i\tau} w_{\tau\zeta}' U_{\tau\zeta}^* = \quad (3.4)$$

$$A_{i\zeta} (P_{i\zeta} - P_{i\zeta-1}) - \bar{g} A_{i\zeta} \Delta X_\zeta \rho_{i\zeta} \text{COS}\Theta - \frac{1}{2} \left( \frac{\Delta X_\zeta f \Phi^2}{D_h \rho_l} + K v^* \right) \Big|_{i\zeta} \dot{m}_{i\zeta} \frac{\dot{m}_{i\zeta}}{A_{i\zeta}} - f_T \Delta X_\zeta \sum_{\tau \in i} w_{\tau\zeta}' (U_{i\zeta}' - U_{i\zeta}^n),$$

where;

- $\bar{g}$  : Gravitational constant.  
 $P_{i\zeta}$  : Pressure.  
 $\Theta$  : Channel inclination relevant to the vertical.  
 $f$  : Single phase friction coefficient.  
 $\Phi$  : Two phase flow friction multiplier.  
 $K$  : Pressure drop coefficient for spacer grids.  
 $f_T$  : Lateral turbulent momentum balance factor.  
 $v^*$  : Specific volume  $\left( \frac{x^2}{\alpha\rho_v} + \frac{(1-x)^2}{(1-\alpha)\rho_l} \right)$ .  
 $D_h$  : Hydraulic diameter.  
 $U'_{i\zeta}$  : Effective velocity  $\left( \frac{\dot{m}_{i\zeta}}{A_{i\zeta}} v^* \right)$ .  
 $U'^n_{i\zeta}$  : Effective velocity at previous time step.  
 $U^*_{i\zeta}$  : Effective velocity related to the cross flow.

The lateral momentum balance equation is described by eq. (3.5) as follows:

$$\frac{\Delta X_\zeta}{\Delta t} (w_{\tau\zeta} - w_{\tau\zeta}^n) + w_{\tau\zeta} U'_{\tau\zeta} + w_{\tau\zeta-1} U'_{\tau\zeta-1} = \frac{S_\tau}{l_\tau} \Delta X_\zeta P_{\tau\zeta-1} - \frac{1}{2} \left( K_G \frac{\Delta X_\zeta v^*}{S_\tau l_\tau} \right)_{\tau\zeta} |w_{\tau\zeta}| w_{\tau\zeta}, \quad (3.5)$$

where  $U'_{\tau\zeta}$  is the dynamic velocity,  $l_{\tau\zeta}$  is the distance between centroids of neighboring sub-channels and  $K_G$  the lateral gap pressure loss coefficient. For the fuel elements, SCF uses a 2D heat conduction model with mathematical discretization in finite difference form. After some simplifications of the heat transfer equation, SCF solves eq. (3.6);

$$\rho(\bar{r}, T) C_p(\bar{r}, T) \frac{\partial}{\partial t} T(\bar{r}, t) = \frac{1}{r} \frac{\partial}{\partial r} r k(\bar{r}, T) \frac{\partial}{\partial r} T(\bar{r}, t) + q''(\bar{r}, t), \quad (3.6)$$

where;

- $\bar{r}$  : Position vector.  
 $T$  : Temperature.  
 $\rho(\bar{r}, T)$  : Coolant density.

$C_p(\vec{r}, T)$  : Heat capacity.

$T(\vec{r}, t)$  : Coolant temperature.

$k(\vec{r}, T)$  : Thermal conductivity.

$q'''(\vec{r}, t)$  : Volumetric heat flux.

Finally, due to the requirements imposed by some simulations (see Chapter 7), new thermo-physical properties related to the fuel thermal conductivity ( $k$ ), specific heat ( $C_p$ ) and heat transfer coefficient for the gap between fuel and cladding ( $h_{\text{gap}}$ ) were implemented inside SCF, which tend to extend also the capabilities of SCF to model the most important benchmarks nowadays.

### 3.2.3 Boron dilution model

In PWRs boric acid ( $\text{H}_3\text{BO}_3$ ) is used as a soluble neutron absorber in the primary coolant to compensate for fuel burn-up, Xenon poisoning and to provide the necessary sub-criticality of the core during refueling and maintenance. In the sixties, studies on boron dilution transients were based on slow boron dilution events due to a malfunction of the chemical and volume control system (CVCS). During the last decade, safety studies for low power and shut-down conditions of NPP have been performed in several countries, for which a local boron dilution in the reactor core by a slug of pure water or water of reduced boron concentration occurs. This slug of deborated water mixes with borated water in the primary system and due to 3D mixing effects variations of the boron concentration occur in time and space at the core entrance [Teschendorff01] in either an homogeneous (ideal) or heterogeneous (real) way. Causes for boron dilution transients could be of two kinds: unintentional injection of deborated water from outside the primary cooling system (slow progression) and separation of primary coolant into highly borated water and almost boron free water by evaporation and condensation (relatively fast and difficult to analyze). The description of boron transport within the primary circuit and core of PWRs is challenging for TH codes. The solution of the boron transport equations is needed for the modelling of the so-called boron dilution transients following a SBLOCA (after loop-seal clearing). In this case, the mixing is a key mechanism determining the positive reactivity insertion in the core. From this, the implementation of boron transport models in TH codes is a requirement in order to predict these kinds of boron dilution scenarios with coupled codes.

In the last year, a boron transport model was implemented in SCF. For this purpose, assumptions must be made, e.g. boron is present only in the liquid phase (the vapor pressure of the boron compounds is too low to expect any boron to be present in the vapor), there is no precipitation of boron from the solution and no thermal stratification of boron will be considered in the model [Garber01]. Since mixing in the downcomer and in the core region is surely a 3D phenomenon that cannot be handled with

1D codes, SCF provides a suitable tool to perform this type of transients. There are several parameters that should be addressed while implementing a boron transport model to describe the behavior of boron during, e.g. boron dilution transients in PWRs:

1. An accurate cell mesh and time step should be envisaged in order to observe the deborated slug formation and minimize numerical diffusion (Courant condition).
2. Include flux limiters which introduce a larger reduction of the numerical diffusion so as to obtain a precise convective boron transport.
3. Include turbulence models for a physical prediction of boron mixing.

SCF solves first the boron mass balance in the axial direction through a successive gradient method, where a Superbee flux limiter, equation (3.7), is used (Superbee and in particular, Super-C shows much less sensitivity to Courant numbers than other schemes [Leonard01]). The effect of this flux limiter is to do a second order accurate flux conservation for smooth parts of the solution and for regions near sharp gradients it will switch to the first order upwind flux conservation. Therefore, flux limiters ensure that the solution gets the best of both second order and first order methods.

$$\phi(r) = \max[0, \min(2r, 1), \min(r, 2)] , \lim_{r \rightarrow \infty} \phi(r) = 2 . \quad (3.7)$$

In addition, an upwind resolution is applied at the boundaries (first and last nodes along the axial length). Second, the lateral mixing is solved using a donor-cell method where the cross flow is taken into account for each gap between sub-channels. The donor-cell scheme is one of the simplest flux conserving schemes; it has strong similarities to the upstream differencing scheme where the difference comes mainly when either the velocity is space dependent or the grid is non-equidistant. For the boron dilution model implemented in SCF (explicit scheme), the following steps exemplify the procedure.

1. Solution of the convection eq. (3.8),

$$\frac{d[\rho(i, z) \times (boron)]}{dt} = - \frac{d[\rho(i, z) \times (v_n) \times (boron)]}{dz} . \quad (3.8)$$

2. Discretization relative to the level of resolution (finite difference).
3. Calculation of the boron concentration at the cell boundaries, eq. (3.9): two possibilities in the axial direction.

- a) Upwind (diffusive) scheme, low resolution:  $boron_{i,z}^n = boron_{i,z}^n$  for positive flow direction ( $v_z > 0$ ) and  $boron_{i,z}^n = boron_{i,z+1}^n$  for negative flow direction ( $v_z < 0$ ).

$$\sum_{i=1}^{channels} boron\_boundary(i, [1, z]) = boron(i, [1, z]) \rho(i, [1, z]) \left( \frac{1 - x(i, [1, z])}{\rho(i, [1, z]) - \rho_{st}(i, [1, z]) \alpha(i, [1, z])} \right), \quad (3.9)$$

where;

- $v$  : Flow velocity.  
 $z$  : Maximum (top) axial level.

b) Central scheme, high resolution:  $boron_{i,z}^n = \left( \frac{boron_z + boron_{z+1}}{2} \right)$ .

4. Successive gradients scheme for the third step.
5. Boron concentration for the rest of the axial cells and application of the flux limiter as shown in eq. (3.10);

$$\sum_{i=1}^{channels} \left( \sum_{z=2}^{max-1} boron(i, z) = boron\_upwind - \phi(r) (boron\_upwind - boron\_central) \right). \quad (3.10)$$

6. Boron concentration of the flow through the gaps between enclosing channels for the cross flow diffusion and superposition with the axial boron diffusion.

### 3.3 The reactor dynamic code COBAYA3

#### 3.3.1 General description of the code

COBAYA3 (CBY) is a core simulator based on the NDE for LWRs with the possibility for coupling its calculations with TH codes (COBRA-III, COBRA-TF, FLICA-4, SIMULA-TH and SCF). It solves the diffusion equation in multi-group and three dimensions for rectangular and triangular grids, including kinetics formulation for transients and criticality search. Moreover, CBY can perform solutions for local base calculations and full core through domain decomposition in alternate dissections (making the programming suitable for parallelization) [Jimenez01]. The objective of this methodology is to distribute the memory in multiple pre-processors and simultaneously solve the different sub-domains. This code also includes subroutines of the mathematical libraries LAPACK, SPARSKIT and HIPS to solve the system of linear equations by direct or iterative methods. CBY is divided in two solvers which are described in the following subsections.

1. ANDES: Nodal (FA) level solver.
2. COBAYA3k: Cell (PBP) level solver.

The diffusion equation solved by CBY introduces interface discontinuity factors (*idf*) in order to achieve a solution similar to the one provided by the transport calculations. These discontinuity factors are discretized by first order differencing; giving rise to more accurate gradients and continuity in the values of the interface. Now then, the Fick's law implemented in CBY is as the following eq. (3.11);

$$J_g = -D_g \nabla \phi_g = -D_g \frac{\pm \phi_g \mp idf_g^{surface} \phi_g}{W_g / 2}, \quad (3.11)$$

where;

- $D_g$  : Diffusion coefficient.  
 $\phi_g$  : Neutron flux.  
 $idf_g^{surface}$  : Interface discontinuity factor.  
 $W_g$  : Size of the neutronic node.

The diffusion kinetics equation together with the precursors balance equation is solved for each time step, where the system can change due to the global feedbacks, internal inertia of the code, or external perturbations [Jimenez01]. CBY also applies a synthetic factorization of the flux to be able to use longer time steps during a time dependent solution. A first order implicit discretization is used for the time derivatives (precursor's evolution is also treated with this kind of discretization).

In order to obtain  $k_{eff}$  and fission source distributions (convergence of the scattering and fission source is required) CBY use the source iteration method or outer loop iterations. The drawback of this method is its low convergence ratio; therefore, two acceleration approaches are used in the code, namely the Wielandt shift (allow to reduce the error for the power iteration method) and one-group acceleration [Lozano02], [Lozano03]. After every iteration CBY recomputes the Eigenvalue as given in eq. (3.12);

$$k_{eff} = \frac{fission}{absorption + leakage}. \quad (3.12)$$

One of the peculiar characteristics of CBY is its capability for parallelization. This process is achieved through a domain decomposition method (where the diffusion calculation is solved at local level) in the radial direction, while the axial direction is kept in the same domain for better coupling with TH

(axial mapping of N nodes with TH elements). This methodology reduces significantly numerical errors since the BCs of each dissection are calculated in the central plane of each sub-domain of the assembly.

### 3.3.2 The nodal solver ANDES

For nodal based calculations, CBY uses the algorithm Analytic Nodal Diffusion Equation Solver (ANDES) which solves the multi-group 3D diffusion equation based on an Analytic-Coarse-Mesh-Finite Difference-Method (ACMFD) [Lozano02]. The COBAYA3 module Pre-ANDES however, is in charge of the XSs update considering the actual TH feedback parameters. This method includes an extra coupled equation (expression that relates interfacial currents and average fluxes between adjacent nodes) which considers coarse meshes and spectral phenomena. ANDES is able to perform calculations by using homogenized XSs and heterogeneity factors included in the libraries in addition to simulate steady state and transient problems by solving the time dependent multi-group diffusion equation and the delay neutrons balance equation. The working scheme of ANDES looks as in Fig. 10.

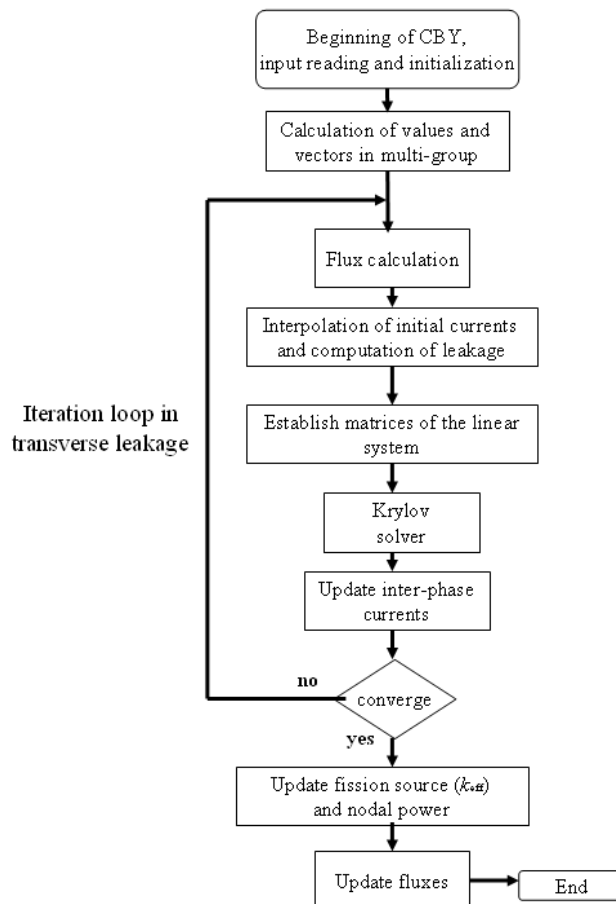


Fig. 10. Iterative steady state solution scheme of ANDES (nodal solver of COBAYA3).

As mentioned, the objective of the ACMFD method is to solve the diffusion equation for a coarse mesh spatial discretization. This method is based on an analytic expansion of the flux in the center of each N node. To do that ANDES uses three types of interpolations for calculating the transverse leakage: flat, square and cubic, where the greatest degree of polynomial interpolation leads to a higher precision in the solution. These transverse leakages are needed to decouple the equations (for obtaining the flux) used in 2D and 3D, leading to an analytic solution which assumes a specific profile in the center of the node for the leakage.

ACMFD is a procedure to define the coefficients required for the nodal coupling departing from an analytical solution of the multi-group diffusion equation. This method is a more rigorous formulation of the Coarse Mesh Finite Difference method (CMFD). In addition, it uses coupling coefficients between N nodes (nodal coupling) to establish simple balance nodal equations by introducing only the average nodal flux. ANDES is able to refine the axial and radial meshes (nodes) in sub-divisions, leading to an increasing number of nodes taking into consideration the ACMFD. After some simplifications and considering the advantages of the previous methodologies, the average current in a node and the average flux in the adjacent nodes is;

$$|J_g\rangle = D_g A^{j-1} \frac{A^f |\overline{\phi}_g\rangle - |\phi_g^s\rangle}{W_g/2}, \quad (3.13)$$

where  $|J_g\rangle$ ,  $|\overline{\phi}_g\rangle$  and  $|\phi_g^s\rangle$  are the vectors representing the average interface current, average interface flux and average nodal flux per energy group. The diagonal matrix  $D_g$  represents the diffusion coefficients, and  $A^{j-1}$  and  $A^f$  are the complete matrices obtained through analytic developments of size (energy\_groups x energy\_groups) and  $W_g$  is the width of the node in the desired direction [Jimenez01]. With this continuity relationship is possible to obtain the final equation for nodal coupling. For steady state calculations ANDES employs a power iteration method for calculating the Eigenvalue of the problem through a relatively simple formulation, as seen in eq. (3.14). This technique consists in generating a sequence of normalized vectors which converge iteratively to a dominant Eigenvalue which is associated with the greatest Eigen value.

$$FM^{-1} |S_{n,g}\rangle = k_{\text{eff}} |S_{n,g}\rangle. \quad (3.14)$$

In addition, the methods Bi-CGSTAB and GMRES with and without preconditioning have been implemented in ANDES to solve the linear systems. It was proven first, that the implemented methods had no coding errors and second, that the Bi-CGSTAB method with preconditioner ILU(0) is optimal to solve the system. It was the fastest method among the other iterative schemes tested [Jimenez01].

### 3.3.3 The cell solver COBAYA3k

COBAYA3k is a multi-group 3D diffusion solver that uses a finite difference method on fine meshes at pin level. This solver implements the technique of alternate dissections, which consists on dividing the geometry in sub-domains in the radial direction so that each of these sub-domains represents a closed problem, leading to individual solutions [Jimenez03]. This feature is supported with the fact that the currents at the interface, eq. (3.15), depend only on the ratio of the currents ( $J_g^{p,n}$ ) and the flux ( $\phi_g^p$ ) and the geometrical and material properties of each sub-domain.

$$J_g^{p,n} = \frac{\phi_g^p}{\frac{idf_g^{p \rightarrow n}}{J_g^{p,n}} \pm \frac{h_p}{2D_g^p}}. \quad (3.15)$$

The term  $idf_g^{p \rightarrow n}$  is the discontinuity factor that accounts for the transport correction to minimize the homogenization errors. The previous relation is the link to couple each of the neutron multi-group balance equations given in eq. (3.16).

$$\nabla(-D_g \nabla \Phi \phi_g) + \sum_{a,g} \phi_g + \sum_{\forall y \neq g} \sum_{s,g \rightarrow y} \phi_g = \frac{\chi_g}{k_{eff}} \sum_{\forall y} \nu \sum_{f,y} \phi_y + \sum_{\forall y \neq g} \sum_{s,y \rightarrow g} \phi_y, \quad (3.16)$$

where;

$\chi_g$  : Fission spectrum for group  $g$ .

$k_{eff}$  : Criticality Eigenvalue.

$\sum_{f,g}$  : Fission XS for group  $g$ .

$\sum_{a,g}$  : Absorption XS for group  $g$ .

Even though diffusion theory is considerably faster than other transport approximations, nowadays is still very demanding in terms of computational power to perform PBP solutions for big 3D geometries. Each of the sub-domains decomposed by COBAYA3k is formed of quarters of FA which use as BCs the currents at the corresponding interfaces (required to accelerate the convergence of the exact boundary conditions of the sub-domains while attenuating the high frequency noise). This fact will be fundamental to exploit hybrid solutions for CBY as described in Chapter 5.

The number of iterations to achieve convergence is reduced significantly when using the solver ANDES to obtain an initial guess for the solution (in this case ANDES is used only as an acceleration method to provide a precise solution of the fission source). In addition, COBAYA3k is able to solve steady state and transient solutions at scales of individual pins, mini-cores or full cores at pin levels. These characteristics place CBY as one of the few solvers in the world that could be coupled with TH codes to resolve 3D cores at pin level [Jimenez04]. The solver also calculates the diffusion equation through finite difference at pin level including a transport correction factor to account for homogenization errors (discontinuity factors). Similar to ANDES, COBAYA3k uses numerical methods such as GMRES, Bi-CGSTAB and PGMRES to solve the linear system of equations through iterative schemes.

---

## 4 Integration and testing of SUBCHANFLOW in the NURESIM platform

The integration process of a code inside SALOME is the first step for developing coupling schemes within the NURESIM platform. To do this, knowledge about the platform is compulsory in addition to the consideration of a strict order of steps to be followed for the proper integration. The following subsections illustrate this process which required significant knowledge of informatics and the development of subroutines and modules necessary for the integration and coupling.

### 4.1 Main steps for the integration of SUBCHANFLOW

In order to implement SCF inside SALOME several requirements have to be satisfied in terms of structure, development of subroutines and modularization of the code [Bestion01]. The experience obtained from the integration of other codes inside the platform such as CBY, DYN3D and FLICA4 [Royer01] is a fundamental step towards the understanding of the integration of SCF within SALOME as a new component. Next, the global steps followed for the implementation of the code are presented.

1. Modularization of SCF respecting its functionality and general structure. Reorganization is required to provide services such as independent initializations and calculations, mesh creation and post-processing. Each module should be independent in terms of functionality, but clearly linked with the other modules for initialization and flow of information. Each module should be able to perform its solution and to transfer its information to other modules.
2. Development of FORTRAN subroutines in charge of reading and writing files in MED format. The MED model has been chosen as a reference format for meshes, supports and fields manipulation.
3. Creation of the appropriate C++ interface necessary for calling the different FORTRAN subroutines that constitute the already modularized source code of SCF.
4. Use of the tool “hxx2salome” which generates automatically the API, necessary for applying the code inside SALOME [EDFCEA01].

The structure of the code required by the tool “hxx2salome” to perform the wrapping (integration) is illustrated in Fig. 11, where the “src” and “modules” contain the main source code and its modules respectively. The description of this figure is presented in the next page.

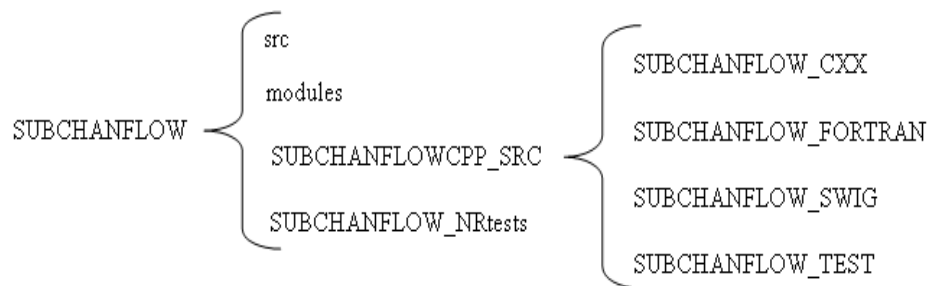


Fig. 11. Directory tree of SUBCHANFLOW which allows its integration inside SALOME.

*SUBCHANFLOW\_CXX*: The file `subchanflow.cxx` performs the link between the FORTRAN subroutines and the required C++ interface for the wrapping inside SALOME. This `subchanflow.cxx` file could be used only after the correct variables and functions of C++ and FORTRAN have been declared in a second file, `subchanflow.hxx`, as external variables.

*SUBCHANFLOW\_FORTRAN*: Contains the file `subchanflow.f`. Here, the main FORTRAN source of SCF is divided in subroutines (modularized) so that these modules can be later called from the C++ interface (C++ class functions and headers) in *SUBCHANFLOW\_CXX*.

*SUBCHANFLOW\_SWIG*: This folder is devoted to take the C++ declarations (recall `subchanflow.hxx`) and create wrappers needed to access the C++ class functions from Python. It uses the software SWIG, which receives as input an interface file (`subchanflow.i`) and then produces the file `subchanflow_wrap.cxx` that must be compiled and linked to the rest of the program.

*SUBCHANFLOW\_TEST*: This subdirectory includes python scripts as an additional method for testing the correct compilation of the C++ class. These Python scripts use the *SUBCHANFLOW\_SWIG* modules obtained through the SWIG in the compilation of the *SUBCHANFLOW\_SWIG* subdirectory.

*SUBCHANFLOW\_NRtests*: The folder contains special YACS diagrams that are ready to be used independently following a specific order. This is useful when several coupled models need to be run consecutively without the intervention of a user.

Once the code is prepared for the integration (modularization scheme), the structure followed in Fig. 11 must be created. At the level of *SUBCHANLOWCPP\_SRC* a predefined installation script must be modified to install correctly the component. These modifications involve changing the paths so that the code can find the corresponding pre-compiled libraries. Due to the philosophy of SALOME while dealing with coupled schemes (mesh superposition for information exchange) the creation of a well defined mesh (avoid overlapping points or volumes) is necessary for a proper information exchange making use of MED files (refer to Chapter 3.1). For the generation of PBP meshes the steps to follow

are the same as the steps for creating nodal based meshes for square geometries; the only difference is the scale of the problem.

Once the code has been properly integrated in the platform as a new component, the interaction with other codes is done through the YACS module of SALOME or via Python scripts. This could include coupled calculations (feedbacks, mesh superposition and computational roots) or stand alone solutions. In Appendix D additional information is given in this matter, where Fig. 81 shows a steady state computational route for a stand alone SCF simulation. Moreover, coupled solutions using YACS, computational flows, online visualizations and post-processing capabilities are shown there.

#### 4.2 Testing of the SUBCHANFLOW integration in the NURESIM platform

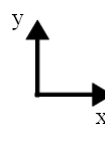
To demonstrate the functionality of SCF inside the NURESIM platform, different problems related to mini-cores consisting of PWR fuel assemblies were selected to be simulated with SCF using both the fluid centered and rod centered sub-channel approach since the neutronic nodalization at pin level (rod centered) differs from the traditional sub-channel nodalization. The need for having two types of meshes derive from the spatial discretization implemented in the N and TH and the treatment of feedbacks inside the platform. The first step was to verify the need to have two meshes instead of one (rod and coolant centered). If SCF is able to obtain accurate results while implementing rod centered sub-channels in a reasonable amount of time, then there is no need to have two different meshes. Although some studies were performed in the past [Espiel01], it was still uncertain the advantages or disadvantages of this type of modeling. For this purely TH study four different pin clusters were modeled (3x3 rods and eleven axial levels). All of them contained the same number of fuel rods (eight heated rods and one instrumentation rod), same operating conditions, thermo-physical properties and power distribution (as seen in Table 4 and Fig 12).

Table 4. Normalized axial power distribution for the (3x3) pin cluster model.

Axial level	0	1	2	3	4	5	6	7	8	9	10
power	0.5	0.6	0.7	0.8	0.9	1.0	0.9	0.8	0.7	0.6	0.5

Fig 12. Normalized radial power distribution for the (3x3) pin cluster model (top view).

0.95	0.95	0.95
0.95	0.00	0.95
0.95	0.95	0.95



The only difference between the models is the number of sub-channels in the pin cluster and their spatial arrangement, as seen in Fig. 13.

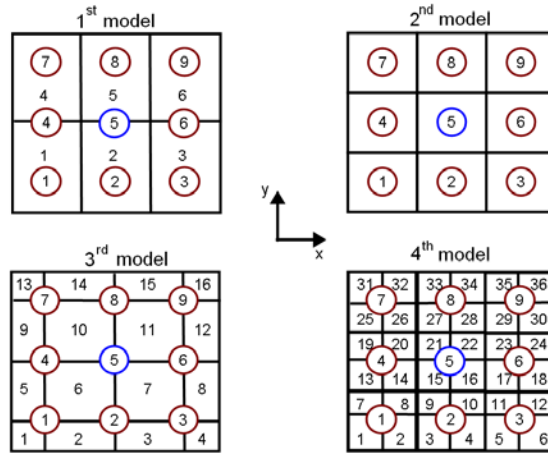


Fig. 13. Study of different sub-channel discretizations implemented in four models.

After running the stand alone steady state SCF simulation with a cross flow friction factor of 0.7 it was noted that rod and coolant temperatures did not suffered drastic deviations on the temperature profile between each other, leading to a maximum fuel rod centre line temperature ( $T_{CL}$ ) difference of  $T = 0.99$  K (between 1<sup>st</sup> model and 4<sup>th</sup> model). Selected parameters which support the predictions with these models are shown in Appendix C, Fig. 73 and Fig. 74. The biggest difference however appears when revising the convergence of each solution. It can be noted that the coolant centered sub-channel model (3<sup>rd</sup>) converges faster than the other models; after nineteen iterations compared to twenty-four for the 1<sup>st</sup> model, thirty-two for the 2<sup>nd</sup> model (rod centered discretization) and thirty-nine for the 4<sup>th</sup> model. The flow error (defined in Chapter 3.2.1) predicted by SCF vs. iteration number for these four models is shown in Fig. 14.

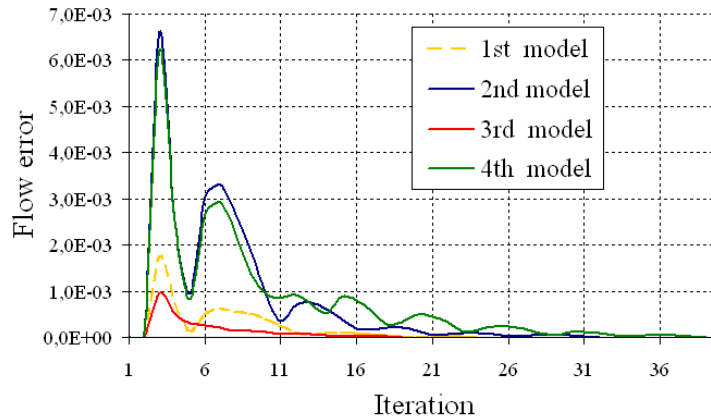


Fig. 14. Convergence evolution for the 1<sup>st</sup>, 2<sup>nd</sup>, 3<sup>rd</sup> and 4<sup>th</sup> models (Fig. 13).

In addition, a mini-core consisting of a 3x3 FAs is simulated with SCF using two different sub-channel radial discretizations for the TH domain: one is rod centered and the other is coolant centered. Recall that feedbacks inside SALOME are exchanged between the N field and the TH field by mesh superposition. In this approach, the values of each field are stored in a one dimensional array of size 6480 for a coolant centered discretization (this value is obtained by multiplying the number of sub-channels in one plane with the number of axial levels, e.g.  $(18 \times 18) \times 20 = 6480$ ). In this array, the 6480 values of the power distributions, moderator temperature/density, or fuel temperature are stored. But the neutronic mesh will have 17x17 cells in one radial plane, which differs from the 18x18 sub-channels in one radial plane of the TH domain. Hence any mesh superposition of the N and TH meshes will fail since there are more TH meshing elements than N ones.

Difficulties are found when filling out the Doppler temperature field in SALOME since now the TH mesh ( $18 \times 18 = 324$  values in one plane) is filled out with the number of rods ( $17 \times 17 = 289$  values in one plane) corresponding to the Doppler temperature. The fields are initialized to zero, which means that the field corresponding to the Doppler will have the “real” temperature for the first 289 values of the array, but the remaining thirty five values will have a temperature equal to zero Kelvin. These differences are reflected while exchanging the parameters, when the N code encounters very strong temperature discontinuities in radial and axial directions, leading to more iterations for convergence and non physical results (e.g. neighboring nodes with temperature differences of hundreds of degrees).

To avoid this, two types of meshes for the TH were developed for pin base simulations: one mesh used for the exchange of the moderator density or temperature (fluid mesh), and the other one for the exchange of the Doppler temperature (structural mesh). To study in detail the differences that provide both meshes, a square mini-core composed of nine FAs with a 17x17 rods configuration was investigated with SCF. Geometrical specifications were taken from the OECD/NEA and US NRC PWR MOX/UO<sub>2</sub> (simplify the terminology as PWR MOX/UO<sub>2</sub>) core transient benchmark [Downar06]. For this specific case a MOX type of FA and eight UO<sub>2</sub> type FAs were implemented with a power distribution related to the enrichment and position of the fuel pins (no CRs were modeled and the MOX FA is surrounded by the UO<sub>2</sub> FAs). Fig. 15 shows the normalized radial power distribution used in one quarter of the two FAs modelled (lower right corner of the assembly). The normalized axial power distribution for both types of assemblies followed a cosine shape with a maximum (unity) at half core.

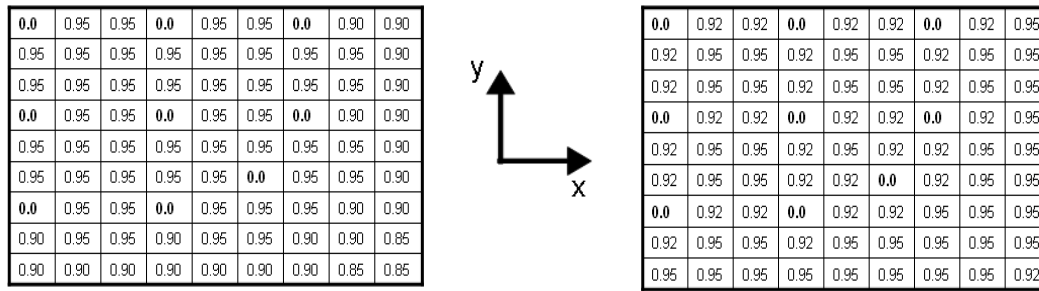


Fig. 15. Normalized radial power map for 1/4 of a PBP FA: MOX FA (left), UO2 FA (right).

The only difference between the two mentioned models was the number of sub-channels, the neighboring sub-channels, distance between edge sub-channels and gap widths. All other parameters were kept constant and equal for both types of meshes, e.g. thermo physical properties, power distribution, operating conditions, geometry, convergence criteria and TH correlations. The meshes generated by SCF inside SALOME are shown in Fig. 16. Specifically, Fig. 16 ((a) and (b), coolant centered) and ((c) and (d), rod centered) illustrate clearly the difference between the two types of radial discretizations.

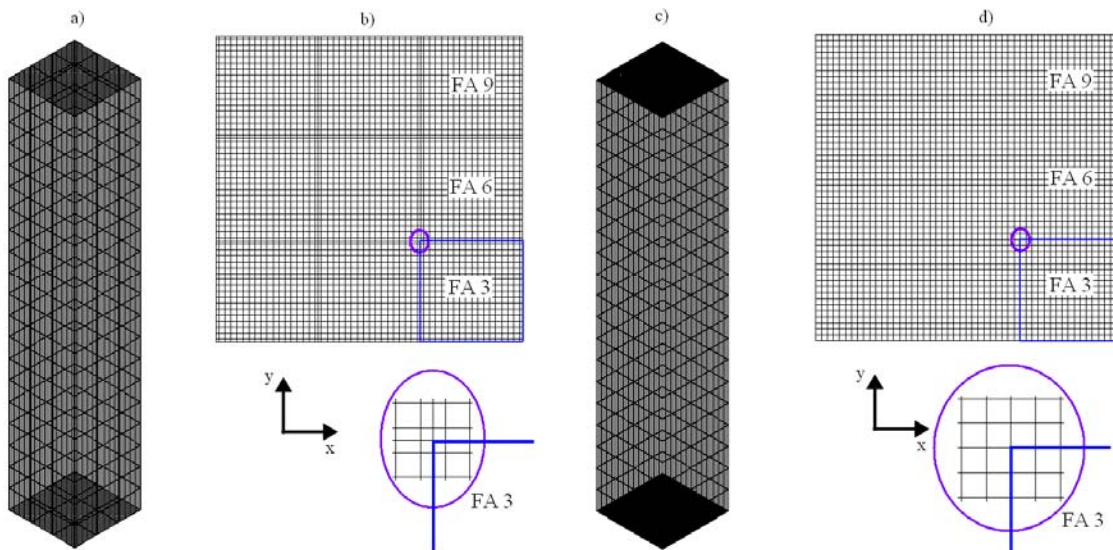


Fig. 16. Coolant centered mesh isometric view (a) and top view (b), and rod centered mesh isometric view (c) and top view (d).

Bundle or averaged parameters predicted by SCF for the two types of meshes were the same. Differences were encountered comparing the channel and fuel rod parameters predicted by SCF using the coolant and rod centered approach. For example, with the coolant centered approach SCF underestimated the  $T_{CL}$  by a maximum of  $\sim 7.0$  K. On the other hand, SCF needed a simulation time ( $t_{total}$ ) of  $t_{total} = 29.0$  min 19.0 s using the coolant centered discretization and  $t_{total} = 42.0$  min 29.3 s using the rod centered discretization. Outputs related to these models are shown in Appendix C, Fig. 75 and Fig. 76.

Several mechanisms influence the differences encountered between both solutions, the ones discussed hereafter. Even though the gap width ( $S_r$  in the right hand side of eq. (3.2)) influences the heat generation for each sub-channel the temperature difference between consecutive iterations during a convergence loop might be assumed to be small enough to significantly increase the energy for coolant centered sub-channels, especially at the end of the calculation, when the flow error is reduced as seen in Fig. 14. In rod centered sub-channels this difference is bigger due to the radial discretization, where strong temperature gradients are encountered leading to more iterations for convergence. Only the direct energy release to the coolant and the energy calculated through the linear heat rate are affected through the heated perimeter, which differs between coolant centered and rod centered individual sub-channels, especially when dealing with highly heterogeneous media (presence of CR, instrumentation tubes, etc.). A similar analysis is applied to the momentum balance in the axial direction, where mixing is influenced partly by the axial effective velocity between consecutive iterations, as in eq. (3.4). Finally, the momentum balance in the lateral direction is sensitive not only to the gap width, but also to the distance between neighboring sub-channels as shown in the first term on the right hand side of eq. (3.5), where the effect is enlarged especially in sub-channels located at the edges.

Based on these investigations it can be stated that the coolant centered sub-channel model converges faster than the rod centered sub-channels model. In addition, the coolant centered mesh underestimates the local Doppler temperatures. In conclusion, the analysis of mini-cores based on rod centered discretizations does not exhibit strong influence on the final result, especially when modeling relatively homogeneous cores. Consequently the rod centre sub-channels discretizations will be used in the frame of this dissertation.

---

## 5 Extensions of SUBCHANFLOW and COBAYA3 for hybrid solutions

The impossibility nowadays to perform PBP whole core simulations based on transport solutions ( $S_n$ ,  $P_n$  and MOC) and the knowledge that extreme TH conditions challenge the integrity of the safety barriers during transients (mainly localized in certain core regions) drive the development of hybrid solutions. This hybrid coupling between N and TH allow the prediction of local safety parameters in a direct way. As mentioned in Chapter 2.6, the development of hybrid solutions for N and TH aims to reduce the computational time of core simulations preserving sufficient accuracy compared to PBP solutions. Due to the N limitations, very little research has been done in this area in the past years. Since CBY includes a nodal and cell solver based on the improved diffusion approximation, the implementation of hybrid solutions is very attractive. In addition, CBY is based on a “domain decomposition in alternate dissection methodology” (discussed in Chapter 3.3), making it suitable for a hybrid “embedded” multi-scale method approach. On the other hand, SCF is usually applied using either a sub-channel discretization or a fuel assembly discretization consisting on both nodal and cell based meshes. In this connection it is important to modify the SCF source code so that the exchange of mass, momentum and energy between the cells of different size in the radial direction are described in an appropriate way.

### 5.1 SUBCHANFLOW: Extensions for hybrid analysis

#### 5.1.1 Description of the methodology

The main idea of hybrid solutions for the TH domain is the mixing of coarse meshes with refined meshes. In terms of sub-channel analysis, this philosophy is extended to multiple neighboring sub-channels for one equivalent channel. SCF was adapted to perform this type of solutions with a maximum number of forty neighboring sub-channels. In fact, this number was derived through empirical observations since typical PWRs have a 17x17 rod configuration, leading to  $17 + 17 = 34$  neighbors for one nodal based parallel channel (following a rod centered discretization). Fig. 17 illustrates this approach. The numbers one, two and three are TH channels representing one FA each. Numbers four and onwards represent the sub-channels (“hybrid FA”).

For BWRs the analysis is simplified since each fuel assembly is housed in a canister and hence flows between adjacent assemblies are not possible. Due to the monotonic increase of the neighboring sub-channel indices in SCF while creating its input deck, the maximum numbers of sub-channels encoun-

tered by a nodal based fuel assembly are the ones provided by two PBP assemblies. This means that the cross flow between adjacent sub-channels and channels should be properly handled in the momentum, mass and energy equations, as depicted in Fig. 17, where the arrows indicate the cross flow exchange. For modeling purposes the gap width between nodal base FA (channels) and pin base sub-channels should be equivalent to the gap width of successive sub-channels since the lateral pressure loss coefficient is adapted to this type of geometries in SCF.

The influence of this substantial increase of neighboring sub-channels for one parallel channel is reflected directly while calculating of, e.g. the turbulent mixing. The mixing coefficient is a function of the gap width and the mass flux, where the sum of the areas of two sub-channels separated by a gap “ $\tau$ ” is critical for calculating the average mass flux used. This mixing coefficient is separated between boiling and non boiling states, which is later on used to obtain the total mass flow, enthalpy, boron concentration and momentum into an axial cell due to mixing. For solving the energy equation, the thermal conductivity between consecutive sub-channels is averaged by using the distance between sub-channels and gap width between them (applied to PWRs). This distance and gap width are visualized in Fig. 17.

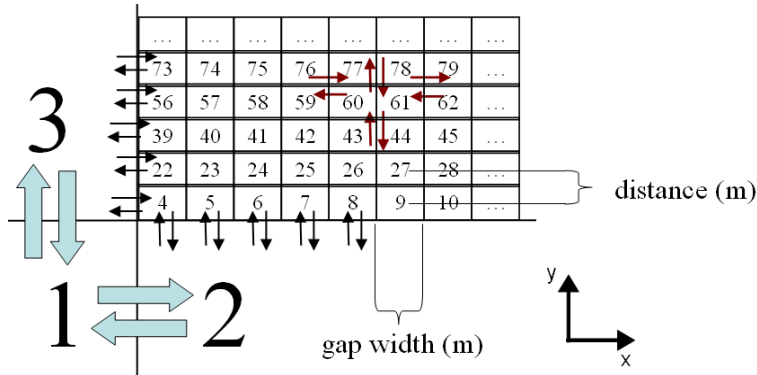


Fig. 17. Neighboring sub-channels related to hybrid TH solutions.

For the calculation of the pressure loss coefficient the total linear momentum rate due to mixing for each axial node should be considered, implying a strong link between the geometrical parameters defining the neighboring sub-channels and the flow characteristics. Considering the pressure gradient solver (either SOR or Gauss elimination procedure) the coefficient matrix  $[A]$  and the homogeneous vector  $[B]$  solving eq. (5.1), are strongly dependent on the total number of gaps (neighboring sub-channels) and the ratio between gap width and distance between sub-channel centroids.

$$\left( [A] \left\{ \frac{\partial p}{\partial x} \right\} = [B] \right) \quad (5.1)$$

Other influences are considered while specifying the forced cross flow at certain gaps and certain axial locations and while calculating the total boron concentration. In this case the convection term (depending on the calculated turbulent mixing) is specified at the cell boundaries and the boron concentration influenced by the flow through the gap enclosing two sub-channels. In addition to the work done inside the source of SCF to extend the neighboring sub-channels, substantial work was performed in the wrapping of SCF inside the NURESIM platform for this purpose. Special subroutines devoted to the mesh creation for hybrid geometries were implemented. Finally the development of a pre-processor to facilitate the development of input decks for SCF to handle large problems for hybrid solutions was compulsory.

### 5.1.2 Verification of the thermal-hydraulic hybrid scheme

The purpose of this study is to verify the validity of the TH hybrid solutions of SCF and to demonstrate the functionality of the code inside and outside the NURESIM platform. This is done performing stand alone simulations using hybrid discretizations for the TH domain. In this connection, is also important to show how much computational time can be gained.

For the verification purpose, eight different types of TH test cases were developed. In Table 5 both the definition and the SCF results for each test case are presented. In all cases, the problem consists of a PWR mini-core of 3x3 FA at hot full power (HFP), where the central FA is a MOX one and the others (surrounding the central FA) are UO<sub>2</sub> assemblies. The definition of the test cases is based on the PWR MOX/UO<sub>2</sub> benchmark. The operating conditions and modeling issues are presented in Appendix A, being the same for all cases. The core active height is divided in fifteen nodes in the axial direction for all models. The normalized power distribution follows a cosine shape in the axial direction with a maximal value (unity) at half core height. The radial power distribution is similar as the one indicated in Fig. 15. The maximum Doppler temperature predicted by SCF for each test case (located in the central FA) and the simulation time needed for each test case are summarized in Table 5.

Table 5. SUBCHANFLOW stand alone hybrid tests of a 3x3 PWR mini-core.

<b>Test case</b>	<b>Nodal base assemblies</b>	<b>Pin by Pin assemblies</b>	<b>Computation time (s) [% reduction]</b>	<b>Maximum Doppler temperature (K)</b>
8	0	9	599.7 [ref]	866.77
7	1	8	517.3 [13.7]	866.75
6	3	6	332.4 [44.5]	866.74
5	5	4	188.6 [68.5]	866.74
4	6	3	123.4 [79.4]	866.74
3	7	2	67.7 [88.7]	866.73

Table 5 (continued)

Test case	Nodal base assemblies	Pin by Pin assemblies	Computation time (s) [% reduction]	Maximum Doppler temperature (K)
2	8	1	22.7 [96.2]	866.73
1	9	0	0.12 [99.9]	866.00

Based on the conclusions drawn in Chapter 4, all hybrid models have rod centered discretization. The reference case is a full PBP solution (test case eight) which is the basis for the comparison of the simulation time gained by the different cases with hybrid solutions in (%). Similarly, the reference temperature is set to the PBP calculation. It is clear that the hybrid solution reduces significantly the computational time while preserving the precision in the results. Fig. 18 shows the eight different types of hybrid assemblies (17x17 each) mentioned in Table 5 at half height of the active core (hottest point). The Doppler temperature predicted by SCF (top view of the mini-core) is shown in this figure.

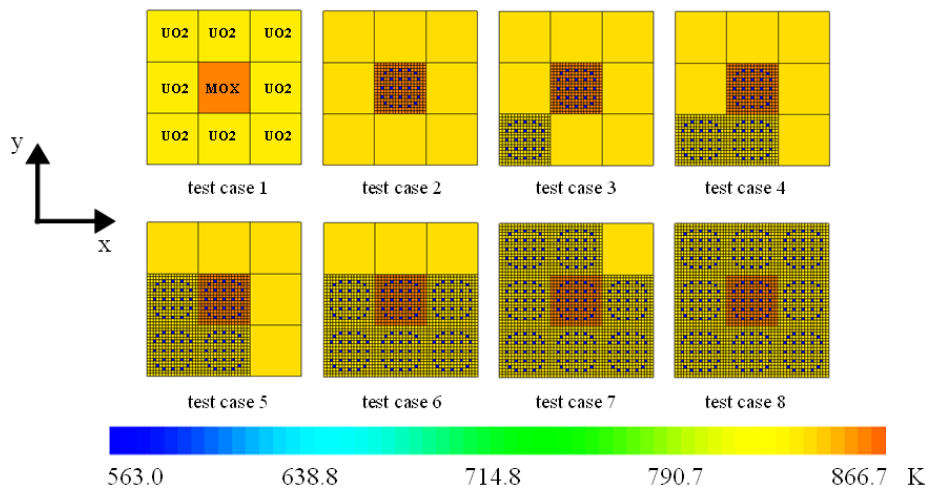


Fig. 18. Doppler temperature calculated for the hybrid mini-core tests at half core height.

The two extreme hybrid cases (test case two and test case eight) show consistency in the solution. The location of the maximum Doppler temperature is the same for both assemblies (central MOX FA) and the difference in temperature between the full PBP solution and the one hybrid solution is equivalent to  $T = 0.5$  K as seen in the previous table. Further parameters predicted by SCF that support this statement are shown in Appendix C, Fig. 77 and Fig. 78. The color scale on Fig. 18 shows a large difference of approximately  $T = 300.0$  K. This is to indicate that the water rods (twenty-five in total for each FA) have the same temperature as the one of the core inlet and no heat is produced in these rods along the core height. Fig. 19 (a) shows the location of the hottest pins and Fig. 19 (b) the temperature deviation for all pins in the central MOX FA compared to the maximum Doppler temperature obtained by SCF with the full PBP solution. The “x” axis represents the seventeen rods in the “x” direction of

the central FA and the “y” axis represents the seventeen rods in the “y” direction of the FA, all of them for test cases two to eight.

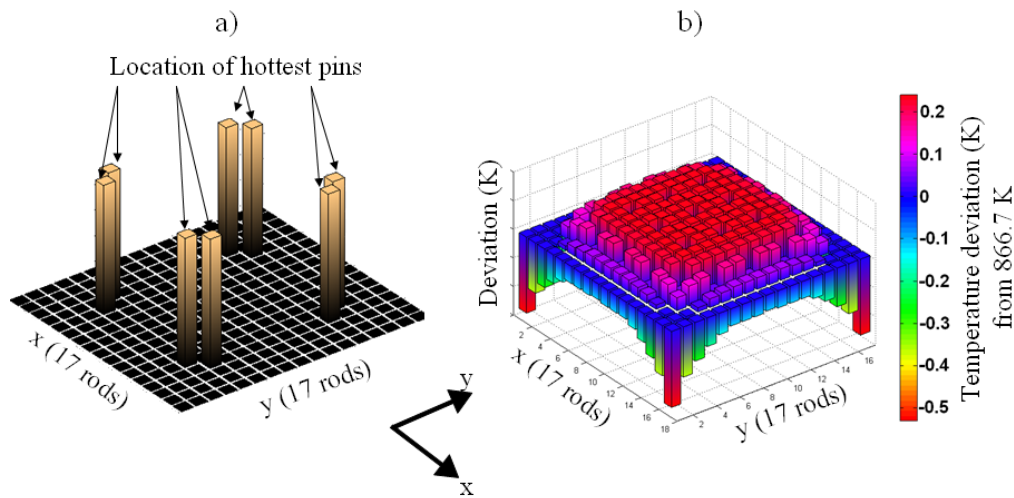


Fig. 19. Hottest pin location (a) and Doppler temperature deviation (b) between the central hybrid FA for test case two and the central FA for the full PBP solution test case eight.

## 5.2 COBAYA3: Extensions for hybrid analysis

### 5.2.1 Description of the methodology

The extension of CBY to perform hybrid solutions was done in close cooperation with the code developers. The main objective is to adapt the domain decomposition methodology of CBY for hybrid steady state coupled simulations of LWR cores with CBY/SCF. For this purpose, the following general steps were carried out:

1. Adapting the input deck of CBY for the selection of hybrid assembly(ies) (the hybrid assembly corresponds to the PBP discretization).
2. Correct reading of the XSs at nodal and pin level (two different libraries are needed).
3. Application of the explicit hybrid scheme between the nodal solver ANDES and cell solver COBAYA3k.

The scheme is based on “embedded” type of calculations, where ANDES (FA solver) provides BCs to COBAYA3k (PBP solver) and vice versa until convergence (based on the current to flux ratio) is achieved between two consecutive PBP solutions. The idea is to obtain a logical sequence between the solvers ANDES, COBAYA3k and sub-routines in charge of setting the BCs in the place of interest.

The global iteration procedure for the solution approach is shown in Fig. 20, where the solvers interact explicitly.

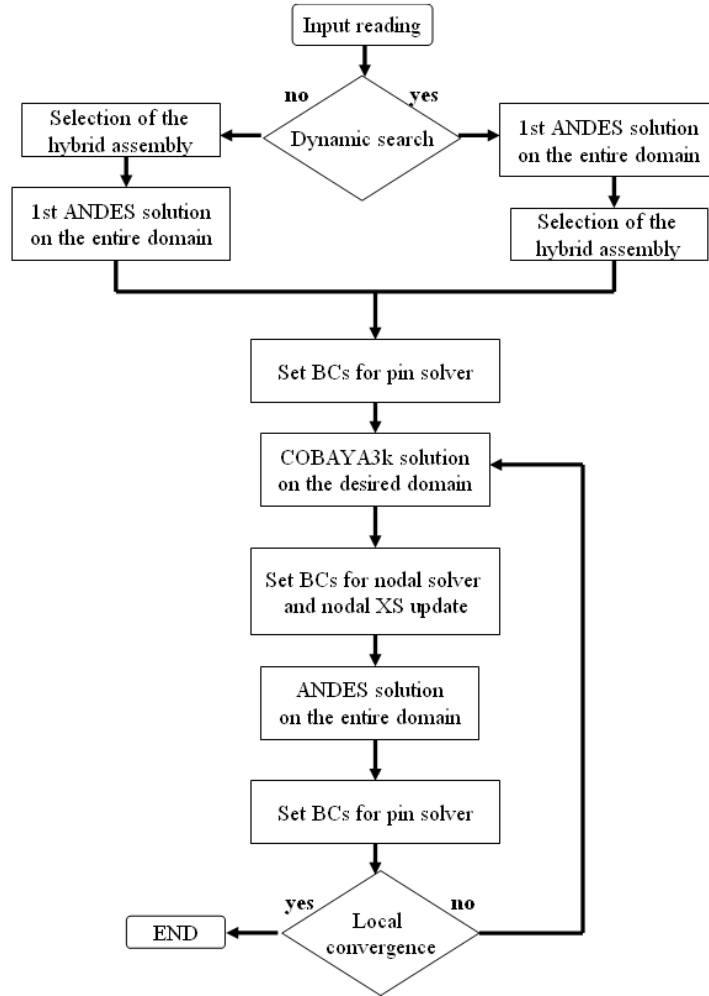


Fig. 20. Calculation scheme for the hybrid treatment of the neutronic code COBAYA3.

First of all, a full core solution at FA level is conducted by the nodal kernel (ANDES). The global solution provides the BCs at the domain borders to be calculated at pin level. Hereby the following data have to be provided by the FA level solution: nodal average fluxes, neutron sources, currents  $(x,y,z)$ , nodal XSs, precursor's concentration and interface currents. COBAYA3k performs its calculation only for the assembly of interest, leading to a N solution only for that specific domain. The BCs for the nodal solver are set including the homogenized nodal XSs. As mentioned in Chapter 3.3 (description of the code CBY), each fuel element is divided in quarters leading to four sub-domains per FA. Then, if modeling a 3x3 mini-core (section inside the blue rectangle, Fig. 21 (b)) with reflectors (section between the gray and the blue rectangles), the domain arrangement looks as follows.

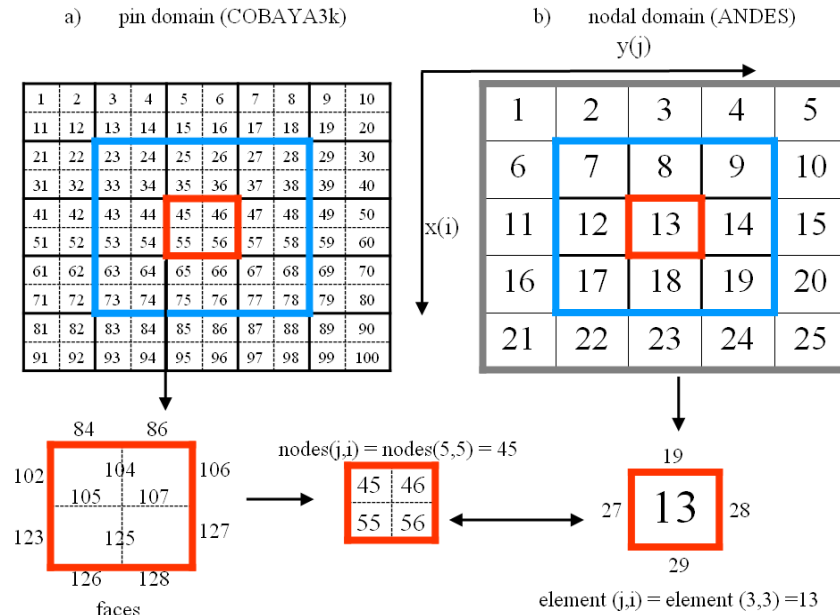


Fig. 21. Mapping (N discretization) scheme for data exchange between ANDES and COBAYA3k.

From Fig. 21, the assembly of interest is the number 13 (red), which is divided in sub-domains 45, 46, 55 and 56. After an initial full nodal solution, ANDES provides the BCs (subroutine nod2lo) corresponding to faces 84, 86, 102, 106, 123, 126, 127 and 128 which are used by COBAYA3k to solve the PBP nodes 45, 46, 55 and 56. Similarly, the BCs provided by the pin solver (subroutine lo2nod) are set to faces 19, 27, 28 and 29 for ANDES. For the development of hybrid solutions with CBY, new sub-routines and modules were implemented in its source code. In addition, three additional issues needed to be emphasised:

1. Input deck reading.
2. Selection of the hybrid assembly and axial match for the material types.
3. Convergence between the nodal based and pin based solvers.

The selection of hybrid assemblies is done through a radial map given in the input deck. For this procedure the array that contains the map KEXYK (NEY, NEX) is later on translated to the nodal “x(i)” and “y(j)” positions. For dynamic allocation, the subroutine potandes.F (computes the power distribution) is in charge of selecting the assemblies with the highest peaking factor and set the coordinates “x(j)” and “y(j)”. The correspondence between the radial and axial types for the PBP solution is done through MNFTK, leading to the array KNKH (global variable in the hybrid module) that is used to give the material composition for the pins.

The parameters that rule the convergence criterion are found in the subroutine POSTSWEEP, which is also in charge of renormalizing the nodal values. Convergence (necessary to decide if the iteration loop between the two solvers reaches an end) is achieved based on the cell flux for steady state or is limited by a maximum number of iterations. For the hybrid solution the flux error (difference between two calculations) obtained between two consecutive PBP iterations is limited to  $10.0^{-6}$ . The solution approach is exhibited in a flow diagram composed by the subroutines needed for the hybrid calculation (Fig. 22). For more details about the flow of information to perform full ANDES or COBAYA3k solutions, refer to [Lozano02] and [Herrero02]. Only the most important subroutines are shown for the sake of simplifications, however, the diagram and de condensed description of the subroutines involved give an idea of the sequence and steps needed to perform hybrid solutions.

1. Subroutine *init.F*: Initialize flags and allocate general arrays based on the input deck.
2. Subroutine *postini.F*: Creates MED meshes and direct the steady state and transient solutions. For the hybrid scheme, it is in charge of creating the sub-domains to be used in each type of dissection excluding the reflectors. The sweep is forced to only one type of dissection, e.g. central, and therefore each active FA is a sub-domain. *PREANDES* sets rod cusping parameters from CR positioning in case of transients. *PREFBKANDES* performs the nodal initialization of moderator temperature and density, and fuel temperature.
3. Subroutine *preLuloop.F*: Initializes control variables for the loops over  $k_{\text{eff}}$ , it calls *FBKANDES* which is in charge of reading the nodal XSs and performs the interpolation according to the input variables. It equates nodal parameters saved under the hybrid global variables to alternate between ANDES and COBAYA3k. Calculation of the 3D power distribution is done after an ANDES call (also necessary for a dynamic search of the hybrid assembly). *NOD2LO* is needed to pass the nodal values calculated by the nodal solver to the local solver: nodal average flux, external neutron source, nodal fission source, surface average net currents  $(i, j, z)$ , surface average fluxes over  $(i, j, z)$ , interface fluxes and current to flux ratios.

$$LOCAL\_parameter(E, i, j, z)_{local\_nodes} = NODAL\_parameter(E, i, j, z)_{local\_nodes}$$

This subroutine also saves the values in auxiliary variables depending on energy and nodes  $(D_{(E,n)}, \sigma_{a(E,n)}, \sigma_{f(E,n)}, \sigma_{s(E,n)})$  so that in *LO2NOD* only the nodes that need to be replaced with the PBP solution are overlapped and the other nodes are equated with the auxiliary variables to keep their FA base characteristics. These values include kinetic parameters.

4. Subroutine PBPSolver.F: Manages local calculations (SWEEP is in charge of this task) and directs the single or multi-processor solver for full core simulations with sweeping. The DRIVER subroutine initializes parameters for convergence and forces the solution to be performed for the first type of domain. It runs the local solver over each box (sub-domain of interest) and convergence is checked at this level. Through ANDESKSOLVER a calculation for heterogeneity factors is done and LO2NOD passes the nodal values calculated by the local solver to ANDES via related commons.

$$NODAL\_parameter(E,i,j,z)_{nodal\_nodes} = LOCAL\_parameter(E,i,j,z)_{nodal\_nodes}$$

The elements correspond to the pin nodes and the new fluxes are equated to the old fluxes previously saved at NOD2LO. The XSs for the specific element (nodal) are updated with the homogenized XSs coming from the PBP solution. Finally, a nodal solution is done and convergence between two consecutive local calculations is verified.

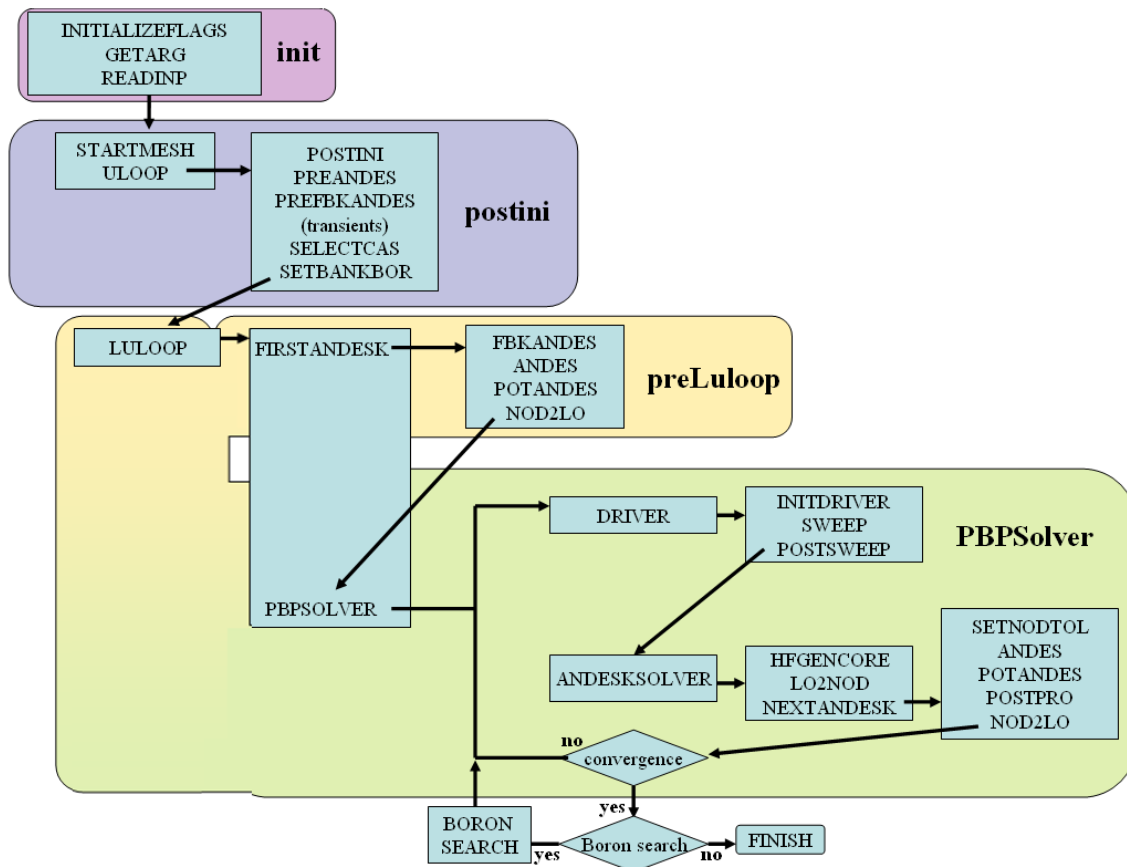


Fig. 22. Hybrid solution scheme implemented in the neutronic code COBAYA3.

### 5.2.2 Verification of the neutronic hybrid scheme

To verify the consistency of the N hybrid solution, a 5x5 mini-core (including reflectors) in 2D geometry was modeled based on the specifications of the PWR MOX/UO<sub>2</sub> benchmark. The advantage of this specific benchmark is that XSs at FA and pin level are available. The model assumes similar UO<sub>2</sub> assemblies, where the central assembly ( $x = 3, y = 3$ ) is to be resolved by the local kernel COBAYA3k. Additionally, a search for critical boron was done (amount of boron necessary to achieve  $k_{\text{eff}} = 1.0$ ), giving rise to a more complex problem due to the internal iterations between kernels needed to obtain the critical boron concentration. The verification was done based purely on the CBY solver, where the hybrid solution was compared to a full nodal based solution and a full PBP base solution. The Table 6 shows relevant parameters used for the modeling of the mini-core.

Table 6. Model parameters for the hybrid mini-core study.

5x5 mini-core (nodal based, cell based and hybrid)				
Total power	MW	60.0	Nodes per cell	4
Inlet temperature	K	560.0	Radial BC	void
Inlet mass flow rate	kg/s	739.0	Axial BC	reflective
Inlet pressure	MPa	15.39	Energy groups	8

Comparison of selected parameters obtained by the different solution approaches are given in Table 7.

Table 7. Comparison of the results predicted by ANDES, COBAYA3k and the hybrid scheme.

Parameter	ANDES(nodal)	COBAYA3k (cell)	HYBRID
Calculation time ( $t_{\text{total}}$ )	1.6 s	1.0 min 59.0 s	7.3 s
Deviation from NODAL solution	0.0 s	106.0 s	44.0 s
System $k_{\text{eff}}$	0.99999998	1.00000090	1.00000004
Final $B_{\text{ppm}}$ concentration (ppm)	881.7	826.7	877.3

The multiplication factor needed a precision of about 0.01 pcm for comparison purposes due to the similarity of the numbers. In addition, the 2D normalized radial peaking factors were compared between the full nodal solutions given by ANDES, the nodal solution given by the hybrid scheme and the full local solution given by COBAYA3k as depicted in Fig. 23. The local solution given by the hybrid scheme was also compared with the full local solution given by COBAYA3k.

NODAL					LOCAL					HYBRID				
0,0	0,0	0,0	0,0	0,0	0,0	0,0	0,0	0,0	0,0	0,0	0,0	0,0	0,0	0,0
0,0	0,731	1,097	0,731	0,0	0,0	0,725	1,102	0,725	0,0	0,0	0,733	1,094	0,733	0,0
0,0	1,097	1,686	1,097	0,0	0,0	1,102	1,690	1,102	0,0	0,0	1,094	1,688	1,094	0,0
0,0	0,731	1,097	0,731	0,0	0,0	0,725	1,102	0,725	0,0	0,0	0,733	1,094	0,733	0,0
0,0	0,0	0,0	0,0	0,0	0,0	0,0	0,0	0,0	0,0	0,0	0,0	0,0	0,0	0,0

Fig. 23. Radial peaking factors ( $F_{xy}$ ) calculated by ANDES, COBAYA3k and the hybrid solution.

For safety analysis is important only the highest value of the power ( $F_{xy}(\text{local}) = 1.690 > F_{xy}(\text{hybrid}) = 1.688$ ). It can be concluded that the hybrid solution under predicts the pin power compared to the full PBP solution, but is more conservative than the one of the nodal based solution ( $F_{xy}(\text{nodal}) = 1.686 < F_{xy}(\text{hybrid}) = 1.688$ ). For the central assembly, Fig. 24 shows the deviation (in %) between pin powers (in KW). There, the error represents the accuracy of the hybrid solution with respect to the PBP solution and is calculated as,

$$\left( \frac{PBP\_2D\_normalized\_power - HYBRID\_2D\_normalized\_power}{PBP\_2D\_normalized\_power} \right) \times 100. \quad (5.2)$$

It is noted that higher discrepancies are located at the edge of the FA, where nodal and local BCs are applied. The maximum deviations between the hybrid central FA and the central full PBP FA lie in the order of 2.5 %.

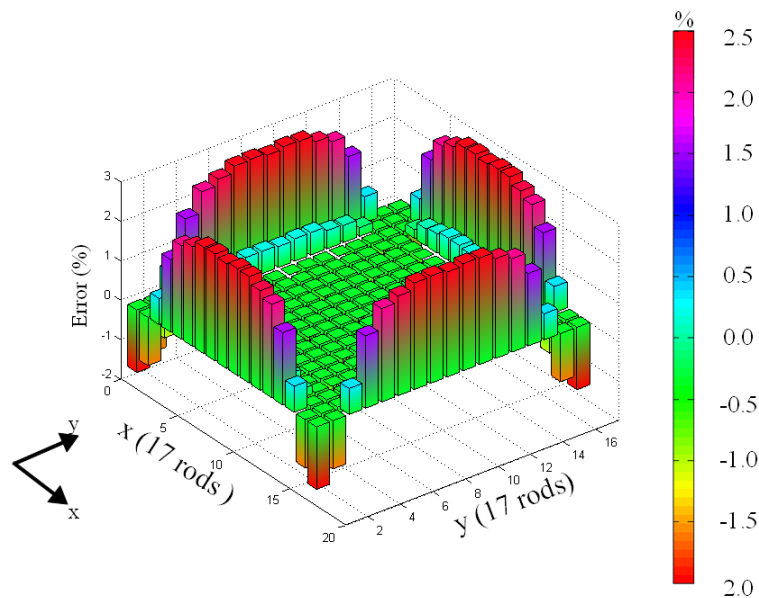


Fig. 24. Deviation (in %) for the hybrid solution from the PBP reference solution for the central FA.

In addition, a full 3D PWR core based on [Downar06] was analyzed using the hybrid scheme to demonstrate the capability of the hybrid scheme for analyzing real cores. The core is assumed to be at

a HFP state and the simulation is done for steady state conditions. Details about the modeling and operating conditions are given in Appendix A. Three different cases are investigated:

1. Case 1: Full nodal core solution with no hybrid assemblies.
2. Case 2: Nodal core solution with the central FA as hybrid domain.
3. Case 3: Nodal core solution with four fuel elements located around the CR ejection position based on the hybrid approach.

In Table 8 a comparison of the selected parameters (computational time,  $k_{\text{eff}}$ ,  $F_{xy}$  and the axial peaking factor ( $F_z$ )) predicted by the pure nodal whole core simulation and by the two hybrid cases mentioned above is shown. For obvious reasons, a full PBP solution was not performed, so only nodal parameters are compared. The nodal base solutions used homogenized XSs with eight energy groups. The same number of energy groups in the XSs for the PBP simulation in the hybrid domains.

Table 8. Hybrid results for the 3D PWR MOX/UO2 full core simulation.

Parameter	ANDES(nodal)	1 HYBRID FA	4 HYBRID FAs
	Case 1	Case 2	Case 3
$t_{\text{total}}$	2.0 min 15.0 s	1.0 h 44.0 min	3.0 h 33.0 min
Iterations(nodal-local)	0	22	49
System $k_{\text{eff}}$	1.14598	1.14615	1.14614
$F_{xy}$	2.255	2.248	2.260
$F_z$	1.482	1.481	1.481

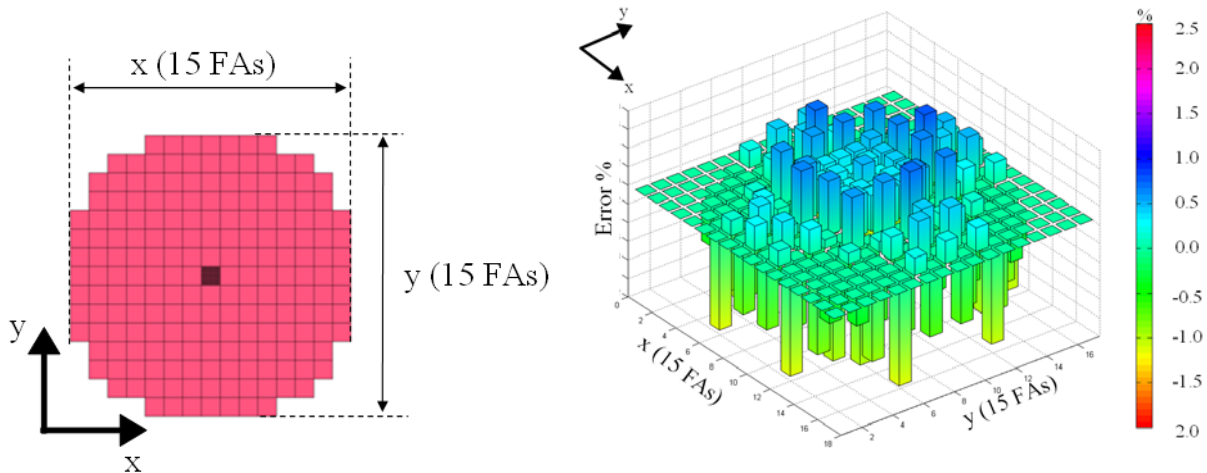


Fig. 25. Deviation (in %) of the radial power predicted by CBY for the second case (hybrid solution) and the one predicted by the first case (full nodal solution).

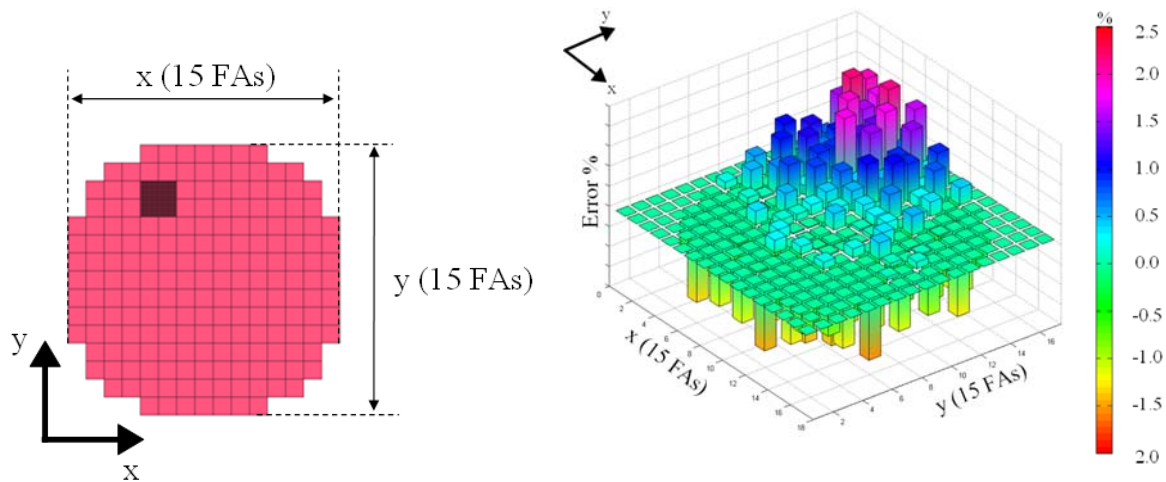


Fig. 26. Deviation (in %) of the radial power predicted by CBY for the third case (hybrid solution) and the one predicted by the first case (full nodal solution).

It can be observed in these figures that the deviation increases with increasing number of hybrid assemblies, reaching a maximum value of 2.5 % if the full nodal solution (first case) is considered as reference.

To perform a coupled steady state simulation with CBY/SCF using the hybrid solutions in both domains (N (CBY) and TH (SCF)), further developments are needed. Hereafter, the most important areas for developments are listed.

1. Integration of new components in SALOME for the generation of hybrid meshes for both SCF and CBY.
2. Extension of the wrapping routines, e.g. CXX and FORTRAN to set the pin powers and obtain the feedbacks to and from hybrid fields.
3. Extension of CBY capability to use the hybrid meshes based on the wrapping of SCF by importing the MED. The mesh generation tool of CBY can be bypassed, where the nodal power is assigned to the N nodes (ANDES solution) and the pin power is assigned to the cells (COBAYA3k calculation).
4. The TH feedback is also considered independently for ANDES and COBAYA3k, where a specific component called “pasopasath2nk” set the TH sub-channel parameters in the hybrid (PBP) FA and the TH channel parameters in the rest of the FA, commons for ANDES.

Details about this process are found in the next chapter.

---

## 6 Development of a coupling scheme between COBAYA3 and SUBCHANFLOW

In this chapter the implementation of a coupling scheme between the N code CBY and the TH code SCF within the NURESIM platform for nodal based (square and hexagonal geometries) steady state and transient simulations is described. In addition, the coupled hybrid scheme involving both codes is presented. Finally, the developed coupled solutions are verified using a benchmark exercise.

### 6.1 Coupled solutions at nodal level

The philosophy behind the coupling within the NURESIM platform is based on the mesh superposition and mesh independency between N and TH models. The interpolation tool is fundamental in this novel methodology. The coupling approach between CBY and SCF is divided in two groups, coupled solutions for steady state simulations and coupled solutions for transients. Even though the actual coupling is similar in nature (e.g. feedback parameters), the interaction between the N and TH follows a different scheme. For developing a coupling approach between N and TH special attention should be given to the treatment of the feedback parameters and their iteration between the different physical phenomena involved.

The flow of information between N and TH domains (and vice versa) is shown in Table 9.

Table 9. Flow of information between N and TH (exchange of parameters).

<i>Neutronics</i>	$\leftrightarrow$	<i>Thermal-hydraulics</i>
1. Mapping for the N and TH domains for transferring the power (radial and axial) from one N node/cell to another TH fuel rod.		1. Mapping for the TH and N domains for transferring ( $T_{Dopp}$ , $T_{mod}$ , $D_{mod}$ , $\alpha$ and $B_{ppm}$ ) from one TH channel/sub-channel to another N node/cell.
2. Power is obtained by calculating the energy released for each node or cell based on the fission rate.		2. Convergence of the TH solution leading to the acquisition of TH parameters ( $T_{Dopp}$ , $T_{mod}$ , $D_{mod}$ , $\alpha$ and $B_{ppm}$ ) based on a given 3D power distribution.
3. An update of the XSs is done thanks to their parameterization in terms of the parameters $T_{Dopp}$ , $T_{mod}$ , $D_{mod}$ , $\alpha$ and $B_{ppm}$ obtained by the TH.		3. Update of the power density is done based on the power distribution obtained by the N.

### 6.1.1 COBAYA3/SUBCHANFLOW: Coupling for steady state simulations

For steady state analysis, an iterative explicit coupling scheme was developed, where one code provides the boundary conditions to the other one. In Fig. 27 the general flow diagram of this explicit scheme is shown (solution of the N and TH equations independently). Each solver is called independently and it runs using its own numerical scheme. This scheme needs additional iterations for the different codes to assure the convergence of the coupled system.

In the coupling approach, CBY starts at iteration ( $it$ ) = 0 with pre-defined operating conditions (the initial XS interpolation is done based on a flat distribution of the inlet core temperature which in fact is preserved as the reflector temperature along the simulation). The first feedback (power density, where  $F_{ax}$  represents the axial power and  $F_{rad}$  the radial power) is transferred from the N to the TH so that SCF can perform its first calculation and obtain the parameters  $T_{Dopp}$ ,  $T_{mod}$ ,  $D_{mod}$ ,  $B_{ppm}$ <sup>1</sup> and  $\alpha$  (for the specific case of BWR, void reactivity feedback plays an important role). Based on these new boundary conditions, a TH solution is obtained and TH parameters are passed to the N to perform the XS update and calculate the new power densities. The iteration continues until convergence is reached.

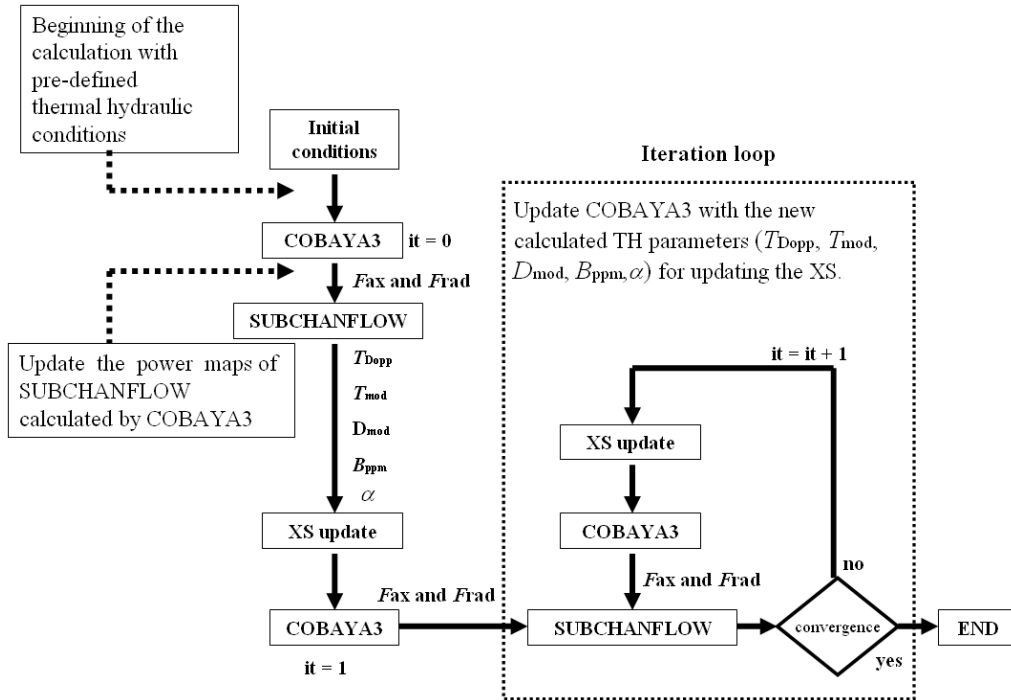


Fig. 27. Iterative scheme between CBY and SCF for steady state calculations.

<sup>1</sup> The boron concentration does not depend on the N feedback; however, this concentration is calculated for each TH sub-channel (axially) during boron dilution transients. The N solution does depend on this boron concentration.

In order to accelerate the convergence of the solution between the N and TH and to avoid oscillations, a relaxation factor of  $\lambda = 0.7$  was applied to all the feedback parameters inside the N code (XS feedback interpolation was done using a damped value which takes 0.7 of the value at  $it = n$  and 0.3 of the value at  $it = n - 1$ ). This damping factor has shown very good performance in other implementations of coupled N/TH codes, e.g. (CBY/COBRA-III/TF). The iterative process ends when predefined convergence criteria are fulfilled.

The modeling of the coupled steady state system in SALOME as illustrated in Fig. 28. The feedback exchange between SCF and CBY is done through MED fields inside SALOME. Each field (power,  $T_{Dopp}$ ,  $T_{mod}$ ,  $D_{mod}$ ,  $B_{ppm}$  and  $\alpha$ ) is created and filled out through the MED interaction (memory structure AB). Through this memory structure data is interpolated (accounting for flexible mesh structures) so that the correct feedback spatially speaking can be exchanged between the N and TH domains. For other coupling schemes that do not involve the usage of the MED, an average must be done for the feedback purpose. This step is avoided while coupling inside the SALOME platform. Here, the feedback or exchange of information is done automatically through the mesh superposition technique, which allows having different meshes with different radial and axial discretizations. In this case the use of an interpolation tool (Chapter 3.1.1) is compulsory.

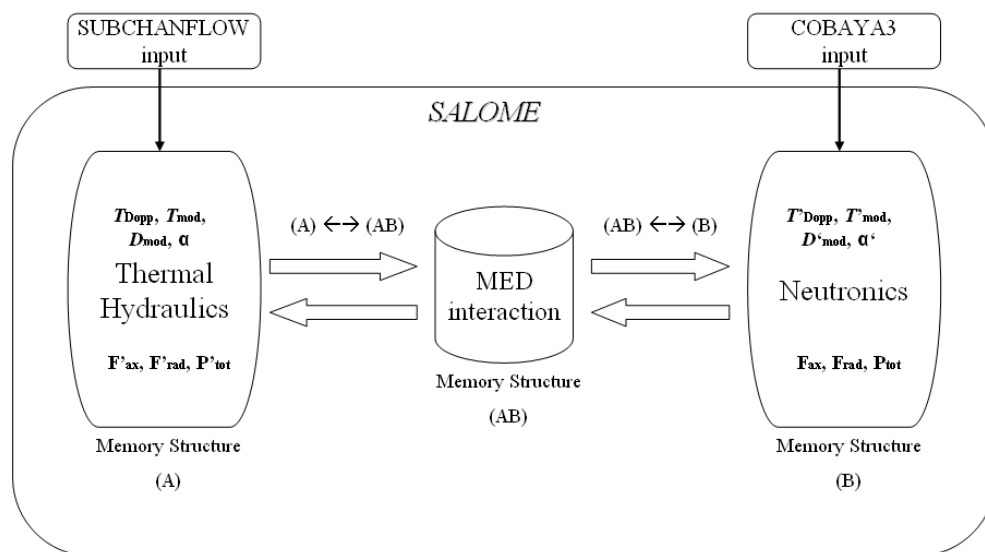


Fig. 28. Coupling inside SALOME (CBY/SCF) based on the MED structure for feedback exchange.

For the spatial discretization in the radial direction concerning nodal (FA) level solutions, one N node corresponds to exactly one TH channel (with one equivalent pin for the total number of pins in the fuel assembly with similar dimensions and thermo-physical material properties). This philosophy will be of great use specially when dealing with hexagonal geometries. Fig. 29 shows this matching between both domains for a simple case of nine fuel assemblies and nine equivalent pins. In this figure, 264

heated pins are condensed in one pin with equivalent power (Fig. 29 (a)), and which releases this power to the FA or channel (Fig. 29 (b)).

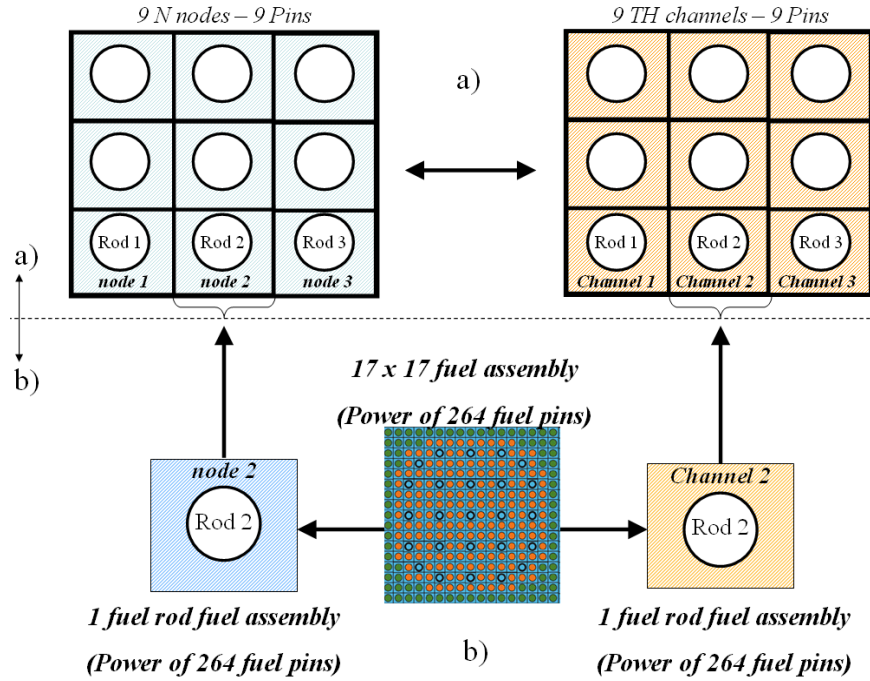


Fig. 29. Radial mapping between the N (left-blue) and TH (right-cadmium orange) domains for nodal base solutions.

In equations (6.1) and (6.2) the feedbacks obtained by the N ( $T_{\text{mod-N}}^{\text{node1}}$ ,  $D_{\text{mod-N}}^{\text{node1}}$ ) are equivalent to the TH parameters calculated ( $T_{\text{mod-TH}}^{\text{chan1}}$ ,  $D_{\text{mod-TH}}^{\text{chan1}}$ ), e.g. for the first channel. In the same way the power density obtained by the TH for rod one ( $Power^{\text{rod1}}_{\text{TH}}$ ), is the same as the power calculated by the N for this rod ( $Power^{\text{rod1}}_{\text{N}}$ ), as in eq. (6.3). A similar process is done for the Doppler temperature, exemplified in eq. (6.4).

$$T_{\text{mod-N}}^{\text{node1}} = T_{\text{mod-TH}}^{\text{chan1}} . \quad (6.1)$$

$$D_{\text{mod-N}}^{\text{node1}} = D_{\text{mod-TH}}^{\text{chan1}} . \quad (6.2)$$

$$Power^{\text{rod1}}_{\text{N}} = Power^{\text{rod1}}_{\text{TH}} \quad (6.3)$$

$$T^{\text{rod1}}_{\text{Dopp-N}} = T^{\text{chan1}}_{\text{Dopp-TH}} \quad (6.4)$$

Even though the spatial mapping for nodal base solution facilitates the exchange of information between codes, there are still issues to consider due to the possible differences in the axial discretization. For hexagonal geometries, some bugs were found in the interpolation tool. First of all an error in the exchange of the feedback parameters between the N and TH domain was identified leading to an error in the order of 50.0% of the interpolated value (e.g. total power ( $P_{\text{tot}}$ ) calculation by the N is  $P_{\text{tot}} = 100.0$  W and the power obtained by SCF to perform its TH solution is  $P_{\text{tot}} = 150.0$  W). Consequently, an alternative solution was envisaged and implemented based on a one-to-one mapping between the CBY and SCF domains. For this purpose, the hexagonal FAs were divided in six triangular nodes for the N domain while the TH domain was kept as hexagonal channels. To assure consistent information exchange between the two domains, care must be taken for the feedback parameters. The nodal normalized power is averaged on the six nodes so that it corresponds to one TH channel (a fuel rod) and the parameters ( $T_{\text{Dopp}}$ ,  $T_{\text{mod}}$ ,  $D_{\text{mod}}$ ,  $B_{\text{ppm}}$  and  $\alpha$ ) are passed directly to the six N nodes without averaging. The validation of this implemented one to one mapping is presented in Chapter 7.1.2. There, a coupled solution that includes the use of the interpolation tool and the use of the one-to-one mapping scheme is presented.

### Convergence criteria for steady state

Since the coupling of the N and TH domains is realized in an iterative process solving separately both problems, criteria for the convergence were defined for the coupled simulation. The steady state iteration loop between CBY and SCF is presented in Fig. 27, where the convergence criteria are based on both the N and TH parameters (as discussed in Chapter 2.4.2). The convergence criteria are set by the user as needed. For the validation process of the coupling, the following convergence criteria were defined:

1.  $\varepsilon_N = 10.0^{-6}$  for the multiplication factor and total power.
2.  $\varepsilon_T = 10.0^{-4}$  for the fuel Doppler temperature, moderator temperature and moderator density.

These relative variations are derived from the difference of the selected parameters between two consecutive iterations, e.g. if the variation of  $k_{\text{eff}}$  is less than a defined criterion; eq. (6.5), convergence is assumed to be achieved. A diagram of this iterative process is shown in Fig. 30. Is important to mention that N parameters account for global effects ( $k_{\text{eff}}$  and  $P_{\text{tot}}$ ) while TH parameters account for local effects, e.g. a maximum Doppler temperature is established after comparing the Doppler temperature for each rod and axial level. A similar approach applies for  $T_{\text{mod}}$  and  $D_{\text{mod}}$ .

$$\left| \frac{X^n - X^{n-1}}{X^n} \right| \leq \varepsilon_X, \text{ where } X = P_{\text{tot}}, k_{\text{eff}}, T_{\text{Dopp}}, T_{\text{mod}} \text{ and } D_{\text{mod}}. \quad (6.5)$$

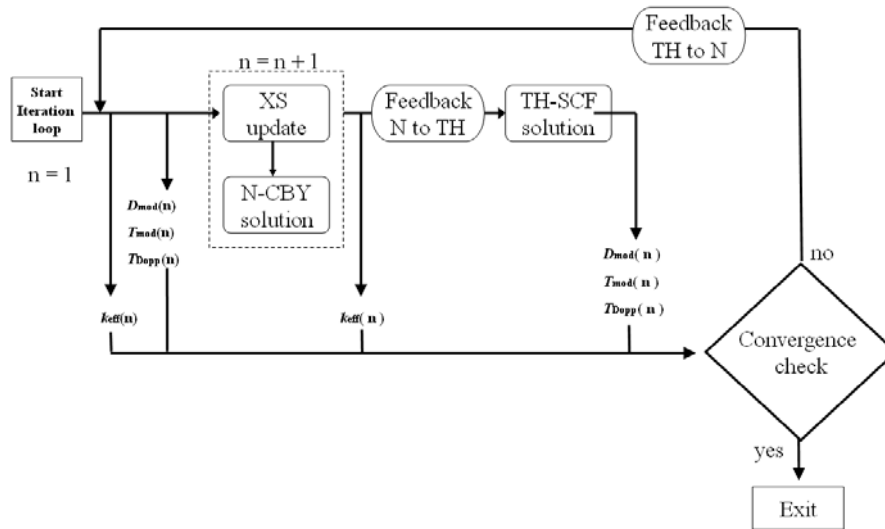


Fig. 30. Steady state convergence loop for the CBY/SCF coupling scheme.

### 6.1.2 COBAYA3/SUBCHANFLOW: Coupling for transient simulations

The coupling CBY/SCF approach for transient analysis is similar to the one developed for steady state simulations in the sense that the spatial mapping between the two domains (N and TH) is done through a mesh superposition inside SALOME together with the use of in-built interpolation routines of the platform. The treatment of the “feedback” is also similar (in terms of the exchanged parameters) but the main difference is the temporal coupling approach implemented to advance the solution of each code and the synchronization of the time step between the involved codes.

Although transient solutions (for different coupled codes, Chapter 2.4, Table 2) follow different coupling schemes for the time advancement, the scheme used for CBY/SCF was selected based on the capabilities of the involved codes. The XS update in CBY to solve the neutron balance equation is done after the TH feedback is taken into account at each time step, see Fig. 31.

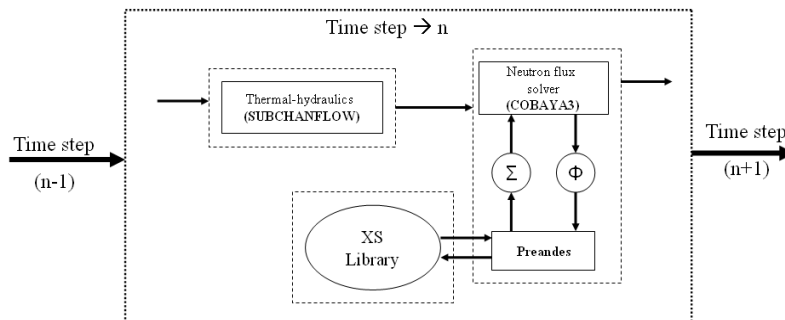


Fig. 31. Feedback interaction at every time step  $\rightarrow n$ .

The coupling approach follows an OS type of scheme by considering the PMs implemented in SCF. A more detailed description of this method is shown in Fig. 32. The CBY transient solution starts from a restart file saved at the end of the coupled steady state simulation in order to save time in the initialization of the transient. Steps 2b and 6b represent only the change of solution (the N code ended its simulation and the TH is ready to start its simulation). The predicted axial and radial normalized PMs at  $t = t_1$  s are transferred into SCF, which in turn performs a transient solution from  $t = 0.0$  s to  $t = t_1$  s. The new calculated TH parameters ( $T_{Dopp}$ ,  $T_{mod}$ ,  $D_{mod}$ ,  $B_{ppm}$  and  $\alpha$ ) are then passed to CBY and used to update the Xs at time  $t = t_1$  s. At this point CBY performs a transient solution from  $t = t_1$  s to  $t = t_2$  s. Based on this iterative process, a computational route was developed in SALOME for the YACS supervision module. The coupled scheme ends when the total time reaches the maximum time chosen by the user in SALOME. As the scheme is an OS in time, parametric studies were performed to identify the optimal selection of the time step size for typical transients, discussed in Chapter 7.

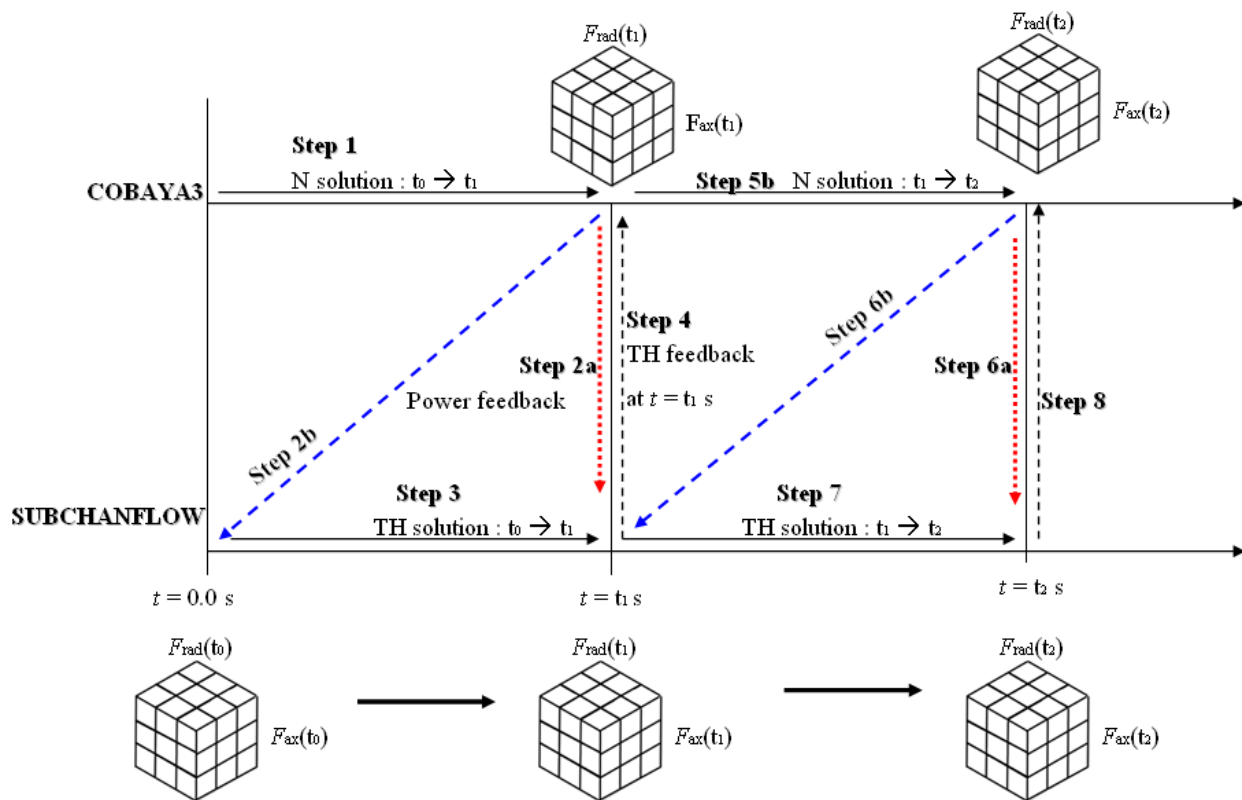


Fig. 32. Operator splitting approach for the coupled scheme CBY/SCF.

The Table 10 describes the steps followed during the time advancement, related to Fig. 32.

Table 10. Temporal coupling scheme between CBY and SCF.

Step	Running code	Starting time (s)	End time (s)	Used parameters for predicting the N or TH solution
1	CBY(N)	$t = 0.0$	$t_1$	Input parameters from converged steady state
2a	Power distribution at $t_1$ , passed to SCF			
3	SCF(TH)	$t = 0.0$	$t_1$	Input parameters and PM at $t_1$
4	TH feedback to CBY from the results of SCF obtained at $t_1$			
5a	XS update			
5b	CBY(N)	$t_1$	$t_2$	Parameters at $t_1$
6a	Power distribution at $t_2$ , passed to SCF			
7	SCF(TH)	$t_1$	$t_2$	PM at $t_1$ and PM at $t_2$
8	TH feedback to CBY from the results of SCF obtained at $t_2$			

The use of PMs is very important for performing time dependent solutions with SCF. The philosophy consists of using two different power distributions between two consecutive time steps, so that the shape of the power density follows a more accurate pattern between those two steps. If no power maps are used, the power shape remained constant between time steps, leading to an under prediction of local parameters. This issue was discussed in detail in [Gomez01].

For instance, four nodes (each with rod power of  $P_{rod} = 1.0$  W) represent a total power of  $P_{tot} = 4.0$  W at time  $t = 0.0$  s. At this time a local perturbation of the flux is encountered, e.g. due to a rod ejection transient, leading to a total power increase of 10.0%. Even though the total power is preserved at  $t = t_1$  s ( $P_{tot} = 4.4$  W for both cases), the local parameter at some regions could be underestimated by not using the PMs. This could be critical for analyzing rod ejection transients to calculate local safety parameters.

To obtain properly converged steady states results; an automatic adjustment of the maximum number of axial flow error iterations was implemented. This option is selected only during the first steady state step ( $t = 0.0$  s) for the TH while performing a transient solution, leading to a convergence up to the level of  $10.0^{-8}$  for the flow error and an increase of axial flow iterations of 500. After this initial step, the convergence parameters (SOR convergence, axial flow error and steady state flow error criteria) return to the pre-defined values set in the input deck of SCF. The initial attempt for the coupling was established to follow a fully implicit approach (ideal for fast transients due to the freedom while dealing with small time steps). However, the N code CBY is not able to perform these types of calculations, namely, continuous iterations at one specific time step. Therefore, the OS scheme was selected as the temporal coupling methodology. The coupled solution methodology is illustrated in Fig. 33.

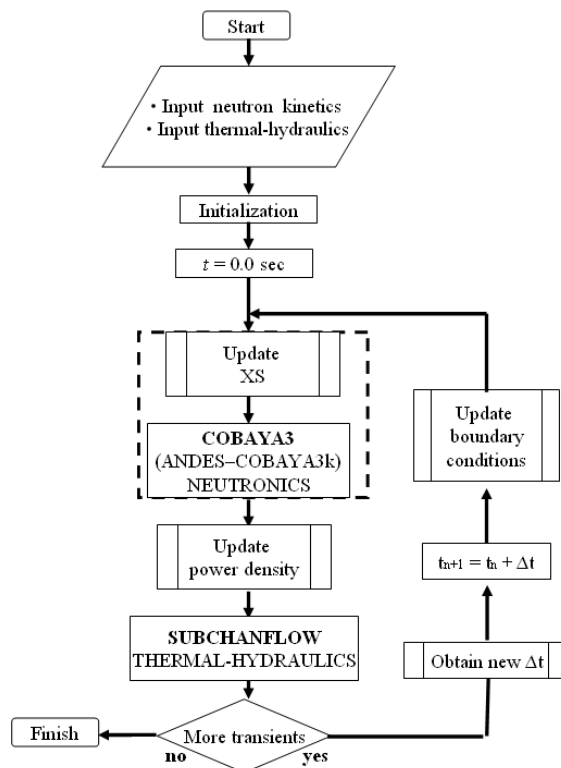


Fig. 33. CBY/SCF solution methodology for an OS coupling approach in SALOME.

At pin level, steady state and transient coupling schemes between both the N and TH domains follow a similar approach as for nodal base calculations (iterative and OS schemes respectively). Therefore, the only difference between both geometrical scales is the spatial mapping in the radial direction and the feedback management.

## 6.2 Coupling scheme for steady state hybrid core analysis

For hybrid core simulations special algorithms were developed for the wrapping (SALOME integration) of SCF and CBY into the NURESIM platform. The main difficulty encountered was the feedback handling between N and TH due to the absence of a hybrid mesh generator tool for CBY. To solve this, a substantial programming effort was done to bypass the interpolation tool and the mesh generation tool of CBY and to import the TH mesh from SCF to CBY, as a N mesh. In this case the two meshes, structures and fields have the same number of elements and therefore a one to one mapping was adopted.

The coupling methodology follows the diagram shown in Fig. 27, where the hybrid N solver starts the iteration process. After convergence (see Chapter 6.1.1) the power field is filled up with the new 3D normalized power distribution. At this time it is important to place into the nodal fuel elements the nodal power and into the local elements the cell power calculated by CBY for the hybrid FA. For this

purpose, two important arrays are critical for the correct management of the fields. Their name, however, is arbitrary.

1. PINPOW2SCF (axial levels, [FA pins] X [hybrid FAs]): Contains the pin power values for each axial level and each cell of the total number of hybrid FAs.
2. NODPOW2SCF (axial levels, total no. of active nodal FA): Contains the nodal power values for each axial level and each node of the total number of FA.

Additional information was required in the input deck of CBY, where the TH channels (first and last) of each hybrid FA needed to be specified for the coupling. With this, the power field based on the SCF mesh is filled out (data are placed in each of the nodes for the field) with the power distribution. For the power feedback, SCF reads this field and place, element by element, the N power for each fuel rod. SCF does not distinguish between PBP and nodal FA due to its sub-channel philosophy and hence, it provides a one to one feedback flow between the field and the rods, as shown in eq. (6.6) and eq. (6.7).

$$Power_{rod(n)-subchannel}^{TH} = Power_{cell(n)}^N \quad (6.6)$$

$$Power_{rod(n)-channel}^{TH} = Power_{node(n)}^N \quad (6.7)$$

After a converged TH solution performed with the new power distribution, the hybrid TH fields containing the new TH variables ( $T_{mod}$ ,  $D_{mod}$ ,  $T_{Dopp}$  and  $B_{ppm}$ ) are then set into auxiliary arrays of CBY. This step is necessary to organize the data obtained from the TH fields (SALOME interface). Table 11 illustrates the arrays that the N code uses to perform the XS interpolation.

Table 11. Parameters (arrays) needed by ANDES and COBAYA3k for the XS update.

ANDES (nodal solver)			COBAYA3k (pin solver)		
Auxiliary array	Step →	For XS interpolation	Auxiliary array	Step →	For XS interpolation
U(kg/m <sup>3</sup> )	paso_th2nk	RHONOD	UCT	pasa_th2nk	BU2
TAG (K)		TMODNOD	TAGCT		BTAG2
TEFDOPLER(K)		TFNOD	TEFDOCT		BTEFD2
BOROTH(ppm)		BORO3D	BOROTHCT		BBOROP2

The TH parameters are set into the auxiliary arrays for both the nodal and pin solver through a special black box of CBY (setFeedback). The subroutines paso\_th2nk and pasa\_th2nk are called consecutively to update the global arrays used for the XS interpolation. Due to the nature of the coupling, a hybrid

solution is performed considering an initial state and therefore, logical variables related to the first hybrid calculation are set to value after the update. The TH feedback is a critical step for the hybrid coupled solution, nodal and pin arrangements should be considered as in equations (6.8), (6.9) and (6.10), where  $PARAM$  could be the  $D_{mod}$ ,  $T_{mod}$  or  $B_{ppm}$ .

$$\sum_i^{hybrid-FA} PARAM_{avg(i)}^N, T_{Dopp,avg(i)}^N = \sum_i^{hybrid-FA} \frac{\sum_j^{FA-pins} (PARAM_{(i,j)}^{TH}, T_{Dopp,(i,j)}^{TH})}{FA-pins}, \quad (6.8)$$

$$T_{Dopp}^{N-node(n)} = T_{Dopp}^{TH-channel,rod(n)}, \quad PARAM^{N-node(n)} = PARAM^{TH-channel(n)}, \quad (6.9)$$

$$T_{Dopp}^{N-cell(n)} = T_{Dopp}^{TH-subchannel,rod(n)}, \quad PARAM^{N-cell(n)} = PARAM^{TH-subchannel(n)}. \quad (6.10)$$

For coolant and pin parameters the information is set directly from channels/sub-channels to nodes/cells. For the hybrid assembly however, an average is done considering (Fig. 34);

1. The total number of heated pins for the Doppler temperature.
2. The total number of sub-channels for the  $T_{mod}$ ,  $D_{mod}$  and  $B_{ppm}$ .

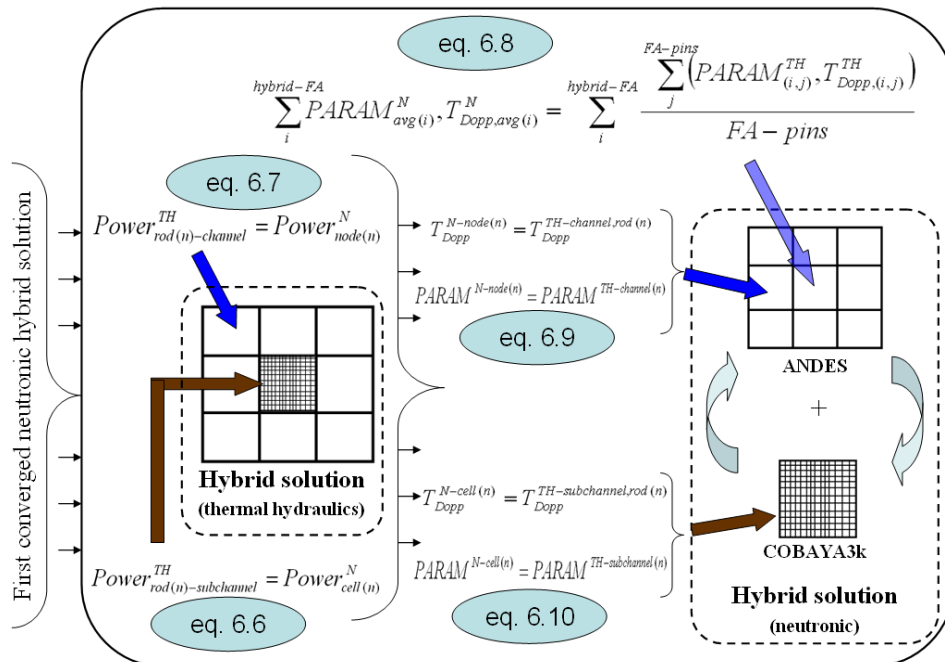


Fig. 34. Steady state convergence loop for the coupled hybrid scheme (CBY/SCF).

### 6.3 Verification of the developed nodal coupling scheme in SALOME

In addition to the validation of the coupled scheme CBY/SCF described in Chapter 7, verification of the correct implementation of the TH code SCF and its coupling with CBY was performed. For this purpose, the first case of the LWR core transient benchmarks was chosen. The objective of this section is only to verify the integration of SCF inside SALOME, its coupling with CBY and study the behavior of the code in the platform. Stand alone calculations were also performed; however, it was decided to use a problem which involve the coupling with N for the purpose of validation. Detailed analysis of the results will not be commented, this analysis will be done in Chapter 7.1.1, where a more recent benchmark with similar characteristics to the LWR core transient benchmark will be described and discussed (the OCDE/NEA and US NRC PWR MOX/UO<sub>2</sub> core transient benchmark).

#### 6.3.1 NEABEN - LWR transient, case A1 (description and modeling)

The NEABEN LWR core transient benchmark [Franklin01] comprises a wide series of cases involving steady state and transient solutions, in addition to conditions at HZP and HFP of a LWR core. For the verification purpose, only the case A1 was modeled, which involves a steady state and a transient scenario. This benchmark is characterized by the extraction of the central CR of a PWR core (the modeling is done at FA level). The simulation is done from  $t = 0.0$  s to  $t = 1.0$  s and the CR ejection occurs within  $t = 100.0$  milliseconds (ms) (departing from a converged steady state). During the full transient period, the boron concentration and position of the non-active CRs remained constant. Fig. 35 represents the top view of the core where the 157 FA (parallel channels and nodes for the TH and N) are shown. The Fig. 35 also shows the location of the CRs in one eighth of the core. The central CR is to be extracted; the other two types of CRs are positioned at 0 steps (X) and 228 steps (C) from the bottom reflector.

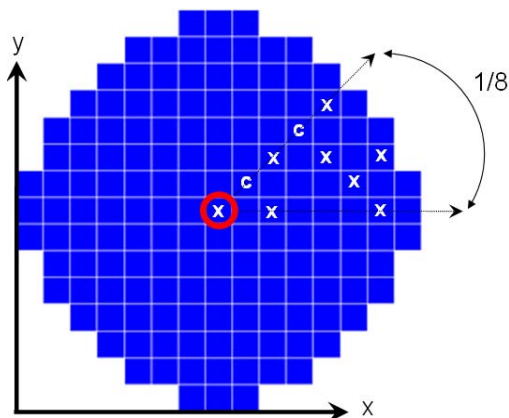


Fig. 35. Location of control assemblies in 1/8 of the core, NEABEN benchmark.

Parameters such as Doppler temperature and total power predicted by CBY/SCF will be compared with the reference solution obtained by the PANTHER code and the coupled solution CBY/COBRA (III and TF). In addition, the meshing, field management, coupled scheme N/TH and post-processing capabilities of SCF and SALOME will be discussed. The initial steady state is characterized by a HZP at  $P_{\text{tot}} = 2775.0$  W, inlet temperature fixed at  $T_{\text{in}} = 559.15$  K, exit pressure ( $P_{\text{out}}$ )  $P_{\text{out}} = 15.5$  MPa and total core mass flow rate ( $\dot{m}_{\text{in}}$ ) of  $\dot{m}_{\text{in}} = 12839.0$  kg/s. More details about the benchmark such as geometrical configuration, thermo-physical properties and additional operating conditions can be found in [Fraikin01].

The case A1 was modeled with conditions similar to the reference and CBY/COBRA (III and TF), where eighteen axial levels and four nodes per FA in the radial direction (this radial discretization will play an important role in the benchmark, as discussed in the next section). The steady state and transient coupling schemes follow the strategy discussed in Chapter 2, which will be used also for the validation process. A convergence criterion of the steady state was achieved based on  $\varepsilon_{\text{N}} = 1.0^{-5}$  and TH parameters equal to  $\varepsilon_{\text{T}} = 1.0^{-4}$ .

### 6.3.1.1 Selected results for the NEABEN benchmark

Steady state CBY/SCF convergence was reached after the first iteration, which is typical for HZP conditions. On the contrary for HFP ( $P_{\text{tot}} = 2775.0$  MW) convergence is a more challenging issues (refer to Chapter 7.1.2, the TMI-1 MSLB benchmark). The Table 12 illustrates the steady state results obtained with CBY/SCF compared to the reference solution (PANTHER) and to other coupled solutions obtained with CBY/COBRA (III-TF). Here the critical boron concentration, radial peaking factor, nodal peaking factor ( $F_{\text{q}}$ ) and Doppler temperature are compared.

Table 12. Steady state results for the NEABEN LWR transient benchmark at HZP.

Code	Critical boron (ppm)	$F_{\text{xy}}$	$F_{\text{q}}$	$T_{\text{Dopp}}$ (K)
PANTHER (ref)	567.7	1.909	2.874	559.15
CBY/SCF	561.6	1.911	2.892	559.05
CBY /COBRA-III	561.6	1.909	3.007	559.15
CBY /COBRA-TF	562.6	1.909	3.007	559.15

Table 12 shows good agreement between the predictions using CBY/SCF and the reference. The relative error lies in the range of 0.62% and the Doppler temperature changes by  $T = 0.1$  K. Based on the steady state converged solution, the transient problem was performed. The relative total power evolution (Fig. 36 (a)) and the corresponding core average Doppler temperature (Fig. 36 (b)) predicted by CBY/SCF are compared to the predictions of other coupled codes. There it can be observed that the

global power trend predicted by CBY/SCF inside the NURESIM platform is quite similar to the one of the reference solution but it is reached with some delay. The Doppler temperature predicted starts to increase slower than the other predictions and is underestimated through the whole transient time.

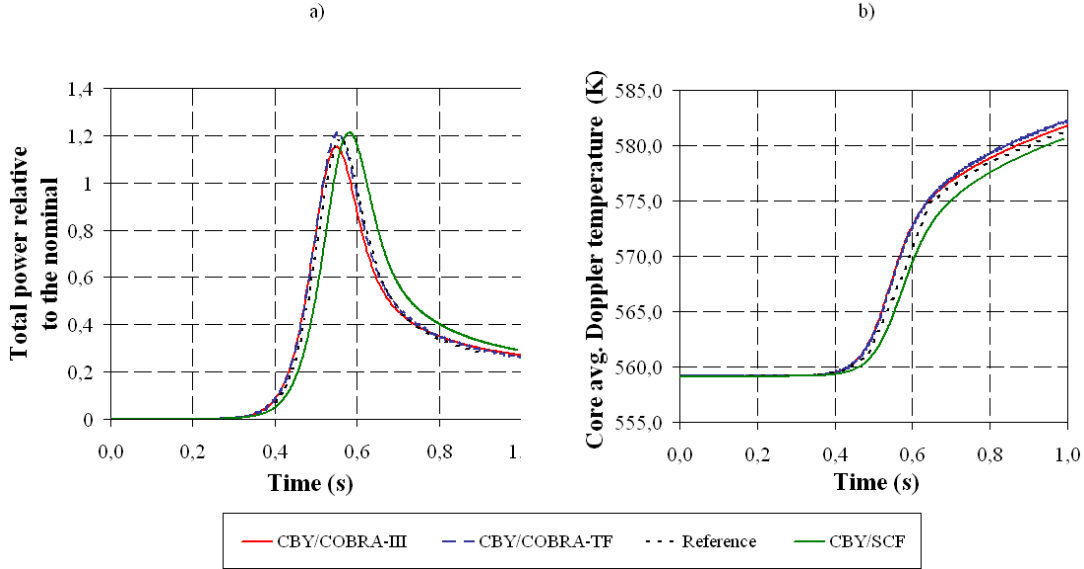


Fig. 36. Normalized power (a) and avg. Doppler temperature (b) vs. time, NEABEN benchmark.

It must be noted that the radial nodalization of the neutronic domain influences considerably the results. If only one radial neutronic node per FA is considered in the CBY/SCF simulation, the predicted power peak is lower than the one of the reference solution. Furthermore the structure of the mesh and fields management were verified using the post-processing capabilities of SALOME since the coupling is based on the mesh superposition concept.

The next Fig. 37 shows the structured mesh of CBY and SCF. This mesh is composed of non equidistant axial levels, in addition to the 157 FAs (radial) of the problem. For the coupled solution, the mesh superposition between CBY and SCF needed to be verified in order to assure that the passing of variables between the domains is correct. After using the interpolation tool (INTERP\_2\_5D) between both meshes, the final results are promising. The correspondence between them is almost 100.0%. This means that the feedback (N or TH) will pass from one field to another (e.g. from node to channel and vice versa) with almost no error. Fig. 37 (a) shows the correspondence of the N code mapping to the TH mapping. The matching between the axial and radial nodes is almost unity (red color on the scale) and the greatest difference is located at the top edge (dark blue). This difference is attributed to the numerical error encountered while positioning the edges (vertex) of each square element in space. In other words, the location of those nodes on the edge is not exact, superposition is not 100.0% and therefore there is a very small mismatch. The Fig. 37 (b) represents the correspondence of the TH code mapping to the N. In this case the correspondence is similar and almost perfect. At the end, the N to

TH and the TH to N feedback is multiplied by this correspondence. It is also seen that the N domain (Fig. 37 (a)) implements four nodes per FA to perform its N solution, and the TH domain one channel per FA.

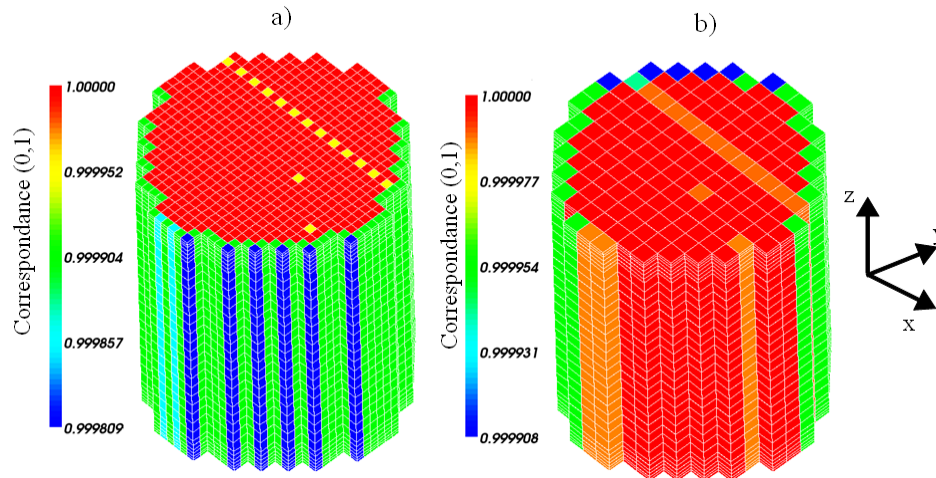


Fig. 37. MED philosophy: Mesh superposition and correspondence between the N and TH domains.

Once verified that the interpolation tool performs as required, the TH and N fields are verified. These fields representing the normalized power, Doppler temperature, moderator temperature, and moderator density are fixed picture frames at the power peak time ( $P_{\text{tot}} = 1.21$  relative to nominal at  $t = 0.58$  s) taken from the post-processor of SALOME. The  $t = 0.0$  s condition is not relevant since the transient departs from a HZP where no local disturbances are expected. Fig. 38 (a) shows a cosine shape of the power in the axial direction. The mesh refinement at the bottom and top of the core exhibits a more accurate solution and therefore, a shape change of the power distribution when moving from fine to coarse meshing elements. The 3D radial power (Fig. 38, (b)) shows a peak in the central region consistent to the predictions derived from the fact that the rod located in the centre is fully extracted.

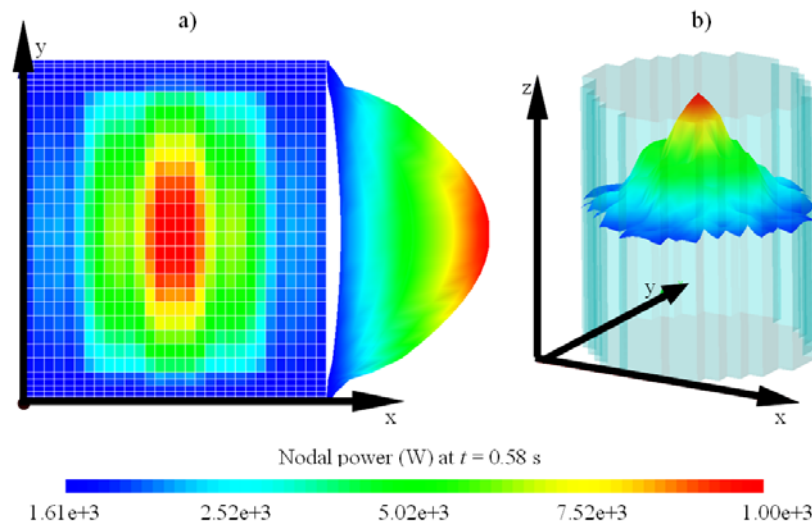


Fig. 38. Axial (a) and radial (b) power distribution making use of the SALOME post-processing capabilities.

In Fig. 39 (a) the radial distribution of the moderator temperature is shown, which agree with the radial density distribution, Fig. 39 (b). The Doppler temperature (Fig. 39 (c)) also shows consistent correspondence with the radial power (Fig. 39 (d)), where energy is concentrated in the centre of the core. Consequently, it can be concluded that the fields are properly used in SALOME, which is an important prerequisite for the correct coupling between CBY and SCF.

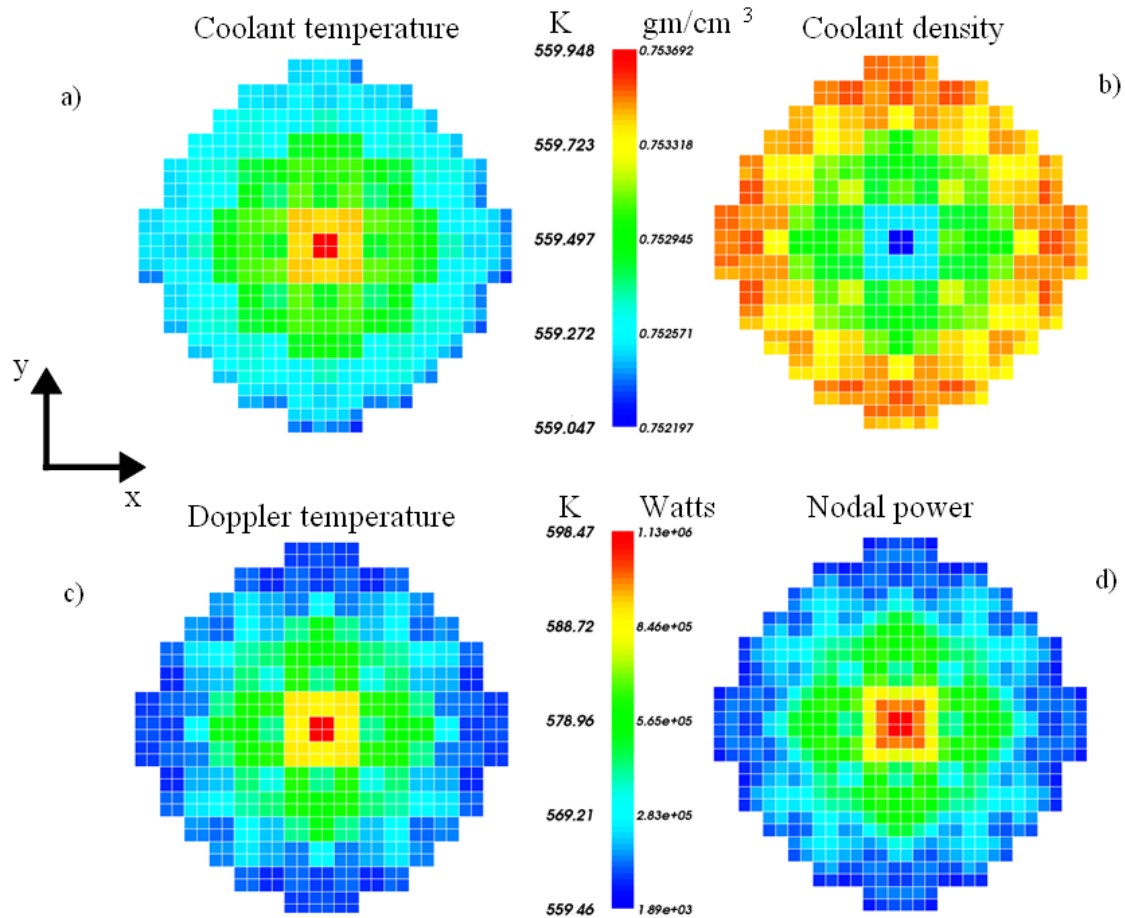


Fig. 39. Coolant temperature (a), coolant density (b), Doppler temperature (c) and total power (d) of the NEABEN benchmark at the core center and power peak time.

It is recommended to analyze the results of this benchmark together with Fig. 84 (in Appendix D). There, the online visualization capability of the NURESIM platform to simulate the transient of the NEABEN benchmark is shown.

---

---

## 7 Validation of the COBAYA3/SUBCHANFLOW coupling

Before the validation process, the verification of the implementation of SCF inside the platform was performed in Chapter 4. In addition, the coupling between the integrated codes CBY and SCF for steady state and transient scenarios was verified in Chapter 6.3. The verification and validation of the N code (CBY) inside SALOME has been realized by [Jimenez01] using benchmark problems. For the validation process of the coupled scheme CBY/SCF at nodal level, four transient benchmarks for square geometries are studied. In addition, one benchmark problem for hexagonal geometries is also investigated. Lastly, a 3D hybrid model for a PWR core is developed for the validation of the coupled N/TH hybrid scheme implemented in CBY/SCF inside the NURESIM platform. All the results presented in the following subsections were obtained with the coupled CBY/SCF code inside SALOME. Table 13 lists the international benchmarks selected for the validation purpose.

Table 13. Benchmarks used for the validation process of the coupling CBY/SCF.

<b>Benchmark – Nodal Square</b>		<b>Case</b>	<b>Type</b>	<b>Condition</b>
1	NEABN LWR core transient benchmark [Fraikin01] (Chapter 6.3)	A1	Steady State	HZP
		A1	Transient	From HZP
2	OECD/NEA and US NRC PWR MOX/UO2 core transient benchmark [Downar06]	2a	Steady State	HZP/HFP
		4a	Transient	From HZP
3	PWR Main Steam Line Break Benchmark (MSLB) [Ivanov02]	2	Steady State	HFP
		2a	Transient	From HFP
4	PWR MOX/UO2 boron dilution transient [Kli- em01/02]	Steady State		HZP
		Transient		From HZP
<b>Benchmark – Nodal Hexagonal</b>		<b>Case</b>	<b>Type</b>	<b>Condition</b>
5	KALININ-3 Coolant Transient Benchmark [Ivanov03]	3a	Steady State	HZP
		3b	Steady State	HFP
		3b	Transient	From HFP
<b>Hybrid coupling</b>		<b>Type</b>		<b>Condition</b>
6	PWR MOX/UO2 - one hybrid FA (base on [Downar06])	Steady State		$P_{tot}$ at 16.2 % from nominal

The first three benchmarks are focused on the analysis of PWR steady states and transients. The fourth benchmark represents a typical boron dilution transient, departing from a HZP state and being an appropriate test to validate the boron dilution model implemented in SCF and the transfer of boron in the

boron fields (feedback) using the peculiarities of the NURESIM platform. The fifth benchmark provides unique plant data obtained in a VVER-1000 reactor type that is very much appropriate for the validation of CBY/SCF. The last one depicts the innovative part of the coupling, where hybrid solutions are studied for a full PWR core.

In the following sections, the specifications of the benchmarks and the description of the scenarios are presented first. Based on this information, core models for CBY and SCF were developed. Subsequently the CBY/SCF coupled solutions were performed inside SALOME for square (nodal and pin base solutions) and hexagonal (nodal) geometries under steady state and/or transient conditions.

## **7.1 3D nodal simulations of PWR cores**

### **7.1.1 Validation of CBY/SCF using the OECD/NEA and US NRC PWR MOX/UO<sub>2</sub> core transient benchmark**

For the validation of CBY/SCF three of the four cases problems defined in the OECD/NEA PWR MOX/UO<sub>2</sub> benchmark were selected (the reactor core is based on the four-loop Westinghouse PWR power plant). Two cases are related to a steady state and one to a transient scenario. The benchmark is suitable for testing the coupling's predictions for a simulation which involves fast transients (rod ejection accidents, REAs) for nodal based cartesian geometries. These types of reactivity accidents lead to a sudden power excursion which could damage the integrity of a fuel rod. A sensitivity study was conducted for the temporal discretization of CBY/SCF.

This benchmark was selected for three main reasons. Firstly, after the transient the core ends in an asymmetrical radial configuration, giving rise to challenges on feedback handling. Secondly, the small neutron fraction provided by the MOX fuel elements lead to stronger transients in terms of local disturbances (challenges due to the heterogeneity of its FAs). Finally, the good agreement in the results between all the participants of the benchmark provides confidence for the error margins.

#### **7.1.1.1 Description of the cases and boundary conditions**

The benchmark selected cases for the code validation are shortly described below.

1. Case 1: The first one corresponds to a HFP steady state at nominal conditions. The TH parameters for this case are: core inlet temperature  $T_{in} = 560.0$  K, upper plenum pressure  $P_{out} = 15.5$  MPa, core thermal power  $P_{tot} = 3565.0$  MW and total core mass flow rate  $\dot{m}_{in} = 15849.4$  kg/s.

A critical boron concentration of  $B_{\text{ppm}} = 1683.6$  ppm and  $B_{\text{ppm}} = 1675.70$  ppm was used for the simulation using two energy and eight energy groups respectively.

2. Case 2: The second case corresponds to a HZP steady state condition characterized by a core thermal power of  $P_{\text{tot}} = 3565.0$  W, and coolant inlet temperature, upper plenum pressure and mass flow rate are the same as in the first case. A critical boron concentration of  $B_{\text{ppm}} = 1344.0$  ppm and  $B_{\text{ppm}} = 1336.4$  ppm was used for the simulation using two energy and eight energy groups respectively.
3. Case 3: The third case corresponds to a transient scenario (REA) defined by the following assumptions.
  - a. Initial steady state (departing case) corresponds to the HZP condition.
  - b. Ejection of a control rod located in a UO2 FA (see Fig. 40, position forty-two) within  $t = 0.1$  s occurs due to the failure of the CR driven mechanism.
  - c. The whole transient last  $t_{\text{total}} = 1.0$  s.
  - d. Different time steps were used at different periods during the transient.
  - e. The transient is guided purely by N BCs, the TH domain calculates its solution based on the N feedback (no time dependent BCs are given for SCF).

In the Fig. 40 one quarter of the PWR MOX/UO2 core with the location of the control assemblies (green triangles) can be seen. The numbers in this figure represent the identification index provided to each FA for modeling purposes. The FAs have different enrichments and burn-up states as specified in [Downar06]. The reactor core is loaded partially with weapon grade MOX fuel. For this heterogeneous core the delayed neutron fraction ( $\beta$ ) is greater due to the presence of MOX assemblies (the weapon-grade plutonium vector has a high  $^{239}\text{Pu}$  component, which has a large resonance in the thermal energy range and therefore, such plutonium is potentially more sensitive to the thermal spectrum than normal UO2 fuel types).

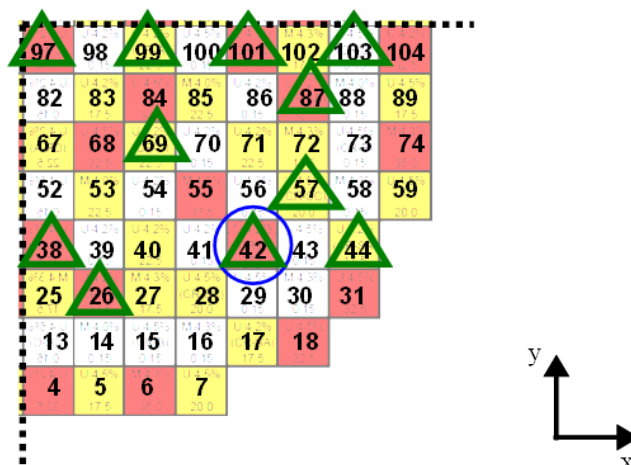


Fig. 40. Top view of the PWR MOX/UO2 benchmark (1/4 core).

### 7.1.1.2 Description of the models used and simulations

For the CBY/SCF simulations of the three cases the same spatial discretization of the core for both N and TH codes was used. The core radial discretization in CBY considers one N node per fuel assembly. In SCF, each FA is represented by one TH node (channel) but considering cross flow along all the borders to the four neighboring channels. In total 193 N and TH radial nodes are considered for the simulation. In the axial direction, the active core ( $z = 3.657$  m) is subdivided in twenty similar nodes in both the N and TH domains (even though the interpolation tool (INTERP\_2\_5D) was used). More details about the modeling of this benchmark are given in Appendix A. The first and second cases were simulated using nodal XSs for both two and eight energy groups. For the third case only two energy groups XSs were used. In CBY/SCF, the Doppler temperature is calculated according to eq. (7.1), as specified in the benchmark.

$$T_{Dopp} = 0.3T_{CL} + 0.7T_s. \quad (7.1)$$

By calculating the Doppler temperature through this approach, more weight is given to the pellet surface temperature ( $T_s$ ) compared to the pellet center line temperature to account for self-shielding, in addition to reduce statistical errors provided by the benchmarks participants. The convergence criteria used for CBY/SCF is the following:  $\epsilon_N = 1.0^{-5}$  for  $k_{eff}$  and total power, and  $\epsilon_T = 1.0^{-4}$  for the Doppler temperature, moderator density and moderator temperature. The first case (HFP) converged in seven iterations for the two energy groups simulation, and nine iterations for the eight energy groups simulation. For the second case (HZP), convergence was achieved within the first iteration using two and eight energy groups. The convergence of steady state solutions are discussed in more detail in the section which describes the TMI-1 MSLB benchmark (Chapter 7.1.2). Moreover, since specific temperature dependent thermo-physical properties for the fuel and cladding were specified in the benchmark, effort for coding these correlations was done inside SCF.

The transient CBY/SCF simulation was performed using the following time steps in CBY (master code).

1. From  $t = 0.00$  s to  $t = 0.25$  s:  $t_{step} = 0.005$  s.
2. From  $t = 0.25$  s to  $t = 0.50$  s:  $t_{step} = 0.001$  s.
3. From  $t = 0.50$  s to  $t = 1.00$  s:  $t_{step} = 0.020$  s.

The time step discretization is refined during the period of the power peak to avoid losing information due to the strong feedbacks present between two consecutive time intervals.

### 7.1.1.3 Selected results for the steady states and transient case

In the Table 14 the main results describing the core neutronic characteristics calculated by CB/SCF are compared with the ones of other codes. These results include the parameters obtained for the first case using two and eight energy groups.

Table 14. Comparison of the results for the HFP scenario of the PWR MOX/UO<sub>2</sub> benchmark.

<b>Codes involved</b>	<b>Energy groups</b>	$F_{xy}$	$F_z$	<b>A.O. %</b>	$T_{Dopp}$ (K)	<b>Boron (ppm)</b>	$T_{CL}$ (K)
PARCS (ref)	2	1.370	1.417	-10.0	835.9	1679.3	-
CBY/SCF	2	1.376	1.415	-10.14	833.4	1683.6	1811.4
CBY/COBRA-III	2	1.374	1.415	-9.62	835.1	1685.4	1814.1
CBY/COBRA-TF	2	1.378	1.416	-9.94	835.4	1682.3	1811.4
SKETCH	2	1.355	1.422	-12.2	836.4	1675.4	-
NUREC	2	1.380	1.424	-10.0	827.7	1683.3	-
PARCS (ref)	8	1.386	1.424	-9.90	836.1	1672.0	-
CBY/SCF	8	1.388	1.421	-10.04	833.5	1675.7	1833.4
CBY/COBRA-III	8	1.386	1.421	-9.54	835.3	1677.4	1836.3
CBY/COBRA-TF	8	1.391	1.422	-9.84	835.6	1674.9	1832.6

It can be stated that the neutronic parameters predicted by CBY/SCF for two and eight energy groups are close to the reference values (calculated with the code PARCS) and to the other CBY solutions coupled with COBRA-III and COBRA-TF. The maximal fuel temperature obtained by CBY/SCF differs by 2.7 K (for two energy groups) and by 2.9 K (for eight energy groups), both compared to CBY/COBRA-III. The maximum difference found in the critical boron concentration lies in the order of 4.3 ppm compared to the reference value.

In Table 15 the peaking factors predicted by CBY/SCF for the second case are compared with simulations done with PARCS for two and eight energy groups. It can be noted that CBY/SCF predicts slightly smaller values than the other solution.

Table 15. Comparison of the results for the HZP scenario of the PWR MOX/UO<sub>2</sub> benchmark.

<b>Codes involved</b>		$F_{xy}$	$F_z$
PARCS	2EG	1.748	1.490
CBY/SCF	2EG	1.740	1.489
PARCS	8EG	1.756	1.498
CBY/SCF	8EG	1.748	1.496

The results predicted by CBY/SCF for the third case (transient simulation) are compared to the results of other codes in Table 16. For this comparison, the results obtained by PARCS are the reference.

Table 16. Comparison of the results for the transient scenario of the PWR MOX/UO<sub>2</sub> benchmark.

Parameter	(reference)	CBY				
		PARCS	SCF	COBRA-III	COBRA-TF	CORETRAN
Power peak	%	142.2	150.8	141.7	143.3	166.2
Peak time	s	0.342	0.350	0.340	0.340	0.33
Max. Reactivity	\$	1.122	1.092	1.093	1.093	1.079
$T_{Dopp}(t = 1.0 \text{ s})$	K	581.95	582.45	582.25	583.35	585.85

It can be seen that the CBY/SCF results are in good agreement with the ones of the reference solution and other codes. In Fig. 41 the evolution of selected parameters predicted by CBY/SCF and other codes for the REA are compared to each other. In addition, for illustrating purpose the position of the bottom part of the CR to be extracted is plotted in Fig. 41 (a). An additional graph plotting the core average coolant temperature evolution is given in Appendix C (Fig. 79).

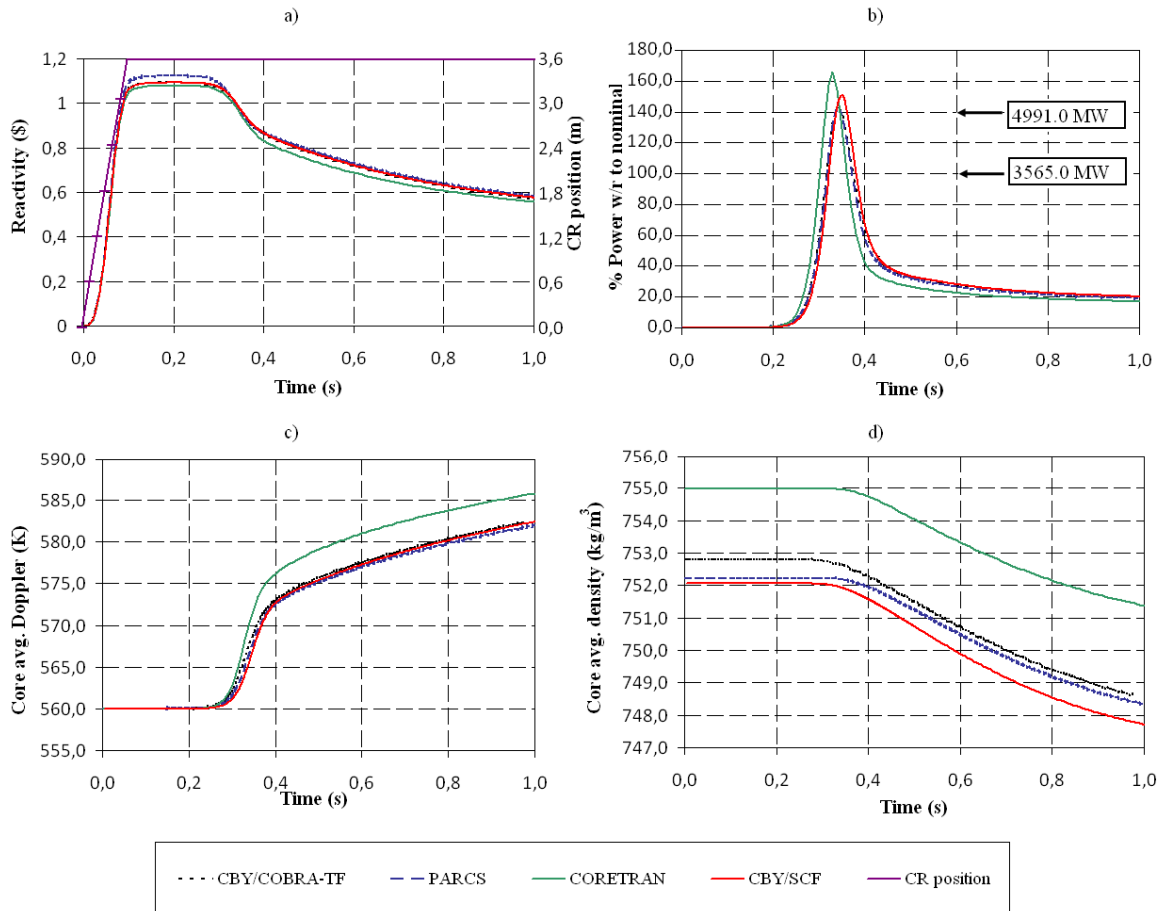


Fig. 41. Reactivity and CR position (a), total power (b), Doppler temperature (c) and moderator density (d) vs. time.

The ejection of the CR (at  $t = 0.1$  s) introduces a positive reactivity above  $\rho = \$1.0$  as illustrated in Fig. 41 (a), making the reactor critical during the beginning of the transient. A significant power increase (peak) is expected after the rod ejection with some delay after the full extraction. Strong feedbacks are expected during the peak (the increase in the  $^{238}\text{U}$  absorption XS when moving from the HZP to a higher power level). This super prompt-critical transient reaches a power peak of 150.8% with respect to nominal power of  $P_{\text{tot}} = 3565.0$  MW at  $t = 0.35$  s as seen in Fig. 41 (b). Later on the power decreases rapidly for a short period of time thanks to the neutron capture in  $^{238}\text{U}$  (Doppler effect). From  $t = 0.35$  s onwards, the power evolution is determined by both the evolution of the Doppler temperature (Fig. 41 (c)) and coolant density (Fig. 41 (d)), which its decrease at  $t = 0.35$  s contributes also to the power reduction. The asymptotic power decay after the burst ( $P_{\text{ab}}$ ) is produced by the source multiplication of delayed neutrons. This  $P_{\text{ab}}$  is larger than the initial power, causing a further increase in the fuel Doppler temperature and a corresponding decrease in the reactivity due to the negative temperature coefficient.

The temporal scheme applied has been optimal for the coupling inside the NURESIM platform; however, a high sensitivity of the OS scheme for different time steps is noticed. Due to this, a parametric study was performed with CBY/SCF to investigate the dependency of the REA simulation from different time steps in CBY. For this study six time steps have been analyzed, from  $t_{\text{step}} = 0.001$  s to  $t_{\text{step}} = 0.007$  s. The simulation time for these models was reduced from  $t = 1.0$  s to  $t = 0.4$  s since the investigation was limited to observe the evolution of the power peak in the range of  $t = 0.345$  s. In Fig. 42, the CBY predictions of the power peak using different time steps is compared to the solution of other codes for the REA.

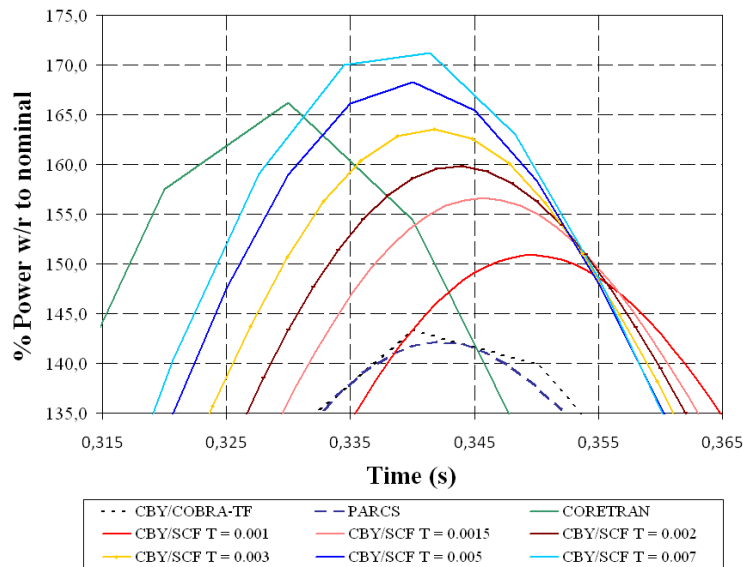


Fig. 42. Time step sensitivity analysis for the PWR MOX/UO2 REA benchmark.

Based on this investigation it can be concluded that simulations done with a time step of  $t = 0.001$  s predicts the closest peak power to the reference solution. By implementing a time step of  $t = 0.005$  s in the CBY/SCF simulation, the predicted power peak deviates from the reference by 18.6%.

In Table 17 the predicted power peak magnitude (in % relative to the nominal power), the time at which the power peak appears, as well as the total computational time to reach  $t = 0.4$  s of the simulation, are shown for the six different time steps used.

Table 17. Sensitivity related to different time steps for the PWR MOX/UO2 benchmark.

<b>Time step (s)</b>	<b>Power peak (% relative to nominal)</b>	<b>Peak time (s)</b>	<b>Simulation time (to <math>t = 0.4</math> s of transient)</b>
0.0070	171.2	0.341	6.0 min 58.0 s
0.0050	168.3	0.340	7.0 min 34.0 s
0.0030	163.6	0.342	9.0 min 23.0 s
0.0020	159.8	0.344	12.0 min 07.0 s
0.0015	156.6	0.346	14.0 min 38.0 s
0.0010	150.8	0.350	16.0 min 32.0 s

Based on these studies, the following conclusions can be drawn:

1. A time step reduction leads to a reduction of the power peak and,
2. a time step reduction leads to a delay of the power peak (the maximum power comes later during the transient).

It has to be noted that the fact of delayed neutrons emission ranging from few milliseconds to minutes is important for the core behavior. In addition, the time for the rod ejection is also critical for this analysis. A fast ejection requires extra refinement of the time step during the peak time. The Doppler feedback comes faster for small time steps since the reactivity decreases a couple milliseconds before (compared to larger time steps) due to the fact that the full CR extraction is accurately managed.

## 7.1.2 Validation of CBY/SCF using the PWR Main Steam Line Break benchmark

The OECD/NEA-US/NRC PWR Main Steam-Line Break (MSLB) benchmark was chosen not only for the purpose of validating the CBY/SCF coupling scheme inside the NURESIM platform, but also for the purpose of demonstration (corroboration of the proper implementation and programming of SALOME's online visualization capabilities). In addition, the benchmark provides a heterogeneous scenario in terms of feedback handling for testing the interpolation tool of SALOME. From the MSLB benchmark, a code-to-code comparison of results is done for steady state and transient scenarios.

### 7.1.2.1 Description of the scenario and boundary conditions

This PWR reactor is a two loop plant with one-through steam generator. It is assumed that the main steam line of loop-A breaks upstream of the main steam isolation valve (MSIV). After the break, a sudden depressurization of the secondary side of the affected loop takes place, leading to a flashing and boil-off of the water inventory. Under these conditions, an increased heat transfer over the affected steam generator is established leading to the under-cooling of the corresponding primary coolant of loop-A. As a consequence of it, half of the core experiences a stronger under-cooling than the other half, resulting in a strong positive reactivity insertion despite SCRAM. This benchmark is very much appropriate to test the 3D modeling with respect to a homogeneous axial discretization. The MSLB scenario consists on the following main events.

1. Break in the main steam line of loop-A. This causes a release of vapor through the break leading to a strong depressurization of the secondary side and cool down of the water in the primary loop.
2. Reactor SCRAM.
3. Emptying of the affected steam generator in the secondary side.

It is assumed that the MSLB occurs when the TMI-1 core is being operated at HFP, end of cycle (EOC) conditions and the equilibrium of the Xe and Sm concentrations. In addition, it is assumed that the most reactivity worth CR stuck-out when SCRAM initiates and stays in the fully extracted position, leaving the core in all rods in (ARI) -1 state. The configuration of the reactor core with the eight CR groups and indication of loop-A and B are shown in Fig. 43. For the critical steady state reactor conditions, the CR banks one to six are completely withdrawn (wd) while the bank group number seven is 90.0% wd from the bottom of the lower reflector. The CR bank number eight (encircled in red) is extracted 100.0% and corresponds to the one which will remain in the stuck position when SCRAM is activated.

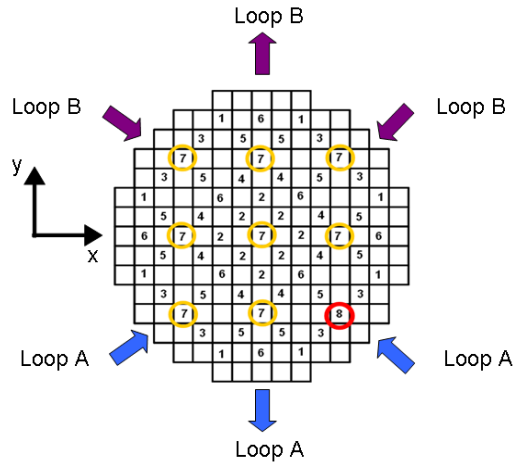


Fig. 43. Control rod position (localization) in the core corresponding to the MSLB benchmark.

In Table 18 the operating conditions used in CBY/SCF for the analysis of the HFP steady state of the TMI-1 core are summarized.

Table 18. Initial operating conditions corresponding to the HFP state of the MSLB benchmark.

Parameter		Value
Inlet temperature	K	562.9
Core nominal power	MW	2772.0
Outlet pressure	MPa	15.72
Core mass flow rate	kg/s	16052.4
Boron concentration	ppm	5.0

The simulation, which consists in a  $t_{\text{total}} = 100.0$  s lasting transient, departs from a HFP state and is guided by time dependent heterogeneous TH BCs (mass flow rate, coolant temperature and core pressure) at the core inlet and outlet (provided by the benchmark team and calculated from an integral TMI-1 plant simulation performed with TRAC-PF1/NEM). The core is divided in eighteen sections (each with specific TH inlet BCs) that map to the channels modeled in SCF and therefore, specific inlet conditions are obtained for each channel (FA) at each time interval. In Fig. 44 the time dependent BCs are shown, where in Fig. 44 (a) and (c) the resulting evolution of the mass flow rate and the coolant temperature connected to the two core halves are exhibited.

The asymmetrical core behavior which occurs during the MSLB evolution can be clearly observed (strong space-time effects). The curves in Fig. 44 (a) and (c) build two groups of lines, one representing the affected loop and the other the intact loop. The depressurization of the primary side caused by the cool-down can be seen in Fig. 44 (d). As a consequence of the break, the steam flow rate in the broken steam generator increases, improving the heat transfer and lowering the core average coolant

temperature as shown in Fig. 44 (b). In fact, this figure is the result of the transient simulation, where the core average coolant temperature is calculated by CBY/SCF. It is seen that the calculated core average coolant temperature lies between the BCs imposed for the affected and intact loops. Because of the difference in temperature between the two loops (affected and intact) a power tilt is expected (attributed to the negative moderator temperature coefficient).

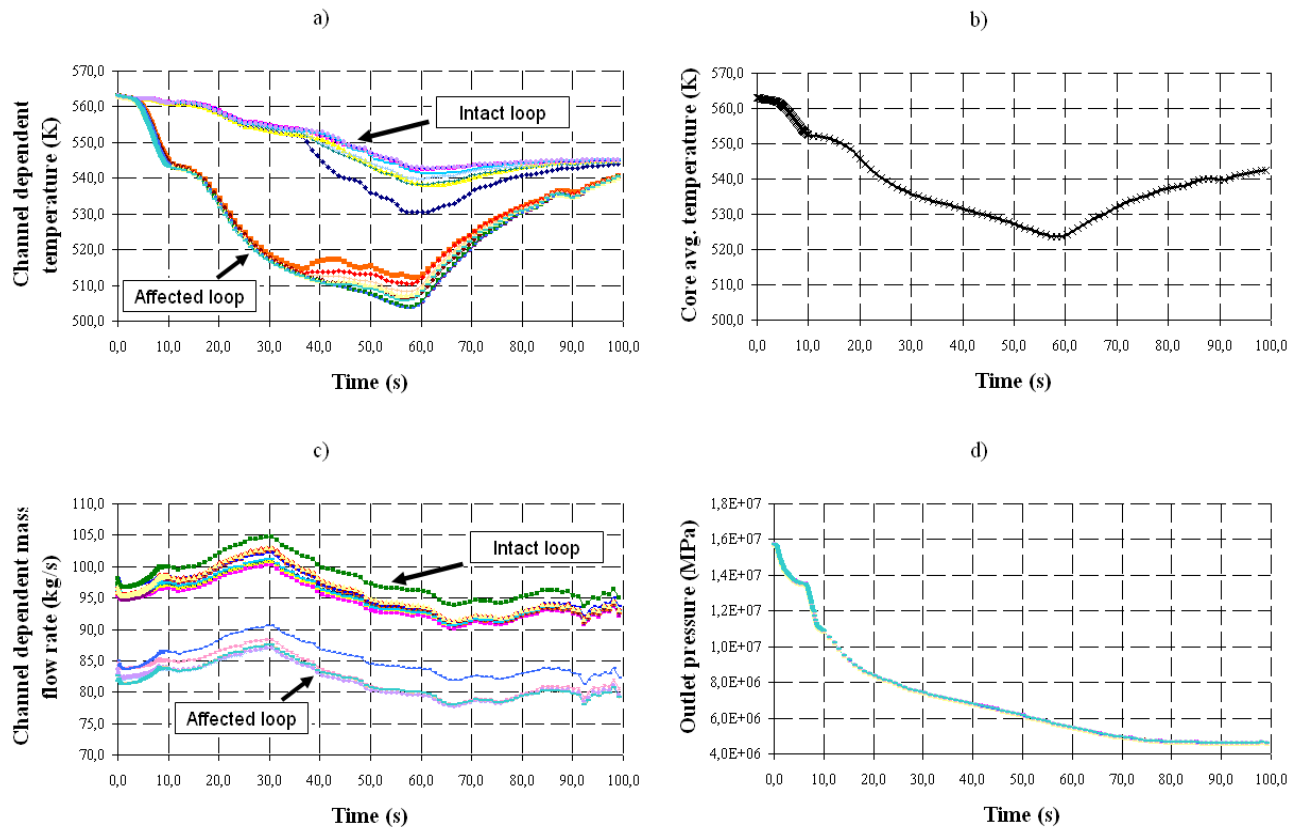


Fig. 44. TH BCs associated to the TMI-1 MSLB benchmark: inlet temperature (a), calculated core avg. coolant temperature (b), inlet mass flow rate (c) and core outlet pressure (d).

### 7.1.2.2 Description of the models used and simulations

For the simulation of the MSLB, a N core model for CBY and a TH core model for SCF were developed. The N model consist of 177 computational nodes i.e. one node per fuel assembly and two axial reflector nodes (bottom and top). The core is subdivided in twenty-four non equidistant axial levels. The importance of this non equidistant axial discretization is crucial for the N and TH models since the core is highly heterogeneous along its active height. Special emphasis has been directed towards different axial compositions which could yield to misleading results in case of neglect. The nodal XSs corresponding to two energy groups are collected in two libraries: one rodded (FA with absorber rods) and one unrodded (FA without absorber rod) in the NEMTAB format. The NEMTAB files were

provided by the benchmark team and they include the homogenized nodal XSs in dependence of the state variables e.g. fuel temperature and coolant density. The XSs of the radial and axial reflectors are also provided in the look-up tables. The Doppler temperature is calculated according to eq. (7.1).

The TH core model consists of 177 channels subdivided in twenty-four non equidistant axial levels. The important aspect while modeling a reactor core with a sub-channel code is the fact that the cross flow between the fuel assemblies can be taken into account based on the physical models implemented in the code, leading to a more realistic description of the TH phenomena in the within the core. A cross flow resistance factor of 0.7 was used in the SCF model. The fuel rod was discretized employing eight radial nodes, two for the cladding and six for the pellet. Moreover, since specific temperature dependent thermo-physical properties for the fuel and cladding were specified in the benchmark, effort for coding these correlations was done inside SCF, which are different from the ones used for the PWR MOX/UO<sub>2</sub> benchmark.

First, a steady state simulation of the core is performed just before the postulated transient. After the successful prediction of the stationary core parameters with CBY/SCF, the transient phase is analyzed using the time dependent BCs derived from the benchmark's specifications for the second exercise. Two steady state cases were analyzed and defined as follows:

1. Case 1: A HFP steady state condition with heterogeneous inlet BCs for the TH domain which are based on the transient BCs at  $t = 0.0$  s. This means that each TH channel is provided with a corresponding coolant temperature, pressure and mass flow rate. This steady state is the departing condition for the transient simulation. Its operating conditions correspond to the ones mentioned in Table 18.
2. Case 2: A HFP steady state condition based on Table 18 with homogeneous inlet BCs.

The convergence criteria used for CBY/SCF is the following:  $\epsilon_N = 1.0^{-5}$  for  $k_{\text{eff}}$  and total power, and  $\epsilon_T = 1.0^{-5}$  for the Doppler temperature, moderator density and moderator temperature. The heterogeneous case converged in ten iterations, differently from the eight iterations needed by the homogeneous case.

The transient CBY/SCF simulation was performed using the following time steps in the CBY code (the third period corresponds to the one where SCRAM is expected to occur).

- |   |  |
|---|--|
| 1) From $t = 0.00$ s to $t = 6.65$ s : $t_{\text{step}} = 0.05$ s | 4) From $t = 8.91$ s to $t = 15.00$ s : $t_{\text{step}} = 0.05$ s |
| 2) From $t = 6.65$ s to $t = 8.68$ s : $t_{\text{step}} = 0.04$ s | 5) From $t = 15.0$ s to $t = 50.00$ s : $t_{\text{step}} = 0.20$ s |
| 3) From $t = 8.68$ s to $t = 8.91$ s : $t_{\text{step}} = 0.02$ s | 6) From $t = 50.0$ s to $t = 100.0$ s : $t_{\text{step}} = 0.50$ s |

### 7.1.2.3 Selected results for the steady states and transient cases

In Fig. 45 the evolution of different convergence parameters as a function of iteration number is shown. This convergence evolution corresponds to the state with heterogeneous BCs (first case). It must be noted that even when the N parameter ( $k_{\text{eff}}$ ) has converged in eight iterations, the TH parameter ( $T_{\text{Dopp}}$ ) requires two more iteration to converge. Strict verification of the TH parameters is as important as the verification of the N parameters for convergence check and consequently, for the TMI-1 benchmark the criteria satisfies  $\varepsilon_N = \varepsilon_T$ . The Fig. 45 also shows the typical graphical interface of SALOME when doing an online study of convergence applied to the heterogeneous steady state. As mentioned at the beginning of Chapter 7.1.2, an important point to verify is the proper programming of the sub-routines in charge of the online visualization capability of SALOME. The screen shot exemplified through Fig. 45 has two objectives:

1. Prove that the online visualization of parameters could be properly handle and observed on the computer screen (extensive programming work done for this purpose).
2. Show the convergence evolution of selected parameters as a function of iteration number.

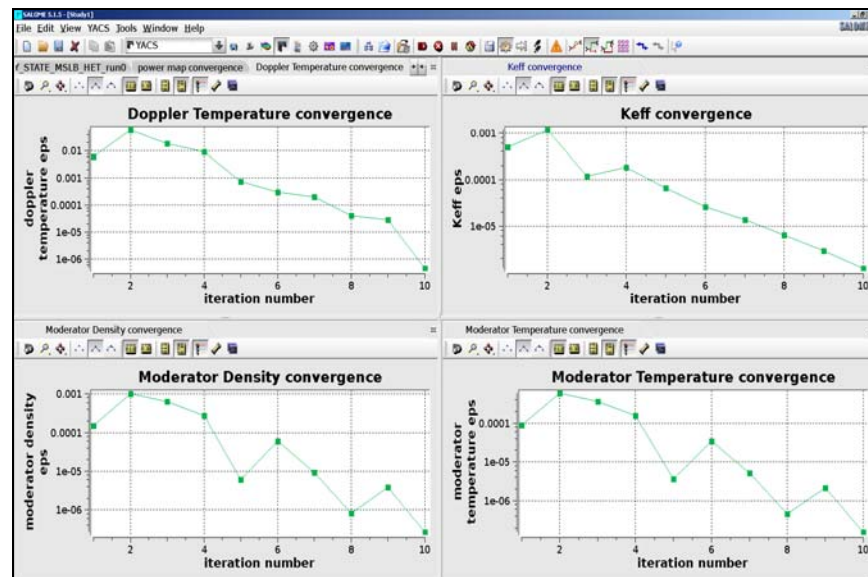


Fig. 45. Steady state convergence for the heterogeneous case of the MSLB benchmark.

Selected results of the converged CBY/SCF solution of the first case (heterogeneous inlet BCs) are given in Table 19. There, selected core parameters such as  $k_{\text{eff}}$ ,  $F_{xy}$ ,  $F_z$ , A.O.,  $T_{\text{Dopp}}$  and  $T_{\text{CL}}$  predicted by CBY/SCF are compared to the predictions of other codes. The reference solution represents the avg. value of the predictions of three benchmark participants (CEA, HZDR (former FZR) and KAERI). It can be observed there that the  $k_{\text{eff}}$  deviation (calculated by CBY/SCF) from the reference

solution amounts for 28.0 pcm while for  $F_{xy}$  and  $F_z$  it is about 0.25% and 0.56% respectively. The CBY/SCF solution marked with \* ('star') was obtained using the interpolation tool. The other CBY/SCF solution is based on the direct mapping between the N and TH domains using external files. For this purpose, substantial work has been done to allow the user to select either the use of the interpolation tool or not. Even though the coupling is still based on the feedback exchange through fields (meshes and supports) the nodal/channel values are passed directly from one field array (e.g. N) to another (e.g. TH). This fact will be especially important for modeling the hexagonal core benchmark presented in Chapter 7.2. By using this direct mapping procedure spatial discrepancies are avoided. The solutions are very similar to each other and the usage of the interpolation tool for square geometries provides consistent results.

Table 19. Steady state HFP results for the heterogeneous case of the MSLB benchmark.

Parameter	Reference	CBY /SCF	CBY /SCF (*)	CBY /COBRA-III
$k_{\text{eff}}$	1.00476	1.00504	1.00504	1.00569
$F_z$	1.0660	1.072	1.072	1.065
$F_{xy}$	1.3334	1.330	1.330	1.3312
A.O. %	-1.356	-1.906	-1.904	-1.460
$T_{\text{Dopp}}$ K	-----	803.4	803.4	803.3
$T_{\text{CL}}$ K	-----	1407.8	1408.0	1421.3

In Table 20 the CBY/SCF results calculated for the second case (homogeneous inlet BCs) are compared to the solution of the reference simulation and to the CBY/COBRA-III solution. The CBY/SCF predictions are close to the values obtained by the other codes. Differences compared to CBY/COBRA-III may be caused by the use of different water properties tables and different modeling of the TH domains. The type of coupling scheme implemented between the codes could also affect the solutions.

Table 20. Steady state HFP results for the homogeneous case of the MSLB benchmark.

Parameter	Reference	CBY/SCF	CBY /COBRA-III
$k_{\text{eff}}$	1.00463	1.00483	1.00474
$F_z$	1.0696	1.080	1.081
$F_{xy}$	1.32903	1.323	1.327
A.O. %	-1.99	-2.40	-2.51
$T_{\text{Dopp}}$ K	-----	803.6	804.15
$T_{\text{CL}}$ K	-----	1411.4	1414.5

The simulation of the MSLB transient phase using the time dependent BCs given in Fig. 44 (a), (c) and (d) was performed with CBY/SCF after a converged steady state solution for the first case was achieved. The plots in Fig. 46 show the predictions of CBY/SCF for the transient. The plots in Fig. 46 (a), (c) and (e) illustrate the comparison of the total power (MW), core average  $T_{\text{Dopp}}$  (K) and core average  $D_{\text{mod}}$  ( $\text{kg}/\text{m}^3$ ) calculated by CBY/SCF with the results of other codes. The plot in Fig. 46 (f) represents the total power as it is shown by the online visualization capability of SALOME. At a first glance it can be seen that the simulation done with CBY/SCF is qualitatively following very well the trend of the reference solution and of the other codes. Merely, the Doppler temperature is slightly under predicted by CBY/SCF, as seen in Fig. 46 (d).

Due to the break in the steam line the secondary side of the affected steam generator depressurizes and boil-off, improving the heat transfer from the primary to the secondary side and hence lowering the average coolant inlet temperature of this loop (effect reflected in the increase of the core average moderator density, Fig. 46 (e)). As the coolant temperature decreases the power increases due to the negative moderator temperature coefficient ( $\sim 50.0 \text{ pcm}/^\circ\text{C}$ ). The core average Doppler temperature then evolves as expected with an initial difference of  $\Delta T = 23.4 \text{ K}$  with respect to the reference and probably due to the discrepancies in the modeling of the initial heterogeneous steady state. Once the SCRAM set point is reached (point encircled in Fig. 46 (f)), the reactor is shutdown as consequence of the SCRAM. Afterwards, the core inlet temperature decrease until the steam generator in the secondary side is empty ( $t = 60.0 \text{ s}$ ). From that point on the primary coolant average temperature starts to increase due to deteriorated heat transfer to the secondary side (empty steam generator). During this period a positive reactivity is inserted in the core. The core reactivity increases continuously, reaching a maximum value when the affected steam generator in the secondary side is empty.

The maximum reactivity predicted by CBY/SCF at the power peak ( $P_{\text{tot}} = 3260.0 \text{ MW}$ ) is  $\rho = \$0.276$  at around  $t = 6.65 \text{ s}$ . Even though the reactor was shutdown, the total power starts to slowly increase reaching a maximum value at around  $t = 60.0 \text{ s}$ . At this point the total power decreases continuously, leaving as the only energy source the decay heat. This effect is seen in Fig. 80 (in the Appendix C), where additional graphs are shown for supporting the presented statements.

The only point where the coupled solution shows deviation from the mean is observed at  $t = 60.0 \text{ s}$ . At this point return to power condition is almost established, however, it vanishes with time. CBY/SCF underestimates at this point the core Doppler temperature, reflected in the power evolution. As seen, the only means to limit the consequences of a possible accident are through the automatic stop of the reactor (SCRAM), boron injection into the primary circuit and by isolating the steam generators to avoid extra cooling of the moderator (only the affected line contribute to this cooling phenomenon). It is worth it to mention that the differences found in the Doppler temperature and therefore total power

during the beginning of the transient ( $t = 0.0$  s) as seen in Fig. 46 (b) and (d), are attributed to the models used for each coupled code for the transient scenario, to the temporal scheme followed by each of them, but mostly, to the N and TH characteristics of the departing steady state affected by e.g. the level of convergence used.

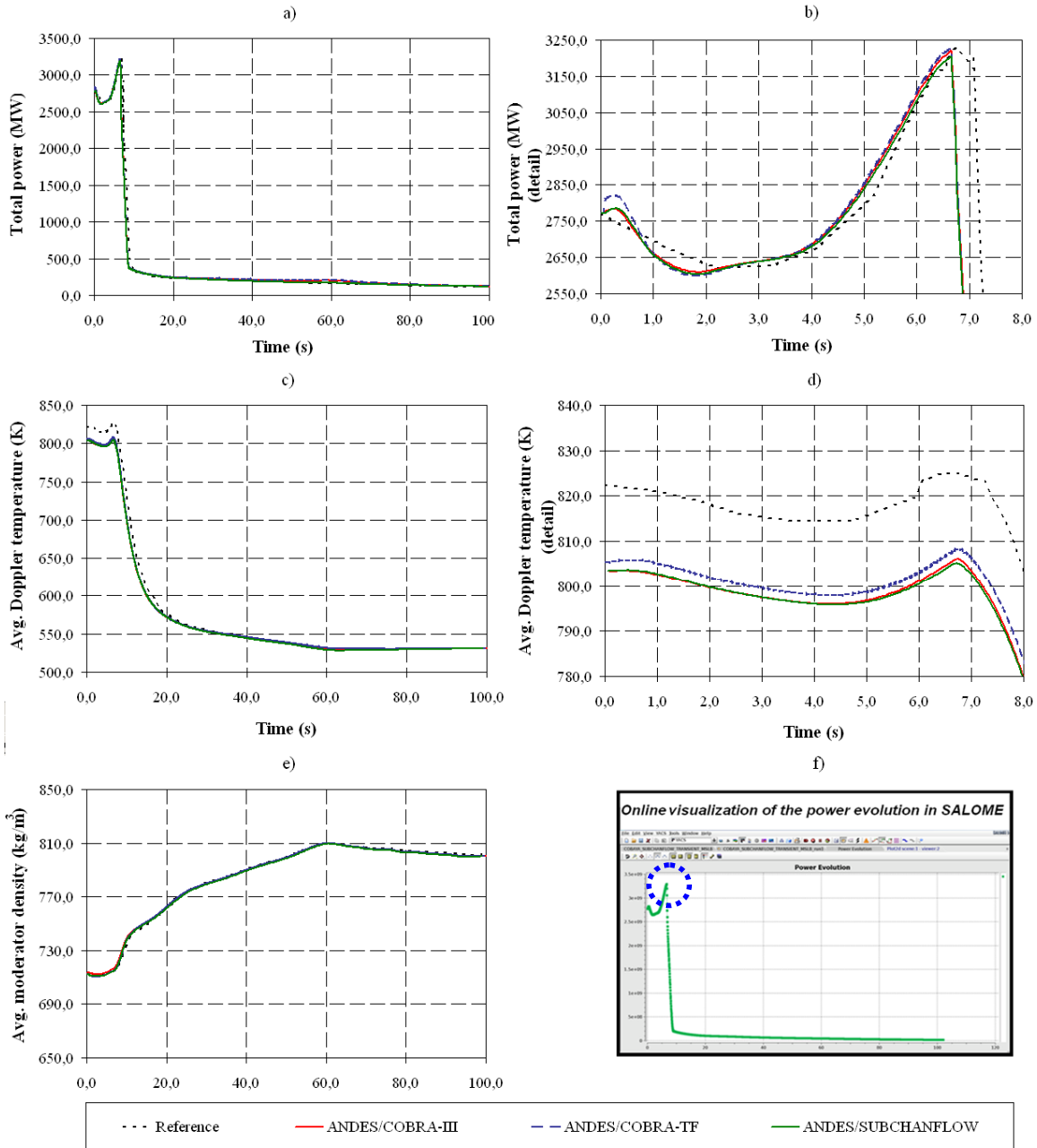


Fig. 46. Total power evolution (a), total power detail at SCRAM (b), core avg. Doppler temperature (c), core avg. Doppler temperature detail (d), core avg. moderator density (e) and online visualization of the total power evolution (f) for the MSLB benchmark.

### 7.1.3 Validation of CBY/SCF by using PWR MOX/UO<sub>2</sub> boron dilution problems

The objective of the analysis of a boron dilution scenario in a PWR is to check the capability of the boron transport model implemented in SCF to simulate these types of transients and to verify the exchange of information regarding the boron concentration between CBY and SCF during coupled CBY/SCF simulations. Additional effort has been dedicated to a proper handling of the boron concentration fields inside SALOME (use of the fields and their feedback) leading to additional challenges for the coupling scheme.

Two boron dilution problems were selected to be analyzed with CBY/SCF [Calleja02]:

Problem 1: Consists on a homogeneous boron dilution in a 3x3 mini-core.

Problem 2: Consists on a heterogeneous boron dilution in a whole PWR MOX/UO<sub>2</sub> core.

The geometrical parameters, material data, operating conditions and main TH parameters for the two boron dilution problems to be investigated are based on the PWR MOX/UO<sub>2</sub> core described in the Chapter 7.1.1 (where the only difference lies on the variation of the boron concentration as a function of time on the TH side). The travelling of a boron-free slug of variable size through the core lead to an insertion of positive reactivity followed by sharp local power peaks accompanied by significant power asymmetries. Hence the power distribution shows significant power distortions. From the safety point of view, it is important to evaluate if the local power peaks may cause local boiling of the coolant leading to DNB. Hereafter, the two boron dilution problems are presented and analyzed.

#### 7.1.3.1 Problem 1: Homogeneous boron dilution in a 3x3 mini-core

For the homogeneous boron dilution problem, it is assumed that the mini-core is at critical HZP conditions and a boron-free slug has been accumulated in the primary piping system before the main coolant pump. At certain time, the main coolant pumps are switched on and the nominal mass flow rate is reached within few seconds. Under these conditions, the boron-free slug is transported to the down-comer and from there to the core entrances. As consequence of the mixing, a coolant volume with reduced boron concentration will reach the core inlet homogeneously within the FAs.

##### 7.1.3.1.1 Description of the first problem and boundary conditions

The homogeneous boron dilution simulations selected (steady state and transient) for the validation of the boron transport model implemented in SCF are shortly described below.

1. Steady state: This first simulation is characterized by a HZP state. The TH parameters and CR position are mentioned in Table 21.

Table 21. Initial conditions (HZP) applied to the 3x3 mini-core boron dilution problem.

Parameter			Value		
Inlet temperature	K	560.0	Core mass flow rate	kg/s	739.08
Core power	W	1.0	Initial boron concentration	ppm	639.2
Outlet pressure	MPa	15.4	Initial CR position		ARO

2. Transient: This second simulation departs from the previously converge steady state, and its initial operating conditions are the same as the ones mentioned in Table 21.

For the temporal analysis of the mini-core, the main TH parameters characterizing a whole core were scaled down (based on [Kliem02], where an in-depth study of a boron dilution is analyzed) e.g. the volume of the boron-free slug to get prompt criticality is estimated to be  $V = 0.932 \text{ m}^3$ . The total transient time is establish to be  $t_{\text{total}} = 25.0 \text{ s}$  and the mini-core departs from a critical condition at HZP ( $k_{\text{eff}} = 1.0$ ). The BCs that guide the transient are given in the TH domain. In Table 22 is shown that the boron concentration is defined for each FA at selected times during the transient. It is also concluded though the analysis of the information given in this table that since all the FAs have the same boron concentration, a homogeneous boron dilution is expected. For the transient analysis it is assumed that the calculation starts just before the deborated coolant reaches the core inlet. At this point the pump flow rate is already at quasi steady sate conditions, leading to the assumption of stationary flow. During the transient the core inlet flow rate, coolant temperature and pressure remain constant.

Table 22. Boron concentration defined for each FA at selected times during the transient for the boron dilution mini-core scenario.

Fuel assembly	Time (s)	Boron concentration (ppm)
1 – 9	0.0	639.25
1 – 9.	1.0	639.25
1 – 9	11.0	435.84
1 – 9	23.0	639.25
1 – 9	25.0	639.25

Is advisable to analyze Table 22 together with Fig. 48 (a), where the core average boron concentration predicted with CBY/SCF and CBY/FLICA4 is shown.

### 7.1.3.1.2 Description of the models and simulations

For the simulation of this problem, N and TH models of the mini-core were developed for CBY and SCF. These models are shortly described hereafter.

The N domain is divided in twenty equidistant nodes in the axial direction, in addition to one node per FA radially. The XSs used by CBY correspond to a two energy groups library generated with the lattice code HELIOS [Beckert01]. Zero flux BCs were applied in the radial and axial direction. In the N side, no CR movement is expected and therefore, the transient is guided purely by TH BCs. The Doppler temperature is calculated according to eq. (7.1).

For the TH, the radial and axial discretization is similar to the N one described in the previous paragraph. The time dependent boron concentration is defined for each FA, which is fixed in the TH input by the use of tables. Moreover, a factor of 0.7 was used for the cross flow between FAs, in addition to a discretization of the fuel rod in eight nodes (two for the cladding and six for the fuel pellet). Specific temperature dependent thermo-physical properties for the fuel and cladding were specified in the benchmark.

Using the models for CBY and SCF described above, the homogeneous boron dilution problem was investigated with CBY/SCF. First of all a steady state simulation is performed. Later on, the transient is calculated with the BCs given in Table 22. The convergence criteria used for the CBY/SCF steady state investigation is the following:  $\varepsilon_N = 1.0^{-5}$  for  $k_{\text{eff}}$  and total power, and  $\varepsilon_T = 1.0^{-4}$  for the Doppler temperature, moderator density and moderator temperature. The CBY/SCF steady state simulation of the critical HZP core state converged after the first iteration.

The description of the boron transport in a reactor core is very challenging for TH codes and hence an appropriate time steps needs to be selected to get physical results and to minimize numerical diffusion. Exploring investigations have shown that even large time steps of  $t_{\text{step}} = 0.01$  s respect the Courant limit (CFL = 0.046). Different axial discretizations for an inlet velocity per channel of  $v_{\text{in}} = 4.61$  m/s were studied to find out the optimal cell size. Based on these studies an axial mesh size of 0.182 cm width was identified as the most suitable for the analysis of boron dilution transients. For the transient CBY/SCF analysis of the mini-core a fixed  $t_{\text{step}} = 0.005$  s was used in both domains.

### 7.1.3.1.3 Selected results for the steady state and transient cases

The CBY/SCF results for the boron dilution mini-core problem are compared to the reference solution, which was obtained with CBY/FLICA4 (the models for this reference solution were created as part of this dissertation; in addition, the simulation was done inside SALOME). In Table 23 selected parameters predicted by CBY/SCF are compared to the ones calculated by CBY/FLICA4. The core parameters predicted by both coupled codes are very close to each other.

Table 23. Selected parameters of the HZP steady state boron dilution mini-core exercise.

Code	$F_z$	$F_{xy}$	A.O. %
CBY/SCF	1.493	1.713	-0.079
CBY/FLICA4	1.497	1.713	-0.089

The transient CBY/SCF simulation was performed after the converged steady state calculation. In Fig. 47 and Fig. 48 selected parameters predicted for the mini-core during the boron dilution transient scenario are plotted. The total power (Fig. 47 (a)), fuel temperature and reactivity (Fig. 47 (b)), boron concentration evolution (Fig. 48 (a)) and moderator temperature and density (Fig. 48 (b)) are shown there. The relatively fast decrease of the core average boron concentration causes a power increase leading to a super-prompt critical state few seconds after the transient started. At around 6.59 s the highest reactivity of  $\rho = \$1.081$  is reached. The energy deposited in the fuel initiates a sharp increase of the fuel temperature. The rapid power increase (maximal power of  $P_{tot} = 329.0$  MW at  $t = 6.69$  s) is stopped by the negative Doppler and coolant temperature reactivity coefficients (at this stage  $(396.5 \text{ pcm}) > 0.9 \beta > (0.9)(417.26)$ ). The maximum cladding temperature is consistent to the Doppler, reaching a value of 604.8 K and well below its safety limit of 1477.15 K. When the boron concentration reaches its minimal value at around  $t = 11.4$  s, the power reaches a second moderate peak. Afterwards it starts continuously to decrease like the reactivity.

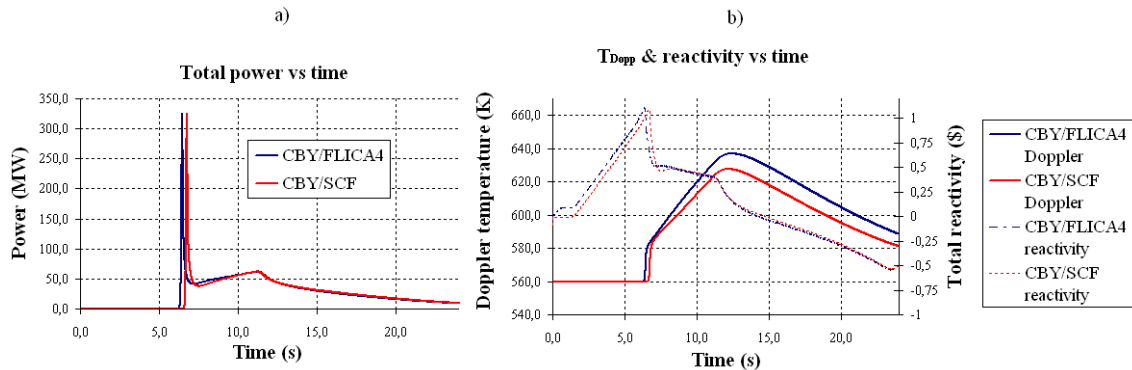


Fig. 47. Total power (a), and Doppler temperature and reactivity (b) evolution for the mini-core.

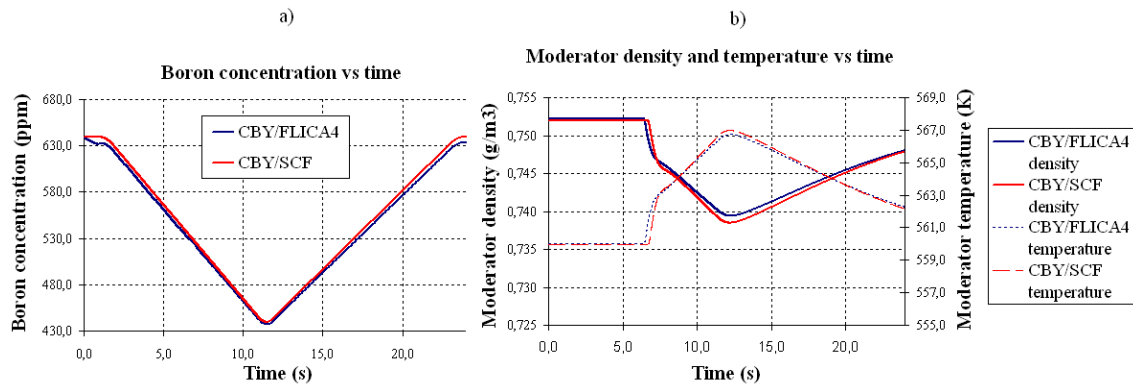


Fig. 48. Boron concentration (a), and moderator density and temperature (b) evolution for the mini-core.

Sensitivity studies were carried out to investigate the influence of the time step on the global parameters related to the mini-core. The predicted power peak difference is about 5.6 MW (1.7%) bigger between two CBY/SCF simulations using a time step of  $t_{\text{step}} = 0.005$  s, instead of  $t_{\text{step}} = 0.001$  s. But it must be kept in mind that a CBY/SCF simulation using a  $t_{\text{step}} = 0.005$  s lasts 7.1 hours while using a  $t_{\text{step}} = 0.001$  s lasts 8.4 hours. As the time step decreases the power peak is reduced (in magnitude) and shifted to the right relative to a power vs. time plot. Nevertheless a stability region is found for values of the time step in the region of  $t_{\text{step}} = 0.002$  s. For this issue the N time scale plays a stronger effect compared to the one of the TH scale since delay neutrons are emitted with a wide range of time scales (as mentioned in Chapter 7.1.1.3). The time for the super-prompt criticality is also crucial for this analysis; it is a fast power burst that requires extra temporal refinement during the peak time.

Based on these exploring studies, the time step was frozen to  $t_{\text{step}} = 0.005$  s for both CBY/SCF and CBY/FLICA simulations. Using this time step, another parametric study was performed regarding the axial nodalization. This axial discretization was varied from twenty to thirty-four axial nodes. In Table 24 a comparison of the peak power and peak time predicted with CBY/SCF for this scenario is given. It can be seen that an increase of the number of axial nodes leads to an increase of the power peak. It can be also observed that CBY/SCF and CBY/FLICA4 did not predict the same power peak and peak time since the boron transport model of both TH codes are different. Also the basic balance equations of SCF and FLICA4 are not the same: FLICA4 is based on a four equation approximation while SCF is based on a three mixture equation approximation. FLICA4 allows also to fix either the CFL for the boron model or to fix the time step. Regarding the coupled scheme CBY/FLICA4, it is important to mention that both codes follow independent time steps, different from CBY/SCF, where the N time step is also used for the TH. In this matter, extensive studies were done within the frame of the NURISP project that helped to chose the correct values, e.g. for the CFL.

Table 24. Boron dilution sensitivity analysis, results with different axial discretization.

<b>Axial nodes</b>	<b>Power peak (MW)</b>	<b>Peak time (s)</b>	<b>TH code</b>
20	325.50	6.46	FLICA4
20	327.45	6.74	SCF
25	327.47	6.74	SCF
29	328.12	6.74	SCF
34	328.05	6.74	SCF

### 7.1.3.2 Problem 2: Heterogeneous boron dilution in a whole PWR MOX/UO<sub>2</sub> core

In case of the heterogeneous boron dilution problem, it is assumed that a slug of deborated water has been accumulated in one of the cold legs of the reactor during outage. The slug has not been recognized by the operator and the normal start-up procedure has been initiated. The main coolant pump is switched on in the loop with the slug reaching full flow rate within  $t = 14.0$  s. Consequently, the slug is transported into the reactor pressure vessel. The mixing of the borated coolant with the coolant of the other loops takes place already in the downcomer region. Due to this mixing, a heterogeneous boron concentration is observed at the core inlet. This problem presents a challenge to test the robustness of the coupling due to the production of vapour in a single FA or localized areas. The time dependent BCs for each FA at the inlet of the reactor core were obtained from calculations with ANSYS-CFX. A core model was done at 1:5 scaled of the mixing test facility ROCOM [Kliem01]. These boron dilution benchmarks were defined within the subproject SP3 of NURISP. The scenario was analysed with DYN3D/FLICA4 and DYN3D/FLOCAL.

#### 7.1.3.2.1 Description of the scenarios and boundary conditions

Three scenarios are investigated for the heterogeneous boron dilution simulation. For the three of them, the transient simulation departs from a steady state characterized by a HZP condition.

First scenario (slug 1): Involves a diluted boron slug entering the core with a volume of  $18.0 \text{ m}^3$ .

Second scenario (slug 2): Involves a diluted boron slug entering the core with a volume of  $20.0 \text{ m}^3$ .

Third scenario (slug 3): Involves a diluted boron slug entering the core with a volume of  $26.0 \text{ m}^3$ .

In Table 25 the operating conditions for these scenarios are presented (the initial HZP state of the transient). The core inlet, flow rate and coolant inlet temperature remained constant during the transient phase.

Table 25. Operating conditions at HZP of the PWR MOX/UO<sub>2</sub> full core boron dilution benchmark.

Parameter			Value		
Inlet temperature	K	473.1	Core mass flow rate	kg/s	4585.68
Core thermal power	W	1.0	Initial boron concentration	ppm	2000.0
Outlet pressure	MPa	3.0	CR position		ARI

It is worth it to mention that an additional simulation was performed with CBY/SCF and which consists on a HFP steady state. In this case, the only parameter that changes for the operating conditions described in Table 25 is the core power, which rises up to its nominal  $P_{\text{tot}} = 3565.0$  MW.

### 7.1.3.2.2 Description of the models and simulations

The neutron physical models for the scenarios described above uses nodal XSs libraries for two energy groups generated with the lattice code HELIOS that includes the boron concentration and the form functions in addition to the moderator density and Doppler temperature. The feedback parameter range considered in the XSs libraries is the following: Moderator density: 13.5 kg/m<sup>3</sup> to 865.8 kg/m<sup>3</sup>, Boron concentration: 0.0 ppm to 2500.0 ppm and Doppler temperature: 473.1 K to 1773.1 K. The core is radially discretized in 193 neutronic nodes; each one representing one FA. In the axial direction, the active core part is subdivided in twenty equidistant nodes. Axial and radial reflectors are also considered in the neutronic model. Zero flux boundary conditions are used in the axial and radial direction.

The TH model of the whole PWR core consists of one TH node per FA, where cross flow between FA borders is permitted (with a factor of 0.7). Axially, the TH domain follows the same discretization as the N model and radially, SCF comprises 193 parallel channels. In addition, the fuel rod discretization in the radial direction is divided in ten nodes (two for the cladding and eight for the fuel pellet). The temperature dependent thermo-physical properties for the fuel and cladding are the same as the once used for the PWR MOX/UO<sub>2</sub> benchmark.

For the analysis of the heterogeneous boron transport problem, a steady state coupled run with CBY/SCF is done first. The steady state follows a convergence criteria of  $\epsilon_N = 1.0^{-6}$  and  $\epsilon_T = 1.0^{-5}$ , leading to total number of two iterations to achieve convergence (recall that the core is characterized by a HZP condition). For the transient simulation, the time step for both CBY and SCF was selected based on the experience gained through the analysis of the homogeneous boron transport mini-core problem. During the transient a variable time step was selected, from  $t = 0.00$  s to  $t = 2.00$  s:  $t_{\text{step}} = 0.010$  s, from  $t = 2.00$  s to  $t = 2.50$  s:  $t_{\text{step}} = 0.005$  s, from  $t = 2.50$  s to  $t = 8.00$  s:  $t_{\text{step}} = 0.001$  s and from  $t = 8.00$  s to  $t = 10.0$  s:  $t_{\text{step}} = 0.005$  s.

The variation of this temporal discretization is not arbitrary. At the beginning of the transient no perturbation are expected and therefore a bigger time step ( $t_{\text{step}} = 0.01$  s) compared to the others is used in order to accelerate the time advancement. At approximately  $t = 3.0$  s a decrease of the core avg. boron concentration is foreseen. The TH code needs a more refined time step to predict accurately the boron transport within the core. Therefore, at  $t = 2.0$  s it was decided to reduce the time step to  $t_{\text{step}} = 0.005$  s. For analyzing the power peak region, the time step was even reduced to  $t_{\text{step}} = 0.001$  s from  $t = 2.5$  s to  $t = 8.0$  s. In this period the maximum reactivity is expected, in addition to the power peak and the minimum boron concentration in the reactor core.

### 7.1.3.2.3 Selected results for the steady states and transient cases

First of all, the stationary core conditions just before the boron transient were predicted with CBY/SCF and compared to the ones of other coupled codes (CBY/SCF, DYN3D/SCF, DYN3D/FLICA4 and DYN3D/FLOCAL). In Table 26 selected results obtained for HZP and HFP conditions by the coupled codes for the stationary core are shown. It is worth to mention that the coupling between DYN3D and SCF was done inside the NURESIM platform making use of the SCF wrapping and coupling scheme developed for CBY/SCF in the frame of this dissertation.

Table 26. HFP and HZP results for the full core boron dilution benchmark.

Parameter	Core State	CBY SCF	DYN3D SCF	DYN3D FLICA4	DYN3D FLOCAL	
$k_{\text{eff}}$	HFP	1.00824	1.008463	1.007172	1.007963	
$F_z$	HFP	1.431	1.423	1.466	1.460	
$F_{xy}$	HFP	1.4175	1.4082	1.401	1.417	
$T_{\text{Dopp}}(\text{max.})$	K	HFP	1136.9	1129.5	-	-
$T_{\text{CL}}$	K	HFP	1877.5	1858.6	-	-
Convergence (iterations)	HFP	8	35	37	27	
$k_{\text{eff}}$	HZP	0.92419	0.92425	0.92474	0.9241	
$F_z$	HZP	1.498	1.470	1.489	1.467	
$F_{xy}$	HZP	2.417	2.410	2.415	2.380	

As can be seen, the predicted N parameters are close to each other considering that the TH codes have different solution models. The transient calculations started from a converged steady state simulation where the core was critical. The evolution of the core average boron concentration in time for the slug volumes defining the three scenarios is shown in the Fig. 49 (calculated with SCF). The transient

simulations are performed taking into account the time dependent boron concentration change shown in this figure.

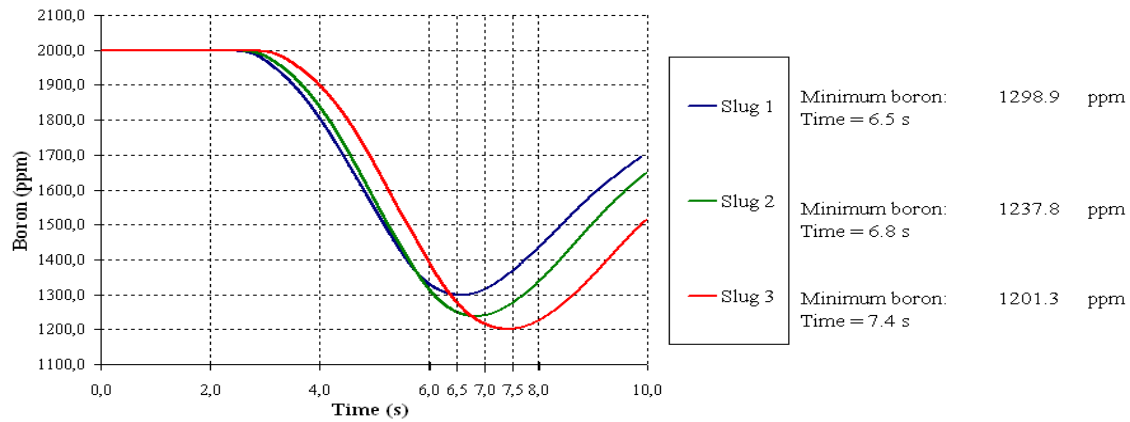


Fig. 49. Core average boron concentration evolution for slugs 1, 2 and 3.

In Fig. 50 is illustrated that a power peak is expected due to the decrease of the boron concentration (leading to a reactivity increase).

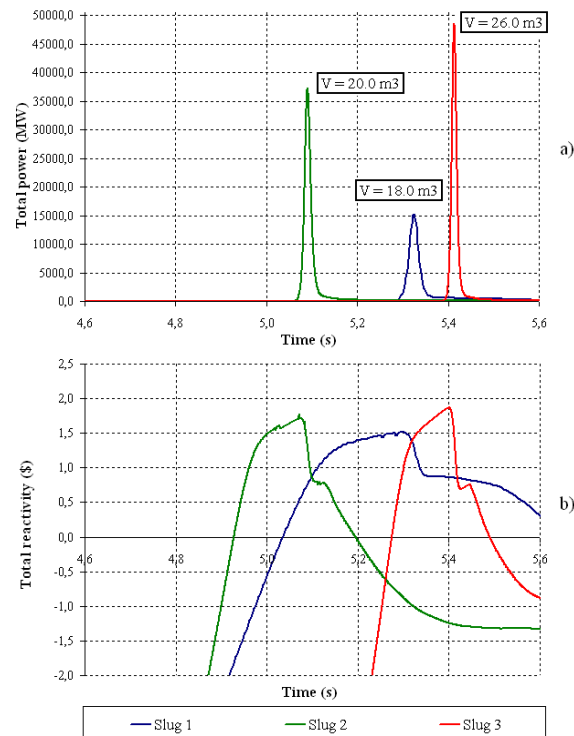


Fig. 50. Detail at around  $t = 5.0$  s for the total power (a) and the total reactivity (b) evolution for slugs 1, 2 and 3.

In Table 27 the comparison of the main results obtained by different coupled codes and the CBY/SCF results with and without using power maps (PMs) for the three scenarios is exhibited.

Table 27. Results obtained for the full core boron dilution transients (slugs 1, 2 and 3).

<b>Coupled codes</b>	<b>Slug Number</b>	<b>Power peak (MW)</b>	<b>Peak time (s)</b>	<b>Maximum reactivity (\$)</b>	<b>Minimum boron (ppm)</b>
CBY/SCF (without PMs)	1	15320	5.31	1.521	1298.9
CBY/SCF (with PMs)	1	12243	5.42	1.468	1300.5
DYN3D/SCF	1	12466	5.55	1.321	1309.5
DYN3D/FLICA4	1	11004	6.01	1.167	1343.4
DYN3D/FLOCAL	1	14888	5.65	1.365	1296.5
CBY/SCF(without PMs)	2	37261	5.09	1.780	1237.8
CBY/SCF (with PMs)	2	34177	5.02	1.695	1235.1
DYN3D/SCF	2	49077	5.10	1.641	1238.5
DYN3D/FLICA4	2	31964	5.54	1.569	1259.9
DYN3D/FLOCAL	2	44900	5.31	1.623	1227.0
CBY/SCF(without PMs)	3	48570	5.41	1.866	1201.3
CBY/SCF (with PMs)	3	44533	5.34	1.847	1198.9
DYN3D/SCF	3	62936	5.42	1.731	1200.8
DYN3D/FLICA4	3	56240	5.84	1.747	1205.8
DYN3D/FLOCAL	3	50881	5.68	1.710	1177.7

As can be seen in this table, two CBY/SCF simulations were performed to demonstrate the importance of the time interpolation using the PMs in SCF. As discussed in Chapter 6.1.2, SCF is able use PMs between two consecutive time steps, leading to a smoother transition of the 3D power distribution between time intervals during a transient with a power change. The solution without PMs is based on the power distribution at the current time step, which over predicts the total power compared to the CBY/SCF solution with PMs. The use of these PMs promotes a type of damping for a time frame taking as the power distribution half of the power density at a previous time step (old time) and half at the current time step (actual time).

From the performed simulations corresponding to the first simulation, the following observations can be made:

1. The code predicts an insertion of positive reactivity in the range of  $\rho = \$1.46$  as illustrated in Fig. 51 (c). This value is consistent with the reactivity added during the dilution process ( $\sim 10.0$  pcm per ppm).
2. The calculated core average boron concentration is illustrated in Fig. 51 (d).
3. As the reactor becomes supercritical during the transient the reactivity is enough to produce a power excursion, Fig. 51 (a, b).

4. The difference in the total power and power peak time predicted by the different codes is mainly due to the boron transport models (as seen in Fig. 51 (d), Fig. 53 (d) and Fig. 54 (d).
5. The numerical diffusivity of the codes plays greatly influence in the simulation results.
6. For this heterogeneous boron transport scenario, the predicted boron concentration from FLICA4 shows large deviations from the predictions of the other coupled codes; FLICA4 also underestimates the boron concentration.
7. The minimum boron concentration predicted by FLICA4 ( $B_{\text{ppm}} = 1343.4$  ppm) appears approximately  $\sim 1.5$  s after the minimum boron concentration predicted by SCF ( $B_{\text{ppm}} = 1298.9$  ppm), leading to additional positive reactivity for SCF in the order of 440.0 pcm. This fact is reflected on the power peak, which differs in terms of magnitude and appearance time.
8. The reactivity evolution predicted by the coupled codes after the peak is driven mainly by the interaction of vapour production at some localized areas in the core. The average Doppler temperature differs by  $T = 8.0$  K, which can be attributed to the differences in the power peak reached during the transient.
9. The use of power maps for CBY/SCF under-predicts the total power compared to the case where no power maps are implemented.
10. In Fig. 51 (b) is clearly shown that the hydraulic and boron transport temporal management follows independent time steps for the FLICA4 solution.
11. For all slug conditions, re-criticality after the power peak is achieved for the simulations done with FLICA4, leading to a second power rise.

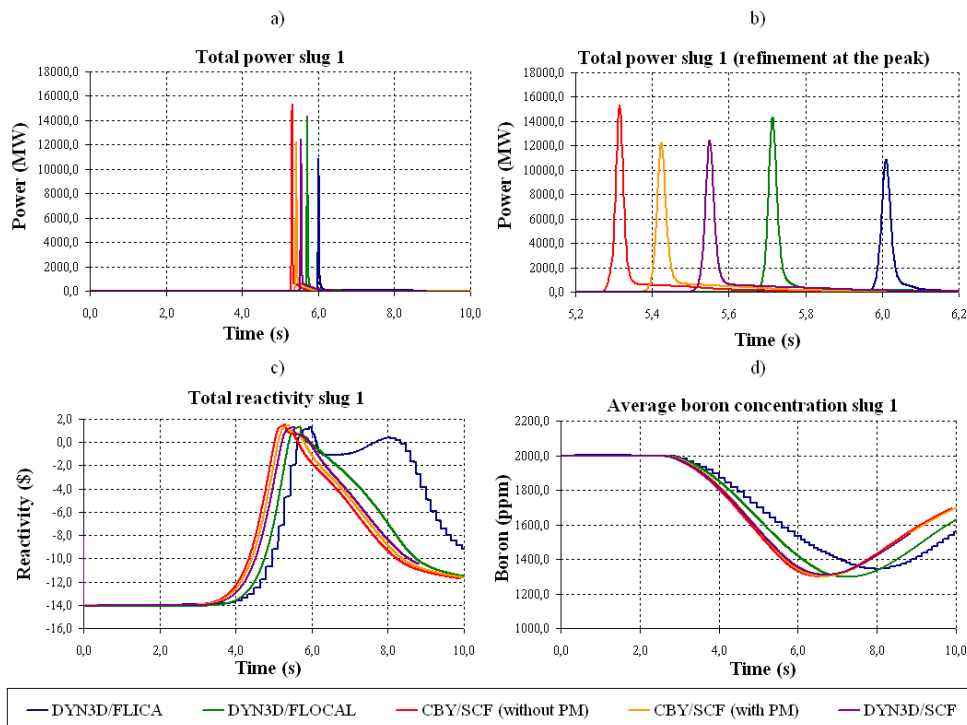


Fig. 51. Boron slug 1: Total power (a, b), total reactivity (c) and boron concentration (d) evolution.

Concerning the last point in the previous list, this return to criticality scenario is influenced by the spatial distribution of boron in the core (recall that this problem is characterized by a very heterogeneous core). This instability provided by FLICA4 for calculating the boron concentration affects the spatial distribution of boron leading to strong re-criticality feedbacks. In Fig. 52 the 3D time evolution of the boron concentration in the reactor core is shown. At the beginning the boron concentration amounts normally to 2000.0 ppm (as specified in the core inlet operating conditions in Table 25). Three seconds after the transient starts, the deborated slug (blue) enters into the core and it leaves the core after five seconds ( $t = 8.0$  s). As time passes, it is shown that the volume of deborated water enters the core and moves from the inlet to the outlet of the core. It can be also observed that the slug deforms while passing through the core and that it also influences the local boron concentration in radial direction. The transport process of the deborated slug for the second and third slug is similar to the one of the first slug.

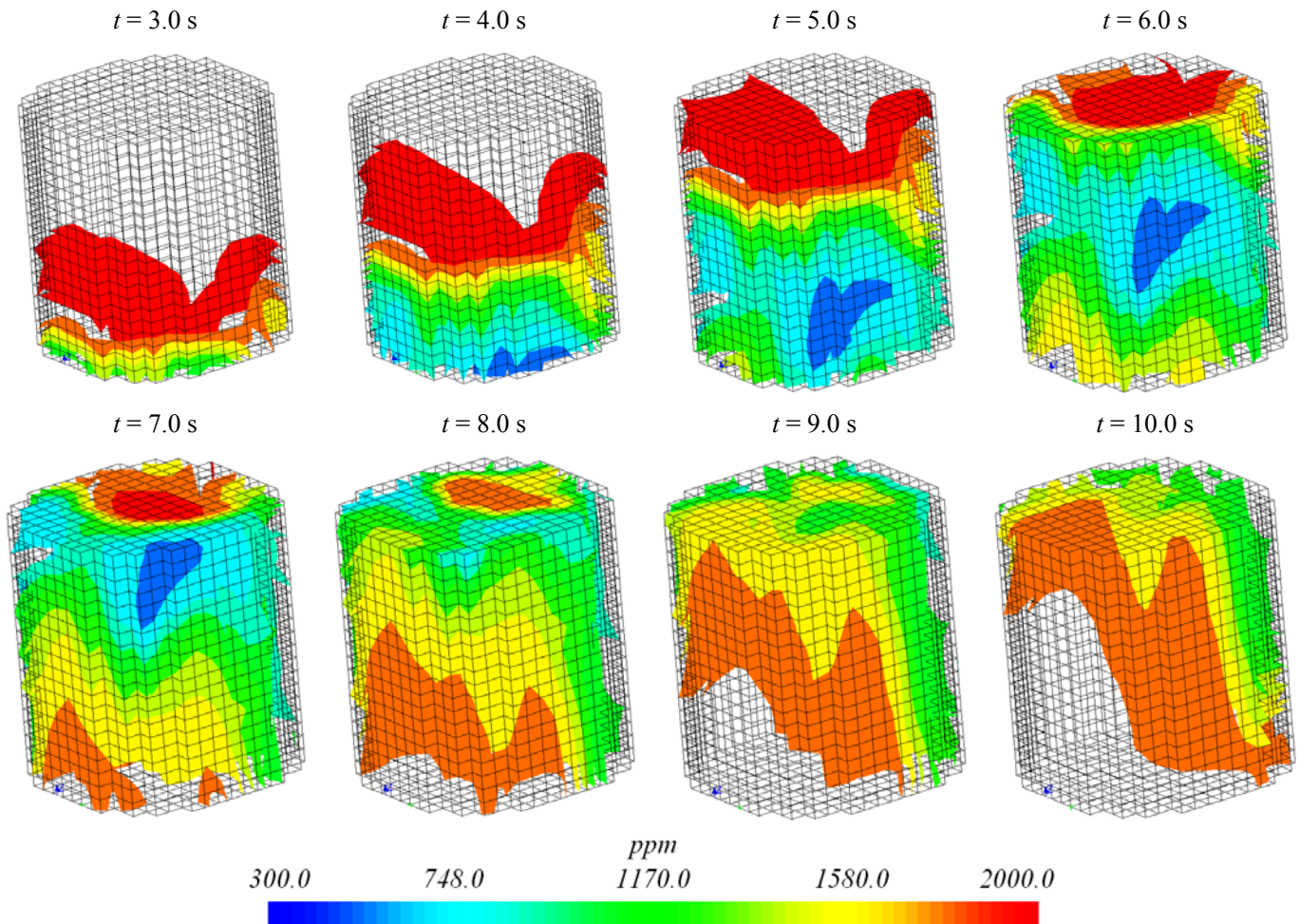


Fig. 52. 3D time evolution of the boron concentration during the transient for the first slug.

For the second scenario (the comparison of selected parameters is illustrated in Fig. 53), the power increase appears later compared to the one of the first scenario. Since the deborated slug volume is

larger than for the first slug, the inserted positive reactivity reaches a value of about  $\rho = 2.0$  as seen in Fig. 53 (c). Due to the appearance of void in some localized zones in the core, the reactivity behaviour after the power peak is influenced by the vapour production. This phenomena affects substantially the TH solution even though void feedback is not contemplated, leading to a strict management of the time step discretization during the power burst.

It is noted that only a time step selection in the order of  $t = 0.001$  s predicts stable results and therefore, all simulations are performed with a time step of  $t_{step} = 0.001$  s. In addition, it is observed that the maximum number of iterations (2000) set in the Bi-CBSTAB algorithm, was not enough to provide convergence inside CBY's internal loop. Hence, the number was increased to 10000 in addition to the increase of maximum number of source iterations (outer loop) from typical 50 to 500.

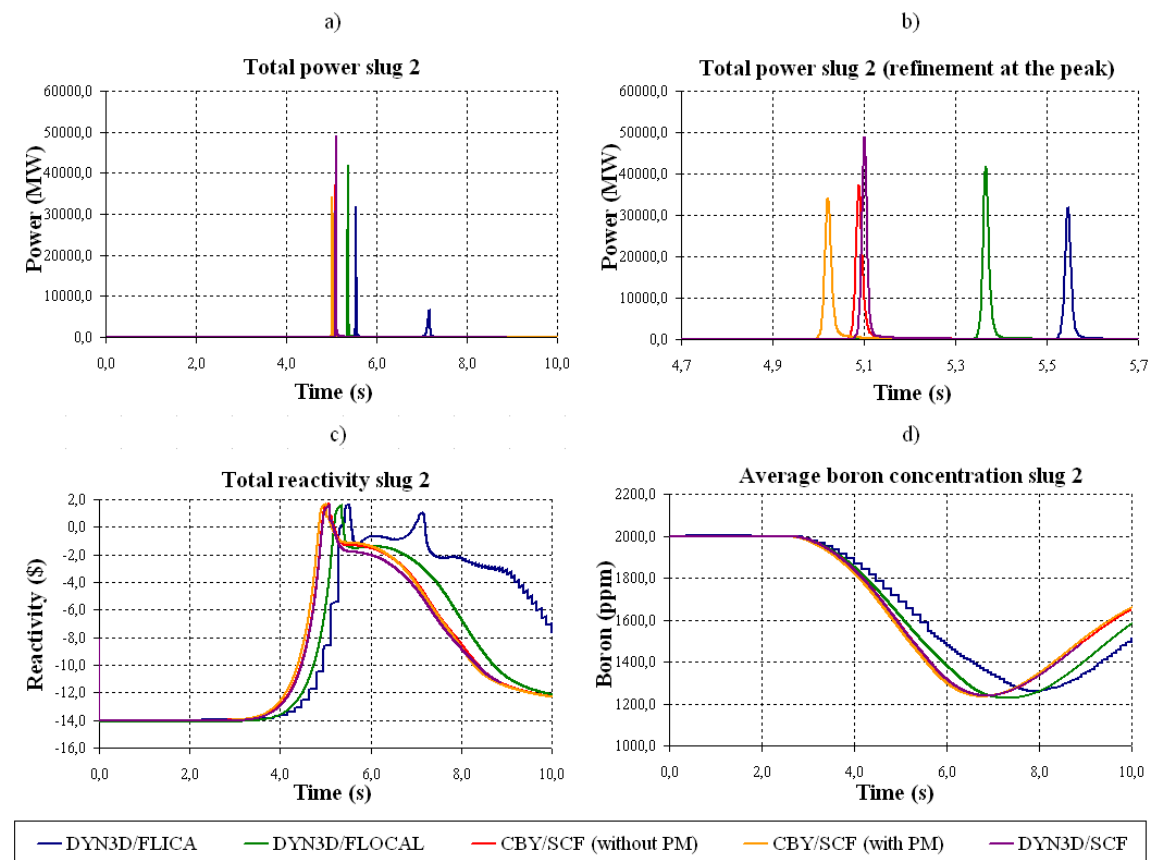


Fig. 53. Boron slug 2: Total power (a, b), total reactivity (c) and boron concentration (d) evolution.

The last simulation (third slug) shows a much greater power increase compared to first and second simulations since the deborated slug is 44.0% larger than the one of the first scenario, as seen in Fig. 54 (a, b). The minimal boron concentration is achieved after  $t = 1.0$  s compared to the case for the first scenario. Nevertheless, the overall behaviour of the main parameters as predicted by the codes is the

same compared to the other two scenarios. This third simulation is the most challenging one to be performed by the coupled codes due to the size of the slug.

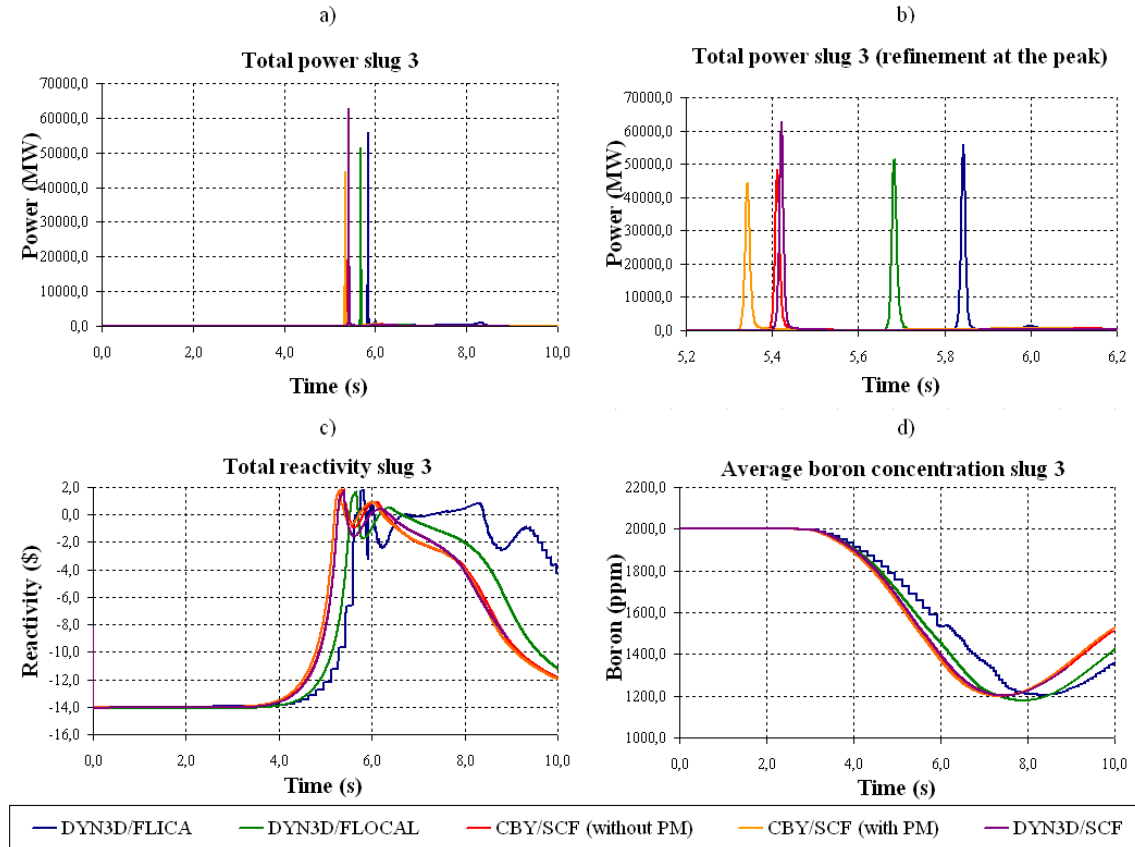


Fig. 54. Boron slug 3: Total power (a, b), total reactivity (c) and boron concentration (d) evolution.

Further studies should investigate the refinement of the time step selection around the power peak to values below  $t = 1.0$  ms. The total simulation time (from  $t = 0.0$  s to  $t = 10.0$  s) is ambiguous. The three cases were run in different environments and sharing the computational power with other users. Nevertheless, it can be concluded that all the simulations lasted between  $t_{\text{total}} = 10.0$  (first slug) and  $t_{\text{total}} = 23.0$  hours (third slug).

The coupled simulations presented here, especially the ones performed with CBY/SCF and DYN3D/SCF, have clearly shown the capability of the new boron transport model implemented in SCF and the friendly use of the coupled system CBY/SCF and DYN3D/SCF inside the NURESIM platform. It must be also noted that the simulation of full core boron dilution scenarios, in which local boiling may appear, are very challenging for the TH solver. SCF needs special combination of options in the input deck. These options are namely the usage of incompressible flow instead of weakly compressible flow. By doing this only the time derivatives are used to solve the energy equation and the

pin heat conduction. Since SCF is a solver for upward weakly compressible flow in bundles, small time steps or even drastic changes in power leading to strong localized gradients, may provoke instabilities while solving the time derivatives from the mass and momentum conservation equations. On the other hand, the numerical diffusion provided by SCF is smaller compared to the one of FLICA4, leading also to an overestimation of the peak powers and hence, to higher maximal fuel temperatures than the predictions of FLICA4.

The differences encountered between the coupled codes are attributed mainly to the differences found in their internal solvers. FLICA4 employs an object oriented pre-processor design to study nuclear reactors (fuel rods, guide tubes, etc...), model unstructured non-conform meshes in the radial direction, and structured in the axial. It also defines transient scenarios in addition to stationary states. Different from SCF, FLICA4 solves the two-phase mixture by a set of four balance equations (mass, momentum and energy of the mixture, and mass of steam) and two closure laws. The mechanical non-equilibrium e.g. different liquid and vapor velocity is taken into account by a drift flux model. The numerical method is finite volume VF9 (this method allows to solve the system of equations over irregular rectangular meshes in 2D) scheme is used to estimate the diffusive fluxes. FLOCAL, which is the own thermal-hydraulic module of DYN3D, consists of a two-phase coolant flow model, a fuel rod model and a heat transfer regime map which range from one phase flow up to superheated steam. Parallel channels are coupled hydraulically by the condition of equal pressure drop over all core channels. Thermal-hydraulic boundary conditions for the core like coolant inlet temperature, pressure, and coolant mass flow rate or pressure drop must be given as input for DYN3D. The model is based on the analytical solution of the Navier-Stokes equations in the potential flow approximation in 3D cylindrical geometry and the diffusion equation for heat transport or soluble poison. The two-phase flow model is closed by constitutive laws for heat mass and momentum transfer, e.g. vapor generation at the heated walls, condensation in the sub-cooled liquid, phase slip ratio, pressure drop at single flow resistance's and due to friction along the flow channels as well as heat transfer correlations. Moreover, the models used for each simulation (concerning, e.g. flow areas, wetted perimeters, pellet discretization and time advancement, among others). In addition to these differences, the steam/water thermo-physical property tables and boron dilution models differ from each other.

Furthermore, the reactor dynamic codes used, CBY and DYN3D, have different solution approaches. Even though the comparison between the nodal expansion method and improved diffusion in the N side to solve the NDE has differences, it is a very good way to quantify the accuracy of the diffusion solver CBY. The reader must recall that even though the neutron physical solution methods are different, the nodal XSs used where the same for both codes.

## 7.2 3D Simulation of a core with hexagonal fuel assemblies at nodal level

### 7.2.1 Validation of CBY/SCF using the Kalinin-3 coolant transient benchmark

The OECD/NEA Kalinin-3 benchmark was selected for the validation of the coupled code CBY/SCF for simulations which involve hexagonal cores. In addition, this benchmark provides extensive measured plant data which is very useful for the validation process of the coupled system and therefore, an accurate evaluation of the simulated parameters compared to the measured data. These data was obtained at the Russian NPP Kalinin Unit #3, a VVER reactor type.

#### 7.2.1.1 Description of the scenario and boundary conditions

The scenario consists on the switch-off of one of the four main circulation pumps (MCP) of loop-1, leading to an asymmetrical core behavior with broad ranges of the parameter changes. The spatial dependent coolant temperature changes, enhancing an insertion of spatially distributed negative reactivity due to the feedback mechanisms and a non-symmetric power distribution. Even though the transient initiates from a HFP condition, a HZP simulation was done for comparison purposes. Therefore, three cases are selected for the simulation.

Kalinin-3 case 1 (exercise 3a): Steady state at HZP conditions.

Kalinin-3 case 2 (exercise 3b): Steady state at HFP conditions (initiates the transient).

Kalinin-3 case 3 (exercise 3b): Transient simulation guided by N and TH BCs.

In Table 28 the main parameters of the HFP and HZP steady state conditions for the Kalinin-3 benchmark are given.

Table 28. Operating conditions at HFP and HZP, Kalinin-3 benchmark.

Parameter		Value (HFP)	Value (HZP)
Inlet temperature	K	560.0	552.15
Core thermal power	MW	2875.0	2.907
Outlet pressure	MPa	15.52	
Core mass flow rate	kg/s	18766.46	
Initial boron concentration	ppm	660.0	

The sequence of main events that the transient ( $t_{\text{total}} = 300.0$  s) follows and which characterizes the benchmark are listed hereafter:

1. At  $t = 0.0$  s, manually switching-off of one of the four MCPs.
2. At  $t = 2.7$  s, CR#10 (marked with blue in Fig. 55) start the insertion departing from an initial position of  $z = 50.0$  cm below the top of the core (see Fig. 56 (b)).
3. After  $t = 60.0$  s CR#9 (marked with red in Fig. 55) starts the insertion process (Fig. 56 (b)).
4. At  $t = 73.0$  s, the reactor power (measured by neutron detectors) stabilizes in the rage of 66.2% - 67.0% of the nominal power (see Fig. 56 (f)).
5. After  $t = 137.0$  s, the coolant flow rate through the core is practically stabilized.
6. At  $t = 180.0$  s CR#10 and CR#9 start a rapid but small stepwise ejection that last  $\sim 10.0$  s.
7. After CR#10 and CR#9 are 43.4% and 100.0% inserted respectively, the transient up to  $t = 300.0$  s is guided purely by TH inlet boundary conditions.

In Fig. 55 the top view of the core is shown with the location of the ten groups of CRs.

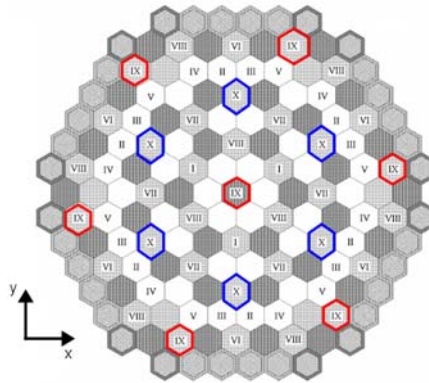


Fig. 55. Top view of the core and control rod position for the Kalinin-3 benchmark.

For the steady state simulations (Table 28 shows its operational parameters) the initial BCs does not change but for the transient simulation, the time-dependent BCs per channel (FA) are defined in SCF, for example, for the FA-mass flow rate, FA-coolant inlet temperature and outlet pressure. Therefore, the analysis of the pump switch-off test with the couple code CBY/SCF is restricted only to the core behavior using time dependent BCs at the core inlet and outlet. The BCs have been calculated using the ATHLET/BIPR/VVER core plant system code (through an integral plant simulation), where core inlet radial distributions are provide for all the 163 FAs. These BCs are defined at each time interval along the transient for  $\dot{m}_{in}$ ,  $T_{in}$ ,  $P_{in/out}$  and the CRs position. As seen in Fig. 56 (c), (d) and (e) the previously mentioned TH parameters are defined for each FA. Due to the extensive number of data points (165), a legend is not used for Fig. 56 (a), (c), (d) and (e); however, the reader should know that each of the colored lines represents the parameter change for a specific FA. It can be observed that during this test a strong asymmetrical thermal behavior of the core is encountered (e.g. maximum deviations

in the order of  $\sim 3.5$  K for the coolant temperature among the FAs). The apparent deviations in the coolant temperature (Fig. 56 (e)) between  $t = 10.0$  s and  $t = 35.0$  s are attributed to the fluctuations in the water level of the affected steam generator. The time evolution of the total power recorded by the neutron flux control system (NFC) and of the calculated core reactivity was added to the Fig. 56 ((f)) for completeness only. They are not used as BC for the CBY/SC analysis of the core behaviour.

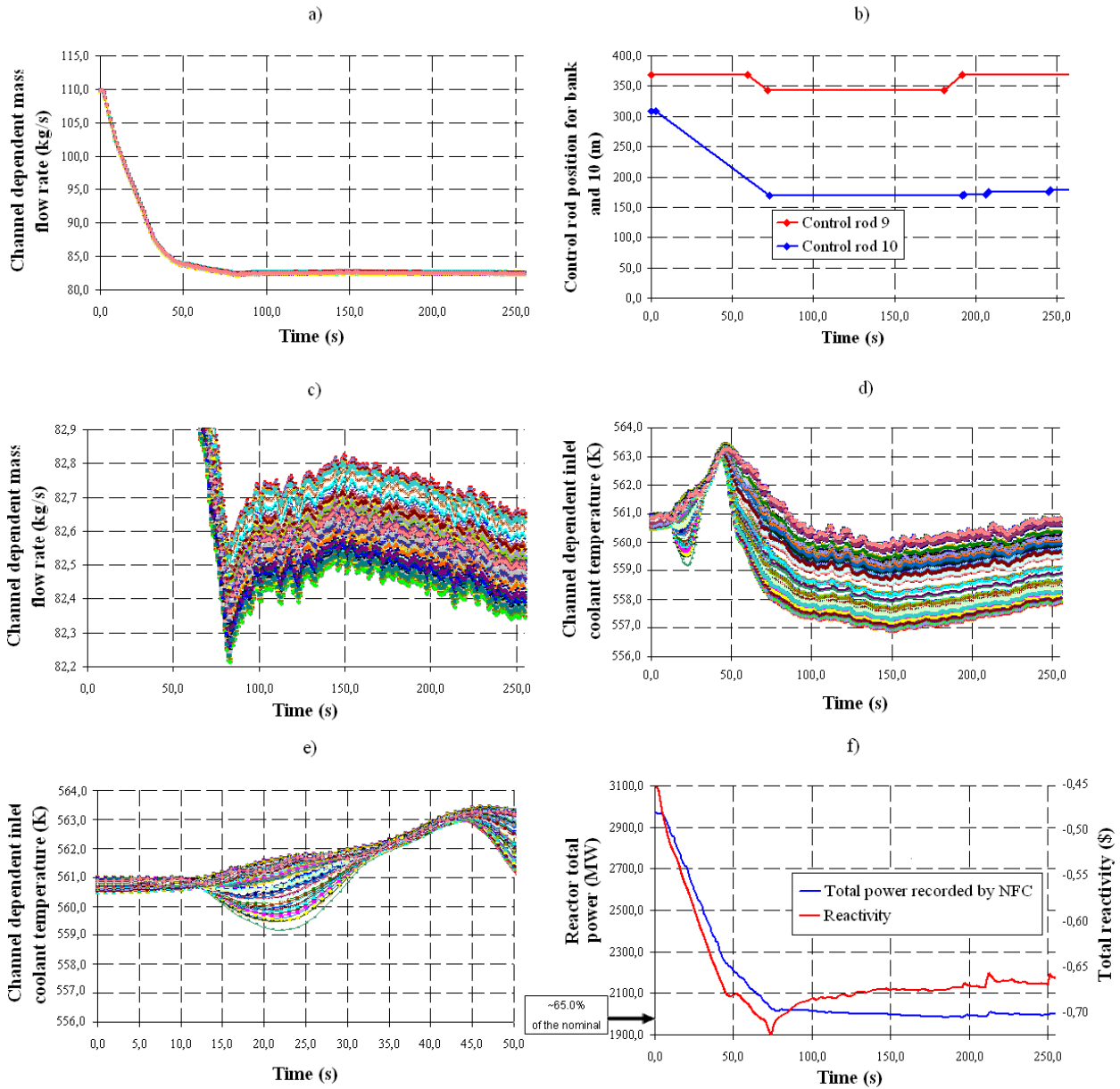


Fig. 56. Time dependent BCs for the Kalinin-3 transient phase: mass flow rate (a), CR position (b), mass flow rate detail (c), coolant temperature (d), coolant temperature detail (e) and power (plant data)/reactivity (f).

### 7.2.1.2 Description of the models used and simulations

In CBY the core is represented by 211 neutronic nodes; each one representing a fuel assembly (163) and a reflector assembly (48). Axially the core is divided into ten equidistant nodes adding for the 3.55 m long active core. Zero flux boundary conditions are used at the radial and axial boundaries of the reactor core. The NEMTAB-like format set of XSs with two energy groups and six delay neutron groups are used for the energy discretization. These XSs were obtained using the TVS-M cross-section generation code as specified in [Ivanov03]. The Doppler temperature is calculated according to eq. (7.1).

For SCF the core model includes the same number of axial levels, 163 parallel channels radially and ten radial nodes for the fuel rod nodalization (two for the cladding and eight for the fuel pellet). A cross flow resistance factor of 1.0 was used between the hexagonal channels. For the material properties, specific temperature dependent thermo-physical properties for the fuel and cladding were specified in the benchmark. Additional information on the models used is given in Appendix A.

For the analysis of the transient scenario, a steady state coupled run with CBY/SCF is done first. The steady state follows a convergence criteria of  $\varepsilon_N = 1.0^{-6}$  and  $\varepsilon_T = 1.0^{-5}$ , leading to total number of twelve iterations to achieve convergence for the HFP state (the HZP converged within the first iteration). During the transient, a fixed time step of  $t_{\text{step}} = 0.1$  s was selected.

### 7.2.1.3 Selected results for the steady state and transient case

The CBY/SCF prediction of selected parameters for the stationary HZP and HFP cases are compared to the predictions of DYN3D/FLOCAL in Table 29. It can be observed that the CBY/SCF predictions are close to the ones of the reference solution (DYN3D/FLOCAL) for both HZP and HFP cases.

Table 29. HFP and HZP steady state results, Kalinin-3 benchmark.

State	Coupled codes	$k_{\text{eff}}$	$F_{xy}$	$F_z$	A.O. %	Max. $T_{\text{Dopp}}$ (K)
HFP	DYN3D/FLOCAL	0.997276	-	-	-	-
HFP	CBY/SCF	0.997202	1.3356	1.1922	-4.65	1339.8
HZP	DYN3D/FLOCAL	1.0108	1.4332	1.3744	12.57	-
HZP	CBY/SCF	1.0116	1.4373	1.4612	17.26	-

The analysis of the transient test phase with CBY/SCF was done for the HFP case only. The core power predicted by CBY/SCF is compared to the measurement data delivered by the benchmark team

in Fig. 57 and Fig. 58. It can be seen there, that the reactor power was recorded by three different methods. The CBY/SCF predictions are very close to the reactor power measured according to the NFC method. In Fig. 57 (a) the total power evolution for the full transient is shown, Fig. 57 (b) and Fig. 58 divide the simulation in two parts, expanded transients from  $t = 0.0$  s to  $t = 80.0$  s and from  $t = 80.0$  s to  $t = 300.0$  s respectively. The rapid insertion of CR#10 produces a step decrease of the total reactivity, leading to a net power reduction of  $\sim 69.9\%$  relative to the nominal. The reactor core average power falls drastically when CR#9 starts its downward movement before stabilizing the power, condition that prevails until the end of the transient. Oscillations are observed after  $t = 80.0$  s mainly due to the fluctuations of the core inlet temperature and mass flow, but also due to the small extraction of CR#9 at  $t = 190.0$  s, and CR#10 at times  $t = 190.0$  s (1<sup>st</sup> arrow),  $t = 208.0$  s (2<sup>nd</sup> arrow) and  $t = 245.0$  s (3<sup>rd</sup> arrow) of about 27.6 cm for both banks, as seen in Fig. 58.

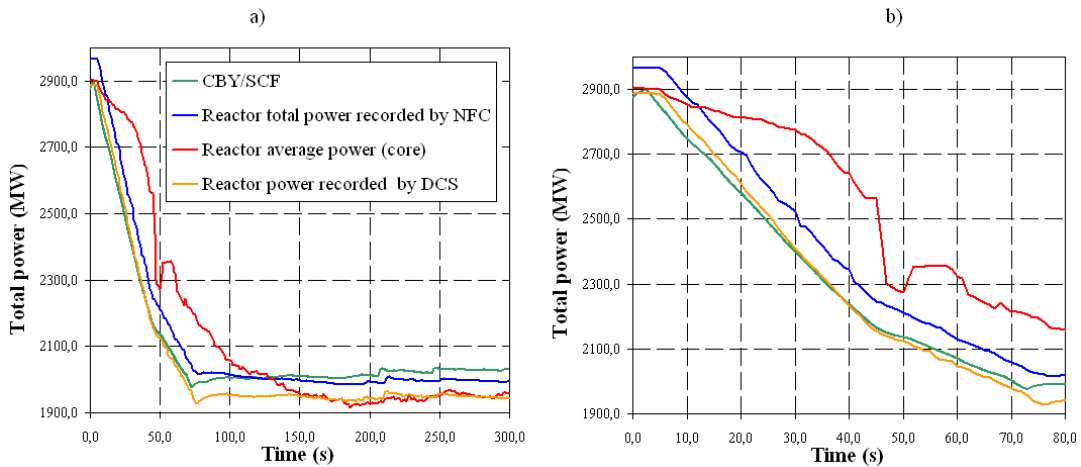


Fig. 57. Kalinin-3 benchmark: Total power evolution (presented for two different time frames).

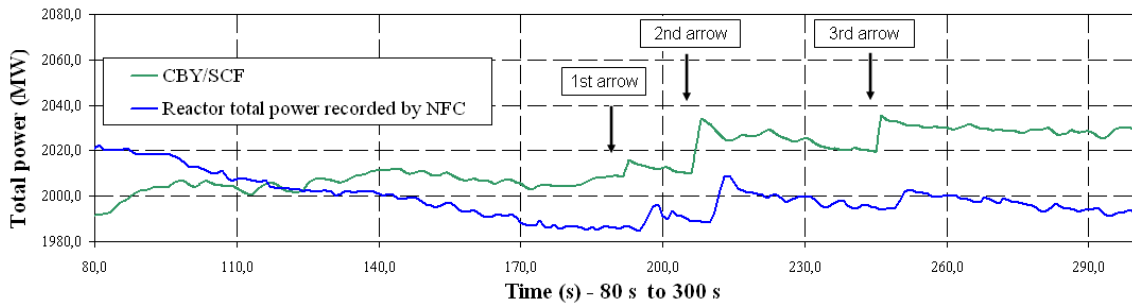


Fig. 58. Kalinin-3 benchmark: Total power evolution from  $t = 80.0$  s to  $t = 300.0$  s.

Even though the different measurements show deviations between each other, the reactor thermal power calculated on the basis of the NFC is a good reference for the CBY/SCF simulation. The other experimental values are provided through the reactor thermal power calculated on the basis of the self powered neutron detector (SPND), or DCS power, and the core average power, leading to the conclusion that the trends of the calculated results are very close to the measured data. The core average

power is calculated on the bases of different measuring and recording devices such as the upper level unit control system (UBLS), the in-core monitoring system (ICMS) and the system of experimental control (SEC). The idea is to calculate the core average power through core TH parameters. The total power however shows a delay compared to the other measurements. This is attributed to the time response of the measurement devices in case of rapid variations of the core conditions. The lower gradient of the load reduction in the time interval from  $t = 42.0$  s and  $t = 74.0$  s is due to the temperature increase at the core inlet (Fig. 56 (d), at about  $t = 45.0$  s), terminating the impact of the negative feedback of the coolant temperature, which increased the gradient of the power reduction due to the increase of  $T_{in}$ . The decrease of the inlet temperature after  $t = 42.0$  s caused an insertion of additional positive reactivity into the core, eq. (7.2), which is reflected in the decrease of the reactor power.

$$\Delta\rho = \frac{\partial\rho}{\partial T} \Delta T_{in}. \quad (7.2)$$

The increase of reactivity seen after  $t = 72.0$  s (Fig. 60 (a), encircled point in blue) is characterized by the decrease of the inlet core temperature ( $\Delta T = 5.0$  K) promoting a very slight increase of the total power. The core outlet pressure also experiences a change, a decrease of 0.4 MPa relative to the initial pressure (nominal) within the first  $t = 100.0$  s and a gradual increase up to 15.45 MPa at the end of the transient. From Fig. 59 and Fig. 60 it can be seen that the total power, reactivity, Doppler temperature, and the moderator temperature and density of the core predicted by CBY/SCF are consistent to each other. The core average moderator temperature increases during the first  $t = 50.0$  s due to the switch-off of the MCP-1, ameliorating the moderation of neutrons in the core. This leads to the power decrease and hence the reduction of the Doppler temperature. The initial decrease of the total reactivity (Fig. 60 (a)) is caused by the insertion of the CR bank # 10. At around  $t = 200.0$  s a smaller reactivity increase is experienced due to the extraction of the CR banks # 9 and # 10.

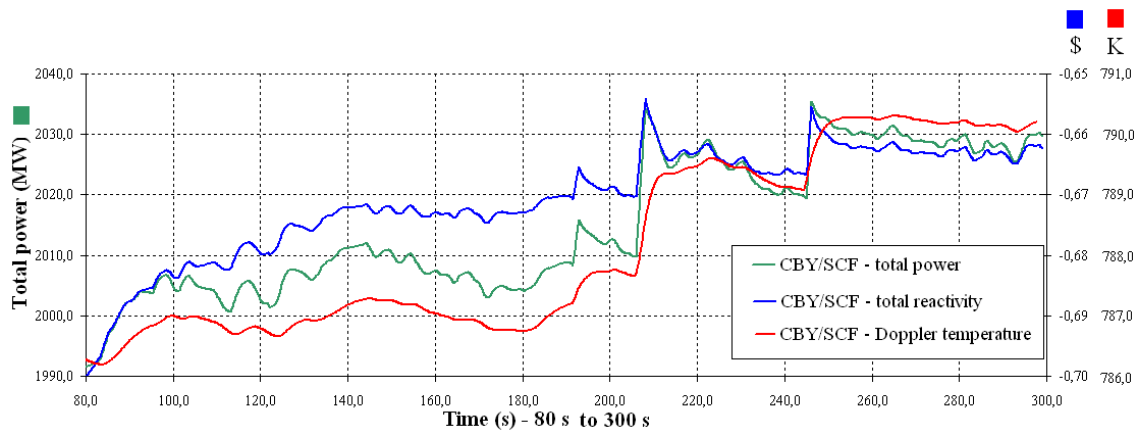


Fig. 59.  $P_{tot}$ , reactivity and  $T_{Dopp}$  evolution for the transient analysis of the Kalinin-3 benchmark.

In addition to the power evolution, the evolution of other parameters such as total reactivity (Fig. 60 (a)) and TH parameters such as core avg. fuel Doppler temperature (Fig. 60 (c)), core average moderator temperature and density (Fig. 60 (b)), and maximal Doppler temperature (Fig. 60 (d)) are shown.

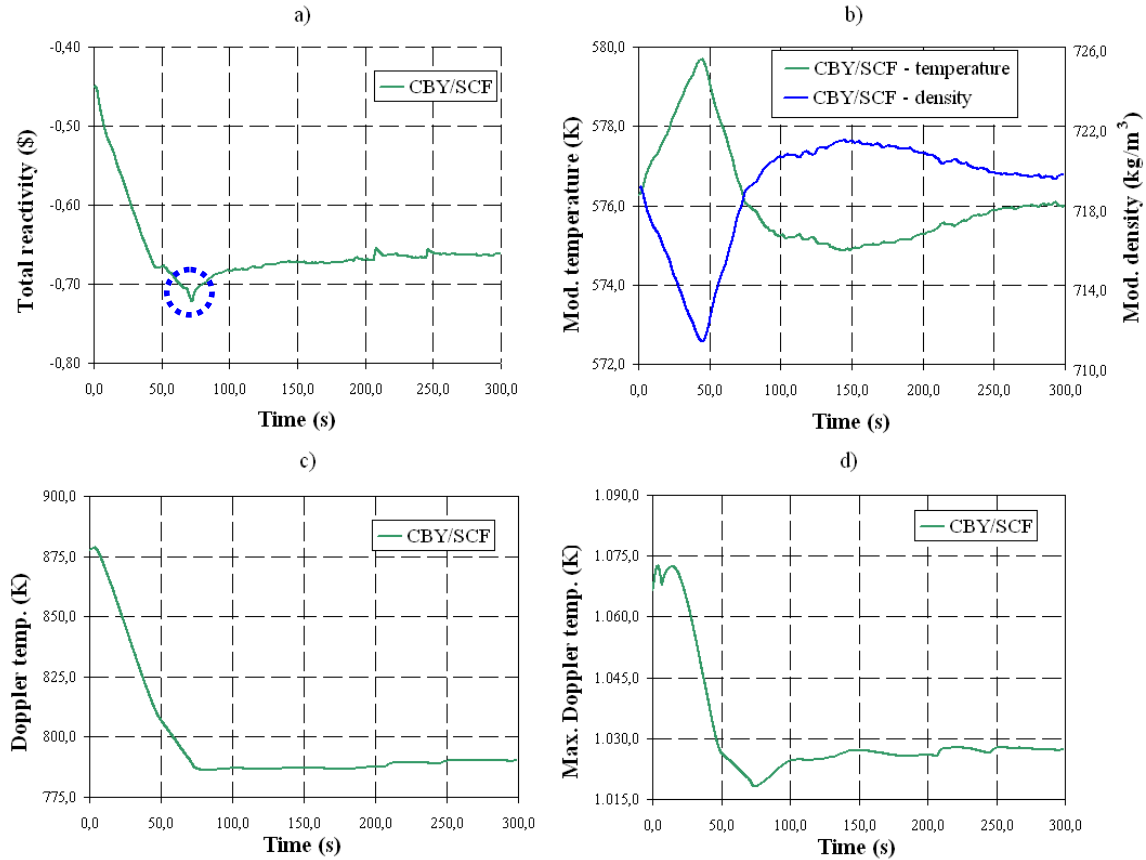


Fig. 60. Total reactivity (a), core avg.  $T_{\text{mod}}$  and  $D_{\text{mod}}$  (b), core avg.  $T_{\text{Dopp}}$  (c) and maximal  $T_{\text{Dopp}}$  (d) for the transient analysis of the Kalinin-3 benchmark.

Due to the rapid reduction of mass flow rate at the beginning of the transient the core inlet temperature experience an increase of about  $T = 2.0$  K (leading to a negative reactivity insertion of about 5.0 pcm). A local sector of the core suffers a decrease in the inlet temperature of about  $T = 1.0$  K compared to the rest of the core. This non-symmetrical cool down is the reason for the non-symmetrical reactivity feedback and radial power distribution in the core.

## 7.3 Code –to-Code validation of the coupled COBAYA3/SUBCHANFLOW hybrid solution

### 7.3.1 Introductory remarks

A new hybrid solution was implemented in CBY/SCF within the NURESIM platform. The code will be applied to analyze the stationary condition of the PWR MOX/UO<sub>2</sub> core. This problem was defined to verify the accuracy of the hybrid solution of CBY/SCF by comparing it with the core simulations obtained with the coupled codes ANDES/CTF (nodal solution) and with COBAYA3k/CTF (full core PBP solution) [Jimenez01]. The advantage of this benchmark is that XSs at nodal level and pin level for eight energy groups exist and hence it represents the only benchmark allowing a verification and assessment of the quality of the hybrid scheme developed. The main objectives of these investigations are:

1. Verification of the correct implementation of the hybrid approach inside the NURESIM platform.
2. Verification of the SCF pre-processor capabilities to automatically generate the necessary TH model combining FA- with sub-channel-based radial discretizations of SCF needed for hybrid solutions.
3. Verification of the hybrid mesh creation of the N domain (CBY) and the proper handling of feedback parameters for hybrid solutions, e.g. the power field at nodal and cell level.
4. Verification of the information exchange (stored in the mesh fields) between the TH and N domains for hybrid schemes.
5. Demonstration of the new capability of CBY/SCF to predict local safety parameters using the hybrid solution approach within the NURESIM platform.

### 7.3.2 Description of the scenario and boundary conditions

A PWR MOX/UO<sub>2</sub> core will be investigated, which material and geometrical data as well as operational conditions correspond to the ones described in [Downar06]. The reactor core state is derived from the transient solution obtained in Chapter 7.1.1, where it is assumed that the reactor core reaches stability after the REA at the simulation time of  $t = 1.0$  s, see Fig. 41. Around this time the PWR core has a core power of  $P_{\text{tot}} = 580.0$  MW (16.2 % of the nominal power). The core TH conditions for this analysis are given in Table 30.

Table 30. Operating conditions at HP for the 3D full core hybrid model.

Parameter		Value
Inlet temperature	K	560.0
Core thermal power	MW	580.0
Outlet pressure	MPa	15.5
Core mass flow rate	kg/s	15849.4
Boron concentration	ppm	1343.5

### 7.3.3 Description of the models used and simulations

For the hybrid simulation of this problem with CBY/SCF, the core was axially divided in twenty equidistant nodes in both CBY and SCF. In addition, the reactor core was modeled as follows:

1. N code (CBY): The nodal and cell homogenized cross sections needed for the CBY/SCF hybrid simulations were also taken from the PWR MOX/UO<sub>2</sub> benchmark, (including data for two and eight energy groups). The whole N core model includes one hybrid FA with reflective BCs in the radial and axial direction. The Doppler temperature is calculated according to eq. (7.1). Two approaches for the level of discretization (nodal and cell) are described hereafter.
  - a. Nodal base approach: Includes 193 FAs (N nodes).
  - b. Cell base approach: Includes one FA located at the ejected CR position represented by 289 cells.

As discussed in Chapter 5.2 (extension applied to CBY for hybrid analysis), for performing hybrid solutions the N nodes are forced to be divided in quarters, leading to four sub-domains per FA. Hence, the number of neutronic nodes increases substantially and the total number of nodes/cells for the N hybrid solution is a result of the following relation,

$$\text{Total elements (4 nodes per FA)} = (\text{total nodes in one plane}) \times 4 \times (\text{total axial levels}) \times 2,$$

$$(193 \times 4 + (17 \times 17 \times 1)) \times 20 \times 2 = 42440.$$

2. TH code (SCF): The cross flow resistance factor between channel/channel, channel/sub-channel, and sub-channel/sub-channel was selected to be 0.7. For the radial discretization two approaches (channel and sub-channel) are needed and described hereafter.
  - a. Channel base approach: This average approach includes 192 FAs represented by 192 parallel channels.
  - b. Sub-channel base approach: One FA located at the ejected CR position represented by 289 sub-channels.

Differently from the N domain, for the TH the number of channels and sub-channels implemented in SCF for the hybrid solution is a result of the following relation,

$$\text{Total elements (rod centered discretization)} = (\text{total rods in one plane}) \times (\text{total axial levels}),$$

$$(192 + (17 \times 17 \times 1)) \times 20 = 9620.$$

Summarizing, the core is modeled with 192 nodal base FA and one PBP FA placed at the location where the maximum power is expected.

The PWR problem was investigated with CBY/SCF using the hybrid solution approach and using the core discretization presented before. For the steady state simulations the following convergence criteria were used: ANDES and COBAYA3k,  $10.0^{-6}$  (value defined for the flux difference between two consecutive PBP iterations, as discussed in Chapter 5.2), for the total power and  $k_{\text{eff}}$ ,  $\epsilon_N = 1.0^{-5}$ , and for the TH parameters:  $\epsilon_T = 1.0^{-4}$ . By considering these convergence criteria, the hybrid solution requires a maximum number of six nodal-local iterations and eleven N-TH iterations to satisfy the selected convergence criteria.

### 7.3.4 Verification of the mesh and field for the hybrid structures

As mentioned in Chapter 6.1.1 (Fig. 28) the coupling between the N and TH domains is based on the mesh superposition and data exchange using the MED format (fields). Verifying that the N hybrid mesh has been successfully created is necessary for setting the power distribution coming from CBY into the power field. In Fig. 61 (a) the automatically generated hybrid mesh of the PWR core together

with the numbering of the FAs indicating the position of the “hybrid FA” is shown (Fig. 61 (b)). This meshing was created in SALOME and is the basis for the feedback exchange between the domains.

To generate the N mesh, CBY makes use of special subroutines in charge of building a new mesh based on a previously defined mesh. In other words, SCF creates its mesh first and CBY uses it to generate the corresponding MED files, which will be used by the solver ANDES (nodal) and COBAYA3k (cell) to set the 3D power distribution. Special care is needed to set the feedbacks in the correct N solver, where nodal powers go to the N nodes and pin powers to the N cells. The structures (e.g. fuel rods) and meshes are ready to build the necessary fields for the data storage and information flow between CBY and SCF. After the first N – TH iteration, power fields and TH fields are created and the feedback parameters are stored. The mapping node/channel and cell/sub-channel is done through a one to one mapping philosophy.

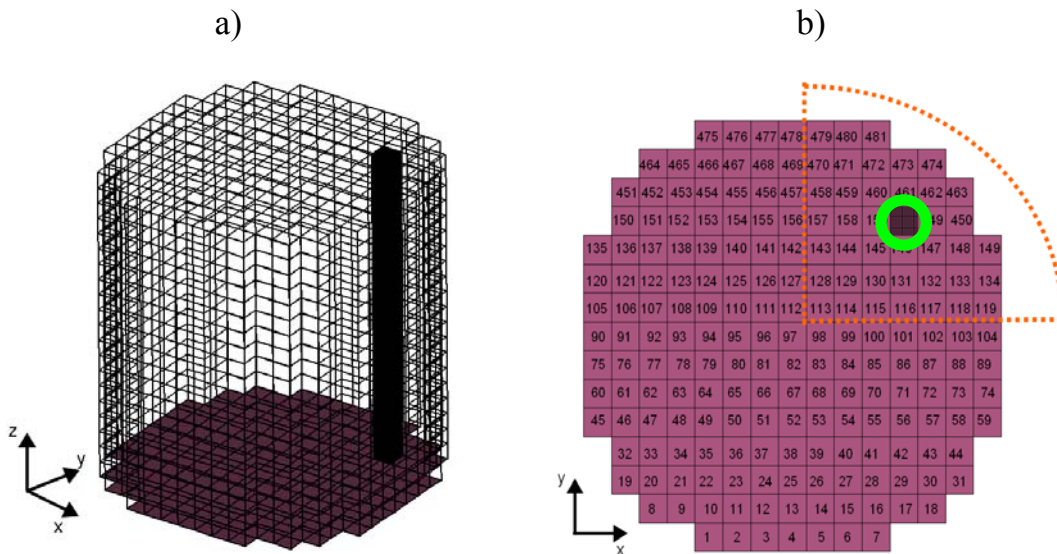


Fig. 61. Generated hybrid mesh for CBY based on the TH (SCF) mesh.

For exemplification, in Fig. 62 the explicit hybrid coupling approach between CBY and SCF implemented in SALOME is depicted. There, the hybrid 3D normalized power field for the N domain (CBY) and the 3D density field of the TH domain (SCF) are shown (only half of the axial core). The iterative process follows the steps listed below.

1. CBY performs its N solution.
2. The power field is updated with the new 3D power distribution.
3. SCF obtains the power feedback from the MED file.
4. SCF performs its TH solution.
5. The TH fields ( $T_{Dopp}$ ,  $T_{mod}$ ,  $D_{mod}$ ,  $B_{ppm}$ ) are updated with the new TH parameters.
6. CBY obtains the TH feedback from the MED fields.

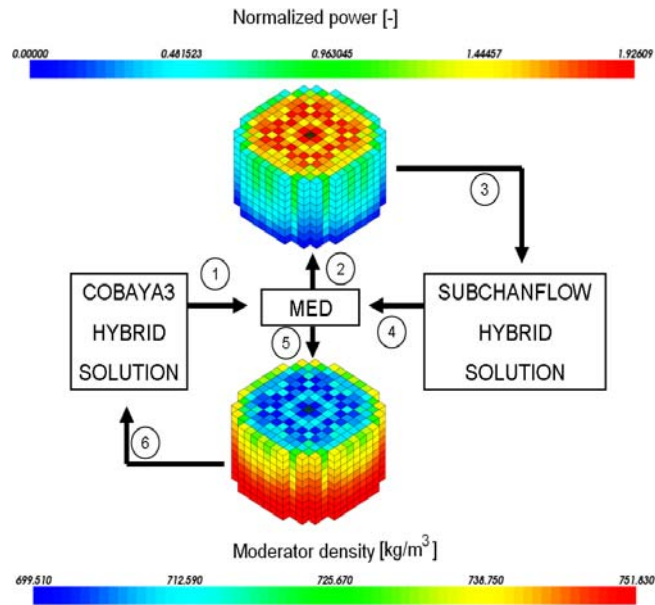


Fig. 62. Hybrid coupled solution scheme inside SALOME using hybrid fields.

### 7.3.5 Selected results of the CBY/SCF hybrid steady state solution

First of all, in Table 31 selected parameters predicted by the CBY/SCF hybrid solution are compared to the full nodal solution of ANDES/CTF and to the full PBP solution obtained by COBAYA3k/CTF. There, the needed calculation time of each code is also presented.

Table 31. Main results for the 3D full core HP hybrid model.

Parameter		ANDES/CTF	COBAYA3k/CTF	CBY/SCF
		NODAL	PBP	Hybrid
$k_{\text{eff}}$		1.00170	0.99982	1.00174
$F_{xy}$		3.742	3.807	4.049
$F_z$		1.468	1.486	1.465
$F_q$		5.759	5.927	5.872
A.O.	%	-6.17	-6.07	-4.22
$T_{\text{Dopp}}$ (avg.)	K	598.9	598.9	598.8
$T_{\text{Dopp}}$ (max.)	K	812.5	867.7	960.4
<b><math>T_{\text{CL}}</math> (hottest rod)</b>	<b>K</b>	<b>1090.2</b>	<b>1238.4</b>	<b>1441.2</b>
$D_{\text{mod}}$ (avg.)	kg/m <sup>3</sup>	0.7456	0.7456	0.7450
Total calculation time		1.0 h 3.0 min	1.0 d 13.0 h 16.0 min	4.0 h 48.0 min

From this comparison several conclusions can be drawn:

- 1) The global parameter  $k_{\text{eff}}$  of the three solutions are close to each other. Between the full PBP solution and the hybrid solution there is a difference of 192.0 pcm.
- 2) Bigger differences are found in the Doppler temperature (and fuel pellet center line temperature). The hybrid model is overestimating the maximum cladding temperature predicted by the full PBP solution by approximately 200.0 K. Similarly, it predicts a higher Doppler temperature (92.7 K) as compared to the one of the full PBP. The reasons for these deviations are attributed to several parameters, listed hereafter.
  - a. Geometrical parameters and differences in the TH models used for the hybrid FA and full PBP solution.
  - b. Reduce of accuracy for the feedback method exchange using the MED memory.
  - c. Discrepancies in the N solution at nodal and cell level in the hybrid method. Errors may add up to larger values.
  - d. Refinement level is limited to the TH solution (mesh dependency).

In Fig. 63 (a) the Doppler temperature of the fuel rod number 416 predicted by the CBY/SCF hybrid approach is compared to the Doppler temperature of the fuel assembly 159 predicted by the nodal solution and to the core averaged Doppler temperature. This shows the capability of the CBY/SCF hybrid approach to predict not only the FA with the highest power but also the hottest fuel pin. In Fig. 63 (b), the radial distribution of the fuel rod temperature predicted for the hottest pin by the CBY/SCF hybrid approach is compared to the one of the fuel assembly 159 (neighboring FA of the hybrid one calculated according to the nodal approach). Is advisable to analyze Fig. 63 (a, b) and refer to the values given previously in Table 31.

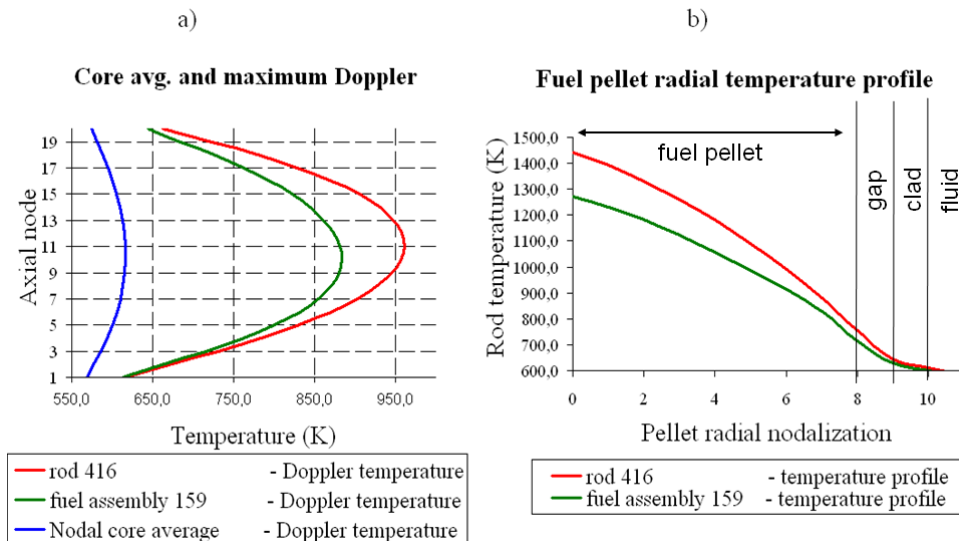


Fig. 63. Axial shape of the Doppler temperature (a) and fuel pellet radial temperature profile (b).

Similar to the previous figure, local safety parameters which include the inner and outer cladding temperature are plotted Fig. 64.

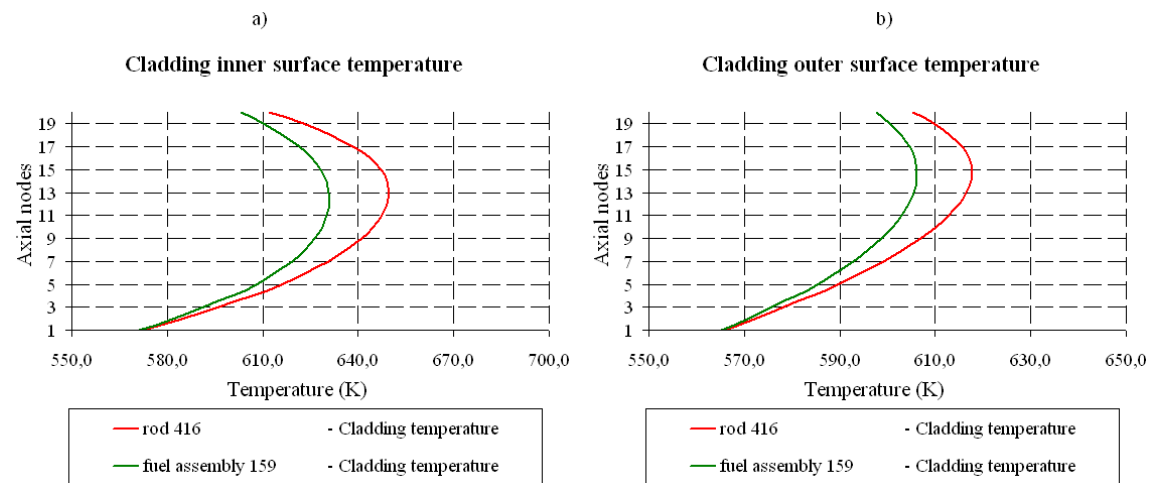


Fig. 64. Axial shape of the Doppler temperature (a) and fuel pellet radial temperature profile (b).

The Fig. 65 represents 2D normalized radial FA power for the core quarter where the “hybrid FA” is located (orange section in Fig. 61 (b)). This normalized power distribution predicted by CBY/SCF hybrid approach is compared to the 2D normalized power distribution calculated by the PBP approach.

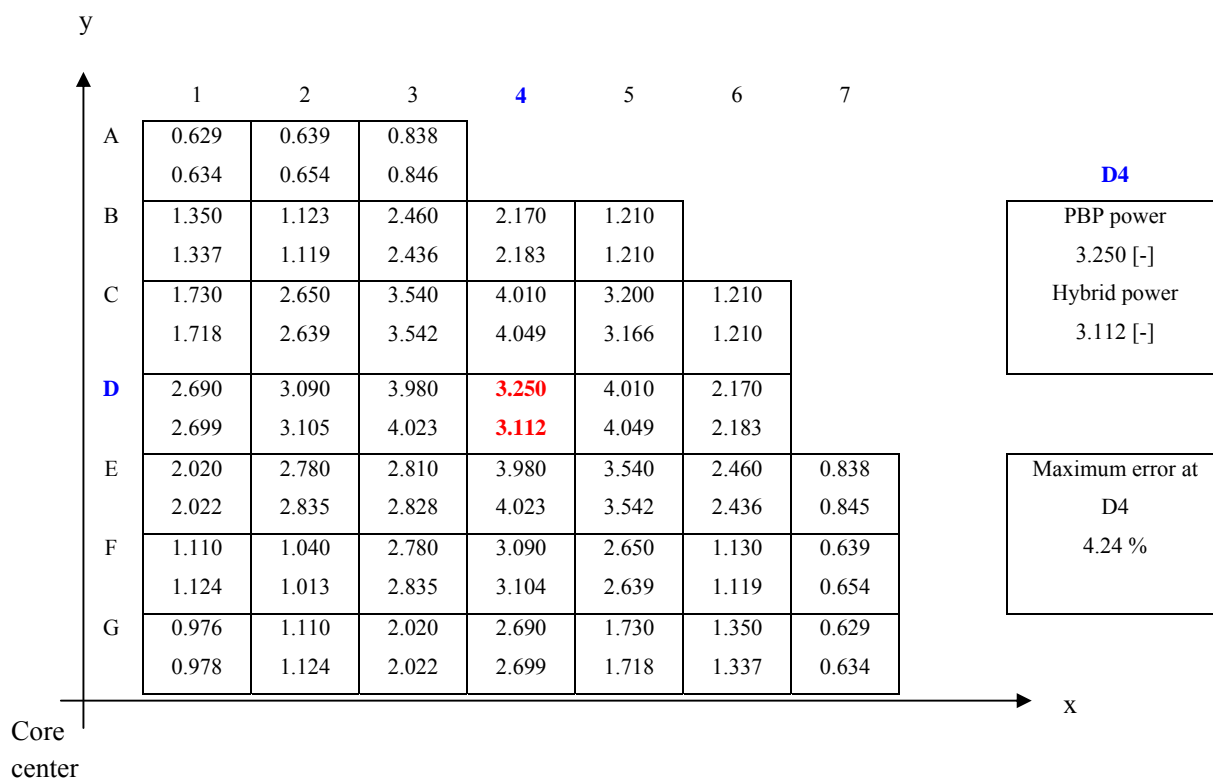


Fig. 65. Comparison of the FA base normalized 2D power distribution of one fourth of the core according to the benchmark specifications for the PBP computation and the hybrid CBY/SCF simulation.

The maximum error found for the nodal parameters between the PBP and the hybrid solution amounts to 4.24%, while the reduction of computational time is of  $t = 32.0$  hours. This error is found at the location of the “hybrid FA” (assembly of interest) where the CR is ejected, as seen in Fig. 65-D4). In Fig. 66, Fig. 67 and Fig. 68 the isometric top view, the isometric bottom view and the 2D top view of the errors in the pin power prediction for the “hybrid FA” between the CBY/SCF hybrid solution and the full PBP solution (reference) are exhibited. The comparison of the pin power predicted by CBY/SCF hybrid approach and the PBP solution obtained for the assembly of interest (Fig. 65-D4), shows that the maximal relative error in the 2D normalized radial power distribution is 3.85%. This error represents the accuracy of the hybrid solution with respect to the PBP solution and is calculated as explained in Chapter 5.2.1, Fig. 24.

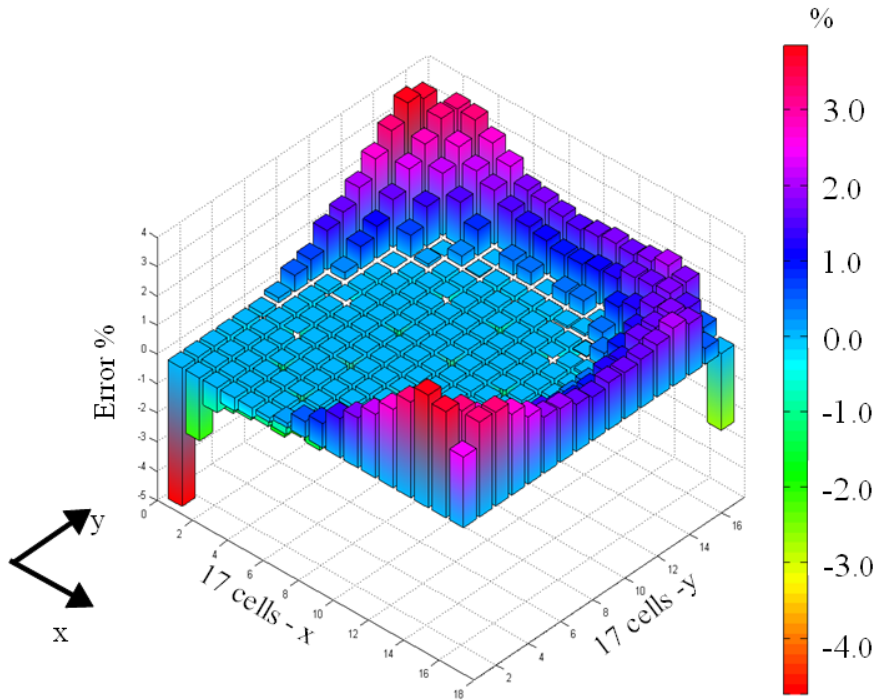


Fig. 66. Hybrid FA: Percent error between the PBP (reference) and the hybrid solution (isometric top view of the FA).

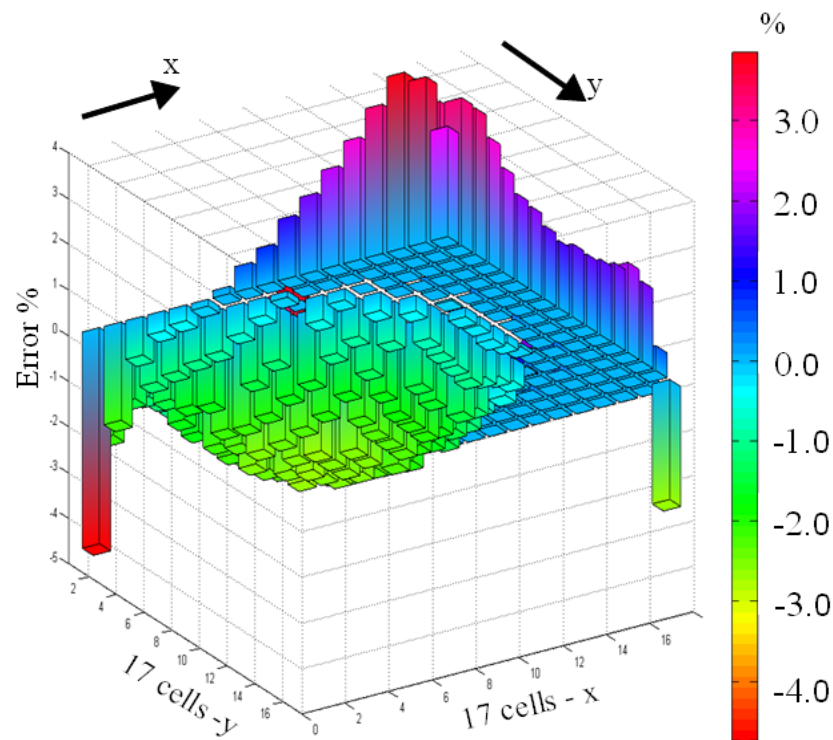


Fig. 67. Hybrid FA: Percent error between the PBP (reference) and the hybrid solution (isometric bottom view of the FA).

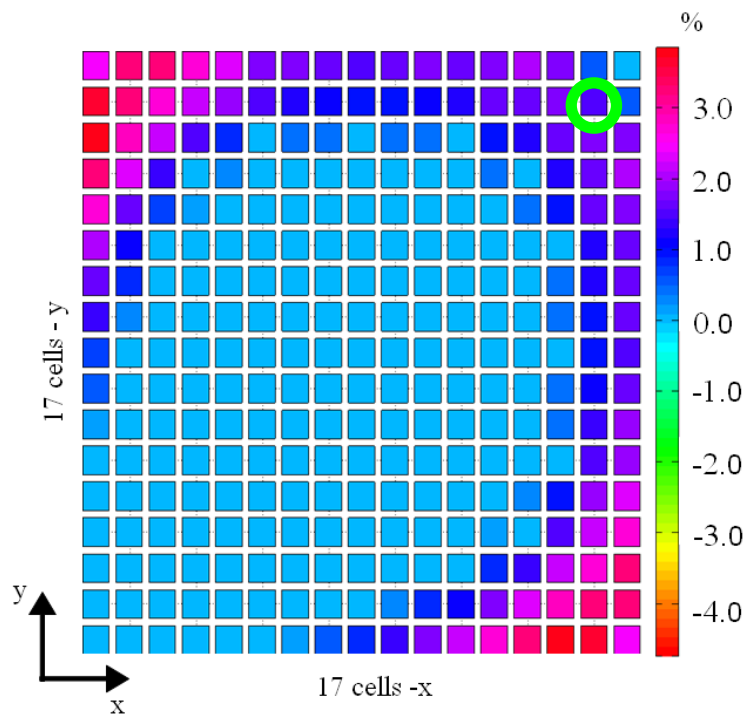


Fig. 68. Hybrid FA: Percent error between the PBP (reference) and the hybrid solution (2D top view of the FA).

As can be seen in Fig. 69, the “hybrid FA” is surrounded by two MOX assemblies (C3, E5) and six UOX assemblies (C4, C5, D3, D5, E3 and E4) with different enrichment and burn-up. Strong discrepancies between the PBP and the hybrid approaches are located at the boundaries of the “hybrid FA”. In Fig. 68 is illustrated that the edges on the top-left and bottom-right experience a higher deviation from the PBP solution (reference). The reason of this is that MOX FAs are located at these boundaries (corners). For example, the delay neutron fraction for MOX FAs is greater than the one of a UOX FA and therefore large discontinuities are found on the limits with MOX FAs. This effect is more pronounced when passing the BCs from a nodal based FA simulation (MOX FA) to a pin based FA simulation (UOX hybrid FA) and vice versa. Further studies are needed to investigate the influence of different transverse leakage interpolations in connection with the implementation of the hybrid solution.

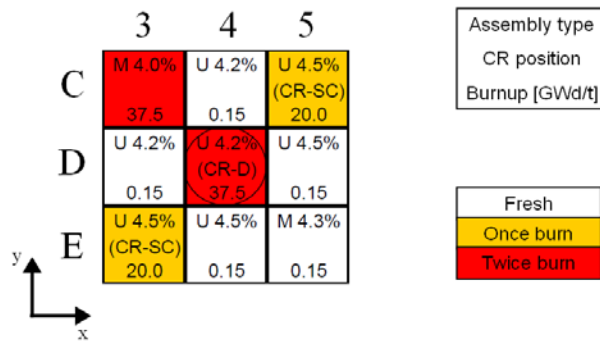


Fig. 69. Configuration of the fuel assemblies surrounding the hybrid (central) assembly.

In Fig. 70 the radial coolant temperature at the core elevation with the highest axial temperature peak as predicted by the CBY/SCF hybrid solution is shown. It clearly demonstrates the new capabilities of the CBY/SCF hybrid approach that allow the direct prediction of local safety parameters at pin level (the FA of interest). In addition, this graph was created using the powerful post-processing capability of the NURESIM platform, where all the simulation data are stored in fields attached to meshes of the different domains (MED format).

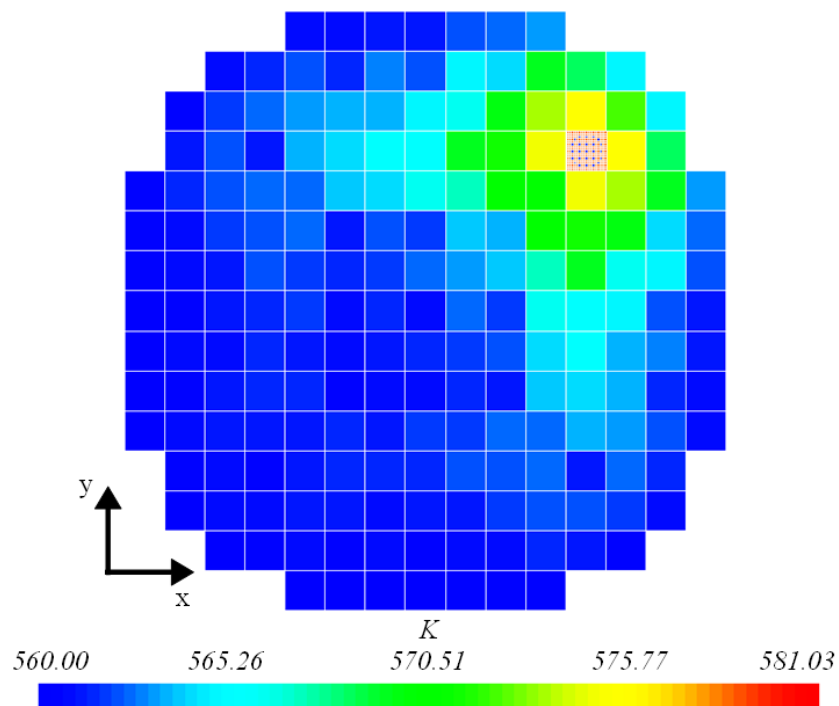


Fig. 70. Coolant temperature at the core exit predicted by the hybrid scheme CBY/SCF.

Finally it can be concluded that the main advantage of the hybrid N/TH approach implemented in CBY/SCF is the direct prediction of local safety parameters, e.g. maximal cladding temperature or maximal fuel temperature in the core region of interest. Due to the combination of a nodal and cell solution, the core behavior under transient conditions can be described in a multi-scale spatial approach with one simulation. In addition, the computing time is very important for industrial-like simulations of whole cores to predict safety parameters. In this sense, the use of the hybrid approach leads to a reduction of the computing time from about one and a half day (PBP solution) to about five hours (CBY/SCF hybrid). This is a very attractive aspect considering that there are still potentials to speed-up the neutronic solvers. Potential applications of this methodology are e.g. control rod ejection accidents (REA), MSLB, ATWS, etc. However, extensions of the hybrid solution to time dependent problems are still necessary to fully take advantage of it in industrial relevant safety analysis.

---

## 8 Summary and conclusions

This dissertation contributes to the further development of the multi-physics and multi-scale European Platform for nuclear reactor simulations, named NURESIM, in the following specific areas:

1. Extension of the NURESIM platform by the fully implementation of a thermal-hydraulic sub-channel code named SUBCHANFLOW.
2. Implementation of both a steady state and transient coupling scheme between SUBCHANFLOW and the neutronics code COBAYA3 for the analysis of nuclear reactor cores for both square and hexagonal fuel assemblies at nodal level. This is done making use of the platform's functionalities such as mesh superposition and automatic interpolation for the involved domains.
3. Implementation of a steady state and transient coupling scheme between SUBCHANFLOW and COBAYA3 for pin-wise solutions of PWR cores with square fuel assemblies.
4. Informatic developments for the platform in order to visualize the meshes (of the different domains involved in the coupling) as well as to facilitate the online visualization of the simulation's results of the developed coupled codes inside SALOME.
5. Extension of SUBCHANFLOW for hybrid solutions (steady state and transient). This goal involved the development of a pre-processor used for input deck generation of big problems.
6. Extension of COBAYA3 for hybrid solutions (steady state) including the extensions needed for the automatic mesh generation of the neutronic domain in a multi-scale approach (nodal and cell wise).
7. Development and implementation of coupling schemes between the extended codes COBAYA3 and SUBCHANFLOW for hybrid solutions of reactor cores at stationary conditions inside the platform.

Moreover, substantial contributions were undertaken for the testing, verification and validation of the developed coupled schemes by both code-to-code comparison or by code-to-data comparison when data was available. The objective was to increase the confidence in the coupled codes for the analysis of reactor core accidental scenarios that are important to assess the safety of nuclear power plants. These contributions are concentrated in the following topics:

1. Verification of the implementation of SUBCHANFLOW in the NURESIM platform and its coupling with COBAYA3 by the analysis of the NEABEN LWR core transient benchmark.
2. Verification of the stand alone hybrid solution capability of the codes SUBCHANFLOW and COBAYA3 for steady state simulations.

3. Validation of the nodal coupling scheme between COBAYA3 and SUBCHANFLOW using different benchmark problems. For square fuel assemblies (code-to-code comparison) the following benchmarks were analyzed: PWR MOX/UO<sub>2</sub> core transient benchmark, PWR TMI-1 MSLB benchmark and PWR MOX/UO<sub>2</sub> boron dilution simulation.

The third benchmark was also used for the validation of the boron dilution transport model implemented in SUBCHANFLOW. For hexagonal fuel assemblies (code-to-data comparison) plant data measured in the VVER type plant Kalinin-3 was used to validate the prediction capabilities of COBAYA3/SUBCHANFLOW. Moreover, the validation of the COBAYA3/SUBCHANFLOW hybrid solution was done by a code-to-code comparison based on the steady state problem for PWR core derived from the PWR MOX/UO<sub>2</sub> benchmark.

Based on the extensive validation work listed above it can be stated that the prediction capability of the new coupled code based on both the nodal/cell level and the hybrid approach has been successfully demonstrated. In addition, the new functionalities of the NURESIM platform were tested and used in the frame of the developments done in this dissertation. Despite the few bugs related to the interpolation tool for hexagonal geometries, the coupling scheme performs as expected. To overcome these bugs, alternative solutions were developed and implemented so that the coupled code COBAYA3/SUBCHANFLOW could be applied to simulate cores with hexagonal fuel assemblies. This alternative solution was based on the direct mapping between the neutronic and thermal-hydraulic domains facilitating the realization of a consistent coupling which bypassed the standard interpolation tool.

With respect to the development of accurate multi-scale multi-physics methods a coupled scheme between a 3D neutron diffusion reactor dynamic code and a sub-channel base thermal-hydraulic code, both which interact inside the NURISP platform, is presented. The advantages for this revolutionary scheme includes the use of improved neutron diffusion for reactor dynamic solutions and precise nodal/channel (hexagonal and square geometries) and cell/sub-channel (square geometries) base analysis of LWRs. It also include extensions for hybrid solutions (non-conform geometries), accurate boron transport schemes, geometrical flexibility in terms of radial and axial discretizations, simplification of code input deck generation by the use of a pre-processor and optimization of the coupled solution. Ultimately, the coupling scheme between the reactor dynamic code COBAYA3 and the thermal-hydraulic code SUBCHANFLOW promises substantial advances in the prediction of local safety parameters. This coupled solution is suited for LWR transients where there is a strong coupling between neutronics and thermal-hydraulics.

## 9 Outlook

Despite the described extensions, developments and implementations performed in the frame of this dissertation, there are still many areas where future efforts should be concentrated. These efforts for improving the work done are listed hereafter:

Developments related to the core simulator COBAYA3:

1. Improvement in COBAYA3 to perform consecutive iterations over one time step (for transient analysis), leading to the development of fully implicit coupling schemes inside the SALOME platform.
2. Exploit the parallel capabilities of COBAYA3 (in SALOME) to accelerate the solution.
3. Verification and validation of the dynamic selection for the hybrid assembly (ies).
4. Extension of the hybrid scheme to time dependence safety-relevant solutions.
5. Developments in COBAYA3 to create hybrid meshes based on its own input.

Developments related to the thermal-hydraulic code SUBCHANFLOW:

1. Extension of the SUBCHANFLOW pre-processor for pin-by-pin hexagonal geometries.
2. Extensions of the SUBCHANFLOW pre-processor to account for bypass channels of BWR fuel assemblies (this includes the creation of thermal connection tables for SUBCHANFLOW between assembly cases and by-pass channels and proper handling of the bypass intersection sub-channels).
3. Automatic adjustment of the minimum axial flow iterations (thermal-hydraulics) for smooth transients.
4. Automatic adjustment of the solution method in case of strong density gradients (use of incompressible flow instead of weakly compressible flow).

Developments related to the SALOME wrapping (directly or indirectly):

1. Integration of the SUBCHANFLOW pre-processor inside the SALOME platform as a black box of the component SUBCHANFLOW. This is absolutely necessary in case of dynamic search of hybrid assemblies for coupled solutions.
2. Testing and further verification and validation of the already integrated structural and fluid meshes for SUBCHANFLOW (for hexagonal and square geometries). This will avoid the forced usage of rod center discretizations for PBP or hybrid assemblies, leading to faster convergence.

3. Independent mesh generation and field handling for SUBCHANFLOW.
4. Exploit the parallel capabilities of the SALOME platform.

Developments related to the code coupling inside SALOME:

1. Modification of the wrapping in order to be able to run in the next version of SALOME, V-6.
2. Use of the new interpolation tool: MED\_REMAPER.
3. Examine in detail BWRs and their corresponding transients (void feedback already implemented for COBAYA3 and SUBCHANFLOW, verification and validation needed).
4. Extensive testing of the steady state hybrid scheme by modeling mini-cores and full cores with different boundary conditions.

---

## 10 References

[Alcouffe01] R.E. Alcouffe, PARTISN: A time-dependent Parallel Neutral Particle Transport Code System, *Report LA-UR-08-07258*, Los Alamos National Laboratory, Nevada, USA, November, 2008.

[Aumiller01] D.L. Aumiller, E. T. Tomlinson and R.C. Bauer, Incorporation of COBRA-TF in an integrated code system with RELAP5-3D using semi-implicit coupling, *RELAP5 International Users Seminar*, Utah, USA, September 4-6, 2002.

[Anglar01] H. Anglar, Applied Reactor Technology and Nuclear Safety, *Internal report: draft*, Stockholm, June, 2009.

[Ansys01] ANSYS-CFX-Solver Theory Guide, *Release 12.0*, ANSYS, Inc. April, 2009.

[Armand01] A. Armand, The resistance During the Movement of a Two-Phase System in Horizontal Pipes, *vol. 828 or AERE-Lib/Trans, Izvestiya Vsesojuznogo Teplotekhnicheskogo Instituta*, 1946.

[Azmy01] Y. Azmy, The three-dimensional discrete ordinates neutral particle transport code TORT: An Overview, *OECD/NEA report*, December 2-3, 1996.

[Baerd01] C. Baerd, P. Hilton, S. Lider and D. Risher, 2006, Methodology for Coupling Physics and Systems Codes for Accident Simulations, *PHYSOR*, Vancouver, September, 2006.

[Baudron01] A. Baudron, N. Crouzet, C. Döderlein and E. Royer, Unstructured 3D MINO/FLICA4 coupling in SALOME Application to JHR transient analysis, *International Conference on the Physics of Reactors*, Interlaken, Swiss, September, 2008.

[Bazin01] P. Bazin and M. Pelissier, CATHARE 2 V25\_1: description of the base revision 6.1 physical laws used in the 1D, 0D and 3D modules, *CEA/DER/SSTH/LDAS/EM/2005-038*, 2006.

[Beckert01] C. Beckert and R. Koch, Reactor cell calculations with the codes HELIOS, MCNP and TRANS-FAY: comparison of the results, *Annual Report 2004 – Wissenschaftlich-Technische Berichte: FZR 155*, May, 2005.

[Bestion01] D. Bestion, D. Cacuci, J.M. Aragonés, P. Caddington, L. Dada and C. Chauliac, NURESIM: A European Platform for Nuclear Reactor Simulation, *Internal report*, 2006.

[Bertolotto01] D. Bertolotto, Coupling a system code with computational fluid dynamics for the simulation of complex coolant reactivity effects, *Ph.D. thesis*, École Polytechnique Fédérale de Lausanne, Swiss, 2011.

- [Blasius01] H. Blasius, Das Ähnlichkeitsgesetz bei Reibungsvorgängen in Flüssigkeiten, *Forshungs-Arbeit des Ingenieur-Wesens 131*, Germany, 1913.
- [Bonalumi01] R.A. Bonalumi, W.S. Liu, W. Yousef and J. Pascoe, A Two Unequal Fluids Model For Thermal-Hydraulics Analysis, *1<sup>st</sup> International Conference on Numerical Methods in Nuclear Engineering*, Montreal, 1983.
- [Bosso01] S. Bosso, R. Van Parys, C. Schneidisch and J. Zhang, Analysis of the main steam line break accident with loss of offsite power with the fully coupled RE-LAP5/PANTHER/COBRA3C\_TE code package, *NURETH-11*, Avignon, October, 2005.
- [Bowman01] S.M. Bowman, SCALE 6: Comprehensive nuclear safety analysis, *Nuclear Technology*, vol. 174, May, 2011.
- [Bruna01] G. Bruna, F. Dubois, F. Fouquet, E. Hourcade, J.C. Pallec, C. Poinot, E. Richebois, E. Royer, HEMERA: a 3D coupled core-plant system for accidental reactor transient simulation, *ICAPA 7th*, Nice, 2007.
- [Burwell01] J. Burwell, The thermohydraulic code ATHLET for analysis of PWR and SWR systems, *Proc. Of the 4<sup>th</sup> Int. Topical Meeting on Nuclear Reactor Thermal-Hydraulics NURETH-4*, Karlsruhe, Germany, October 10-13, 1989.
- [Busch01] R. Busch, A primer for criticality calculations with DANTSYS, *report LA-13265, VC-714*, Los Alamos, August, 1997.
- [Cadinu01] F. Cadinu, T. Kozlowski and P. Kudinov, Study of algorithmic requirements for a system-to-CFD coupling strategy, *KTH Internal report*, 2008.
- [Calleja01] M. Calleja, R. Stieglitz, V. Sanchez, J. Jimenez and U. Imke, A coupled neutronic/thermal-hydraulic scheme between COBAYA3 and SUBCHANFLOW within the NURESIM simulation platform, *PHYSOR, Advances in Reactor Physics*, USA, April 2012.
- [Calleja02] M. Calleja, J. Jimenez, U. Imke and V. Sanchez, Validation of the Coupling between COBAYA3 and SUBCHANFLOW for the Simulation of Boron Dilution Transients, *Annual meeting of the spanish nuclear society*, Caceres, Spain, 2012.
- [Cardoni01] J.N. Cardoni, Nuclear Reactor Multi-physics Simulations with Coupled MCNP5 and STAR-CCM+, *Ph.D. thesis*, University of Illinois at Urbana-Champaign, USA, 2011.
- [Chiba01] G. Chiba, M. Tsuji and Y. Shimazu, Development of the hierarchical domain decomposition boundary element method for solving the three-dimensional multiregion neutron diffusion equations, *Nuclear Science and Technology*, August, 2001.

- [Cho01] N. Cho, Fundamentals and Recent Developments of Reactor Physics Methods, *Nuclear Engineering and Technology*, February, 2005.
- [Christinne01] M. Christinne, M. Avramova, Y. Perin and A. Seubsrt, Coupled TORT-TD/CTF Capability for High-Fidelity LWR Core Calculations, *PHYSOR*, 2010.
- [Christensen01] B. Christensen, Three-dimensional Static and Dynamic Reactor Calculations by the Nodal Expansion Method, *Risø National Laboratory internal report*, DK-4000 Roskilde, Denmark, May, 1985.
- [Cole01] R.K. Cole, Coupling of MELCOR to other Codes under an Executive Program using PVM Message Exchange, *RELAP User's Seminar*, Utha, USA, September, 2002.
- [Collins01] S. B. Collins, Multi-scale Methods for Nuclear Reactor Analysis, *Ph.D. thesis*, University of Michigan, Chicago, USA, 2011.
- [Cooper01] International cooperation, Use and Development of Coupled Computer Codes for the Analysis of Accidents at Nuclear Power Plants, *IAEA report no. 1539*, Vienna, November, 2007.
- [Coppolani01] P. Coppolani, N. Hassenboehler, J. Joseph, J.F. Peterot, J.P. Py and J.S. Zampa, La Chaudiere des réacteurs à eau sous pression, *EDP Science INSTNIAEA-TECDOC report no. 1539*, 2004.
- [Coulomb01] F. Coulomb, Domain Decomposition and Mixed Finite Elements for the Neutron Diffusion Equation, *3<sup>rd</sup> International Symposium*, Houston, USA, Chapter 25, 295-313, 1989.
- [Criekingen01] S. Van Criekingen, PARAFISH: a Parallel FE – Pn Neutron Transport Solver based on Domain Decomposition, *Annals of Nuclear Energy*, August, 2010.
- [Crouzet01] N. Crouzet, NURISP SP3-Multi-Physics Group, *NURISP General Seminar, Karlsruhe*, 2012.
- [DAuria01] F. D'Auria and A. Bousbia-Salah, Use of coupled code technique for best estimate safety analysis of nuclear power plants, *Progress in nuclear energy, Volume 49, Issue 1*, 2007.
- [Demazier01] C. Demazier, M. Stálek and P. Vinal, Comparison of the U.S. NRC PARCS Core Neutronics Simulator Against In-Core Detector Measurements for LWR Applications, *International Agreement Report no. NUREG/IA-0414*, April, 2012.
- [Diop01] C. Diop, O. Petit, E. Dumontiel, F.X. Hugot, Y.K. Lee, A. Mazzolo and J.C. Trama, TRIPOLI-4: A 3D continuous energy Monte Carlo transport code, *PHYTRAI: First International Conference on Physics and Technology of Reactors and Applications*, Marrakech, Morocco, March 14-16, 2007.

- [Dittus01] P. Dittus, L. Boelter, Heat transfer in automobile radiators of the tubular type, *University of California Publications in Engineering*, vol. 2, no. 13, pp. 443-261, 1985.
- [Downar01] T. Downar, Coupled Codes for Multi-Physics Nuclear Reactor Simulation, *Lecture-report*, Purdue University, USA, July, 2006.
- [Downar02] T. Downar, T. Kozlowski and R.M. Miller, Analysis of the MSLB Benchmark with the coupled neutronic and thermal-hydraulic code RELAP5/PARCS, *PHYSOR*, 2000.
- [Downar03] T. Downar, D. Weber, T. Sofu, D. Pointer, A. Tentner and Z. Zhong, Extension of Integrated Neutronic and Thermal-Hydraulic Analysis Capabilities of the “Numeric Nuclear Reactor” Software System for BWR Applications, *PHYSOR*, Vancouver, Canada, September, 2006.
- [Downar04] T. Downar, Y. Xu and A. Ward, Multi-Physics Coupled Code Reactor Analysis with the US NRC Code System TRACE/PARCS, *PHYSOR*, Vancouver, Canada, September, 2006.
- [Downar05] T. Downar, V. Seker and J. Thomas, Reactor physics simulations with coupled Monte Carlo calculation and computational fluid dynamics, *ICENES*, Istanbul, June, 2007.
- [Downar06] T. Downar and T. Kozowski, PWR MOX/UO<sub>2</sub> Core Transient Benchmark, *Nuclear Science, NEA/NSC/DOC*, 2006.
- [EDFCEA01] EDF, CEA and DEN, Integration of meshers as plug-ins into SMES – Use of SMDS API(SMESH SALOME MODULE), *Internal report no. OC*, October, 2006.
- [EDFCEA02] EDF R&D, ANL, ORNL and IBM, SALOME Demonstration, *report presented at SALOME: A unified computational framework (orkshop)*, Paris, France, February, 2009.
- [Espiel01] F. Espiel, High Accuracy Modeling for Advanced Nuclear Reactor Core Designs Using Monte Carlo Based Coupled Calculations, *Ph.D. thesis*, Pennsylvania State University, USA, 2010.
- [Ferrouk01] M. Ferrouk, S. Aissani, F. D’Auria, A. DelNevo and A. Bousbia, Assessment of 12 CHF prediction methods, for an axially non-uniform heat flux distribution, with the RELAP5 computer code, *Nuclear Engineering and Design*, 2008.
- [Ferroukhi01] H. Ferrouki and P. Coddington, Three dimensional space time kinetic analyses with CORETRAN and RETRAN3D of the NEACRP PWR rod ejection benchmark, *Technical report no. INIS-CH-034*, March, 2001.
- [Finnemann01] H. Finnemann, K. Ivanov, A. Baratta and T. Beam, Nodal kinetics model upgrade in the Penn State coupled TRAC/NEM codes, *Annals of Nuclear Energy*, 1999.

- [Fraikin01] R. Fraikin, NEA-NSC 3-D PWR Core Transient Benchmark: Uncontrolled Withdrawal of Control Rods at Zero Power, *OECD report no. NEA/NSC(93)*, 1993.
- [Fridman01] Fridman, E. and Leppänen, On the Use of the Serpent Monte Carlo Code for Few-group Cross Section Generation, *Ann. Nucl. Energy*, 38 (2011) 1399-1405, June 2011.
- [Garber01] D. Garber and D. Diamond, A model for boron transport and reactivity in a BWR, A *Brookhaven National Laboratory report no. BNL-NUREG-29866*, 1981.
- [Gaston01] D. Gaston, H. Park, S. Kadioglu, R. Martineau and W. Taitano, Tightly Coupled Multiphysics Simulations for Pebble Bed Reactors, *Mathematics and Computation*, New York, USA, May, 2009.
- [Gaston02] D. Gaston, G. Hansen, S. Kadioglu, D.A. Knoll, C. Newman, H. Park, C. Permann and W. Taitano, Parallel Multiphysics Algorithms and Software for Computational Nuclear Engineering, *Journal of Physics: Conference Series 180*, 2009.
- [Geist01] A. Geist, A. Beguelin, J. Dongarra, PVM (Parallel Virtual Machine): User's Guide and Tutorial, *MIT press*, USA, 1994.
- [Gicquel01] L. Gicquel, Computer codes used by the nuclear regulatory authorities, *Report no. UKEPR-0002-147-issue 03*, 2011.
- [Gomez01] A. Gomez, V. Sanchez, U. Imke and R. Macian, DYN3D: A best estimate coupled system for the evaluation of local safety parameters, *KTG*, Berlin, Germany, 2011.
- [Gomez02] A. Gomez, V. Sanchez, S. Kliem, A. Gommlich and U. Rohde, DYN3D/FLICA coupling and Integration of DYN3D inside the NURESIM Platform, *17<sup>th</sup> Pacific Basin Nuclear Conference*, México, 2010.
- [Gomez03] A. Gomez, 2011, Further Developments of Multiphysics and Multiscale Methodologies for Coupled Nuclear Reactor Simulations, *Ph.D. thesis*, Technical University of Munich, Munich, 2011.
- [Gommlich01] A. Gommlich, S. Kliem, U. Rohde, A. Gomez and V. Sanchez, Coupling of the neutron-kinetic core model DYN3D with the Thermal-hydraulic code FLICA4 within the NURESIM platform, *Annual Meeting of the German Nuclear Society*, Berlin, Germany, May 4-6.
- [Grandi01] G. M. Grandi, Effects of the Discretization and Neutronic Thermal Hydraulic Coupling on LWR Transients, *NURETH-13*, Japan, September 27-October 2, 2009.

- [Guelfi01] A. Guelfi, D. Bestion, M. Boucker, P. Bouldier, P. Fillion, M. Grandoto, J. Hérard, E. Hervieu and P. Péturaud, NEPTUNE: A new software platform for advance nuclear thermal hydraulic, *Nuclear Science and Engineering Vol. 156*. 281-324, 2007.
- [Herrero01] J. Herrero and J. Jimenez, COBAYA3 Developers Manual, *Internal Report*, Department of Nuclear Engineering, Universidad Politécnica de Madrid, May, 2010.
- [Herrero02] J. Herrero, Advanced multi-scale pin-by-pin/core methods in three-dimensional geometries and multigroups for Light Water Reactors calculations, *Ph.D. thesis*, Department of Nuclear Engineering, Universidad Politécnica de Madrid, May, 2010.
- [Imke01] U. Imke, V. Sanchez, Validation of the Subchannel Code SUBCHANFLOW Using the NUPEC PWR Test (PSBT), *Science and Technology of Nuclear Installations*, Article ID 465059, June, 2012.
- [Ishii01] M. Ishii and T. Hibiki, Thermo-Fluid Dynamics of Two-Phase Flow, *Springer*, Purdue University, August, 2006.
- [Ivanov02] K. Ivanov, A. Baretta and T. Beam, Pressurized Water Reactor Main Steam Line Break (MSLB) Benchmark: Final Specifications, *Nuclear Energy Agency*, 1999.
- [Ivanov03] K. Ivanov, V.A. Tereshonok, S.P. Nikonov, M.P. Lizorkin, K. Velkov and A. Pautz, KALININ-3 coolant transient benchmark: Switching off of one of the four operating main circulation pumps at nominal reactor power, *OECD report no.NEA-1848/04 zz-KALININ3*, 2008.
- [Ivekovic01] I. Ivekovic, Burn-up Dependent Fuel Properties in Fuel Management Core Calculation, *7<sup>th</sup> International Conference on Nuclear Option in Countries with small and medium Electricity Grids*, 2008.
- [Jackson01] C.J. Jackson and H. Finnemann, Verification of the Coupled RELAP5/PANBOX System with the NEACRP LWR Core Transient Benchmark, *International Conference on Mathematics and Computations, Reactor Physics and Environmental Analyses*, Portland, USA, April 30-May 4, 1995.
- [Jeong01] J.J. Jeong, K. S. Ha, B. D. Chung and W. J. Lee, A Multi-Dimensional Thermal-Hydraulic System Analysis Code: MARS 1.3.1, *Journal of the Korean Nuclear Society*, June 1999.
- [Jimenez01] J. Jimenez, Desarrollo e implementación de la descomposición en subdominios del acoplamiento neutrónico-termohidráulico mediante disecciones alternadas con un sistema de cálculo multiescala, *Ph.D. thesis*, Universidad Politécnica de Madrid, 2010.
- [Jimenez02] J. Jimenez, Zimmermann, O. Zerkak and Ph. Emonot, Presentation of the Multi-Physics Subproject of the NURISP European Project, *37<sup>th</sup> Annual meeting of the Spanish Nuclear Society*, Burgos, Spain, 2011.

- [Jimenez03] J. Jimenez , J.J. Herrero, D. Cuervo and J.M. Aragonés, Whole Core Pin-by-Pin Coupled Neutronic-Thermal-hydraulic Steady state and Transient Calculations using COBAYA3 code, *17<sup>th</sup> Pacific Basin Nuclear Conference*, Cancún, Q.R., México, 2010.
- [Jimenez04] J. Jiménez, D. Cuervo and J.M. Aragonés, A domain decomposition methodology through alternate dissections for coupled neutronic and thermal-hydraulic analyses in COBAYA3, *Nuclear Engineering and Design*, 2010.
- [Junge01] O. Junge and M. Dellnitz, Set Oriented Numerical Methods for Dynamical Systems, *Internal Report, Department of mathematics and computer science University of Paderborn*, November, 2004.
- [Kazimi01] M. Kazimi and N. Todoreas, Nuclear Systems I – Thermal Hydraulic Fundamentals, *Hemisphere P. Corporation*, USA, 1990.
- [Kazimi02] M. Kazimi and M. Massoud, A Condense Review of Nuclear Reactor Thermal-Hydraulic Computer Codes for Two-Phase Flow Analysis, *Energy Laboratory Report No. MIT-EL 79-018*, 1980.
- [Keco01] M. Keco, N. Debrecin and D. Grgic, Applicability of Coupled Code RELAP5/GOTHIC to NPP Krsko MSLB Calculation, *Nuclear Energy for New Europe*, 2005.
- [Kliem01] S. Kliem, S. Mittag, A. Gommlich and P. Apanasevich, Definition of a PWR boron dilution benchmark, *A Collaborative Project NURISP report*, February, 2011.
- [Kliem02] S. Kliem, Ein Modell zur Beschreibung der Kühlmittelvermischung und seine Anwendung auf die Analyse von Borverdünnungstransienten in Druckwasserreaktoren, *Ph.D. thesis*, August, 2010.
- [Kliem03] S. Kliem and Y. Kozmenkov, Comparative analysis of a pump coast-down transient using the coupled code systems DYN3D-ATHLET and DYN3D-RELAP5, *PHYSOR*, 2012.
- [Kothe01] D. Kothe, Consortium for Advance Simulation of Light Water Reactors, *Internal report*, USA DOE, 2010.
- [Kulikowska01] T. Kulikowska, An Introduction to the Neutron Transport Phenomena, *Workshop on Nuclear Data and Nuclear Reactors*, 2012.
- [Lanfranco02] M. Lanfranco and T. Schlenberg, Coupled ERANOS/TRACE for HPLWR 3 pass core analysis, *Mathematics and Computation*, New York, USA, May, 2009.
- [Leclaire01] N. Leclaire, I. Duhamel, E. Gagnier, Y. Lee and C. Venard, Experimental validation of the French cristal V1.0 package, *American Nuclear Societ- Integration Criticality Safety into Resurgence of Nuclear Power*, Knoxville, September, 2005.

- [Leonard01] B.P. Leonard, The ultimate conservative difference scheme applied to unsteady one-dimensional advection, *Computer Methods in Applied Mechanics and Engineering*, North Holland, May, 1990.
- [Lewis01] E. Lewis and W. Miller, Computational Methods of Neutron Transport, *John Wiley and Sons, Inc.*, New York, 1984.
- [Lozano01] J. Lozano, J.M. Aragonés and N. García, Transient analysis in the 3D nodal kinetics and thermal-hydraulics ANDES/COBRA coupled system, *International Conference on the Physics of Reactors*, Interlaken, September, 2008.
- [Lozano02] J. A. Lozano, Desarrollo de un Código Nodal Analítico de Difusión Neutrónica en Multigrupos para Reactores en Geometías 3D Rectangulares y Hexagonales, *Ph.D. thesis*, Universidad Politécnica de Madrid, 2009.
- [Lozano03] J. Lozano, J. Jiménez, N. García and J. M. Aragonés, Extension of the analytic nodal diffusion solver ANDES to triangular-Z geometry and coupling with COBRA-IIIc for hexagonal core analysis, *Annals of Nuclear Energy*, 2010.
- [Macian01] R. Macian, J. Juanas, T. Barrachina and R. Miró, Uncertainty and Sensitivity analysis in the neutronic parameters generation over the coupled thermalhydraulic-neutronic nuclear power plant simulations, *Mathematics and Computation*, New York, May, 2009.
- [Marleau01] G. Marleau, R. Roy and A. Hébert, DRAGON : A collision probability transport code for cell and supercell calculations, *Internal report IGE-157*, Insitute de Génie Nucléaire, École Polytechnique de Montréal, Montréal, Québec, 1994.
- [Mcnp01] MCNP Monte Carlo Team, X-5, MCNP5\_RSICC\_1.30, *LA-UR-04-5921-approved for publication*, Los Alamos National Laboratory, Los Alamos, USA, 2004.
- [Megnaud01] F. Magnaud, Resolution of the neutron transport equation in CRONOS code, *R-Report 12353 CEA; Saclay*, France, 1994.
- [Monferrer01] C.P. Monferrer, S. Chiva, R. Miro, R. Pellacani and R. Macian, A procedure for Coupled CFD-Neutronic Calculations using ANSYS CFX 12.1 and PARCS, *Eccomas thematic conference on COUPLED PROBLEMS*, KOS Island, Greece, June, 2011.
- [Mousseau01] V. Mousseau and M. POPE, Accuracy and efficiency of a coupled neutronic and thermal-hydraulic model, *Nuclear Engineering and Technology, VOL 41*, September, 2009.
- [NEA01] NEA Co-operation, Neutron/Thermal-hydraulics coupling in LWR Technology: State of the Art Report, *Nuclear Science*, 2004.

- [Papukchiev01] A. Papuckchiev, G. Lerchl, C. Waata and T. Frank, Extension of the Simulation Capabilities of the 1D System Code ATHLET by Coupling with the 3D CFD Software Package ANSYS CFX, *NURETH-13*, Ishikawa, 2009.
- [Parisi01] C. Parisi, F. D’Auria and V. Malof, RBMK Coupled Neutronics/Thermal-Hydraulics Analyses by Two Independent Code Systems, *PHYSOR*, Vancouver, Canada, September, 2006.
- [Polidori01] M. Polidori, Implementation of Thermo-Physical Properties and Thermal-Hydraulic Characteristics of Lead-Bismuth Eutectiv and Lead on CATHARE Code, *ENEA report Rds/2012/51/*, September, 2010.
- [Perez01] J. Perez, Development of CFD thermal hydraulics and neutron kinetics coupling methodologies for the prediction of local safety parameters for LWR, *Ph.D. dissertation*, Karlsruhe Institute of Technology, 2013.
- [Ragusa01] J. Ragusa and V. Mahedevan, Consistent accelerated schemes for nonlinear coupling problems in reactor analysis, *PHYSOR*, Vancouver, September, 2006.
- [Ragusa02] J. Ragusa, Y. Wang and W. Bangerth, Three dimensional h-adaptivity for the multigroup neutron diffusion equations, *Progress in Nuclear Energy*, 51, 543-555, 2009.
- [Relap01] Relap5-3D Team, RELAP5-3D Code Manual Volume I: Code structure, system models and solution methods, *Report no. INEEL-EXT-98-00834*, February, 2001.
- [Reuss01] P. Reuss, Précis Neutronique, *EDPF Science INSTN-ENEN – ISBN:978-2-7598-0041-4*, 2003.
- [Rodriguez01] S.B. Rodriguez, Using the Coupled MELCOR-RELAP5 Codes for Simulation of the Edwards Pipe, *Report no. SAND2002-2828C*, 2002.
- [Rohde01] U. Rohde, U. Grundmann, S. Mittag and S. Kliem, DYN3D Version 3.2: Code for Calculation of Transients in Light Water Reactors (LWR) with Hexagonal or Quadratic Fuel Elements, *A Wissenschaftlich-Technische Berichte report no. FZR-434 ISSN 1437-322X*, Rossendorf, Germany, 2005.
- [Royer01] E. Royer, O. Zerkak, P. Coddington, N. Crouzet, J. Jimenez and D. Cuervo, LWR MULTI-PHYSICS DEVELOPMENTS AND APPLICATIONS WITHIN THE FRAME OF THE NURESIM EUROPEAN PROJECT, *Mathematics and Computation*, Monterey California, USA, April, 2007.
- [Royer02] E. Royer, I. Toumi, CATHARE-CRONOS-FLICA coupling with ISAS: A powerful tool for nuclear studies, *ICONE 6*, San Diego, California, USA, 1998.
- [Sanchez01] V. Sanchez, U. Imke and R. Gomez, SUBCHANFLOW: A thermal-hydraulic sub-channel program to analyse fuel rod bundles and reactor cores, *17<sup>th</sup> Pacific Basin Nuclear Conference*, Cancún, Mexico, 2010.

- [SanchezR01] R. Sanchez, S. Santandreas and E. Martinolli, APOLLO2 YEAR 2010, *Nuclear Engineering and Technology*, October, 2010.
- [Seubert01] A. Seubert, K. Velkov and S. Langenbuch, The time-dependent 3D discrete ordinates code TORT-TD with thermal-hydraulic feedback by ATHLET models, *International Conference on the Physics of Reactors*, Interlaken, September, 2008.
- [Seubert02] A. Seubert, S. Langebuch, K. Velkov and W. Zwermann, Applicability of deterministic and Monte Carlo neutron transport models coupled with thermo-fluid dynamics, *Eurosafe*, 2006.
- [Spore01] J. Spore, et al., LA-UR-00-910 TRAC-M/FORTRAN 90. *Theory Manual*. Los Alamos National Laboratory, Los Alamos, N., 2000.
- [Stosic01] Z. Stosic, Enhancing the scope of applications of standard thermal hydraulic codes by linking with others, *Proc of the ASME International Conference on Nuclear Engineering*, vol.1 part B, New Orleans, 1996.
- [Taitano01] W. Taitano, H. Park and D. Gaston, Tightly Coupled multiphysics simulations for pebble bed reactors, *Mathematics and Computation*, 2009.
- [Teschendorff01] V. Teschendorff, K. Umminger and F. Weiß, Analytical and experimental research into boron dilution events, *PHYSOR*, 2012.
- [Thomas01] J.W. Thomas, Methods for Coupling Computational Fluid Dynamics and Integral Transport Neutronics, *PHYSOR*, 2004.
- [Todreas01] N. Todreas and M. Kazimi, Nuclear Systems II – Elements of Thermal Hydraulic Design, *Taylor and Francis*, 2001.
- [Toumi01] I. Toumi, A. Bergeron, D. Gallo, E. Royer, D. Caruge, FLICA-4: a Three-dimensional Two-phase Flow Computer Code with Advanced Numerical Methods for Nuclear Applications, *Nuclear Engineering and Design*, Vol. 200, pp139-155, 2000.
- [Trace01] TRACE team – Division of Risk Assessment and Special Projects of the US NRC, TRACE V5.0 Theory Manual, Washington D.C., USA, 1997.
- [Uam01] K. Ivanov, M. Avramova, I. Kodeli and E. Sartori, Benchmark for uncertainty analysis in modeling (UAM) for design, operation and safety analysis of LWRs, *Nuclear Energy Agency*, 2007.
- [Vedovi01] J. Vedovi, A. Bousbia, F. D’Auria and G. Galassi, Analysis of the OECD/DOE/CEA VVER1000 CT-1 Benchmark using RELAP5/PARCS coupled codes, *NURETH-11*, Avignon, France, October, 2005.

- [Velkov01] K. Velkov and Y. Périn, Advanced Coupled Code Systems for Transient and Accident Analysis of European LWRs, *Eurosafe-GRS*, Köln, Germany, 2011.
- [Vojtek01] I. Vojtek, Heat Transfer Processes During Intermediate and Large Break LOCAS, *International Agreement report-NUREG/IA-0002*, Germany/USA, 1986.
- [Watson01] J. Watson, Implicit Time Integration Method for Simultaneous Solution of a Coupled Non-Linear System, *Ph.D. thesis*, Pennsylvania State University, USA, 2010.
- [Weber01] D. Weber, T. Sofu and W. Yang, High-Fidelity Light Water Reactor Analysis with the Numerical Nuclear Reactor, *Nuclear Science and Engineering: paper 155,395-408*, May, 2006.
- [Zahid01] M. Zahid, A Users Manual for FENAT: A Two-dimensional Multigroup Diffusion Theory Finite Element Neutral Atom Transport Code, University of California Los Angeles, USA, 1986.
- [Zerkak01] O. Zerkak, I. Gajev, A. Manera, T. Kozolowski, A. Gommlich, S. Zimmer, S. Kliem, N. Crouzet and A. Zimmermann, Revisiting temporal accuracy in neutronics/T-H code coupling using the NURESIM LWR simulation platform, *NURETH-14*, Toronto, Canada, September, 2011.
- [Zhang01] H. Zhang and E. Lewis, An adaptive approach to variational nodal diffusion problems, *Nuclear Science and Engineering: paper volume 137, pages 14-22*, January, 2001.
- [Zhong01] Z. Zhong, T.J. Downar, H.G. Joo and J.Y. Cho, Benchmark Analysis of the DeCART MOC Code with the VENUS-2 Critical Experiment, *PHYSOR*, Lagrange Park IL, USA, April, 2004.

---

## Nomenclature

Symbol	Definition	Units
$A_{i\zeta}$	: Cross sectional surface area (sub-channel $i$ at axial level $\zeta$ )	[m <sup>2</sup> ]
$A_z$	: Cross sectional surface area at axial level $z$ .	[m <sup>2</sup> ]
$B_{\text{ppm}}$	: Boron concentration.	[ppm]
$C_p$	: Specific heat capacity (general).	[J/(kg⊙K)]
$C_p(\bar{r}, T)$	: Specific heat capacity, function of space and temperature.	[J/(kg⊙K)]
$C_\tau$	: Thermal conductivity related to gap $\tau$ .	[W/(m⊙K)]
$C_{\tau,ij}$	: Thermal conductivity through gap $\tau$ (sub-channel $i$ and axial level $j$ ).	[W/(m⊙K)]
$D_g$	: Diffusion coefficient.	[cm]
$D_h$	: Hydraulic diameter.	[m]
$D_{\text{mod}}$	: Coolant density.	[kg/m <sup>3</sup> ]
$d_{ij}$	: Distance between sub-channel centroids (pin distance).	[m]
$E$	: Energy group ( $E \neq E'$ ).	[eV]
$E'$	: Energy group ( $E' \neq E$ ).	[eV]
$\bar{e}_{i\tau}$	: Normalized transverse flow direction.	[-]
$F_{in}$	: Avg. force per unit length (fluid on the solid) in $n = x$ or $z$ .	[N]
$F_p$	: Prompt fission source.	[-]
$F_q$	: Nodal peaking factor.	[-]
$\vec{F}_{wk}^m$	: Net shear force at fixed wall boundary.	[N = kg·m/s <sup>2</sup> ]
$F_{xy}$	: Normalized radial peaking factor.	[-]
$F_z$	: Normalized axial peaking factor.	[-]
$f$	: Single phase friction coefficient.	[-]
$f_T$	: Lateral turbulent momentum balance factor.	[-]
$G_n$	: Mass flux for $n = i$ or at axial level $n = \zeta$ .	[kg/m <sup>2</sup> ]
$g$	: Neutronic energy group index ( $g \neq y$ ).	[-]
$\bar{g}$	: Gravitational constant.	[m/s <sup>2</sup> ]
H	: Energy index (for reference).	[-]
$h_{\text{gap}}$	: Heat transfer coefficient related to the gap.	[W/(m <sup>2</sup> ⊙K)]
$h_{i\zeta}$	: Enthalpy of the mixture for sub-channel $i$ at axial level $\zeta$ .	[J/kg]

Symbol	Definition	Units
$h_{i\zeta}^n$	: Enthalpy of the mixture at previous time step.	[J/kg]
$h_{k^*}$	: Enthalpy (for phase $k^*$ ).	[J/kg]
$h_n$	: Enthalpy of the phase $n = \text{liquid or vapor}$ .	[J/kg]
$h_{\text{mix}}$	: Enthalpy of the mixture.	[J/kg]
$h_n$	: Enthalpy for sub-channel $n = i$ or axial level $n = j$ .	[J/kg]
$h^*$	: Characteristic enthalpy related to $W_{ij}^{*n}$ .	[J/kg]
$h_{kj}^*$	: Gap characteristic enthalpy.	[J/kg]
$h_{k^*s}$	: Stagnation enthalpy (for phase $k^*$ ).	[J/kg]
$h_\tau$	: Heat transfer coefficient related to gap $\tau$ (general).	[W/(m <sup>2</sup> ⊙K)]
$h_{\tau\zeta}$	: Heat transfer coefficient related to gap $\tau$ and axial level $\zeta$ .	[W/(m <sup>2</sup> ⊙K)]
$i$	: Current thermal-hydraulic sub-channel.	[-]
$J$	: Total number of neighbouring sub-channels.	[-]
$J_g$	: Neutronic current.	[n/(cm <sup>2</sup> ⊙eV⊙s)]
$j$	: Neighbouring sub-channel for sub-channel $i$ .	[-]
$K$	: Pressure loss coefficient for spacer grids.	[-]
$K_G$	: Lateral gap pressure loss coefficient.	[-]
$k$	: Neighbouring sub-channel for sub-channel $j$ .	[-]
$k^*$	: Coolant phase (liquid or vapor).	[-]
$k(\vec{r}, T)$	: Thermal conductivity as a function of space and temperature.	[W/(m⊙K)]
$k_{\text{eff}}$	: Multiplication factor (Eigenvalue).	[-]
$k_{ij}$	: Thermal conductivity between sub-channel $i$ and sub-channel $j$ .	[W/(m⊙K)]
$l_\tau$	: Distance between neighboring sub-channels.	[m]
$M$	: Momentum index (for reference).	[-]
$\dot{m}_i$	: Axial mass flow rate for sub-channel $i$ .	[kg/s]
$\dot{m}_{in}$	: Mass flow rate at the reactor core inlet.	[kg/s]
$\dot{m}_{i\zeta}$	: Axial mass flow rate for sub-channel $i$ and axial level $\zeta$ .	[kg/s]
$\dot{m}_{i\zeta}^n$	: Axial mass flow rate at previous time step.	[kg/s]
$\dot{m}_{k^*}$	: Axial mass flow rate (for phase $k^*$ ).	[kg/s]
$N$	: Atom density of the material.	[atoms/cm <sup>3</sup> ]

Symbol	Definition	Units
$n$	: Subscript referring to a time step.	[-]
$\vec{n}_z$	: Normal vector in flow direction.	[-]
$P_{ab}$	: Power after burst.	[W]
$P_i$	: Pressure of current sub-channel $i$ .	[Pa]
$P_{i\zeta}$	: Pressure of sub-channel $i$ and axial level $\zeta$ .	[Pa]
$P_{in}$	: Pressure at the core inlet.	[Pa]
$p_{k^*}$	: Pressure (for phase $k^*$ ).	[Pa]
$P_{out}$	: Pressure at the core outlet.	[Pa]
$P_{rod}$	: Power released by a fuel rod.	[W]
$P_r$	: Heated perimeter.	[m]
$P_{tot}$	: Total power (thermal power).	[W]
$P_w$	: Wall wetted perimeter.	[m]
$P_{\tau\zeta}$	: Pressure at gap $\tau$ and specific axial level $\zeta$ .	[Pa]
$Q_{sk}^*$	: Rate of volumetric heat generation (for phase $k^*$ ).	[W/m <sup>3</sup> ]
$q_{ij}$	: Linear heat rate from sub-channel $i$ to sub-channel $j$ .	[W/m]
$q_{jk}$	: Linear heat rate from sub-channel $j$ to sub-channel $k$ .	[W/m]
$\dot{q}_i$	: Sub-channel $i$ linear heat rate generation.	[W/m]
$q_{r\zeta}'$	: Linear heat rate from pin to coolant at axial level $\zeta$ .	[W/m]
$q_{ij}''$	: Surface heat flux at the wall.	[W/m <sup>2</sup> ]
$q_{r\zeta}''$	: Surface heat flux from pin to coolant.	[W/m <sup>2</sup> ]
$q_{wk}''$	: Surface heat flux at the wall (for phase $k^*$ ).	[W/m <sup>2</sup> ]
$q_{\tau}''$	: Heat transfer from rod to bulk fluid.	[W/m <sup>2</sup> ]
$q'''(\vec{r}, t)$	: Volumetric heat flux as a function of space and time.	[W/m <sup>3</sup> ]
$q_k'''$	: Volumetric heat flux (for phase $k^*$ ).	[W/m <sup>3</sup> ]
$r$	: Index of pin rod.	[-]
$\vec{r}$	: Position vector.	[m]
$r_Q$	: Total power directly released in the coolant.	[W]
$S$	: External neutron sources.	[n]
$S_d$	: Delay neutron source.	[n]
$S_{ij}^y$	: Gap between rods along the “y” direction.	[m]

Symbol	Definition	Units
$S_{\tau}$	: Gap width.	[m]
$T$	: Temperature (general).	[K]
$T(\vec{r}, t)$	: Temperature as a function of space and time.	[K]
$T_{CL}$	: Pellet center line temperature (maximum fuel temperature).	[K]
$T_{Dopp}$	: Doppler temperature.	[K]
$T_i$	: Coolant temperature of sub-channel $i$	[K]
$T_{in}$	: Core inlet temperature.	[K]
$T_{i\zeta}$	: Coolant temperature (sub-channel $i$ , axial level $j$ ).	[K]
$T_{i\zeta}^n$	: Coolant temperature (sub-channel $i$ , axial level $j$ ) at previous time step.	[K]
$T_j$	: Coolant temperature of sub-channel $j$ .	[K]
$T_k$	: Coolant temperature of sub-channel $k$ .	[K]
$T_{mod}$	: Coolant temperature.	[K]
$T^N$	: Temperature used by the neutronics.	[K]
$T_{avg}^N$	: Average temperature used for the neutronics hybrid analysis.	[K]
$T_S$	: Pellet surface temperature.	[K]
$T^{TH}$	: Temperature used by the thermal-hydraulics.	[K]
$T_{wall}$	: Wall temperature.	[K]
$t$	: Time.	[s]
$t_n$	: Time step index.	[-]
$t_{step}$	: Time step size.	[s]
$t_{total}$	: Total simulation time.	[s]
$U_{ij}^*$	: Effective velocity related to the cross flow.	[m/s]
$U'_{i\zeta}$	: Effective velocity for sub-channel $i$ and axial level $\zeta$ .	[m/s]
$U'^n_{i\zeta}$	: Effective velocity at previous time step.	[m/s]
$U'_{\tau\zeta}$	: Dynamic velocity.	[m/s]
$u_k^*$	: Stagnation energy (for phase $k$ ).	[J]
$V$	: Volume.	[m <sup>3</sup> ]
$v$	: Flow velocity (general).	[m/s]
$v_{in}$	: Core inlet flow velocity.	[m/s]
$v_n$	: Flow velocity for sub-channel $n = i$ or $j$ , or axial level $n = z$ .	[m/s]
$v_n^*$	: Characteristic velocity in direction $n=z$ or $x$ related to $W_{ij}^{*n}$	[m/s]

Symbol	Definition	Units
$v^{*}$	: Specific volume.	$[m^3/kg]$
$W_g$	: Neutronic width of the nodes.	$[m]$
$W_{ij}$	: Diverse cross flow from sub-channel $i$ to $j$ .	$[kg/s]$
$W_{ij}^{*n}$	: $n$ parameter transfer from $i$ to $j$ .	$[kg/(m^3s)]$
$W_{\tau\zeta}^n$	: Transverse mass flow at previous time step.	$[kg/(m^3s)]$
$w_{\tau\zeta}$	: Transverse mass flow due to pressure gradients at current time step.	$[kg/s]$
$w_{\tau\zeta}^n$	: Transverse mass flow due to pressure gradients at previous time step.	$[kg/s]$
$w'_{\tau\zeta}$	: Cross flow due to mixing.	$[kg/(m^3s)]$
$X^n$	: General parameter at current iteration number $n$ .	$[-]$
$X^{n-1}$	: General parameter at previous iteration number $n-1$ .	$[-]$
$x$	: Flow quality.	$[-]$
$y$	: Neutronic energy group index ( $y \neq g$ )	$[-]$
$z$	: Maximum (top) axial level.	$[-]$

## Greek symbols

Symbol	Definition	Units
$\alpha$	: Void fraction.	$[-]$
$\alpha(i, j)$	: Void fraction of sub-channel $i$ and axial level $j$ .	$[-]$
$\beta$	: Delayed neutron fraction.	$[-]$
$\beta_{i\zeta}$	: Mixing coefficient between $i$ and $j$ .	$[-]$
$\Gamma_{k^*}$	: Mass exchange rate.	$[kg/(m^3s)]$
$\Delta t$	: Differential time.	$[s]$
$\Delta X_{\zeta}$	: Differential length between axial nodes $\zeta$ .	$[m]$
$\Delta x'$	: Transverse length (distance between rods).	$[m]$
$\varepsilon_N$	: Convergence criteria related to neutronic parameters.	$[-]$
$\varepsilon_T$	: Convergence criteria related to the thermal hydraulic parameters.	$[-]$
$\varepsilon_X$	: Convergence criteria related to an $X$ general parameter.	$[-]$

Symbol	Definition	Units
$\zeta$	: Axial level used for the thermal hydraulic discretization.	[W]
$\Theta$	: Channel inclination relevant to the vertical.	[rad]
$\lambda$	: Relaxation factor for feedback management.	[-]
$\nu$	: Total fission yield.	[-]
$\bar{v}_{k^*z}$	: Mass velocity.	[m/s]
$\xi$	: Viscous dissipation term.	[W]
$\rho$	: Reactivity.	[\$]
$\rho(i, z)$	: Density for sub-channel $i$ at axial level $z$ .	[kg/m <sup>3</sup> ]
$\rho(\bar{r}, T)$	: Density as a function of space and temperature.	[kg/m <sup>3</sup> ]
$\rho_i$	: Density related to sub-channel $i$ .	[kg/m <sup>3</sup> ]
$\rho_{i\zeta}$	: Density of the mixture at current time step.	[kg/m <sup>3</sup> ]
$\rho_{i\zeta}^n$	: Density of the mixture at previous time step.	[kg/m <sup>3</sup> ]
$\rho_{i\zeta}''$	: Effective density.	[kg/m <sup>3</sup> ]
$\rho_{i\zeta}''^n$	: Effective density at previous time step.	[kg/m <sup>3</sup> ]
$\rho_{k^*}$	: Density (for phase $k^*$ ).	[kg/m <sup>3</sup> ]
$\rho_n$	: Vapor density of phase $n = \text{liquid } (l) \text{ or vapor } (v)$ .	[kg/m <sup>3</sup> ]
$\rho_{st}$	: Vapor density at saturation temperature.	[kg/m <sup>3</sup> ]
$\Sigma_{a,g}$	: Macroscopic absorption cross section.	[1/cm]
$\Sigma_f$	: Macroscopic fission cross section.	[1/cm]
$\Sigma_{f,y}$	: Macroscopic fission cross section (group $y$ ).	[1/cm]
$\Sigma_{s,g}$	: Macroscopic absorption cross section (group $g$ ).	[1/cm]
$\Sigma_{s,g \rightarrow y}$	: Macroscopic scattering cross section (from $g$ to $y$ ).	[1/cm]
$\Sigma_{s,y \rightarrow g}$	: Macroscopic scattering cross section (from $y$ to $g$ ).	[1/cm]
$\sigma_a$	: Microscopic absorption cross section.	[1/cm]
$\sigma_{a,g}$	: Microscopic absorption cross section (group $g$ ).	[1/cm]
$\sigma_f$	: Microscopic fission cross section.	[1/cm]
$\sigma_s$	: Microscopic scattering cross section.	[1/cm]

$\tau$	: Index of gaps between sub-channels.	[-]
$\Phi$	: Two phase flow multiplier.	[-]
Symbol	Definition	Units
$\phi$	: Flux limiter.	[-]
$\phi(\vec{r}, E', t)$	: Neutron flux as function of space, energy and time.	[n/(cm <sup>2</sup> ·eV·s)]
$\phi_g$	: Neutron flux related to energy group $g$ .	[n/(cm <sup>2</sup> ·eV·s)]
$\phi_g^s$	: Average nodal flux.	[n/(eV·s)]
$\phi_{ir}$	: Heated perimeter fraction for a specific sub-channel.	[-]
$\phi_y$	: Neutron flux related to energy group $y$ .	[n/(cm <sup>2</sup> ·eV·s)]
$\chi_{dk}(E)$	: Delay neutron emission spectra as function of energy.	[eV <sup>-1</sup> ]
$\chi_g$	: Fraction of neutrons produced by fission.	[-]
$\chi_p$	: Neutrons precursor's spectra.	[-]
$\Omega$	: Neutron angular dependence.	[rad]

---

# **APPENDIXES**

Appendix A: Details on the models used for the validation process.

Appendix B: Additional exercises.

Appendix C: Support for Chapters four to seven.

Appendix D: Functionalities and modules of the NURESIM platform.

## Appendix A: Details on the models used for the validation process

The following tables show in a condensed manner, more details on the modeling implemented to CBY and SCF for the simulations found in Chapters 5, 6 and 7. This could be used a useful guide if similar benchmarks or exercises are modeled with other coupled codes.

### *Simulation of hybrid schemes (independent N and TH) – Chapter 5.1.1, 5.2.1*

Table 32. Modeling parameters for the hybrid models (independent CBY and SCF).

Neutronics CBY (mini-core)		Thermal-hydraulics SCF (mini-core)	
Axial levels [-]	20 even	Axial levels [-]	20 even
Fuel assemblies [-]	9 nodes	Fuel assemblies [-]	9 parallel channels
Assemblies to control [-]	0	Assembly pitch [m]	0.2142
Radial nodalization [-]	4 nodes/FA	Cross flow factor [-]	0.5
Radial reflector [-]	Void	TH properties [-]	From SCF
Axial reflector [-]	Void	Gap conductance [W/(m <sup>2</sup> K)]	10,000.0
Damping factor [-]	0.7	Fuel rod nodalization [-]	10
Feedback [-]	$T_{Doppler}, T_{mod}, \rho_{mod}$	Channel/sub-channel area [m <sup>2</sup> ]	2.59e-2 / 9.277e-5
Time step [s]	0.0	Wetted perimeter [m <sup>2</sup> ]	8.54 / 2.87e-2
Energy groups [-]	8	Heated perimeter [m <sup>2</sup> ]	7.60 / 2.87e-2
Delay neutron groups [-]	6	Rod out diameter [m]	9.166e-3
Bottom refl. Width [cm]	21.57	Fuel diameter [m]	7.902e-3
Upper refl. Width [cm]	21.57	Clad thickness [m]	0.573e-3
Total power [MW]	166.24	Total power [MW]	100.0
Mass flow rate [kg/s]	739.08	Mass flow rate [kg/s]	739.08
Inlet temperature [K]	560.0	Inlet temperature [K]	562.99
Outlet pressure [MPa]	15.4	Outlet pressure [MPa]	15.4

### *Simulation of hybrid schemes (full 3D PWR core) – Chapter 5.1.1, 5.2.1*

Table 33. Modeling parameters for the hybrid models (independent CBY and SCF).

Neutronics CBY (full 3D PWR MOX/UO2 core)			
Axial levels [-]	20 even	Energy groups [-]	8
Fuel assemblies [-]	193 nodes	Delay neutron groups [-]	6

Table 33 (continued)

Assemblies to control [-]	0	Bottom refl. Width [cm]	21.42
Radial nodalization [-]	4 nodes/FA	Upper refl. Width [cm]	21.42
Radial reflector [-]	Void	Total power [MW]	3565.0
Axial reflector [-]	reflective	Mass flow rate [kg/s]	15849.4
Damping factor [-]	-	Inlet temperature [K]	560.0
Feedback [-]	-	Outlet pressure [MPa]	15.5

### Verification of the PWR NEABEN LWR core transient benchmark – Chapter 6.3

Table 34. Modeling parameters for the NEABEN LWR transient benchmark.

Neutronics CBY		Thermal-hydraulics SCF	
Axial levels [-]	16 even	Axial levels [-]	16 even
Fuel assemblies [-]	157 nodes	Fuel assemblies [-]	157 parallel channels
Assemblies to control [-]	1	Assembly pitch [m]	0.21606
Radial nodalization [-]	4 node / FA	Cross flow factor [-]	0.7
Radial reflector [-]	Void	TH properties [-]	From benchmark
Axial reflector [-]	Void	Gap conductance [W/(m <sup>2</sup> K)]	10,000.0
Damping factor [-]	0.7	Fuel rod nodalization [-]	10
Feedback [-]	$T_{Doppler}, T_{mod}, \rho_{mod}$	Channel area [m <sup>2</sup> ]	0.024951
Time step [s]	0.001	Wetted perimeter [m <sup>2</sup> ]	8.856
Energy groups [-]	2	Heated perimeter [m <sup>2</sup> ]	7.893
Delay neutron groups [-]	6	Rod out diameter [m]	0.9517e-2
Bottom refl. width [cm]	30.1	Fuel diameter [m]	8.239e-3
Upper refl. width [cm]	30.1	Clad thickness [m]	0.573e-3

### Validation of the PWR MOX/UO2 benchmark – Chapter 7.1.1

Table 35. Modeling parameters for the PWR MOX/UO2 benchmark.

Neutronics CBY		Thermal-hydraulics SCF	
Axial levels [-]	20 even	Axial levels [-]	20 even
Fuel assemblies [-]	193 nodes	Fuel assemblies [-]	193 parallel channels
Assemblies to control [-]	1	Assembly pitch [m]	0.2142
Radial nodalization [-]	1 node / FA	Cross flow factor [-]	0.7
Radial reflector [-]	Void	TH properties [-]	From benchmark

Table 35 (continued)

Neutronics CBY			Thermal-hydraulics SCF	
Axial reflector	[-]	Void	Gap conductance [W/(m <sup>2</sup> K)]	10,000.0
Damping factor	[-]	0.7	Fuel rod nodalization [-]	10
Feedback	[-]	$T_{Doppler}, T_{mod}, \rho_{mod}$	Channel area [m <sup>2</sup> ]	0.023634
Time step	[s]	0.001	Wetted perimeter [m <sup>2</sup> ]	8.650
Energy groups	[-]	2 and 8	Heated perimeter [m <sup>2</sup> ]	8.050
Delay neutron groups	[-]	6	Rod out diameter [m]	0.9166e-2
Bottom refl. width	[cm]	21.42	Fuel diameter [m]	7.902
Upper refl. width	[cm]	21.42	Clad thickness [m]	0.573e-3

### ***Validation of the TMI-1 MSLB benchmark – Chapter 7.1.2***

Table 36. Modeling parameters for the PWR MSLB benchmark.

Neutronics CBY			Thermal-hydraulics SCF		
Axial levels	[-]	24 uneven	Axial levels	[-]	24 uneven
Fuel assemblies	[-]	177 nodes	Fuel assemblies	[-]	177 parallel channels
Assemblies to control	[-]	1	Assembly pitch	[m]	0.21811
Radial nodalization	[-]	1 node / FA	Cross flow factor	[-]	0.7
Radial reflector	[-]	Void	TH properties	[-]	From benchmark
Axial reflector	[-]	Void	Gap conductance [W/(m <sup>2</sup> K)]		11,356.0
Damping factor	[-]	0.7	Fuel rod nodalization	[-]	10
Feedback	[-]	$T_{Doppler}, T_{mod}, \rho_{mod}$	Channel area	[m <sup>2</sup> ]	2.564
Time step	[s]	0.05, 0.04, 0.02	Wetted perimeter	[m <sup>2</sup> ]	7.859
Energy groups	[-]	2	Heated perimeter	[m <sup>2</sup> ]	7.141
Delay neutron groups	[-]	6	Rod out diameter	[m]	1.0922e-2
Bottom refl. width	[cm]	21.81	Fuel diameter	[m]	9.390e-3
Upper refl. width	[cm]	21.81	Clad thickness	[m]	0.33655e-3

### ***Validation of the PWR MOX/UO2 boron dilution transient mini-core – Chapter 7.1.3.1***

Table 37. Modeling parameters for the MOX/UO2 boron dilution (3x3) mini-core.

Neutronics CBY			Thermal-hydraulics SCF		
Axial levels	[-]	17 even	Axial levels	[-]	17 even
Fuel assemblies	[-]	9 nodes	Fuel assemblies	[-]	9 parallel channels
Assemblies to control	[-]	0	Assembly pitch	[m]	0.2142

Table 37 (continued)

Neutronics CBY			Thermal-hydraulics SCF		
Radial nodalization	[-]	1 node/FA	Cross flow factor	[-]	0.7
Radial reflector	[-]	Zero flux	TH properties	[-]	From benchmark
Axial reflector	[-]	Zero flux	Gap conductance	[W/(m <sup>2</sup> K)]	10,000.0
Damping factor	[-]	0.7	Fuel rod nodalization	[-]	8
Feedback	[-]	$T_{Doppler}, T_{mod}, \rho_{mod}$ , Boron	Channel area	[m <sup>2</sup> ]	2.559e-2
Time step	[s]	0.01	Wetted perimeter	[m <sup>2</sup> ]	8.549
Energy groups	[-]	8	Heated perimeter	[m <sup>2</sup> ]	7.602
Delay neutron groups	[-]	6	Rod out diameter	[m]	0.9166e-2
Bottom refl. width	[cm]	21.51	Fuel diameter	[m]	7.902e-3
Upper refl. width	[cm]	21.51	Clad thickness	[m]	0.573e-3

### *Validation of the PWR MOX/UO2 boron dilution transient full-core – Chapter 7.1.3.3*

Table 38. Modeling parameters for the MOX/UO2 boron dilution 3D full core.

Neutronics CBY			Thermal-hydraulics SCF		
Axial levels	[-]	17 even	Axial levels	[-]	17 even
Fuel assemblies	[-]	193 nodes	Fuel assemblies	[-]	193 parallel channels
Assemblies to control	[-]	0	Assembly pitch	[m]	0.2142
Radial nodalization	[-]	1 node/FA	Cross flow factor	[-]	0.7
Radial reflector	[-]	Zero flux	TH properties	[-]	From benchmark
Axial reflector	[-]	Zero flux	Gap conductance	[W/(m <sup>2</sup> K)]	10,000.0
Damping factor	[-]	0.7	Fuel rod nodalization	[-]	10
Feedback	[-]	$T_{Doppler}, T_{mod}, \rho_{mod}$ , Boron	Channel area	[m <sup>2</sup> ]	2.559e-2
Time step	[s]	0.01	Wetted perimeter	[m <sup>2</sup> ]	8.549
Energy groups	[-]	8	Heated perimeter	[m <sup>2</sup> ]	7.602
Delay neutron groups	[-]	6	Rod out diameter	[m]	0.9166e-2
Bottom refl. width	[cm]	21.51	Fuel diameter	[m]	7.902e-3
Upper refl. width	[cm]	21.51	Clad thickness	[m]	0.573e-3

**Validation of the KALININ-3 transient benchmark – Chapter 7.2**

Table 39. Modeling parameters for the Kalinin-3 cooling transient benchmark.

Neutronics CBY			Thermal-hydraulics SCF		
Axial levels	[-]	20 even	Axial levels	[-]	20 even
Fuel assemblies	[-]	163 nodes	Fuel assemblies	[-]	163 parallel channels
Assemblies to control	[-]	2	Assembly pitch	[m]	0.236
Radial nodalization	[-]	6 nodes / FA	Cross flow factor	[-]	1.0
Radial reflector	[-]	Zero flux	TH properties	[-]	VVER-100CT1
Axial reflector	[-]	Zero flux	Gap conductance	[W/(m <sup>2</sup> K)]	5,000.0
Damping factor	[-]	0.7	Fuel rod nodalization	[-]	10
Feedback	[-]	$T_{Doppler}, T_{mod}, \rho_{mod}$	Channel area	[m <sup>2</sup> ]	2.559e-2
Time step	[s]	0.01	Wetted perimeter	[m <sup>2</sup> ]	9.667
Energy groups	[-]	2	Heated perimeter	[m <sup>2</sup> ]	8.920
Delay neutron groups	[-]	6	Rod out diameter	[m]	0.91e-2
Bottom refl. width	[cm]	23.6	Fuel diameter	[m]	7.56e-3
Upper refl. width	[cm]	23.6	Clad thickness	[m]	0.69e-3

**Validation of the hybrid coupled scheme (3D PWR MOX/UO2 core) – Chapter 7.3**

Table 40. Modeling parameters for the Kalinin-3 cooling transient benchmark.

Neutronics CBY			Thermal-hydraulics SCF		
Axial levels	[-]	20 even	Axial levels	[-]	20 even
Fuel assemblies	[-]	193 nodes + 1 hybrid	Fuel assemblies	[-]	481 parallel channels
Assemblies to control	[-]	2	Assembly pitch	[m]	0.236/1.2e-2
Radial nodalization	[-]	4 nodes / FA	Cross flow factor	[-]	0.7
Radial reflector	[-]	Void	TH properties	[-]	MOX benchmark
Axial reflector	[-]	Void	Gap conductance	[W/(m <sup>2</sup> K)]	10,000.0
Energy groups	[-]	2	Fuel rod nodalization	[-]	10
Delay neutron groups	[-]	6	Channel area	[m <sup>2</sup> ]	2.59e-2/9.27e-5
Bottom refl. width	[cm]	21.42	Wetted perimeter	[m <sup>2</sup> ]	8.54/2.87e-2
Upper refl. width	[cm]	21.42	Heated perimeter	[m <sup>2</sup> ]	7.6/2.878e-2
Total power	[MW]	580.0	Rod out diameter	[m]	0.91e-2
Mass flow rate	[kg/s]	15849.4	Fuel diameter	[m]	7.90e-3
Inlet temperature	[K]	560.0	Clad thickness	[m]	0.573e-3
Outlet pressure	[MPa]	15.5	Boron concentration	[ppm]	1343.5

## Appendix B: Additional exercises

### *Description of the problem: 1 fuel assembly at HFP (steady state)*

Five different steady state cases are presented for a single fuel assembly at nodal base. Table 41 exemplifies the only differences between the models. All models are simulated at 3D HFP state with even (equidistant) axial discretization.

Table 41. Differences between the simulated models for one FA at HFP.

Parameter	Model A	Model B	Model C	Model D	Model E
Boron (ppm)	0.0	2000.0	2000.0	2000.0	0.0
Energy groups	2	2	8	8	8
Nodes per FA	1	1	1	4	4

The operating conditions for both neutronics and thermal-hydraulics are shown in Table 42.

Table 42. Operating condition for all models A, B, C, D and D (one fuel assembly).

Total power	MW	18.47
Inlet temperature	K	560.0
Exit pressure	MPa	15.34
Inlet flow rate	Kg/s	82.12

### Modeling

#### Common N and TH

Axial nodes:	17
Assembly pitch:	21.42 cm
Core active height:	365.76 cm

#### Neutronics

Material type:	unrodded U45 with 15% burn-up
Reflector nodes:	2 (one at the top and one at the bottom)
Delay neutrons groups:	6
Radial BC:	reflective
Axial BC:	void

#### Thermal-hydraulics

Flow area:	2.56 m <sup>2</sup>
------------	---------------------

Wetted perimeter: 8.549 m  
 Heated perimeter: 7.60 m  
 Rod diameter: 0.9166e-2 m  
 Fuel diameter: 7.902e-3 m  
 Clad thickness: 0.573e-3 m  
 Gap conductance: 10000.0 W/(m<sup>2</sup>K)  
 Number of heated pins per assembly: 264

Initial power distribution: Flat with normalized power = 1.0 (radial and axial)

The material thermo-physical properties are taken from the already implemented UO<sub>2</sub> material in SUBCHANFLOW. In addition, the damping used by COBAYA3 to account for the TH feedback is 0.7.

## Results

The Table 43 exemplifies the main parameters for comparison obtained for all the models.

Table 43. Main results for models A, B, C, D and E (one fuel assembly).

Parameter		Model A	Model B	Model C	Model D	Model E
$k_{\text{eff}}$		1.2233	1.0622	1.0621	1.0621	1.2239
$F_z$		1.501	1.428	1.433	1.433	1.512
A.O.	%	-22.23	6.53	6.57	6.57	-22.59
Core avg. $T_{\text{Dopp}}$	K	811.1	808.4	808.5	808.5	812.4
Core avg. $T_{\text{mod}}$	K	583.7	580.6	578.3	580.6	583.8
Maximum $T_{\text{CL}}$	K	1360.9	1312.8	1316.4	1316.4	1368.8
Convergence (iterations)		5	5	4	4	5

### *Description of the problem: 3x3 mini-core at steady state and transient conditions*

Three different cases were modeled for this 3x3 mini-core at nodal base. The first is a HFP state with no transient envisaged, the second is a HZP state which provide the initial BC for the REA transient. This simulation has specific interest because it provides a realistic scenario where a strong N-TH feedback is expected. The operating conditions for both neutronics and thermal-hydraulics are shown in Table 44.

Table 44. Operating conditions at HFP and HZP for the 3x3 mini-core REA transient.

Parameter		HFP	HZP
Total power	MW	100.0	1.0e-6
Inlet temperature	K	560.0	
Exit pressure	MPa	739.08	
Inlet flow rate	kg/s		

## Modeling

### Common N and TH

Axial nodes: 17

Assembly pitch: 21.42 cm

Core active height: 365.76 cm

### Neutronics

Material type 1: rodged U45 with 15% burn-up (Fig. 71, yellow)

Material type 2: un-rodged MOX43 with 15% burn-up (Fig. 71, blue)

Reflector nodes: 2 (one at the top and one at the bottom)

Energy groups: 8

Delay neutrons groups: 6

Radial BC: zero flux (radial reflectors are modeled)

Axial BC: zero flux (axial reflectors are modeled)

Steps for control rod: total height 219.45 steps (0 steps → bottom, 219.45 steps → top)

### Thermal-hydraulics

Flow area: 2.56 m<sup>2</sup> (per assembly)

Wetted perimeter: 8.549 m (per assembly)

Heated perimeter: 7.60 m (per assembly)

Rod diameter: 0.9166e-2 m

Fuel diameter: 7.902e-3 m

Clad thickness: 0.573e-3 m

Gap conductance: 10000.0 W/(m<sup>2</sup>K)

Number of heated pins per assembly: 264 (per assembly)

Initial power distribution: Flat with normalized power = 1.0 (radial and axial)

### Transient scenario (departing from HZP state)

Total simulation time: 1.0 s

Time intervals: 3

Initial CR position: Half of the active height (182.8 cm or 109 steps)

t = 0.0 s → 0.1 s: Ejection at a speed of 700 steps per second – time step = 0.001 s

21	22	23	24	25
16	17	18	19	20
11	12	13	14	15
6	7	8	9	10
1	2	3	4	5

Fig. 71. PWR MOX/UO<sub>2</sub> mini-core top view.

$t = 0.1 \text{ s} \rightarrow 0.5 \text{ s}$ : no external perturbations – time step = 0.01 s

$t = 0.5 \text{ s} \rightarrow 1.0 \text{ s}$ : no external perturbations – time step = 0.02 s

## Results

Table 45 shows the results obtained for the steady state models at both HFP and HZP. Important to mention, at HFP state the control rod is fully extracted, at HZP state the control rod is inserted at half of the active core.

Table 45. Steady state results for the mini-core exercise models at HFP and HZP.

Parameter		HFP	HZP
$k_{\text{eff}}$		1.000	1.004
$F_{xy}$		1.663	1.659
$F_z$		1.669	2.556
A.O.	%	-35.9	-86.6
Core avg. $T_{\text{Dopp}}$	K	715.4	559.98
Core avg. $T_{\text{mod}}$	K	573.5	559.98
Maximum $T_{\text{CL}}$	K	1599.7	560.0
Convergence (iterations)		6	1

Table 46. HFP (normalized radial power).

0.0	0.0	0.0	0.0	0.0
0.0	0.7412	1.0930	0.7412	0.0
0.0	1.0930	1.6634	1.0930	0.0
0.0	0.7412	1.0930	0.7412	0.0
0.0	0.0	0.0	0.0	0.0

HFP (normalized radial power distribution)

Table 47. HZP (normalized radial power).

0.0	0.0	0.0	0.0	0.0
0.0	0.7354	1.0998	0.7354	0.0
0.0	1.0998	1.6593	1.0998	0.0
0.0	0.7354	1.0998	0.7354	0.0
0.0	0.0	0.0	0.0	0.0

HZP (normalized radial power distribution)

Table 48. Normalized axial power per node at HFP.

Node	1	2	3	4	5	6	7	8	9	10
power	0.00	0.536	0.947	1.285	.1510	1.632	1.669	1.641	1.567	1.463
Node	11	12	13	14	15	16	17	18	19	
Power	1.341	1.209	1.074	0.941	0.811	0.685	0.564	0.447	0.00	

Table 49. Normalized axial power per node at HZP.

Node	1	2	3	4	5	6	7	8	9	10
power	0.00	0.758	1.446	2.026	2.408	2.556	2.455	2.116	1.572	0.889
Node	11	12	13	14	15	16	17	18	19	
Power	0.414	0.193	0.090	0.042	0.020	0.009	0.004	0.002	0.00	

Several parameters were studied during the transient evolution. The following figures (Fig. 72 (a, b, c, d)) exemplify this in a more detailed manner. Table 50 shows some of the most important parameters in a condensed way. Results are not discussed, this is reserved for Chapter 7.1.1, where a more relevant benchmark is presented and studied in detail.

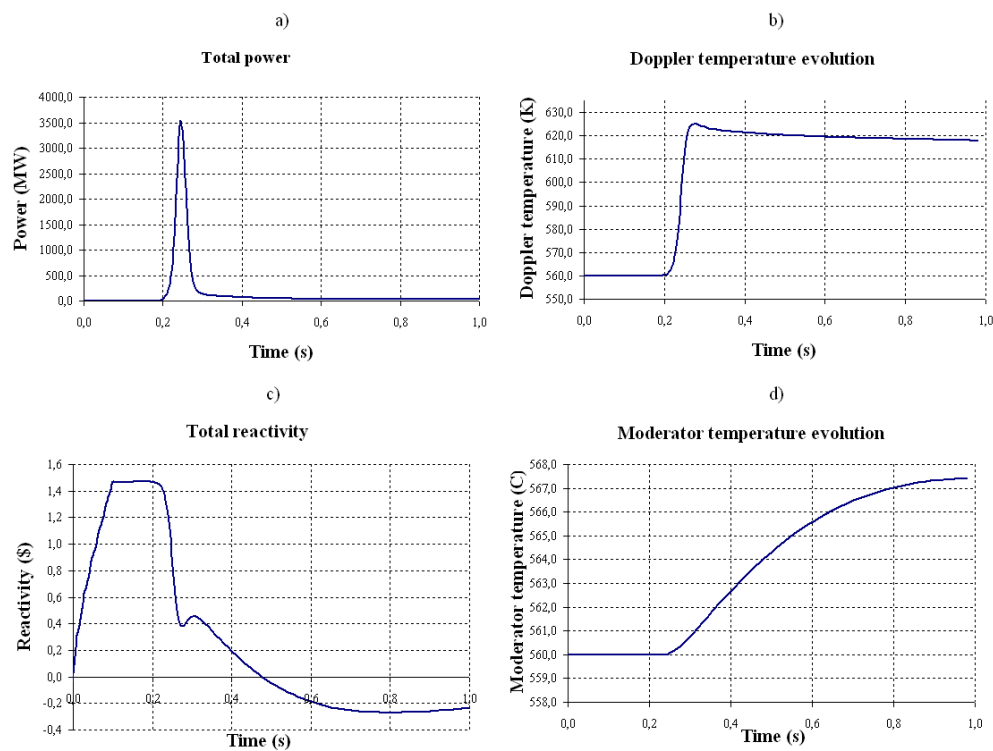


Fig. 72. Total power (a), Doppler temperature (b), total reactivity (c) and moderator temperature (d) evolution for the REA mini-core exercise.

Table 50. Transient parameters obtained for the REA mini-core exercise.

Parameter		CBY/SCF
Power peak	MW	3552.1
Peak time	s	0.245
Max. Reactivity	\$	1.471
$T_{Dopp}$ (max)	K	625.1

## Appendix C: Support for Chapters four to seven

This section is devoted for supporting the results provided in Chapters four to seven. The following figures are listed and described hereafter:

1. Fig. 73: TH output related to the 3x3 pin cluster sub-channel sensitivity analysis (6 sub-channels modeled).
2. Fig. 74: TH output related to the 3x3 pin cluster sub-channel sensitivity analysis (36 sub-channels modeled).
3. Fig. 75: TH output related to the coolant centered discretized 3x3 mini-core.
4. Fig. 76: TH output related to the rod centered discretized 3x3 mini-core.
5. Fig. 77: TH output related to the 3x3 hybrid mini-core with one hybrid FA.
6. Fig. 78: TH output related to the 3x3 hybrid mini-core with nine hybrid FAs.
7. Fig. 79: Plot related to the coolant temperature evolution for the PWR MOX/UO<sub>2</sub> REA benchmark.
8. Fig. 80: Plots related to the evolution of the total power and Doppler temperature (detail around  $t = 60.0$  s) and the total reactivity for the complete transient simulated for the TMI-1 MSLB benchmark.

In Fig. 73 and Fig. 74, the output is condensed in order to show the parameters that are investigated in the discussion. The rest of the outputs show the end of the file, which contain important information such as total computational time and selected TH parameters. Next, a list with the most important parameters shown in the outputs is presented.

1. `tdoppler` = Doppler temperature calculated according to eq. (7.1).
2. `tclave` = Average cladding temperature.
3. `tfuave` = Average pellet temperature.
4. `tfuelc` = Fuel center line temperature.
5. `tfueli` = Pellet surface temperature.
6. `tcladi` = Cladding temperature (inner wall).
7. `tclado` = Cladding temperature (outer wall).
8. `Tfluid` = Fluid temperature in contact with the rod.
9. `total cpu time` = Total time required for the calculation.

```

=====
iteration results: time = 0.0000E+00 s dt = 1.0000E+10 s
=====
iteration index      total no. of      maximum axial
                  internal      flow
                  iterations     error

      24             293             8.7008E-06

*** the solution has used      0.330 s of cpu time

channel enthalpy  temperature  density  equil.  osv  true  void  flow  mass flux  reynolds
no.      (j/kg)    (c)      (kg/m3)  quality quality quality fraction (kg/s) (kg/s/m2) mixture
-----
      6  1.4701E+06  322.73  6.7247E+02  -0.1588  -0.0112  0.0000  0.0000  4.2623E-01  3.0621E+03  4.9810E+05
-----+-----
results for rod 1 fuel type 1 time = 0.0000E+00 s
-----+-----
axial zone  tfluid  tclado  tcladi  tfueli  tfuelc  tfuave  tclave  tdoppler  fcgap  hfcgap
(m)         (c)     (c)     (c)     (c)     (c)     (c)     (c)     (c)       (m)    (w/m/m/k)
-----
1.8288 - 2.0117 309.14 343.62 379.69 494.47 1111.10 776.51 361.65 679.46 1.2548E-05 1.0000E+04

```

Fig. 73. Output 1: First model in Chapter 4.2, Fig. 13.

```

=====
iteration results: time = 0.0000E+00 s dt = 1.0000E+10 s
=====
iteration index      total no. of      maximum axial
                  internal      flow
                  iterations     error

      39             789             7.1789E-06

*** the solution has used      7.390 s of cpu time

channel enthalpy  temperature  density  equil.  osv  true  void  flow  mass flux  reynolds
no.      (j/kg)    (c)      (kg/m3)  quality quality quality fraction (kg/s) (kg/s/m2) mixture
-----
      23  1.4549E+06  320.29  6.7908E+02  -0.1744  -0.0112  0.0000  0.0000  7.0981E-02  3.0597E+03  4.9137E+05
      24  1.4770E+06  323.83  6.6942E+02  -0.1517  -0.0112  0.0000  0.0000  7.1047E-02  3.0625E+03  5.0128E+05
      29  1.4612E+06  321.31  6.7635E+02  -0.1679  -0.0112  0.0000  0.0000  7.0987E-02  3.0600E+03  4.9407E+05
      30  1.4786E+06  324.07  6.6872E+02  -0.1500  -0.0112  0.0000  0.0000  7.1052E-02  3.0627E+03  5.0200E+05
      35  1.4786E+06  324.07  6.6872E+02  -0.1500  -0.0112  0.0000  0.0000  7.1052E-02  3.0627E+03  5.0200E+05
      36  1.4852E+06  325.10  6.6580E+02  -0.1433  -0.0112  0.0000  0.0000  7.1086E-02  3.0642E+03  5.0513E+05
-----+-----
results for rod 1 fuel type 1 time = 0.0000E+00 s
-----+-----
axial zone  tfluid  tclado  tcladi  tfueli  tfuelc  tfuave  tclave  tdoppler  fcgap  hfcgap
(m)         (c)     (c)     (c)     (c)     (c)     (c)     (c)     (c)       (m)    (w/m/m/k)
-----
1.8288 - 2.0117 309.82 344.24 380.30 495.08 1112.09 777.30 362.27 680.19 1.2524E-05 1.0000E+04

```

Fig. 74. Output 2: Fourth model in Chapter 4.2, Fig. 13.

```

Time(s) | Max. Fuel temperature(C) @ | rod | axial : 0.0000E+00 9.396E+021220 12
Time(s) | Tfuelc-Tfuels-Tcladin-Tcladout-Tfluid (C) : 0.0000E+00 9.3967E+02 4.3392E+02 3.5185E+02 3.2635E+02 2.9986E+02
Time(s) | Specific Heat(J/K) | Conductivity(W/m*K) | Density(kg/m3) : 0.0000E+00 2.9109E+02 5.8857E+00 1.0970E+04

Time(s) for maximum power (W) - 2 nominal: 0.0000E+00 1.00E+08 1.0

* no. of external iterations = 500

The maximum Fuel temperature is (C) : 9.3967E+02
The corresponding Doppler T. is (C) : 5.8563E+02
At rod number : 1220
At axial level : 12

Time(s) for maximum power (W) - 2 nominal: 0.0000E+00 1.00E+08 1.000E+00

* total cpu time = 1.7591E+03 s or 29 m 1.9067E+01 s
* solvers (pressure+energy) cpu time = 0.0000E+00 s
* coolant properties cpu time = 0.0000E+00 s

* date 27.11.12
* time 10:53:42

***** end of case *****

```

Fig. 75. Output 3: PBP solution for the coolant centered discretization in Chapter 4.2.

```

Time(s) | Max. Fuel temperature(C) @ | rod | axial : 0.0000E+00 9.468E+021390 12
Time(s) | Tfuelc-Tfuels-Tcladin-Tcladout-Tfluid (C) : 0.0000E+00 9.4682E+02 4.4489E+02 3.5626E+02 3.2803E+02 3.0194E+02
Time(s) | Specific Heat(J/K) | Conductivity(W/m*K) | Density(kg/m3) : 0.0000E+00 2.9168E+02 5.8853E+00 1.0970E+04

Time(s) for maximum power (W) - 2 nominal: 0.0000E+00 1.00E+08 1.0

* no. of external iterations = 500

The maximum Fuel temperature is (C) : 9.4682E+02
The corresponding Doppler T. is (C) : 5.9547E+02
At rod number : 1390
At axial level : 12

Time(s) for maximum power (W) - 2 nominal: 0.0000E+00 1.00E+08 1.000E+00

* total cpu time = 2.5493E+03 s or 42 m 2.9318E+01 s
* solvers (pressure+energy) cpu time = 0.0000E+00 s
* coolant properties cpu time = 0.0000E+00 s

* date 27.11.12
* time 13:28:20

***** end of case *****

```

Fig. 76. Output 4: PBP solution for the rod centered discretization in Chapter 4.2.

```

3.1090 - 3.2918 313.84 320.06 327.48 350.49 435.67 392.12 323.77 376.04 3.3970E-05 1.0000E+04
3.2918 - 3.4747 314.19 317.90 322.37 336.17 385.35 360.37 320.14 350.93 3.5405E-05 1.0000E+04
3.4747 - 3.6576 314.30 315.54 317.03 321.63 337.40 329.44 316.28 326.36 3.6772E-05 1.0000E+04
Time(s) | Max. Fuel temperature(C) @ | rod | axial : 0.0000E+00 9.390E+02 76 12
Time(s) | Tfuelc-Tfuels-Tcladin-Tcladout-Tfluid (C) : 0.0000E+00 9.3903E+02 4.4532E+02 3.5790E+02 3.3009E+02 3.0458E+02
Time(s) | Specific Heat(J/K) | Conductivity(W/m*K) | Density(kg/m3) : 0.0000E+00 2.9190E+02 5.8666E+00 1.0970E+04

Time(s) for maximum power (W) - 2 nominal: 0.0000E+00 1.00E+08 1.0

* no. of external iterations = 44

The maximum Fuel temperature is (C) : 9.3903E+02
The corresponding Doppler T. is (C) : 5.9343E+02
At rod number : 76
At axial level : 12

Time(s) for maximum power (W) - 2 nominal: 0.0000E+00 1.00E+08 1.0

* total cpu time = 2.2742E+01 s or 0 m 2.2742E+01 s
* solvers (pressure+energy) cpu time = 0.0000E+00 s
* coolant properties cpu time = 0.0000E+00 s

* date 12.11.12

* time 09:42:33

***** end of case *****
"hybrid1.txt" 26926L, 2838024C

```

Fig. 77. Output 5: test case two in Chapter 5, Fig. 18.

```

3.1090 - 3.2918 313.93 320.01 327.44 350.44 435.62 392.07 323.72 375.99 3.3970E-05 1.0000E+04
3.2918 - 3.4747 314.28 317.92 322.38 336.19 385.37 360.38 320.15 350.94 3.5405E-05 1.0000E+04
3.4747 - 3.6576 314.40 315.61 317.10 321.70 337.47 329.51 316.35 326.43 3.6771E-05 1.0000E+04
Time(s) | Max. Fuel temperature(C) @ | rod | axial : 0.0000E+00 9.393E+02 1374 12
Time(s) | Tfuelc-Tfuels-Tcladin-Tcladout-Tfluid (C) : 0.0000E+00 9.3932E+02 4.4550E+02 3.5808E+02 3.3028E+02 3.0466E+02
Time(s) | Specific Heat(J/K) | Conductivity(W/m*K) | Density(kg/m3) : 0.0000E+00 2.9190E+02 5.8661E+00 1.0970E+04

Time(s) for maximum power (W) - 2 nominal: 0.0000E+00 1.00E+08 1.0

* no. of external iterations = 45

step = 0 time = 0.0000E+00 delt = 1.0000E+10 completed

The maximum Fuel temperature is (C) : 9.3932E+02
The corresponding Doppler T. is (C) : 5.9364E+02
At rod number : 1374
At axial level : 12

Time(s) for maximum power (W) - 2 nominal: 0.0000E+00 1.00E+08 1.0

* total cpu time = 5.9976E+02 s or 9 m 5.9762E+01 s
* solvers (pressure+energy) cpu time = 0.0000E+00 s
* coolant properties cpu time = 0.0000E+00 s

* date 12.11.12

* time 10:23:33

***** end of case *****
"hybrid_FULLPIN.txt" 241961L, 26166213C

```

Fig. 78. Output 6: test case eight in Chapter 5, Fig. 18.

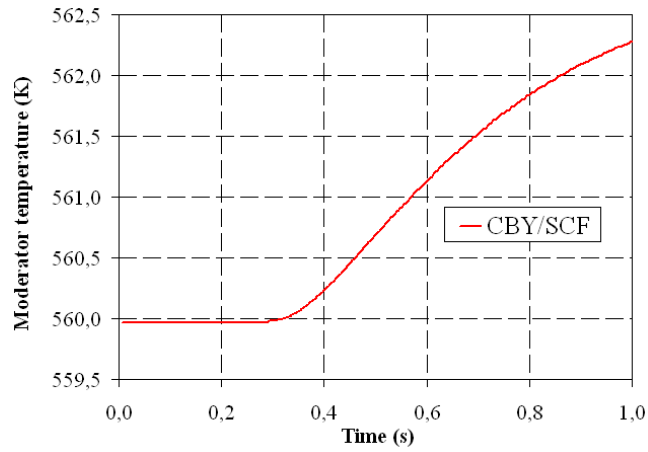


Fig. 79. Coolant temperature evolution for the PWM MOX/UO2 REA benchmark.

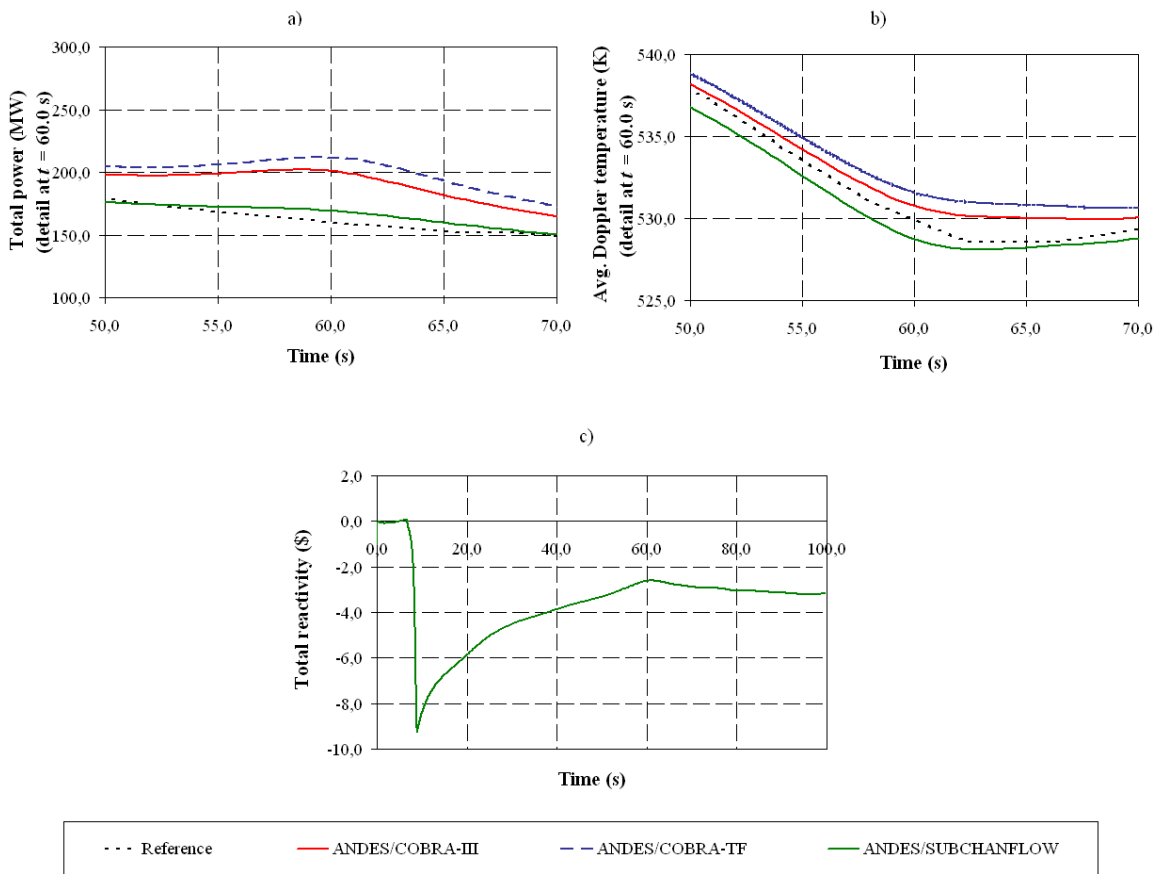


Fig. 80. Total power detail (a), Doppler temperature (b) and total reactivity evolution for the TMI-1 MSBL benchmark.

## Appendix D: Functionalities and modules of the NURESIM platform

As mentioned in Chapter 4, the use of the code is strongly dependent on the capabilities of the NURESIM platform. To be able to use SCF (or any other integrated code) the development of different modules was done in order to perform different tasks. As an example, for a full SCF stand alone calculation, the following tasks (black boxes) are required:

1. Start\_init: Input reading and initialization of variables and arrays.
2. Calculation: Thermal-hydraulic solution.
3. Edit: Printing of results and shut down procedures.

For coupled calculations other modules were programmed, the ones in charge of the feedback management and convergence handling. The codes however, once integrated, interact through the YACS module of the platform or via python scripts. The previously described black boxes can be interconnected inside a new YACS schema window as seen in Fig. 81.

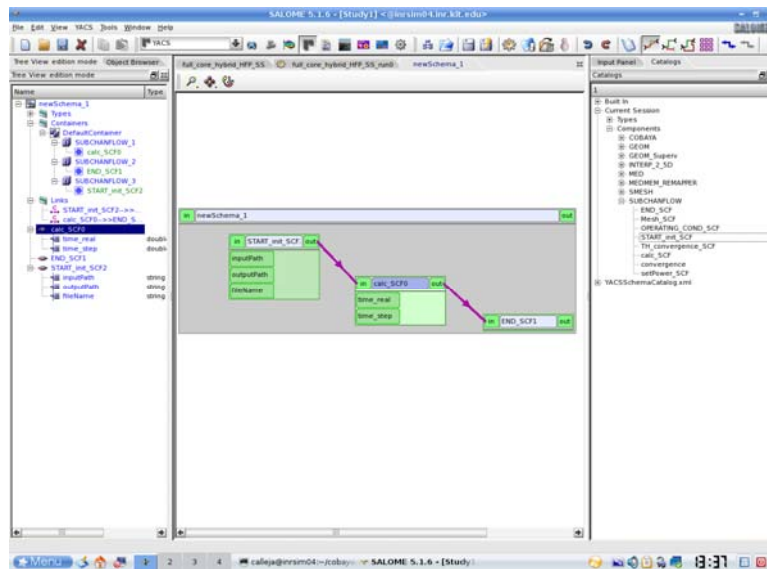


Fig. 81. YACS diagram for a SCF stand alone simulation.

The connection lines which are pink represent the order of execution. Blue lines however, exemplify the flow of information but do not give a specific sequence to the simulation. Therefore, for coupled solutions the order of execution or feedback management could be easily arranged. The Fig. 82 repre-

sents a coupled solution using the integrated codes CBY, SCF and the interpolation tool used for feedback management for steady state.

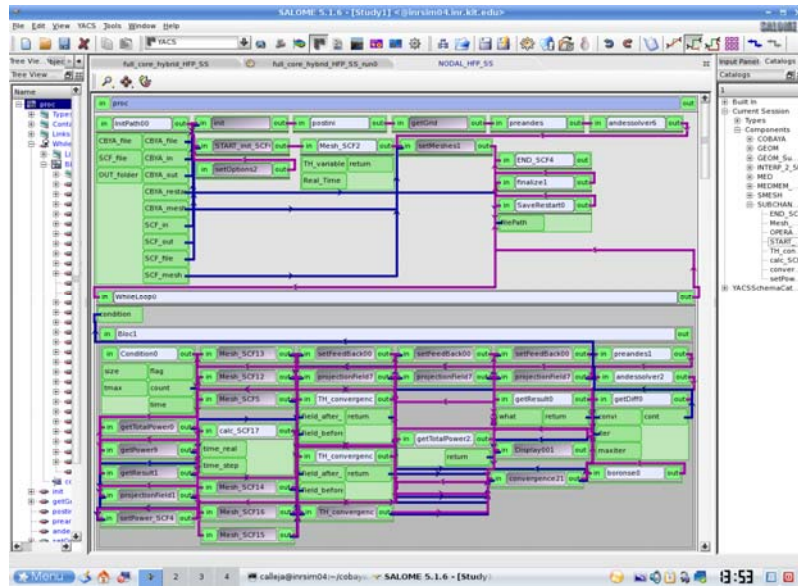


Fig. 82. Coupled CBY/SCF YACS diagram for a steady state simulation.

Similarly, online visualization of changing parameters (e.g. multiplication factor or total power) can be presented as seen in Fig. 83 and Fig. 84.

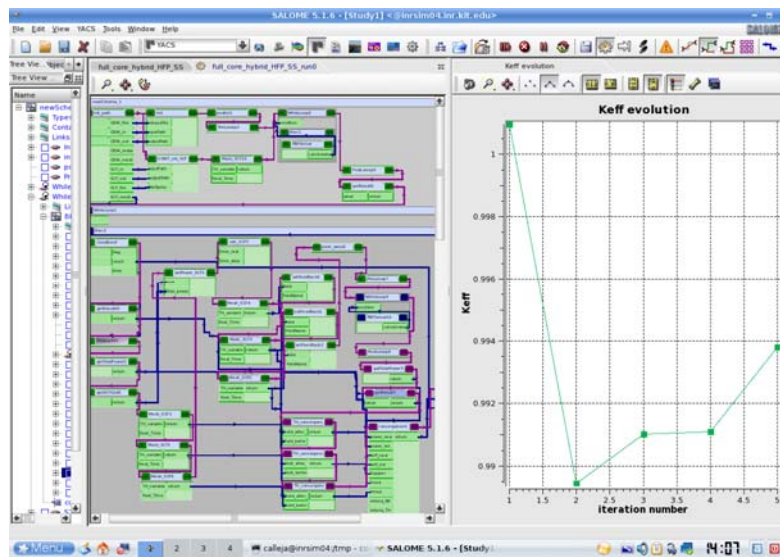


Fig. 83. Online visualization of the  $k_{eff}$  convergence evolution within a YACS diagram of the NURESIM platform.

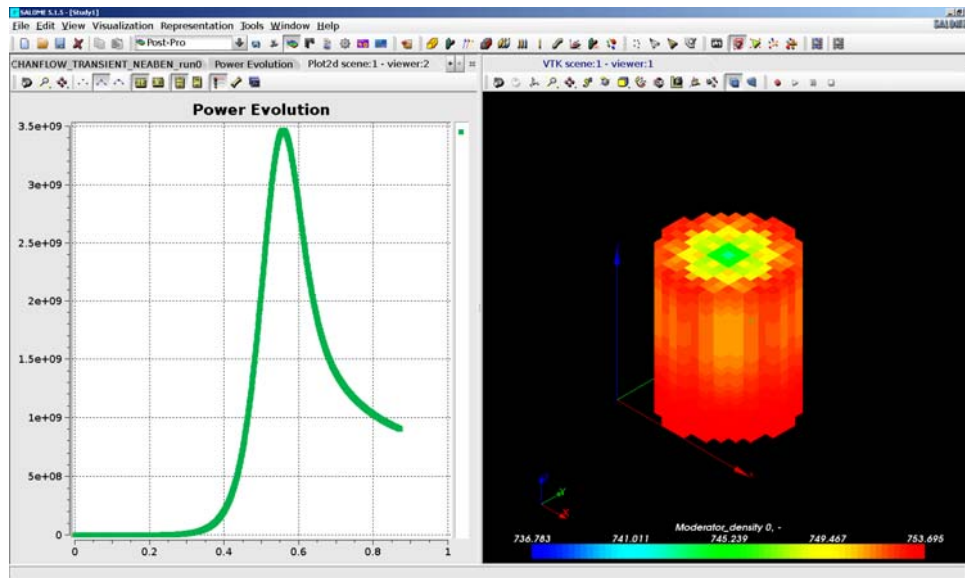


Fig. 84. Online visualization of the total power evolution for a typical REA transient simulation inside the NURESIM platform.

Other functionalities involve the usage of the pre- and post-processing tool of SALOME, the Post-Pro module. With this, verification of meshes and structures could be done, in addition to the visualization of results and sophisticated post-processing of the fields. These capabilities can be seen in Fig. 85, Fig. 86, Fig. 87, Fig. 88 and Fig. 89.

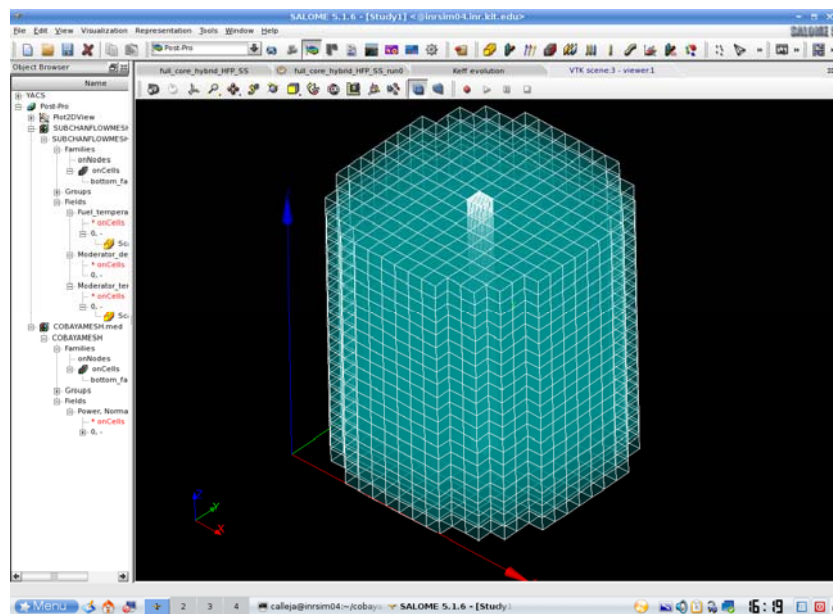


Fig. 85. Verification of the 3D mesh for a full core (one hybrid central assembly) inside SALOME.

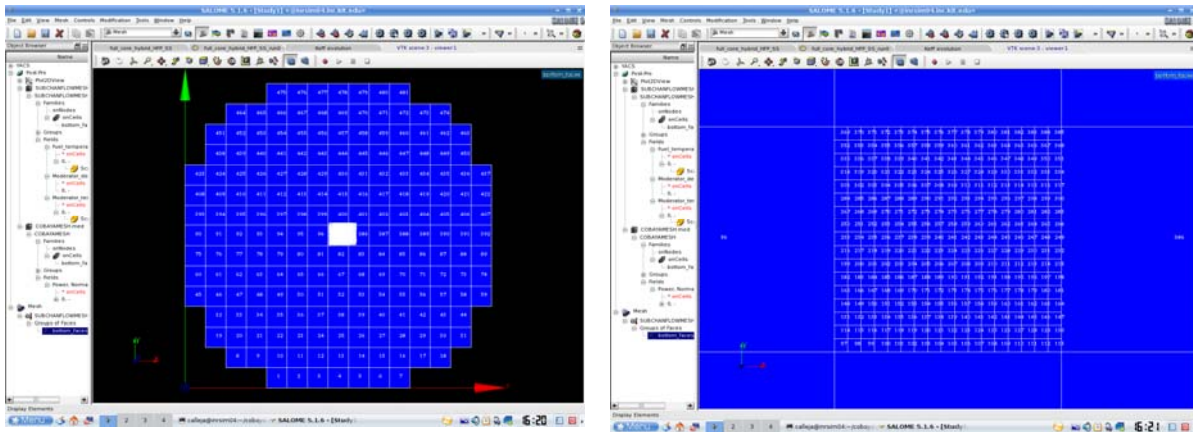


Fig. 86. Representation of the meshing elements (full core – left, hybrid central assembly - right) inside SALOME.

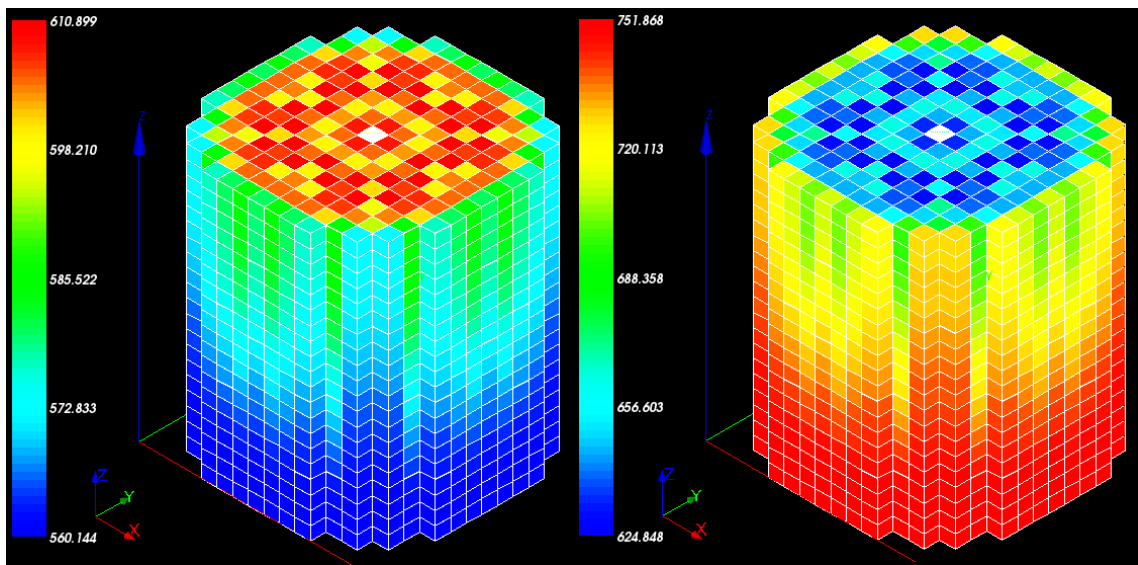


Fig. 87. Display of the moderator temperature field (left) and density field (right) inside SALOME.

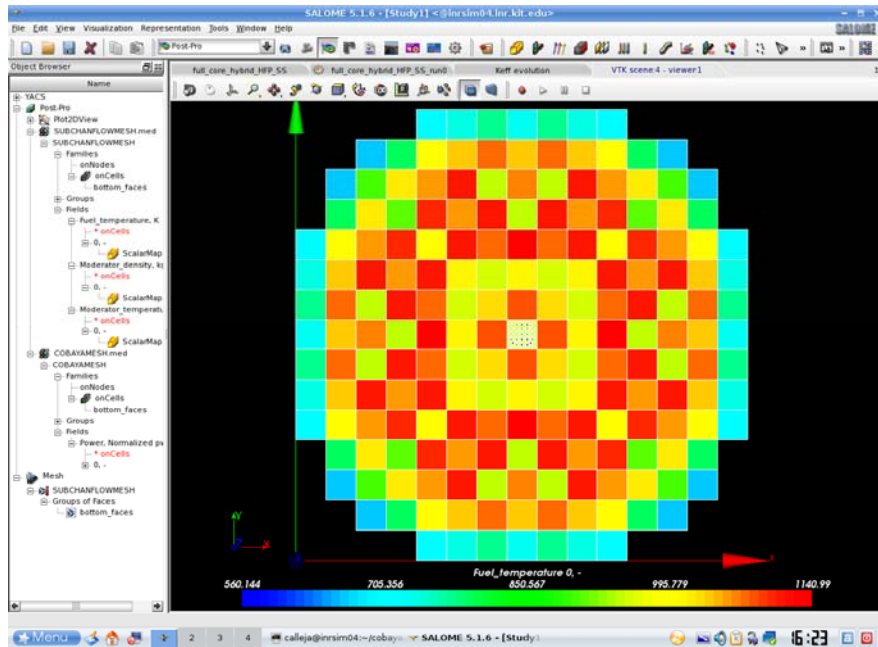


Fig. 88. Doppler temperature field with a horizontal cut at half of the active core.

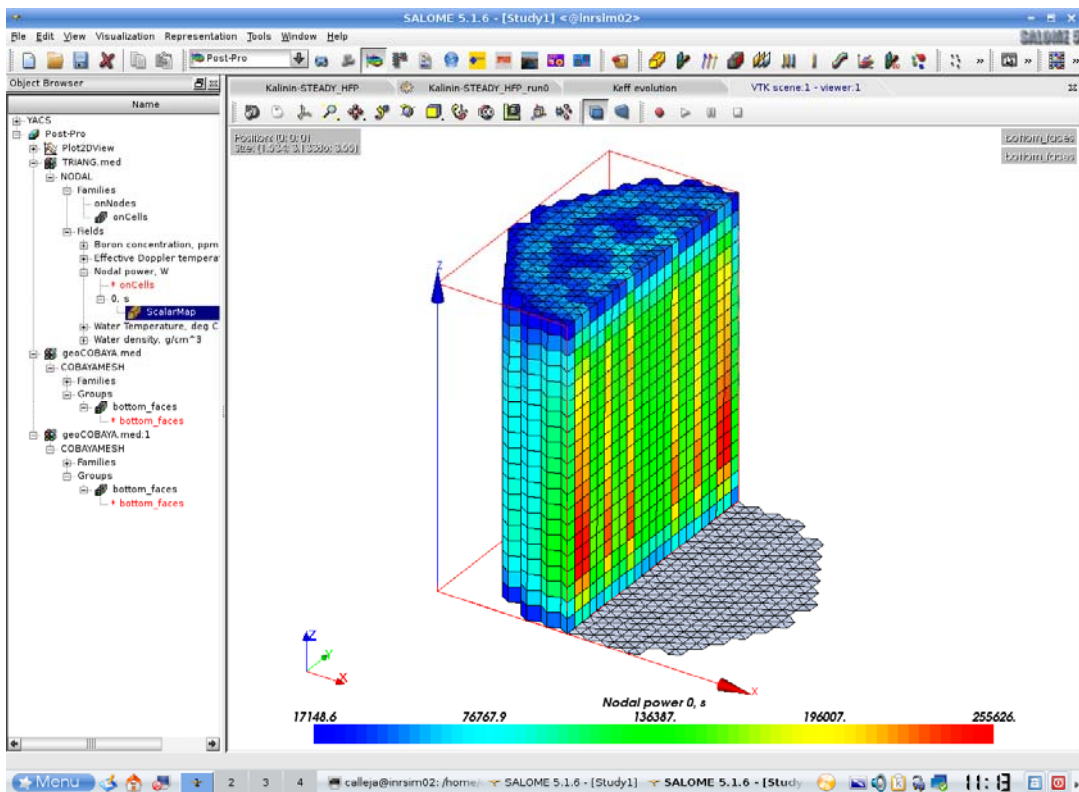


Fig. 89. Vertical cut applied to a 3D power distribution field for a hexagonal reactor core model.

# Curriculum Vitae

# Dr. - Ing. Manuel Calleja Reyna

---

## CONTACT & INFORMATION

Address:

Mobile:  
E-mail: [mancalrey@hotmail.com](mailto:mancalrey@hotmail.com)  
Born: Cuernavaca Mor., Mexico on  
December 19

---

## RESEARCH INTERESTS

Multi-physics (neutronic and thermal-hydraulic coupling), spatiotemporal modeling of nuclear cores, multi-scales, core analysis, aerodynamics and aircraft structures, space mechanics.

---

## EDUCATION

**Karlsruhe Institute of Technology (KIT)**. Karlsruhe, **Germany**.

Ph.D., Nuclear Engineering, *Dissertation*: March 2013.

- Thesis Topic: *Improvements in multi-physics and multi-scale methodologies for safety related investigations of pressurized water reactors within the NURESIM platform.*
- Advisors: Robert Stieglitz, Prof. Dr.-Ing. and Rafael Macián, Univ.-Prof. Ph.D.

**Institut National des Sciences & Techniques Nucléaires (CEA)**. Saclay, **France**.

M.Sc., Nuclear Engineering, Aug 2009.

- Main courses: Nuclear physics, neutron physics, thermal exchange (thermal-hydraulics of nuclear reactors, nuclear materials, nuclear combustion cycles, etc...)
- Master Thesis: *Pressurized thermal shock by ECCS injection after SBLOCA.*
- Institution: TRACTEBEL Engineering (GDF-SUEZ). Brussels, **Belgium**.
- Advisor: Steven Keijers, Ph.D.

**Institut Supérieur de l'Aéronatique et de l'Espace (Supaéro)**. Toulouse, **France**.

M.Sc., Aeronautical Engineering and Space Technology, August 2008.

- Main courses: Propulsion elements, advance aerodynamics, helicopter aerodynamics, advance aircraft structures, fatigue, composite materials, flight dynamics, industrial management, etc...
- Master Thesis: *Optimal input design for light dynamics identification using an hybrid evolutionary algorithm.*
- Institution: ONERA, The French Aerospace Laboratory. Toulouse, France.
- Advisor: Cédric Seren, Ph.D.

**Embry-Riddle Aeronautical University (ERAU)**. Daytona Beach, **USA**.

B.Sc., Aerospace Engineering and Engineering Physics, August 2007.

- **Double Major.**
  - Main courses: Space mechanics, aerodynamics, aerospace materials, advance mathematics, optics, aircraft design, aircraft structures, control systems, quantum mechanics, particle physics, modern and space physics, etc ...
  - *Summa Cum Laude*. GPA: 3.9/4.0 (for both majors).
- 

## RESEARCH EXPERIENCE

**Pos-doctoral position**

August 2013 to August 2016

Division of Nuclear Engineering, Chalmers Institute of Technology.

Supervisor: Christophe Demazière, Prof. Ph.D.

PUBLICATIONS	<ol style="list-style-type: none"> <li>1. M. Calleja, R. Stieglitz, V. Sanchez, J. Jimenez and U. Imke, "A coupled N/TH scheme between COBAYA3 and SUBCHANFLOW within the NURESIM platform," <i>PHYSOR, Advances in Reactor Physics</i>, Knoxville, USA, April 2012.</li> <li>2. M. Calleja, J. Jimenez, U. Imke and V. Sanchez, "Validation of the coupling between COBAYA3 and SUBCHANFLOW for the simulation of boron dilution transients," <i>Annual meeting of the Spanish nuclear society</i>, Cáceres, Spain, 2012.</li> <li>3. M. Calleja, V. Sanchez U. Imke, "Implementation of SUBCHANFLOW in the SALOME platform and coupling with the reactor dynamic code COBAYA3," <i>Jahrestagung Kerntechnik (KTG)</i>, Berlin, May 17-19, 2011.</li> <li>4. M. Calleja, R. Stieglitz, V. Sanchez and U. Imke, "Investigations of boron transport in PWRs with the coupled codes COBAYA3/SCF and DYN3D/SCF inside the NURESIM platform," <i>Annals of Nuclear Energy</i>, Vol. 66, 2014. Pages 74-84.</li> <li>5. M. Calleja, V. Sanchez and J. Jimenez, "Coupling of COBAYA3/SUBCHANFLOW inside the NURESIM platform and Validation Using Selected Benchmarks," <i>Annals of Nuclear Energy</i>, Vol. 71, 2014. Pages 145-158.</li> <li>6. M. Calleja, J. Jimenez, U. Imke, V. Sanchez, J. Herrero and J. Macián, "Implementation of Hybrid Simulation Schemes in COBAYA3/SUBCHANFLOW Coupled Codes for the Efficient Direct Prediction of Local Safety Parameters," <i>Annals of Nuclear Energy</i>, Vol. 70, 2014. Pages 216-229.</li> </ol> <p>Reviewer of several journal papers including: <i>Philosophical Transactions of the Royal Society A</i>, <i>Annals of Nuclear Energy</i>, and <i>Nuclear Technology</i>.</p>
ADDITIONAL PROJECTS	<p><b>Project VEATAL</b> - Design of heavy Airships (Toulouse, France).</p> <ul style="list-style-type: none"> <li>• Project leader (6 members): Representative of the ISAE group. September 2007</li> <li>• Load/unload system, general design, &amp; analysis of the pendulum effect in the load. March 2008</li> </ul> <p><b>Formula - hybrid vehicle</b> (electric-combustion) of Embry-Riddle Aeronautical University.</p> <ul style="list-style-type: none"> <li>• 2nd place of the US National competition in New Hampshire. January 2007</li> <li>• Team in charge of the control system and race scenarios. July 2007</li> </ul> <p>Improvement of the Aerodynamic Performances of the QSJ - Gulfstream Incorporation.</p> <ul style="list-style-type: none"> <li>• Design of the wing/fuselage interface. August 2006</li> <li>• Flight envelope of the Quiet Supersonic Jet (QSJ). December 2006</li> </ul>
TEACHING EXPERIENCE	<p>Tutor and Grader 2005-2007</p> <ul style="list-style-type: none"> <li>• Mathematics department of ERAU. Differential equations and physics for pilots.</li> <li>• Aerospace department of ERAU. Aerodynamics and aircraft structures.</li> </ul> <p>Engineering Education Research. March 2014 to present</p> <ul style="list-style-type: none"> <li>• Course which provides support for teachers, teaching assistants, administrators and departmental heads concerned with improving teaching and learning.</li> </ul>
OTHER EXPERIENCES	<p>Professional Skydiving Tandem Instructor. 1999- Present</p> <ul style="list-style-type: none"> <li>• More than 2000 jumps as instructor and cameramen. Author of several skydiving T.V. shows and advertisements.</li> <li>• Current <b>Private Pilot's license</b>.</li> </ul> <p>Treasurer of the Singapore International Aerospace Association. 2006-2007</p>
LANGUAGES	<p>Spanish, English (fluent), French (current), German (current), Swedish(basic).</p>
COMPUTER SKILLS	<ul style="list-style-type: none"> <li>• Programming: MATLAB, C++, Fortran, Python.</li> <li>• Others: Ansys-CFX, COBAYA3, SUBCHANFLOW, CATIA-V5, Nastran, Star-CD.</li> <li>• Environment: Windows (good skills with office) and Linux.</li> </ul>